https://doi.org/10.15388/vu.thesis.971
https://orcid.org/0009-0001-4851-4292

VILNIUS UNIVERSITY
CENTER FOR PHYSICAL SCIENCES AND TECHNOLOGY

Karolis Daugevičius

Star Clusters in Galactic Discs. Limits of Aperture Photometry Applications

DOCTORAL DISSERTATION

Natural Sciences,
Physics (N 002)

VILNIUS 2026

This dissertation was prepared between 2022 and 2026 at Center for Physical Sciences and Technology, Department of Fundamental Research. The research was supported by the Research Council of Lithuania: project No. S-MIP-24-98 and scholarship for academical accomplishments No. P-DAP-25-132.

Academic Supervisor – Dr. Rima Stonkutė (Center for Physical Sciences and Technology, Natural Sciences, Physics – N 002)

This Doctoral Dissertation will be Defended in a Public Meeting of the Dissertation Defence Panel:

Chairman – Dr. Kastytis Zubovas (Center for Physical Sciences and Technology, Natural Sciences, Physics, N 002)

Members:
Dr. Vidas Dobrovolskas (Vilnius University, Natural Sciences, Physics, N 002),

Dr. Mindaugas Karčiauskas (Center for Physical Sciences and Technology, Natural Sciences, Physics, N 002),

Prof. Dr. Arūnas Kučinskas (Vilnius University, Natural Sciences, Physics, N 002),

Dr. Kārlis Puķītis (University of Latvia, Natural Sciences, Physics, N 002).

The dissertation shall be defended at a public meeting of the Dissertation Defence Panel at 14:00 on 18 September 2026 in Room D401 of the Center for Physical Sciences and Technology.

Address: Saulėtekio av. 3, Vilnius, Lithuania.
Tel. +370 5 264 8884; email: office@ftmc.lt.

https://doi.org/10.15388/vu.thesis.971)
https://orcid.org/0009-0001-4851-4292

VILNIAUS UNIVERSITETAS
FIZINIŲ IR TECHNOLOGIJOS MOKSLŲ CENTRAS

Karolis Daugevičius

Žvaigždžių spiečiai galaktikų diskuose. Apertūrinės fotometrijos taikymų ribos

DAKTARO DISERTACIJA

Gamtos mokslai,
Fizika (N 002)

VILNIUS 2026

Disertacija rengta 2022–2026 metais Fizinių ir technologijos mokslų centro Fundamentinių tyrimų skyriuje. Mokslinius tyrimus rėmė Lietuvos mokslo taryba: stipendija už akademinius pasiekimus nr. P-DAP-25-132 ir projektas nr. S-MIP-24-98.

Mokslinė vadovė – dr. Rima Stonkutė (Fizinių ir technologijos mokslų centras, gamtos mokslai, fizika, N 002)

Gynimo taryba:

Pirmininkas – dr. Kastytis Zubovas (Fizinių ir technologijos mokslų centras, gamtos mokslai, fizika, N 002)

Nariai:
dr. Vidas Dobrovolskas (Vilniaus universitetas, gamtos mokslai, fizika, N 002),
dr. Mindaugas Karčiauskas (Fizinių ir technologijos mokslų centras, gamtos mokslai, fizika, N 002),
prof. dr. Arūnas Kučinskas (Vilniaus universitetas, gamtos mokslai, fizika, N 002),
dr. Kārlis Puķītis (Latvijos universitetas, gamtos mokslai, fizika, N 002).

Disertacija ginama viešame Gynimo tarybos posėdyje 2026 m. rugsėjo mėn. 18 d. 14:00 val. Fizinių ir technologijos mokslų centro D401 auditorijoje.

Adresas: Saulėtekio al. 3, Vilnius, Lietuva.
Tel. +370 5 264 8884; email: office@ftmc.lt.

Acknowledgements

My deepest gratitude goes to my wife Gina Justina, who has stood there by my side throughout my whole academic journey. I am grateful for her patience and understanding during countless sleep-deprived nights I spent working at my computer, and, most importantly, for her endless love and support. She continually motivates me to pursue my goals and be a better person, helps me forget life's difficulties, even if only for a moment when I see her smile, and shows me how much there is to experience and enjoy in the world, particularly culture-wise.

I would also like to thank my parents, Aušra and Gintaras, who instilled in me from an early age the importance of science and education. They have always supported me and encouraged me to choose my own path.

I am extremely grateful to my supervisor, Rima Stonkutė, who consistently encouraged me to become a self-reliant researcher, and, through her own example, taught me to pay attention to even the smallest details. I would also like to thank Vladas Vansevičius, who played an essential role in shaping me as a scientist. Our discussions taught me to approach research both critically and creatively. I am also grateful to Eimantas Kriščiūnas, my roommate-at-work, with whom I have shared a quiet yet fruitful academic partnership.

I would like to thank my friends – Vincas, Rūta, Lukas, Paulius, Auksė, Evaldas, Matas, Greta, and Gedas. I could write a paragraph about each of you and explain why you are important to me, but, as I never thought I would say, there are simply too many of you, so I will summarise. Each of you has made my life more interesting, enjoyable, and fun in countless ways throughout this period of my life, and I have always felt your support.

I am grateful to Natalia Lahén for kindly sharing the `SPHGAL` + `KETJU` model data and for providing helpful comments and suggestions, which were essential for the analysis and discussion presented in the Chapter 6 of this thesis. I also thank Emily L. Hunt for providing clarifications regarding Hunt & Reffert (2024) catalogue data, as well as for additional comments and suggestions valuable for this study. I also appreciate the effort of the community behind developing and maintaining various `Python` packages, that were essential in this work, particularly `matplotlib` (Hunter 2007), `Astropy` (Astropy Collaboration et al. 2013, 2018), `APLpy` (Robitaille & Bressert 2012), `SciPy` (Virtanen et al. 2020). I acknowledge the usage of OpenAI's ChatGPT for improving LaTeX formatting and language editing.

Contents

List of abbreviations

2D, 3D, 4D – two-, three-, four-dimensional
2MASS – Two Micron All Sky Survey
AC – aperture correction
ACS – Advanced Camera for Surveys
AGB – asymptotic giant branch
arcsec – second of arc
CBR – cluster-to-background ratio
CI – colour index
CMD – colour-magnitude diagram
CMF – cluster mass function
CR – cosmic ray
EFF – Elson-Fall-Freeman
FGC – flux growth curve
GC – globular cluster
GMC – giant molecular cloud
HST – *Hubble* Space Telescope
IMF – initial mass function
IR – infrared
JWST – *James Webb* Space Telescope
KDE – kernel density estimate
MIPS – Multi-Band Imaging Photometer for Spitzer
ML – machine-learning
MS – main sequence
MSTO – main sequence turn-off
MW – Milky Way galaxy
yr, Myr, Gyr – year, megayear (a million years), gigayear (a billion years)
OC – open cluster
pc, kpc, Mpc – parsec, kiloparsec, megaparsec
PDF – probability distribution function
PHAT – Panchromatic *Hubble* Andromeda Treasury
PHATTER – PHAT: Triangulum Extended Region
PHAST – Panchromatic *Hubble* Andromeda Southern Treasury
PMS – post-main-sequence stars
PSF – point spread function
PT – Paukščių Takas (santraukoje)
RGB – red giant branch
RSG – red supergiant
SN – supernova
SPS – stellar population synthesis
SSP – single (simple) stellar population
S/N – signal-to-noise ratio
TCD – two-colour diagram
UV – ultraviolet
WFC3 – Wide Field Camera 3
WFPC2 – Wide Field and Planetary Camera 2
YSG – yellow supergiant

Introduction

Motivation

It is widely accepted that a large fraction of stars, at least in the Local Universe, form in clustered environments within galactic discs, such as star clusters, stellar associations, and moving groups (Lada & Lada 2003). The vast majority of these systems dissolve into the general stellar population of their host galaxy within the first few tens of Myr (Lada & Lada 2003; Bressert et al. 2010; Portegies Zwart et al. 2010; Krumholz et al. 2019), making them fundamental building blocks of galactic stellar populations. Only a small fraction of gravitationally bound star clusters survive for longer periods of hundreds of Myr (Lamers 2009; Whitmore 2009). Studies of these long-lived systems are therefore essential for understanding the physical processes governing star formation, as well as the formation and evolution of galactic structures, because star clusters preserve information about the star-formation history of their host galaxies over extended timescales.

Although it is natural to expect that the most detailed studies of clusters are possible in our Galaxy, the Milky Way (MW), such studies are limited to a relatively small local volume of a few kpc (Kharchenko et al. 2013; Hunt & Reffert 2024). This limitation arises because the Solar System is located within the Galactic disc, where interstellar extinction severely obscures the view. Thus, studies of extragalactic star clusters are crucial for gaining knowledge about cluster formation and evolution across a broader range of environments and cluster parameters.

One of the most effective approaches for such studies is aperture photometry, which enables the determination of star cluster physical and structural parameters from measurements of integrated light. The method allows large samples of clusters to be analysed efficiently, making it particularly valuable for studies of nearby galactic discs. However, integrated photometry is susceptible to significant uncertainties and biases (Bridžius et al. 2008; Fouesneau & Lançon 2010; Beerman et al. 2012; Anders et al. 2013; de Meulenaer et al. 2017), primarily introduced by stochastic stellar sampling and complex sky background effects. Although novel methodologies have been developed to tackle and mitigate these issues (e.g., de Meulenaer et al. 2013, 2017; Naujalis et al. 2021), a comprehensive and homogeneous investigation, that would provide a more complete picture of the practical limitations of aperture photometry for extragalactic star cluster studies has been lacking.

Given this, the goal of this thesis is twofold. First, we determine the intrinsic limits of aperture photometry accuracy and applicability for studies of nearby extragalactic clusters. We achieve this by employing stochastic cluster models and their realistic mock observations designed to mimic real clusters observed in the Andromeda Galaxy

(M 31) by the Panchromatic *Hubble* Andromeda Treasury survey (PHAT; Dalcanton et al. 2012; Johnson et al. 2015). The focus on M 31 and the PHAT survey is motivated by the proximity of M 31 and the exceptional quality and spatial resolution of the PHAT data, which together provide unique opportunity for detailed extragalactic cluster study in a spiral galaxy similar to the MW.

The second goal of this thesis is to investigate the star cluster population in the M 31 disc at the boundary of these methodological limitations. By analysing this population, we aim to improve the understanding of star cluster formation and evolution in M 31 and, more generally, in galactic discs similar to that of the MW. This study also serves as a demonstration of the scientific potential of aperture-photometry-based cluster studies and highlights the key areas in which further theoretical, observational, and methodological improvements are needed.

The objective of the thesis

Determine the limitations of aperture photometry in studying star clusters in the discs of nearby galaxies and investigate the structural evolution of clusters in the Andromeda Galaxy (M 31).

The main tasks of the thesis

- Generate a large grid of stochastic star cluster models and and perform their multicolour measurements.
- Determine intrinsic limits of application of aperture photometry imposed by stochastic effects.
- Assess the impact of sky background on the accuracy of aperture photometry.
- Investigate the structural evolution of M 31 disc clusters up to 800 Myr.

Results and statements to be defended

1. For characteristic low-mass ($\lesssim 10^3 M_\odot$) star clusters, randomness of viewing angle introduces intrinsic uncertainties of up to ~0.05 mag in colour indices and up to 20% in structural parameters.
2. In typical M 31 PHAT fields, determination of age, mass, and extinction (assuming known metallicity) is achievable for star clusters at 100 Myr for $M \gtrsim 500\,M_\odot$ and at 1 Gyr for $M \gtrsim 1600\,M_\odot$.
3. Aperture radii used for cluster colour measurement must exceed their half-light radii, R_{50}; the optimal values up to $2\times R_{50}$ are suggested for typical disc clusters in M 31.
4. The cluster mass function in M 31 at 1 Gyr can be recovered down to: $\sim 500\,M_\odot$ in the outer disc, $\sim 1500\,M_\odot$ in star-forming regions, and $\sim 3000\,M_\odot$ in the inner disc.
5. M 31 disc star clusters are initially compact and expand rapidly within first ~30 Myr, with their R_{50} increasing by more than a factor of two.
6. M 31 disc clusters older than 100 Myr exhibit a weak mass–radius relation, $R_{50} \propto M^{0.18\pm0.01}$, that does not significantly depend on galactocentric radius.

Publications included in the thesis

1. Kriščiūnas, E., **Daugevičius, K.**, Stonkutė, R., & Vansevičius, V., *Deriving physical parameters of unresolved star clusters. VII. Adaptive aperture photometry of the M 31 PHAT star clusters*, 2023, A&A, 677, A100

2. **Daugevičius, K.**, Kriščiūnas, E., Cicėnas, E., Stonkutė, R., & Vansevičius, V., *Deriving physical parameters of unresolved star clusters. VIII. Limits of aperture photometry for star cluster studies*, 2024, A&A, 688, A131

3. **Daugevičius, K.**, Stonkutė, R., Kriščiūnas, E., Cicėnas, E., & Vansevičius, V., *Deriving physical parameters of unresolved star clusters. IX. Sky background effects in the aperture photometry*, 2025, A&A, 699, A290

4. Kriščiūnas, E., Stonkutė, R., **Daugevičius, K.**, Cicėnas, E., & Vansevičius, V., *A Catalog of Star Cluster Parameters in the Northeastern Part of the M31 Disk*, 2026, ApJS, submitted for publication

5. **Daugevičius, K.**, Kriščiūnas, E., Stonkutė, R., & Vansevičius, V., *Deriving physical parameters of unresolved star clusters. X. Size evolution of young star clusters in the M 31 disc*, 2026, A&A, submitted for publication

Presentations at conferences

1. **Daugevičius K.**, Stonkutė R., Vansevičius V., *Stochasticity of star cluster parameters*, Open Readings 2023, Vilnius, 2023. (oral presentation)

2. **Daugevičius K.**, Kriščiūnas E., Cicėnas E., Stonkutė R., Vansevičius V., *Žvaigždžių spiečių tyrimo galimybės artimoje Visatoje*, 45-oji Lietuvos Nacionalinė Fizikos Konferencija, Vilnius, 2023. (poster presentation)

3. **Daugevičius K.**, Kriščiūnas E., Cicėnas E., Stonkutė R., Vansevičius V., *The limits of star cluster aperture photometry in the Local Universe*, Open Readings 2024, Vilnius, 2024. (oral presentation)

4. **Daugevičius K.**, Kriščiūnas E., Cicėnas E., Stonkutė R., Vansevičius V., *Limitations of aperture photometry of star cluster studies*, MODEST-24, Warsaw, Poland, 2024. (poster presentation)

5. **Daugevičius K.**, Kriščiūnas E., Cicėnas E., Stonkutė R., Vansevičius V., *Limitations of star cluster studies in the Local Universe*, European Astronomical Society Annual Meeting EAS 2025, Cork, Republic of Ireland, 2025. (poster presentation)

6. **Daugevičius K.**, Kriščiūnas E., Cicėnas E., Stonkutė R., Vansevičius V., *Towards Automated Aperture Photometry of Star Clusters*, Bridging Scales 2025, Matera, Italy, 2025. (poster presentation)

7. **Daugevičius K.**, Kriščiūnas E., Cicėnas E., Stonkutė R., Vansevičius V., *Mass Function of Star Clusters in the M 31 Disc*, Stellar Origins 2025, Vienna, Austria, 2025. (oral presentation)

8. **Daugevičius K.**, Kriščiūnas E., Cicėnas E., Stonkutė R., Vansevičius V., *M 31 disko žvaigždžių spiečių dydžio ir masės funkcijos evoliucija*, 46-oji Lietuvos Nacionalinė Fizikos Konferencija, Kaunas, 2025. (oral presentation)

9. **Daugevičius K.**, Kriščiūnas E., Stonkutė R., Vansevičius V., *Star clusters size evolution in M 31*, Open Readings 2026, Vilnius, 2026. (poster presentation)

10. **Daugevičius K.**, Kriščiūnas E., Stonkutė R., Vansevičius V., *Are star clusters in the M31 disc shaped by the galactic tidal field?* How stars move around and what they tell us about galaxies' masses, formation and evolution – from the Milky Way to giant elliptical galaxies, Sexten, Italy, 2026. (oral presentation)

Summer schools

1. COST NanoSpace James Webb Space Telescope (JWST) Training School, San Cristóbal de La Laguna, Spain, 2023 (on-line)

2. IMPRS-HD Summer School 2023 Unravelling Galaxy Evolution with JWST, Heidelberg, Germany, 2023

3. ORP School on Multi-messenger Astrophysics, Durham, United Kingdom, 2024

Contribution of the author

The author developed all programming scripts used for stochastic star cluster modelling and aperture photometry measurements of mock observations. The author also selected background fields and cleaned them of observational defects. All analyses presented in this thesis, including both simulated cluster measurements and the investigation of the M 31 disc cluster population, were carried out by the author. The interpretation of the results was performed together with the co-authors. The author is the first author of the three publications that form the basis of this thesis. In addition, the author contributed as a co-author of two publications focused on the development of M 31 star cluster aperture photometry and cluster parameter catalogues essential for the analysis presented here.

Chapter 1

Star clusters in the Local Universe

A fundamental issue in studies of star clusters is how these systems should be defined. Numerous different definitions exist in the literature. For example, Lada & Lada (2003) define a cluster as a group of stars with a sufficiently high mass density to resist tidal disruption in its local environment, while Portegies Zwart et al. (2010) describe a cluster as a gravitationally bound group of stars. However, such definitions may also apply to systems not usually regarded as star clusters, such as multiple star systems or even galaxies. The variety of definitions and associated issues have been discussed extensively in the reviews by Krumholz et al. (2019) and Krause et al. (2020). In the context of this thesis, we generally adopt a definition similar to ones proposed in these reviews: a star cluster is a gravitationally bound group of stars within a closed tidal surface, containing at least 12 member stars and not dominated by dark matter. This definition distinguishes star clusters from both multiple stellar systems and galaxies, and requires that the system occupies a region where its self-gravity dominates over external tidal forces. Although the threshold of 12 stars is somewhat arbitrary and origins can be traced back to a historical work of Trumpler (1930), it approximately marks the transition from few-body dynamics to the behaviour of a many-body stellar system.

Regardless of the exact definition, star clusters have played an important role throughout much of human history, from Paleolithic cultures (Rappenglück 2001) up to the modern era. Prime example is one of the nearest and easily visible by naked-eye – Pleiades cluster. In ancient times, the Pleiades served primarily as a marker of seasonal change and formed the basis of early agricultural calendars, as its appearance and disappearance in the night sky indicated planting or harvest periods. The importance of Pleiades in the livelihood of many cultures, lead to it being deeply connected with mythological and religious beliefs across the world, through which its significance transitioned into art, literature, popular culture, and even commercial branding, thus reaching our times.

From the perspective of modern astrophysics, Pleiades also played an important role in the development of our scientific understanding of star clusters. In 1610, Galileo included a sketch of Pleiades in *Sidereus Nuncius* and stated that "the Galaxy is in fact nothing else but a congeries of innumerable stars grouped together in clusters", an idea which can be argued to be remarkably close to the modern view of stellar systems. Over the following centuries, rapid improvements in telescopes and observational techniques led to quickly expanding star cluster catalogues, most notably the *New General Catalogue of Nebulae and Clusters of Stars* (NGC) compiled by Dreyer (1888). One of the most important discoveries in early modern astrophysics also originated from star cluster studies. Using stars in the Pleiades and Hyades clusters, Hertzsprung (1911) found that stellar brightness is related to colour and spectral properties. Shortly afterwards, Russell (1914) independently plotted the absolute magnitudes of Hyades stars as a function of spectral type/temperature. Discovery of these relations led to the development of the Hertzsprung–Russell diagram, or colour-magnitude diagram (CMD), which remains one of the essential tools for understanding stellar evolution. Later studies found that these diagrams differ between clusters, which was eventually recognised as an effect of difference in age. In fact, CMDs are a crucial tool for cluster age derivation up to this day (see Section 2.3).

The modern astrophysical understanding of star clusters and their importance for studying various physical processes across Cosmic time have been well-summarised in a number of extensive reviews published in the last decade (e.g., Bastian & Lardo 2018; Renaud 2018; Krumholz et al. 2019; Adamo et al. 2020; Krause et al. 2020). Here we briefly summarise the current general picture of the lifecycle of star clusters; a more detailed overview can be found in the aforementioned review papers and references therein.

Star clusters typically form hierarchically within the dense cores of giant molecular clouds (GMCs), the densest regions of the interstellar medium. As GMCs undergo gravitational collapse, gas is converted into stars through ongoing accretion and fragmentation. The star formation eventually stops when stellar feedback from the already-ignited stars disperses the remaining gas. In the densest regions, where clusters are forming, star-formation efficiency can become sufficiently high for the resulting stellar systems to remain gravitationally bound after gas removal. Recent studies (Knutas et al. 2025; Pedrini et al. 2026) suggest that clusters emerge from their natal clouds on timescales of ~5–10 Myr. During the first ~100 Myr after gas removal, cluster destruction is driven by strong tidal shocks within their native star-forming regions, as well as through mass loss associated with stellar evolution processes. At later stages, surviving clusters continue to lose mass through two-body relaxation and stochastic shock encounters with GMCs, processes that affect lower-mass systems more strongly. Although the vast majority of clusters dissolve within the first ~10 Myr (Lada & Lada 2003; Lamers 2009; Whitmore 2009; Bressert et al. 2010), those that survive for hundreds of Myr or longer preserve important information about the star-formation history and dynamical evolution of their host galaxies, as well as general physical processes governing star formation.

Detailed, high-resolution, and statistically rich analysis of extragalactic star clusters became possible only in the last few decades, primarily due to launch and operation of *Hubble* Space Telescope (HST). Before, most of the understanding about clusters came from the studies in the Milky Way (MW), and to some extent its nearest large satellites – the Magellanic Clouds. Therefore, in the following Section, we briefly overview the star cluster system of our Galaxy.

1.1 Star clusters in the Milky Way

Historically, Milky Way population of bound star clusters have been divided into two main groups: open clusters (OCs) and globular clusters (GCs). OCs are located primarily in the Galactic disc and generally are young ($\lesssim$1 Gyr; although several notable exceptions of older OCs, such as NGC 188 or M 67, exist), and have masses below $\sim 10^5\,M_\odot$. Since this thesis focuses on disc clusters, the studied systems largely correspond to the classical OC population and trace recent star formation and its properties within galactic discs. Closely related objects are stellar associations, which share many properties with OCs but are gravitationally unbound and usually much more extended (Blaauw 1964; Gieles & Portegies Zwart 2011; Gouliermis 2018; Adamo et al. 2020; Krause et al. 2020).

In contrast, GCs are typically old and massive stellar systems ($t > 1$ Gyr and present-day mass $M \gtrsim 10^4\,M_\odot$), predominantly located in the Galactic bulge and halo. The oldest MW GCs are estimated to be older than $\sim$13 Gyr and therefore provide important constraints on the age of the Universe (Krause et al. 2020); historically, such constraints were available even before those derived from measurements of the Cosmic Microwave Background. GCs also serve as valuable tracers of galaxy assembly and long-term galactic evolution on cosmological timescales (West et al. 2004; Brodie & Strader 2006; Forbes et al. 2018; Kruijssen et al. 2019).

For many years, both OCs and GCs were considered examples of simple stellar populations (SSPs), meaning that all cluster stars formed in a single burst of star formation from chemically homogeneous natal gas cloud and therefore shared the same age and chemical composition. However, this picture has changed significantly in recent decades. It was found that majority of GCs host multiple stellar populations, showing distinct main sequences and significant star-to-star abundance variations in light elements, whereas the SSP approximation remains generally valid for OCs (Bastian & Lardo 2018). This suggests that a more physically motivated distinction may be between clusters comprised of single and multiple populations. Moreover, observations of other galaxies, including Local Group members, have shown that young disc clusters can reach masses comparable to classical GCs (Portegies Zwart et al. 2010; Adamo & Bastian 2015), suggesting that the traditional classification into OCs and GCs is not universal. However, it remains strong due to historical reason, clear distinction in the MW, and transitioned into extragalactic studies due to convenience.

Significant progress in studies of MW OCs began with modern astrometric and near-infrared (IR) surveys. Astrometric data collected with *Hipparcos* satellite enabled the discovery of a significant number of new OCs in the nearby vicinity (Perryman et al. 1997; Platais et al. 1998). Meanwhile, near-IR observations such as the Two Micron All Sky Survey (2MASS; Skrutskie et al. 2006) enabled the detection of more than thousand new nearby OC candidates located in the Galactic disc, obscured by interstellar dust and therefore difficult to detect at optical wavelengths. Based on near-IR data, Kharchenko et al. (2013) produced a catalogue of more than 3000 objects, of which the major fraction were classified as OCs, and for more than 1500 objects basic astrophysical parameters (including age, size and colour excess) were determined for the first time.

The era of the *Gaia* observatory marked another major step of progress in MW cluster studies. High-precision astrometry resulted in a further significant expansion of the known cluster census in the Galactic disc (Cantat-Gaudin 2022; Hunt & Reffert

2024) and enabled detailed star-by-star cluster studies. For example, the catalogue of Hunt & Reffert (2024) contains more than 5600 objects compatible with being bound open clusters. Despite this progress, MW studies remain limited to a relatively small Galactic volume and are affected by strong selection effects (Hunt et al. 2026), primarily caused by interstellar extinction within the disc. This complicates our ability to explore correlations between cluster parameters and environmental trends in the MW, despite having a numerous sample of clusters. Therefore, studies of extragalactic cluster populations are essential for achieving a more complete understanding of cluster formation and evolution across diverse galactic disc environments.

1.2 Cluster systems in nearby galaxies

Although several studies have explored cluster populations within the Local Group discs (e.g., Vansevičius et al. 2009; San Roman et al. 2012; Johnson et al. 2016, 2017; Gatto et al. 2021; Wainer et al. 2022), many of them either relied on rather small statistical samples, covered only narrow cluster parameter regimes, or were limited to only certain relatively small regions of their host galaxies. One of the most limiting factors is that Local Group galaxies due to their proximity occupy large areas on the sky. As a result, obtaining deep, resolved or semi-resolved observations over a substantial fraction of a galactic disc, that would cover variety of environments, with facilities such as the *Hubble* Space Telescope (HST) requires extreme amounts of observational resources, mainly time, having rendered such surveys practically impossible up to recent years. Although this situation is gradually improving through dedicated large-scale surveys being granted time and the era of new generation wide-field observatories, such as *Euclid* and the *Nancy Grace Roman* Space Telescope, homogeneous studies of large cluster samples spanning broad ranges of masses, ages, and environments within the Local Group remain relatively scarce.

Consequently, the most extensive homogeneous investigations of large samples of clusters have mostly focused on galaxies beyond the Local Group. However, such studies are usually limited to relatively massive clusters ($>10^{3.5}$ $M_{\odot}$), because lower-mass systems are difficult to detect and characterise at larger distances. Therefore, detailed studies within the Local Group are needed to probe the low-mass regime and obtain a more complete understanding of cluster formation and evolution in star-forming galactic discs. However, we first briefly review the main results from studies of spiral galaxies beyond the Local Group.

1.2.1 Spiral galaxies outside the Local Group

Here we focus primarily on how cluster sizes vary and correlate with other cluster properties, such as age, mass, and location within the host galaxy, since these relations are central to the analysis presented in Chapter 6. Star cluster structural properties and internal stellar kinematics encode information about the conditions under which clusters formed and how they subsequently evolve under the influence of internal dynamics and environmental effects. Although kinematic data is scarce beyond the MW, and direct real-time observation of cluster evolution is impossible due to astronomical timescales, statistically large cluster samples enable us to investigate various scaling relations between cluster structure and other parameters, a prime example of that being age–radius and mass–radius relations, which allow us to constrain theoretical models of star cluster formation and evolution. It is useful to note here, that a common cluster size estimate in extragalactic studies is the half-light (or effective) radius, R_{50}, which encloses 50% of total cluster's flux.

Over the past two decades, with the help of HST, the cluster age–radius relation has been examined extensively in numerous studies of spiral galaxies beyond the Local Group, sometimes yielding conflicting results. Notably, Larsen (2004) analysed a combined sample of star clusters from 18 nearby spiral galaxies based on archival HST WFPC2 data and found no compelling evidence of significant correlation between cluster age and size. In contrast, a more recent study by Brown & Gnedin (2021), based on young star clusters in 31 galaxies from the LEGUS survey (Adamo et al. 2017; Cook et al. 2019), reported a statistically significant increase in cluster radius with age. Specifically, they found that between 1–10 Myr and 10–100 Myr age bins, the typical effective radius at cluster mass of $10^4\,M_\odot$ grows from 2.36 to 2.51 pc, while clusters with $10^5\,M_\odot$ expand from 3.58 to 4.76 pc. However, no further evolution is observed between the 10–100 Myr and 100–1000 Myr bins.

Considering individual nearby spiral galaxies, the star cluster population in M 51 has been studied extensively. Using HST WFPC2+NICMOS3 data, Bastian et al. (2005) detected a weak tendency for younger clusters to be larger than older ones, but found no robust age–radius correlation overall. In contrast, Lee et al. (2005), based on HST WFPC2 data, reported a weak increase of cluster size with age, defined by a power-law $r \propto t^{\lambda}$, with $\lambda = 0.13 \pm 0.02$ (0.06 ± 0.02 after accounting for the mass–size relation). Using HST ACS data, Scheepmaker et al. (2007) found that cluster radii increase with colour, particularly in $B - V$, and argued that if the colour range reflects an age spread, this implies expansion with age, consistent with Lee et al. (2005). Combining WFPC2 and ACS data and applying a similar methodology to Lee et al. (2005), Hwang & Lee (2010) derived a somewhat stronger age–size relation, with a power-law index $\lambda = 0.25 \pm 0.03$ (0.14 ± 0.03 after correcting for the mass–size relation). More recently, Chandar et al. (2016) analysed ~3800 star clusters in M 51 and found stronger evidence for early expansion: clusters more massive than $3 \times 10^4\,M_\odot$ at ages 100–400 Myr have R_{50} values larger by a factor of ~(3–4) compared to clusters younger than 10 Myr. Overall, the evidence increasingly supports cluster size evolution with age in M 51.

M 83 is another nearby spiral with well-studied star cluster populations. Using observations of two HST WFC3 fields, Bastian et al. (2012) found a significant increase of cluster radius with age. The age–size relation is well described by a $r \propto t^{\lambda}$ power-law with $\lambda = 0.22 \pm 0.04$ in the inner field and $\lambda = 0.24 \pm 0.06$ in the outer field. They interpreted this trend as either a physical effect of cluster expansion or a possible selection effect related to the light profile fitting procedure. Expanding the analysis to seven HST WFC3 fields covering a large fraction of the M 83 disc, Ryon et al. (2015) reported a similar age–radius correlation, best described by a power law with $\lambda = 0.26 \pm 0.07$. Importantly, they were able to reject the fitting procedure effect proposed by Bastian et al. (2012), implying that the observed age–radius relation likely reflects genuine cluster size evolution.

Ryon et al. (2017) examined the sizes of young massive star clusters ($M \geq 5 \times 10^3\,M_\odot$ and $t \leq 200$ Myr) of two LEGUS galaxies, NGC 628 and NGC 1313. In NGC 1313, they found the cluster age–size relation to be broadly similar to that reported for M 83 by Ryon et al. (2015), with a slope of ~0.3. Meanwhile, the correlation in NGC 628 is somewhat weaker, with a slope of ~0.1. Ryon et al. (2017) suggest that this difference may be due to observational limitations: the ability to detect smaller clusters in M 83 and NGC 1313, compared to NGC 628, provides better leverage for constraining the age–radius relation, leading to stronger inferred correlations.

The mass–radius relation is another important and widely studied property of cluster populations. Larsen (2004) reported a shallow trend, $r \propto M^{0.10\pm0.03}$. Mora et al. (2009) performed a similar study of five nearby spiral galaxies based on HST ACS and WFPC2 data, adopting similar methodological approach to Larsen (2004). They found that between these five galaxies power-law slope of the relation varies from 0.16 to 0.34. For clusters from the LEGUS survey, Brown & Gnedin (2021) derived a steep relation, $r \propto M^{0.24\pm0.01}$. Importantly, they found evidence for a possible evolution of the star cluster mass–radius relation with age: the power-law index increases from 0.18±0.03 for 1–10 Myr to 0.28±0.02 for 10–100 Myr, remaining roughly constant at older ages. However, both studies combined clusters from multiple galaxies, thus these trends may reflect only an average mass–radius relation, potentially masking galaxy-to-galaxy variations.

As in the case of the age–radius relation, studies of the mass–radius correlation in M 51 have yielded contrasting results. While Bastian et al. (2005) and Scheepmaker et al. (2007) found no evidence for a correlation between cluster mass and radius, Lee et al. (2005) reported a shallow power-law relation, where radius depends on mass with an index of 0.14±0.03. Similarly, Hwang & Lee (2010) derived a best-fit power-law relation with an index of 0.16±0.02, consistent with the result of Lee et al. (2005).

For M 83, Bastian et al. (2012) found no substantial evidence for a presence of cluster mass–radius relation. In contrast, Ryon et al. (2015) reported a significant correlation, with cluster radius following a power-law of index 0.3±0.1, and, similarly to Brown & Gnedin (2021), noted that the relation strengthens with age. Ryon et al. (2017) found no significant relation between cluster mass and radius in NGC 628, but in NGC 1313 they observed a modest cluster radius increase with mass; however, this trend disappeared when the sample was divided into age bins. A study of super star clusters in the disc of M 82 by Cuevas-Otahola et al. (2021) reported a power-law mass–radius relation with an index of 0.29±0.05. In a review combining star clusters from numerous nearby galaxies, Krumholz et al. (2019) concluded that the mass–radius relation is broadly consistent with a general scaling of constant density $R_{50} \propto M^{1/3}$.

Several studies have investigated correlations between cluster radius and galactocentric distance, R_{GC}, with mixed results. Investigations of this relation can provide important insight into the role of environment in shaping star clusters. In M 51, Bastian et al. (2005) found no clear relation, whereas Scheepmaker et al. (2007) reported a shallow trend, $r \propto R_{GC}^{0.12\pm0.02}$. For M 83, Bastian et al. (2012) observed slightly larger clusters in the outer field, but attributed this to an age difference; similarly, Ryon et al. (2015) found no significant radius–distance correlation once the age–distance relation was accounted for. No significant trends were detected in NGC 628 or NGC 1313 by Ryon et al. (2017). In this context, it is noteworthy that, within the Local Group, San Roman et al. (2012) reported no strong relation in M 33, but found substantial trends in the MW, the Andromeda Galaxy, and the Magellanic Clouds; however, they were determined based on massive/globular clusters.

1.2.2 The Andromeda Galaxy

Since most of the analysis presented in this thesis is focused on the Andromeda Galaxy (M 31), we briefly overview the galaxy, its star cluster system, and previous studies (see Table 1.1 for the main properties of the galaxy). M 31 is the nearest large spiral galaxy, and it is the largest and most dominant member of the Local Group, with a total mass larger than that of the MW (Hammer et al. 2025). At a distance of ~785 kpc, where $1'' \approx 3.8$ pc, modern space-based observatories can resolve its stellar populations and star clusters into individual stars across a wide range of disc environments, enabling detailed investigations of cluster formation, evolution, and disruption processes. This makes M 31 the best candidate for studying these aspects in a spiral galaxy similar to the MW.

The M 31 disc is observed at a high inclination angle of ~77.5° (van der Marel et al. 2019), which complicates detailed analysis of its large-scale structure due to strong projection effects. Although its spiral pattern is not clearly visible in direct images, studies across multiple wavelength ranges have identified several spiral-arm segments in de-projected maps (Tenjes et al. 2017). One of the most prominent disc features is the well-known star-forming "ring of fire" located at a galactocentric distance of ~10 kpc (Gordon et al. 2006; Kang et al. 2012; Lewis et al. 2015; De Somma et al. 2025), whose centre appears to be offset from the galactic centre by ~1 kpc (Block et al. 2006). An additional inner dust ring, offset from the galactic centre by approximately 0.5 kpc, has also been identified (Block et al. 2006). The peculiar morphology of these two off-centre rings has been suggested to be evidence of a relatively recent direct collision with a satellite galaxy, most likely M 32 (Gordon et al. 2006; Block et al. 2006; Dierickx et al. 2014). More generally, M 31 appears to have experienced a more complex evolutionary history than the MW, including several major merger events during the past ~4 Gyr and possibly with a most recent one happening ~2 Gyr ago (Williams et al. 2015; Ferguson & Mackey 2016; Hammer et al. 2018; D'Souza & Bell 2018).

For past few decades, studies of the M 31 cluster population focused primarily on GC-like objects (Barmby et al. 2000; Barmby & Huchra 2001; Barmby et al. 2002; Galleti et al. 2004; Kim et al. 2007; Puzia et al. 2005; Caldwell et al. 2009, 2011; Caldwell & Romanowsky 2016). Early attempts to catalogue disc clusters (Hodge 1979) were later shown to be heavily contaminated by various unbound objects, such as stellar associations. A start of detailed disc cluster studies can be associated with the high-resolution HST observations (Williams & Hodge 2001b,a; Barmby et al. 2009; Hodge et al. 2009, 2010; Perina et al. 2010). However, the cluster samples of these studies were generally small, often consisting of only a few tens of clusters.

The Subaru Suprime-Cam survey of south-western disc region (Kodaira et al. 2004; Narbutis et al. 2008; Vansevičius et al. 2009) can be regarded as a first truly homogeneous and statistically large survey of disc star clusters in the M 31. This survey identified 238 clusters and demonstrated that disc clusters in M 31 are predominantly compact, with a median half-light radius of ~1.5 pc. Importantly, it also revealed a presence of massive intermediate-age clusters in the disc of M 31, that are largely absent in the MW.

The most significant recent advance in studies of the M 31 disc star clusters can be associated with the Panchromatic *Hubble* Andromeda Treasury survey (PHAT; Dalcanton et al. 2012). PHAT is a large-scale HST imaging wide-field survey covering the north-eastern part of the M 31 disc. Observational data were obtained in six broad-band photometric filters using three HST imaging channels, and span spectral range from near-IR to near-ultraviolet (UV): $F275W$ and $F336W$ with Wide Field Camera 3 UVIS (WFC3/UVIS); $F475W$ and $F814W$ with Advanced Camera for Surveys (ACS/WFC); $F110W$ and $F160W$ with WFC3/IR. The survey is divided into 23 parts commonly referred to as "bricks", each consisting of 18 fields arranged in a rectangular 6×3 grid. The footprint of PHAT survey on GALEX and 70 μm Multi-Band Imaging Photometer for *Spitzer* (*Spitzer*/MIPS) maps are shown in Fig 1.1. The survey extends more than 20 kpc from the M 31 centre, covering roughly one-third of the star-forming disc, including the most prominent disc features observed in the north-eastern region. The 50% completeness limit of the PHAT stellar photometry in the $F475W$ passband varies from 24.8 mag in the central regions to 28.2 mag in the outer disc (Williams et al. 2023).

In the context of star cluster studies, Johnson et al. (2012) presented the first PHAT cluster catalogue based on visual identification of cluster candidates in selected survey regions. The full catalogue was later published by Johnson et al. (2015) and contains 2753 cluster candidates. PHAT data have since been used to investigate several aspects of the M 31 cluster population, including the cluster mass function and cluster formation efficiency (Johnson et al. 2016, 2017). PHAT clusters were subsequently studied by Naujalis et al. (2021) and Kriščiūnas et al. (2023), who developed a novel adaptive aperture photometry method to improve photometric accuracy and enable a more reliable derivation of cluster physical parameters (see Section 2.2). This ultimately lead to a catalogue of physical parameters for young ($\lesssim$800 Myr) PHAT clusters (Kriščiūnas et al. 2026). Nevertheless, the survey has not yet been fully exploited to its full potential, in particular for studies of low and intermediate mass clusters.

Furthermore, a similar survey – Panchromatic *Hubble* Andromeda Treasury: Triangulum Extended Region (PHATTER; Williams et al. 2021; Johnson et al. 2022) – has been performed and mapped the central part of the star-forming disc of M 33. Moreover, the PHAT survey itself has been recently extended (albeit only in four filters – UV and optical) by Panchromatic *Hubble* Andromeda Southern Treasury (PHAST; Chen et al. 2025) in the south-western part of the disc. Therefore, there are a lot of potential and unique opportunities for further significant progress regarding studies of star cluster populations in the discs of Local Group galaxies, and new important insights can be expected in the near future.

Table 1.1. Main properties of the Andromeda Galaxy (M 31).

Parameter	Value	Reference
Hubble type	SA(s)b	de Vaucouleurs et al. (1991)
α(J2000); δ(J2000)	$00^h\ 42^m\ 44.3^s$; +41° 16' 9"	McConnachie et al. (2005)
P.A.	37.7°	Chemin et al. (2009)
Inclination angle	77.5°	van der Marel et al. (2019)
Distance	785 ± 25 kpc	McConnachie et al. (2005)
$(m-M)_0$	24.47 ± 0.07 mag	McConnachie et al. (2005)
V_{rot}	~250 km/s	Chemin et al. (2009)
Dynamical mass	$4.5 \cdot 10^{11}$ $M_\odot$	Hammer et al. (2025)

α(J2000) and δ(J2000) – equatorial coordinates of the galaxy centre; P.A. – position angle of the major axis; $(m-M)_0$ – distance modulus; V_{rot} – rotational velocity at a galactocentric distance of 10 kpc.

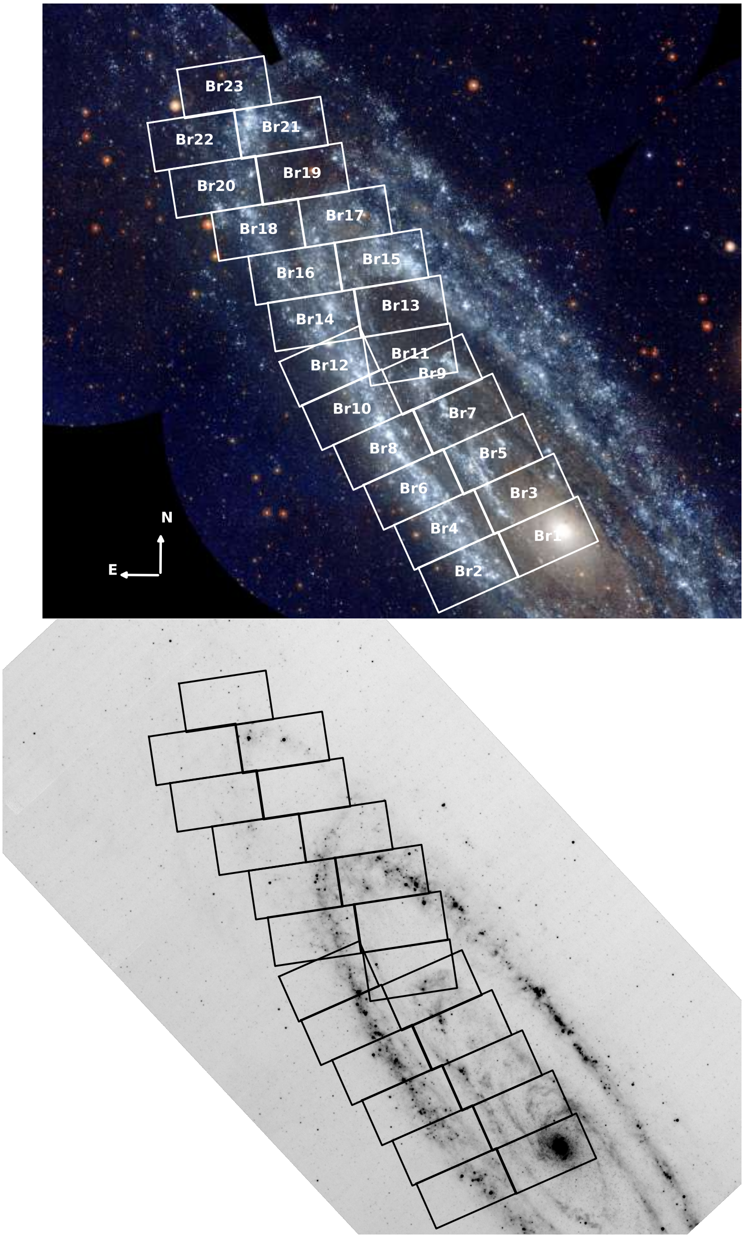

Figure 1.1. Footprint of the PHAT survey overlaid on GALEX FUV+NUV (top panel) and grey-scale 70 μm Multi-Band Imaging Photometer for *Spitzer* (*Spitzer*/MIPS; bottom panel) maps of M 31. White and black contours outline the 23 PHAT survey bricks.

Chapter 2

Aperture photometry in star cluster studies

The content of this chapter is based on Kriščiūnas et al. (2023) and Daugevičius et al. (2024).

2.1 Standard aperture photometry approach

Aperture photometry is one of the most powerful and widely used methods that allows us to study large samples of extragalactic star clusters. This method is based on measuring the total flux within an aperture, typically circular and centred on the cluster, followed by subtraction of the local background contribution. The sky background level is usually estimated using a surrounding annulus centred on the cluster, although in some cases a nearby region of equivalent size is adopted instead. Since a finite aperture does not capture all cluster light, aperture corrections are applied using flux growth curves (cumulative radial flux profiles), artificial clusters, or empirical relations to estimate total integrated fluxes and corresponding magnitudes (Stetson 1987).

The physical parameters of star clusters (age, mass, metallicity, and interstellar extinction) are commonly derived from aperture photometry using stellar population synthesis (SPS) approach. SPS packages such as `Pegase` (Fioc & Rocca-Volmerange 1997) and `Starburst99` (Leitherer et al. 1999) have long been standard tools in stellar population studies, from individual star clusters to entire galaxies. Although technical details of implementation differ, most SPS packages follow similar general principles. A certain star-formation history and stellar initial mass function (IMF, a distribution of initial stellar masses within a population) are chosen. These properties define the distributions of stellar ages and masses within the population. Stellar atmosphere and evolutionary models are then used to compute the integrated spectrum of the artificial population, which can be transformed into magnitudes in different photometric systems. Observed spectra or photometry can be compared with a sample of these theoretical predictions to derive the best-fitting parameters.

Star clusters are usually approximated as a SSP, assuming that all stars formed in a single burst of star formation, and thus share the same age and chemical composition. Standard SPS models typically assume that the IMF is fully sampled, i.e., stellar mass distribution ideally matches the theoretical function.

A widely used approach is to compare observed cluster integrated broad-band magnitudes and colour indices to the theoretical values from SPS models (e.g., Anders et al. 2004; Bridžius et al. 2008). However, it was noticed that such method encounters major problems for low-mass (<10^4 $M_\odot$) clusters, for which the well-sampled IMF assumption is incorrect. In reality for such systems, integrated photometry is strongly affected by stochastic sampling of the IMF, particularly by the random presence of a few massive and luminous stars near the high-mass end of the function (Deveikis et al. 2008; Maíz Apellániz 2009; Fouesneau & Lançon 2010; Beerman et al. 2012; Anders et al. 2013; de Meulenaer et al. 2013). Therefore, young low-mass clusters may contain one or several supergiant stars that can significantly alter the cluster's integrated magnitudes and colours, which can lead to systematically overestimated ages, extinctions, or metallicities when using standard SPS algorithms.

Modern methods account for these stochastic effects, usually by using stochastic cluster models generated through Monte-Carlo sampling of IMF (Deveikis et al. 2008; Fouesneau & Lançon 2010; Fouesneau et al. 2014; de Meulenaer et al. 2013, 2017; Krumholz et al. 2015). In this manner, an extensive grid of models spanning wide range of possible cluster parameters is built, and can be compared with observations to derive cluster physical properties. Since the method developed by de Meulenaer et al. (2013, 2014, 2017) is extensively referred to and used throughout this thesis, we briefly describe it below.

In this algorithm, cluster age, mass, metallicity, and colour excess $E(B-V)$ are estimated by comparing the observed integrated broad-band photometry to a four-dimensional (4D) grid of stochastic models. The model grid is defined by its nodes, where each node corresponds to a specific combination of age, mass, metallicity, and $E(B-V)$ values. The models are generated through random sampling of stellar masses according to the Kroupa (2001) IMF. Integrated photometry is computed using stellar evolutionary models from the PAdova and tRieste Stellar Evolutionary Code (PARSEC)-COLIBRI (Bressan et al. 2012; Marigo et al. 2017), while the standard MW interstellar extinction law is assumed.

The likelihood that a given node represents the photometry of an observed cluster is then evaluated. First, the likelihood of each stochastic cluster model within a node is calculated:

$$L_{\mathrm{model}} = \prod_{f=1}^{F} \frac{1}{\sqrt{2\pi}\,\sigma_f} \exp\left[-\frac{\left(\mathrm{mag}_{f,\mathrm{obs}} - \mathrm{mag}_{f,\mathrm{model}}\right)^2}{2\sigma_f^2}\right], \tag{2.1}$$

where f denotes a specific passband, $mag_{f,obs}$ and mag_f are the observed and model magnitudes in that filter, respectively, and F is the total number of passbands. The likelihood of a node is then obtained by summing up the likelihoods of all stochastic models within that node:

$$L_{\mathrm{node}}(t, \mathrm{M}, E(B{-}V), [\mathrm{M/H}]) = \sum_{n=1}^{N} L_{\mathrm{model},\,n}, \tag{2.2}$$

where N is the number of models in the node. The parameter combination corresponding to the node with the highest likelihood is referred to as `BEST`. The method can also be applied with one or more parameters fixed, for example by assuming solar metallicity.

Although such methods account for stochastic IMF sampling, they still experience significant issues if standard aperture photometry procedures are used to obtain cluster magnitudes and colours. Beerman et al. (2012) showed that for low-mass clusters inclusion of one or several bright post-main-sequence (PMS) stars within the photometric aperture can introduce severe stochastic variations in cluster brightness and colours, strongly affecting the accuracy of derived ages and masses. Moreover, de Meulenaer et al. (2017) demonstrated that bright field stars projected within the aperture can significantly distort photometric measurements, complicating parameter determination and often resulting in age–extinction degeneracies.

2.2 Adaptive aperture photometry

Naujalis et al. (2021) introduced a novel adaptive aperture photometry technique to mitigate the problems associated with bright resolved cluster member and field stars highlighted by Beerman et al. (2012) and de Meulenaer et al. (2017). It was successfully applied to the PHAT star cluster catalogue (Johnson et al. 2015) objects by Naujalis et al. (2021) and Kriščiūnas et al. (2023). Below we summarise the main principles of the approach; a detailed description is provided in the original papers.

The method is based on measuring flux growth curves in each passband using many co-centred apertures with gradually increasing radii using a small step. First, a preliminary aperture enclosing roughly the total cluster flux is selected; this is referred to as the T ("total") aperture. The local sky background can then be estimated from the surrounding area around this aperture.

Accurate determination of the local sky background is crucial for reliable cluster photometry. Although several automated approaches have been proposed (e.g., Barmby & Huchra 2001; Krienke & Hodge 2007; Johnson et al. 2012), they often perform poorly in crowded resolved or semi-resolved fields, such as the discs of Local Group galaxies. These automated algorithms struggle to consistently account for strong local variations of background level and irregularly distributed bright field stars. Such issues can lead to inconsistent background estimates between passbands.

To address this, the adaptive aperture photometry method uses interactive background determination based on the inspection of growth curves, differential flux profiles, and cluster images in all passbands. Initial mean and median background levels are calculated in an annulus extending from $1.2R_{\mathrm{T}}$ to $3.4R_{\mathrm{T}}$, where R_{T} is the radius of T aperture. These values are used to construct the first iteration of the growth curves and differential profiles. The background level in each passband is then adjusted interactively until the growth curves flatten and the differential profiles approach zero within the background annulus. The size of T aperture can be re-adjusted according to the point where the growth curve stabilises and flattens confidently. In practice, Naujalis et al. (2021) and Kriščiūnas et al. (2023) also selected T apertures in such a manner that avoids bright field stars at the edges of apertures. Combining visual inspection of cluster images with cumulative and differential flux profiles enables consistent background determination across all passbands. However, a major downside is that such procedure is very time-consuming.

The key idea of adaptive aperture photometry is measuring a star cluster with two co-centred apertures. The larger one is the aforementioned T aperture and is intended to capture the total cluster flux. Meanwhile, the smaller one called C ("colour") aperture is chosen to include only the central cluster region and exclude bright field stars or evolved cluster members that could distort the measured colour indices. As a result, measurements obtained with the C aperture are less affected by stochastic contamination and provide more colour-consistent cluster fluxes. Notably, in the PHAT studies of Naujalis et al. (2021) and Kriščiūnas et al. (2023), the C aperture radius, R_C, was generally chosen to be equal to or larger than the cluster half-light radius.

Next step is selecting a reference passband used to derive the final colour-consistent magnitudes. In the context of PHAT survey, Naujalis et al. (2021) adopted the $F475W$ passband because it provides the highest signal-to-noise ratio (S/N) and has relatively low contamination by the light of old resolved M 31 field stars compared to other filters. For simplicity, we continue using the PHAT notation here. The aperture correction (AC) in the reference passband is defined as the difference between the magnitudes measured with T and C apertures:

$$F475W_{\mathrm{AC}} = F475W_{\mathrm{T}} - F475W_{\mathrm{CA}}. \tag{2.3}$$

The final colour-consistent magnitudes (C) are then obtained as

$$F\#W_{\mathrm{C}} = F\#W_{\mathrm{CA}} + F475W_{\mathrm{AC}}, \tag{2.4}$$

where "#" denotes the HST three-digit passband code and $F\#W_{\mathrm{CA}}$ are magnitudes measured within the C aperture. This magnitude transformation assumes that the cluster does not exhibit strong colour gradients beyond R_C, and is reliable only in such cases. Colour gradients may arise from effects such as mass segregation, differential extinction across the cluster, or real spatial gradients of stellar populations within given cluster.

Figure 2.1 presents two-colour diagrams (TCDs) for the combined full PHAT M 31 cluster sample from Naujalis et al. (2021) and Kriščiūnas et al. (2023) photometry catalogues (red circles), compared with a distribution of stochastic cluster models (blue shaded region). The models span ages of $\log_{10}(t/\mathrm{yr})$ from 6.6 to 10.1, masses from $10^2\,\mathrm{M}_\odot$ to $10^5\,\mathrm{M}_\odot$, metallicities [M/H]= −2.2 to +0.4, and zero extinction assumed. They were generated using PARSEC-COLIBRI isochrones following the method described in de Meulenaer et al. (2017). Figure 2.1a shows colour indices measured using T apertures, while Fig. 2.1b presents measurements obtained with the C aperture approach.

Most observed clusters align well with the stochastic model distribution. However, the C-aperture photometry shows noticeably better compatibility with the models. In particular, when T apertures are used, clusters appear systematically shifted towards redder colours, especially in $F475W - F814W$. The direction of this shift closely follows the extinction vector (black arrows), indicating that bright red field stars included within the larger apertures can mimic the effects of interstellar reddening. The adaptive aperture method substantially reduces such bias.

Although adaptive aperture photometry technique shows a significant improvement over the standard approach and exhibits strong potential for studies of extragalactic star clusters, overall limitations of integrated photometry methods remain to be fully understood. Investigating these limitations is one of the main goals of this thesis and is addressed in the following Chapters.

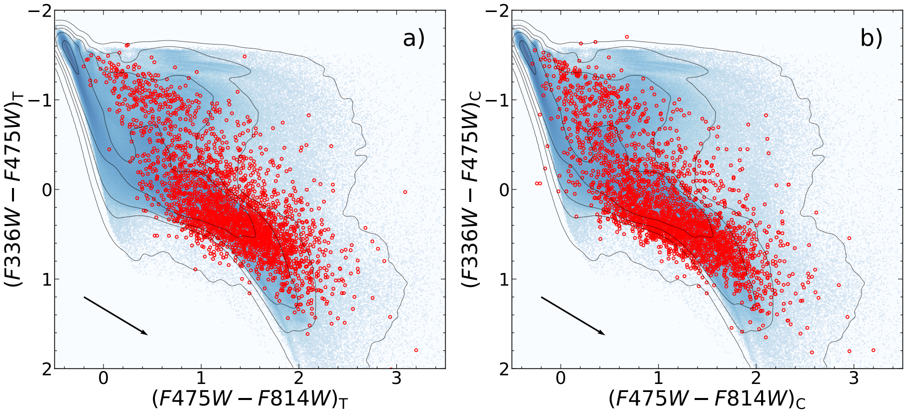

Figure 2.1. Two-colour diagrams comparing combined sample of M 31 star clusters from Naujalis et al. (2021) and Kriščiūnas et al. (2023) (red circles) with the distribution of stochastic cluster models (blue shaded regions; darker colour represents higher model number density). The models are with masses from $10^2\,M_\odot$ to $10^5\,M_\odot$. Panel a) shows colour indices measured using T apertures, while panel b) presents measurements obtained with C apertures. The black arrow marks the extinction vector, calculated using the Fitzpatrick (1999) extinction law with $A_V = 1$.

2.3 Alternative methods for deriving cluster physical parameters

Aperture photometry is not the only approach enabling derivation of star cluster parameters. Therefore, before further discussing the limitations and applicability of aperture photometry, it is useful to briefly review the main alternative methods, together with their strengths and shortcomings. This helps to place aperture photometry into a broader methodological context and highlight its importance in cluster studies.

Several families of methods are used to derive physical parameters of extragalactic star clusters, each exhibiting varying accuracy limits, observational requirements, and caveats. Many currently applied techniques for star clusters in the local Universe ($\lesssim$10 Mpc) rely on broad-band photometry. Among these, the most accurate methods are based on CMDs constructed from photometry of individual resolved cluster member stars. In such algorithms, observed CMDs are compared either with synthetic CMDs generated from simulated stellar populations or fitted with theoretical isochrones (e.g., Dolphin 2002; Johnson et al. 2016; Wainer et al. 2022; Čeponis et al. 2024; Zheng et al. 2025). CMD-based methods can provide highly reliable cluster physical parameters. However, they require sufficiently deep and high-resolution observations to resolve individual upper main-sequence (MS) stars and stars below the MS turn-off (MSTO) point, which are necessary to determine cluster ages accurately. Consequently, CMD fitting approach is mainly applicable to and yields accurate results only for relatively nearby and young star clusters, greatly limiting the number of systems that can be studied in this manner. Wainer et al. (2022) showed that with HST in the neighbouring spiral galaxies M 31 and M 33, robust parameter estimates can be obtained for clusters younger than ~300 Myr and more massive than ~1000 $M_\odot$.

Another approach is based on spectroscopy. In spectroscopic studies, observed integrated cluster spectra are compared either with SPS model spectra or with reference spectra of known stellar populations. Often, the analysis focuses on spectral line indices, i.e., measurements of the strengths of specific absorption features sensitive to stellar population age and metallicity (Vazdekis et al. 2010). Such methods can also provide accurate cluster parameter estimates (e.g., Caldwell et al. 2009, 2011; Caldwell & Romanowsky 2016), because even relatively low-resolution spectra contain substantially more information of specific spectral regions than broad-band photometry and allow parameter degeneracies to be disentangled more effectively. Integrated spectroscopy is particularly useful for old globular-like clusters, for which broad-band photometry often suffers from the age–metallicity degeneracy, especially at ages beyond several Gyr (Worthey 1994). However, accurate spectroscopic measurements require high S/N and are therefore limited to relatively bright and massive GC-like extragalactic clusters, given the capabilities of present-day observatories. Additionally, contamination by bright foreground or background stars projected onto the cluster can significantly affect the measured spectra and bias the derived parameters.

Overall, while both CMD fitting and spectroscopic approaches offer better accuracy in certain regimes, integrated photometry has a much broader range of applicability. It does not require resolving faint individual stars or high-S/N in general, since it is based on the total integrated cluster light. Consequently, aperture photometry can be applied to lower-mass, more distant star clusters in a wider age range, greatly increasing the number of objects available for analysis. This enables us to study star formation and evolutionary histories of galactic discs based on a wider range of star cluster masses, and on longer timescales.

2.4 Structural parameter determination

Several methods are used to derive structural parameters of extragalactic star clusters. In studies based on aperture photometry, one of the simplest and most commonly used techniques is the analysis of flux growth curves, from which parameters such as half-light radius can be determined through interpolation (e.g., Johnson et al. 2012, 2015; Naujalis et al. 2021; Kriščiūnas et al. 2023). It is well-suited in (semi-)resolved conditions, such as those encountered in the PHAT survey.

For unresolved or partially resolved star clusters, structural parameters are commonly derived by fitting analytical two-dimensional (2D) surface brightness models to observed cluster images. The most widely used models are based on the profiles introduced by King (1962) and Elson et al. (1987), which are fitted to cluster images to estimate quantities such as core radius, effective radius, and profile shape parameters (Larsen 1999, 2004; Narbutis et al. 2014; Ryon et al. 2015, 2017; Brown & Gnedin 2021). Such methods require careful treatment of telescope point spread function (PSF), detector sampling, and background contamination.

Various dedicated software packages for such procedures exist, with the most widely used being `ISHAPE` (Larsen 1999) or `GALFIT` (Peng et al. 2002, 2010). In extragalactic studies, artificial cluster tests are usually performed (e.g., Narbutis et al. 2014; Brown & Gnedin 2021) to evaluate the effects of such aspects as finite resolution, crowding, or limited S/N. Synthetic clusters with known properties are inserted into real observations and fitted using same methodology to estimate completeness, systematic offsets, and measurement uncertainties.

Chapter 3

Stochastic star cluster models

The content of this chapter is based on Daugevičius et al. (2024).

To evaluate the limitations and applicability of the aperture photometry method for studying star clusters in the discs of nearby galaxies, we employed stochastic cluster models. For this purpose, we developed an algorithm (Daugevičius et al. 2024) that enables simulating artificial three-dimensional (3D) star clusters and generating realistic images when projecting them onto a two-dimensional (2D) plane from various viewing angles. The part of the algorithm responsible for generating individual cluster member stars is based on the the `SimClust` code (Deveikis et al. 2008), while the modelling of realistic cluster images follows an approach similar to that of Bialopetravičius et al. (2019). All components of the artificial cluster modelling were implemented by using scripts written in `Python`. In the context of this thesis, the algorithm is configured to simulate cluster models and their images so as to mimic real M 31 clusters observed in the PHAT survey (Dalcanton et al. 2012; Johnson et al. 2015). However, it can be readily adapted to produce cluster models as observed in other galaxies or with other instruments. In this Chapter, we describe the main procedures and key details of our star cluster modelling algorithm.

3.1 Sampling of individual stellar masses

Based on radiation magnetohydrodynamics simulations of low-mass star cluster formation, Grudić et al. (2023b) showed that stars do not form in a completely random sequence: massive stars tend to begin forming earlier and finish forming later than the average star. However, their results also indicate that, despite this non-random and correlated nature of star formation, stochastic sampling of stellar masses provides a reasonable description of the end result of star formation in low-mass clusters. Therefore, for simplicity, we adopt fully stochastic sampling to generate the initial masses of individual stars. This approach is widely used in other star cluster studies (e.g. Deveikis et al. 2008; Fouesneau & Lançon 2010; Fumagalli et al. 2011; da Silva et al. 2012; de Meulenaer et al. 2013; Fouesneau et al. 2014; Krumholz et al. 2015).

Stellar masses are sampled stochastically according to the IMF, which specifies the number of stars, dN, born within a given mass interval dm. In this work, we adopt a commonly used Kroupa (2001) IMF, which is defined as a multi-part power law:

$$\xi(\mathrm{m}) = \mathrm{d}N/\mathrm{dm} = C_{\mathrm{IMF}} \cdot b_i \cdot \mathrm{m}^{-\alpha_i}, \tag{3.1}$$

where α_i is the slope of the IMF in the stellar mass range of $[\mathrm{m}_{i-1}, \mathrm{m}_i]$, and C_{IMF} and b_i are function normalisation and continuity constants, respectively. Initial stellar masses are generated in the range from 0.1 to 100 $\mathrm{M}_{\odot}$, within which the Kroupa IMF can be defined by two power-law segments:

$$\begin{cases} \alpha_1 = 1.3, & \mathrm{m} < 0.5\,\mathrm{M}_{\odot}; \\ \alpha_2 = 2.3, & \mathrm{m} \geq 0.5\,\mathrm{M}_{\odot}. \end{cases} \tag{3.2}$$

To sample the initial masses of individual stars, we construct the cumulative initial mass function, $\Xi(\mathrm{m})$, which defines the probability that a star has a mass $\mathrm{m}' \leq \mathrm{m}$. This function is obtained by integrating Eq. 3.1:

$$\Xi(\mathrm{m}) = \int_{\mathrm{m}_{\mathrm{min}}}^{\mathrm{m}} \xi(\mathrm{m}')\,\mathrm{dm}', \tag{3.3}$$

the constants C_{IMF} and b_i are chosen such that Eq. 3.3 remains continuous and its value varies from $\Xi(0.1\,\mathrm{M}_{\odot}) = 0$ to $\Xi(100\,\mathrm{M}_{\odot}) = 1$.

The mass of an individual star is sampled by generating a random number, $\mathrm{rnd}_{\mathrm{m}}$, drawn from a uniform distribution in the range from 0 to 1, and equating this value to the cumulative initial mass function, $\Xi(\mathrm{m}) = \mathrm{rnd}_{\mathrm{m}}$. The corresponding stellar mass is obtained by applying the inverse function:

$$\mathrm{m}_j = F^{-1}(\Xi(\mathrm{m}) = \mathrm{rnd}_{\mathrm{m}}), \tag{3.4}$$

where m_j is the initial mass of the j-th star in the cluster. This ensures that mass sampling is consistent with the IMF.

A graphical illustration of the initial stellar mass sampling method is presented in Fig. 3.1. In panel a), we show an example application of Eq. 3.4 for generating stellar masses. For instance, randomly drawing $\mathrm{rnd}_{\mathrm{m}} = 0.5$ and applying the inverse function yields a stellar mass of $\mathrm{m}_j = 0.276\ \mathrm{M}_{\odot}$ (blue dashed lines), while $\mathrm{rnd}_{\mathrm{m}} = 0.75$ corresponds to $\mathrm{m}_j = 0.532\ \mathrm{M}_{\odot}$ (red dashed lines). Panel b) shows the resulting initial stellar mass distribution for a cluster with $\log_{10}(\mathrm{M}/\mathrm{M}_{\odot}) = 5.0$. In this case, the sampled distribution closely follows the theoretical IMF, with only minor stochastic deviations at the high-mass end ($\mathrm{m} \gtrsim 3\,\mathrm{M}_{\odot}$), indicating that stochastic mass sampling effects are negligible in massive clusters. Panels c) and d) present stellar mass distributions for two independent realisations of clusters with $\log_{10}(\mathrm{M}/\mathrm{M}_{\odot}) = 2.5$. A comparison of these panels demonstrates the strong stochasticity at the high-mass end, as well as noticeable variations at lower stellar masses ($\mathrm{m} \lesssim 1\,\mathrm{M}_{\odot}$), characteristic of low-mass clusters.

The results presented in this thesis are not expected to be sensitive to the adopted Kroupa (2001) IMF. Strong stochastic effects are mainly driven by massive stars ($\gtrsim 1\ \mathrm{M}_{\odot}$). However, at these higher masses various IMFs are very similar (Colman & Teyssier 2020).

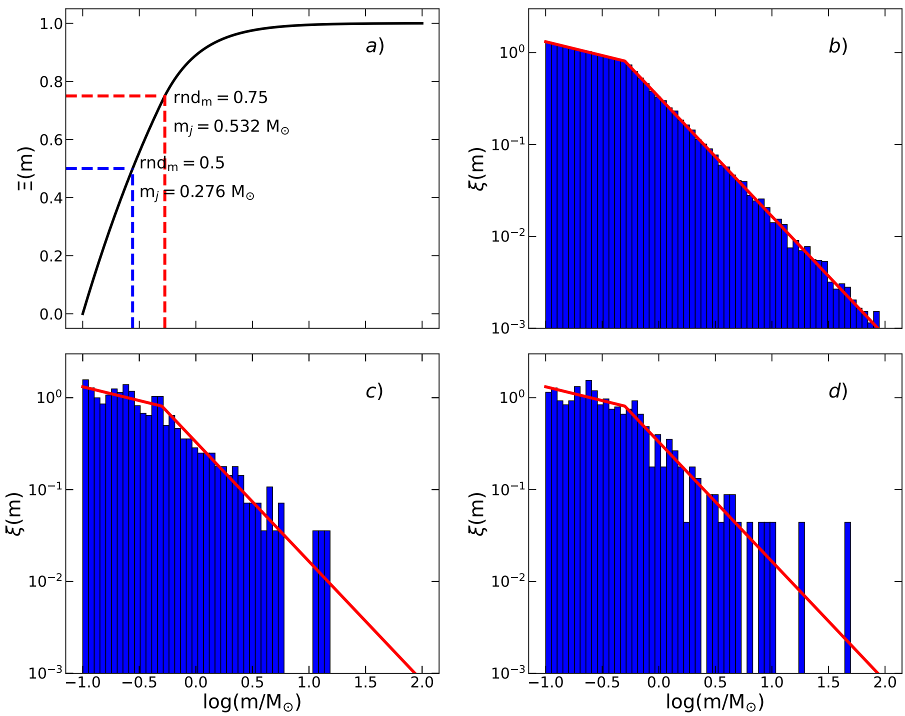

Figure 3.1. Stochastic sampling of individual stellar masses in star clusters. a) Cumulative initial mass function Ξ(m) in the stellar mass range from 0.1 to 100 $M_\odot$ (black line), with an example of its application for stellar mass sampling (blue and red dashed lines). b-d) Initial stellar mass distributions for three simulated clusters: b) $\log_{10}(M/M_\odot) = 5.0$ cluster; c) and d) – two independent realisations of $\log_{10}(M/M_\odot) = 2.5$ cluster. Red curves show the IMF, ξ(m), for an infinite-mass star cluster (i.e., the underlying probability density function).

3.2 Setting spatial distribution of stars

The next step after sampling a mass of an individual star is to assign its position within the modelled star cluster. Stellar positions are distributed according to the empirical Elson-Fall-Freeman (EFF; Elson et al. 1987) radial profile. Numerous studies of star clusters in nearby galaxies (e.g., Elson et al. 1987; Larsen 1999, 2004; McLaughlin & van der Marel 2005; Bastian et al. 2012; Cuevas-Otahola et al. 2020; Brown & Gnedin 2021) have shown that EFF profiles accurately describe the observed structure of young star clusters. Since the goal of our modelling is to reproduce real young clusters as accurately as possible – particularly because such systems are most susceptible to stochastic effects – the choice of the EFF profile is well motivated and justified. The radial density profile of the EFF model is described by the following function:

$$\rho(r) = \rho_0 \left(1 + \frac{r^2}{r_0^2}\right)^{-(\gamma+1)/2}, \tag{3.5}$$

where ρ_0 is the central cluster density; r – de-projected (3D) distance from the cluster's centre; r_0 – EFF scale radius; γ – power-law slope that determines the behaviour of the radial profile in the outer regions of the cluster.

To generate the spatial distribution of stars, we adopt a method originally proposed by Aarseth et al. (1974) for assigning initial positions of stars in dynamical N-body star cluster simulations. It should be noted that this method assumes that all individual cluster stars have equal mass; however, in our implementation stellar positons are assigned independently of mass, effectively assuming no primordial mass segregation. Thus, all stellar masses follow the same underlying spatial distribution, although the presence of a small number of massive stars can introduce stochastic fluctuation in the mass distribution of individual cluster realizations. Nevertheless, it remains an appropriate approach in our case.

This approach is based on constructing the cumulative radial mass profile, M(<r). For the EFF model, it can be derived by integrating Eq. 3.5:

$$\mathrm{M}(<r) = \int_0^r 4\pi x^2 \rho(x)\,\mathrm{d}x = \frac{4\pi\rho_0}{3} r^3 \cdot {}_2F_1\left(\frac{3}{2}; \frac{\gamma+1}{2}; \frac{5}{2}; -\frac{r^2}{r_0^2}\right), \tag{3.6}$$

where ${}_2F_1(a;b;c;z)$ is the Gaussian hypergeometric function. The cumulative mass profile is normalised such that its value ranges from 0 to 1. Similarly to the stellar mass sampling procedure, a random number from a uniform distribution, rnd_r, is generated in the interval [0, 1], and assigned that $\mathrm{M}(<r) = \mathrm{rnd}_r$. The 3D radial distance of the j-th star from the cluster centre, r_j, is then determined by using the inverse function:

$$r_j = F^{-1}(\mathrm{M}(<r) = \mathrm{rnd}_r). \tag{3.7}$$

The method for generating 3D radial distances of individual stars is illustrated in Fig. 3.2. Panel a) shows three cumulative radial cluster mass profiles defined by different EFF model parameters, along with example radii sampled from each profile by drawing $\mathrm{rnd}_r = 0.6$. We emphasize, that in our modelling, the radial profile is defined by two parameters: γ, the power-law slope of the EFF model, and r_c, the core radius as defined by King (1962), and measured in arcsec. Core radius is related to the EFF parameters r_0 and γ as follows:

$$r_c = r_0 \left(2^{2/\gamma} - 1\right)^{1/2}. \tag{3.8}$$

Panel b) of Fig. 3.2 shows a sampled distribution of 3D radial distances for a cluster with $\log_{10}(\mathrm{M}/\mathrm{M}_\odot) = 5.0$. It follows the corresponding probability density function with great accuracy, highlighting negligible stochastic effects in the spatial sampling of massive clusters. Meanwhile, panels c) and d) show results from two independent samplings of cluster with $\log_{10}(\mathrm{M}/\mathrm{M}_\odot) = 2.5$. Both realisations exhibit substantial deviations from the probability density function, as well as evident differences between each other. Just as in the case of stellar mass sampling, this demonstrates significant stochastic effects in lower-mass clusters.

Once the radial distance of an individual star is sampled, two remaining spatial coordinates within the cluster must be assigned. This is done by generating two random numbers from uniform distributions: u_j in the interval [0, 2π] and v_j in [-1, 1]. These numbers are then transformed into spherical coordinates, initially assuming a unit radius ($r_j = 1$):

$$\begin{cases} \phi_j = u_j; \\ \theta_j = \cos^{-1} v_j. \end{cases} \tag{3.9}$$

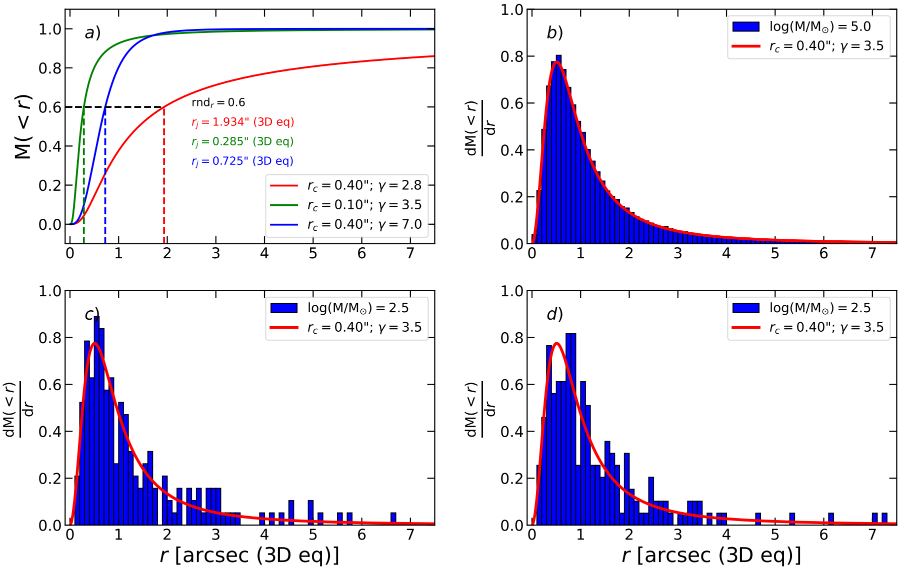

Figure 3.2. Stochastic sampling of 3D radial distances from the cluster centre of cluster member stars. a) Cumulative radial cluster mass profiles, M(<r), for three models with different EFF profile parameters; example of distance sampling with rnd$_r$ = 0.6 is shown for each profile. b-d) Sampled 3D radial distance distributions for three simulated clusters: b) $\log_{10}(M/M_\odot) = 5.0$ cluster; c) and d) – two independent realisations of $\log_{10}(M/M_\odot) = 2.5$ cluster. Red curves show the sampling probability density function dM(<r)/dr.

.

The spherical coordinates are subsequently converted into Cartesian coordinates:

$$\begin{cases} X_j = r_j \cdot \sin\theta_j \cdot \cos\phi_j; \\ Y_j = r_j \cdot \sin\theta_j \cdot \sin\phi_j; \\ Z_j = r_j \cdot \cos\theta_j. \end{cases} \tag{3.10}$$

To generate an entire cluster, the algorithm for sampling individual stars – their initial masses and positions within the cluster – is repeated until the total stellar mass within a defined sphere reaches or slightly exceeds the target cluster mass. In this thesis, we adopt a sphere of radius 7.5″, which corresponds to ∼28.5 pc at the distance of M 31. Once star sampling is complete, we evaluate whether including or excluding the last sampled star results in a total initial mass closer to the target. The option that minimises the deviation from the target mass is adopted as the final cluster model.

3.3 Assigning stellar magnitudes

Once the initial stellar masses and spatial distribution are generated, photometric magnitudes must be assigned to individual stars based to their masses and the age of the modelled cluster. In our algorithm, this is achieved by interpolating isochrones of the corresponding age from the PARSEC-COLIBRI stellar evolution models (Bressan et al. 2012; Marigo et al. 2017). In this study, we adopt isochrones with fixed solar metallicity and assume zero interstellar extinction. Such approach inherently assumes that all cluster members formed in a single burst of star formation, such that all stars share the same age and chemical composition. Nevertheless, this approximation is reasonable for young, low-mass clusters, which are the primary focus of this thesis. The relevant PARSEC-COLIBRI isochrones were obtained using the web-based interface service[1].

Since our goal is to simulate artificial clusters that closely match real M 31 star clusters observed in the PHAT survey, we interpolate isochrones in the corresponding six HST passbands, used in the survey. Absolute magnitudes given in the isochrones are converted to apparent magnitudes using the M 31 distance modulus, $(m - M)_0 = 24.47$ (McConnachie et al. 2005).

In Fig. 3.3, we present CMDs of three simulated clusters with $\log_{10}(\mathrm{M}/\mathrm{M}_\odot) = 3.0$ (panels a–c) and three with $\log_{10}(\mathrm{M}/\mathrm{M}_\odot) = 4.5$ (panels d–f), shown at six different ages together with the corresponding isochrones. A comparison between panels illustrates that low-mass clusters, even when characterised by identical physical parameters (age, mass, and metallicity), can consist of substantially different stellar populations due to IMF stochasticity. In particular, such clusters may contain one or a few stars that are significantly brighter than the rest. This, in turn, can lead to large variations in their integrated photometric properties, complicating the determination of cluster parameters. In contrast, more massive clusters show only marginal stochastic effects, which are largely negligible for integrated brightness and colours given the large number of stars they contain, especially at ages $\gtrsim$30 Myr. Figure 3.3 also demonstrates how the dominant sources of stochasticity in cluster photometry change with age. At young ages, stochastic effects are primarily driven by massive upper MS stars and evolved massive stars, such as yellow/red supergiants (YSGs, RSGs). At older ages, these effects are dominated by red clump, red giant branch (RGB), and asymptotic giant branch (AGB) stars.

An important caveat concerns the choice of stellar evolutionary models used to generate photometry of individual stars. In Fig. 3.4, we compare PARSEC-COLIBRI isochrones with those from BaSTI (Hidalgo et al. 2018) and MIST (Choi et al. 2016; Dotter et al. 2026). At ages of $t \lesssim 10$ Myr, different stellar evolution models are poorly constrained and can behave erratically, treating fast transient evolutionary phases differently. As shown in Fig. 3.4a, PARSEC-COLIBRI isochrones include a detailed description of these short-lived phases and associated changes, whereas MIST models omit them and exhibit abrupt discontinuity around $F814W = 15.5$, immediately jumping down to $F814W \approx 22$, represented by the parallel line. At 10 Myr (Fig. 3.4b), PARSEC-COLIBRI also provide a more detailed treatment of PMS evolution compared to MIST, particularly in their description of the blue loop. Additionally, some models do not cover such young ages at all; e.g., BaSTI isochrones are absent in panels a) and b), as they only start at ∼13 Myr. Consequently, stochastic cluster simulations at these ages are highly sensitive to the adopted isochrone set. At older ages ($t \gtrsim 30$ Myr; Fig. 3.4c-f), differences between isochrone models become more subtle, with the main discrepancies arising from slight offsets in brightness at advanced evolutionary stages, such as the blue loop or red clump.

We also generated 1000 stochastic clusters with $\mathrm{M} = 1000\,\mathrm{M}_\odot$ using each of the

[1] http://stev.oapd.inaf.it/cgi-bin/cmd

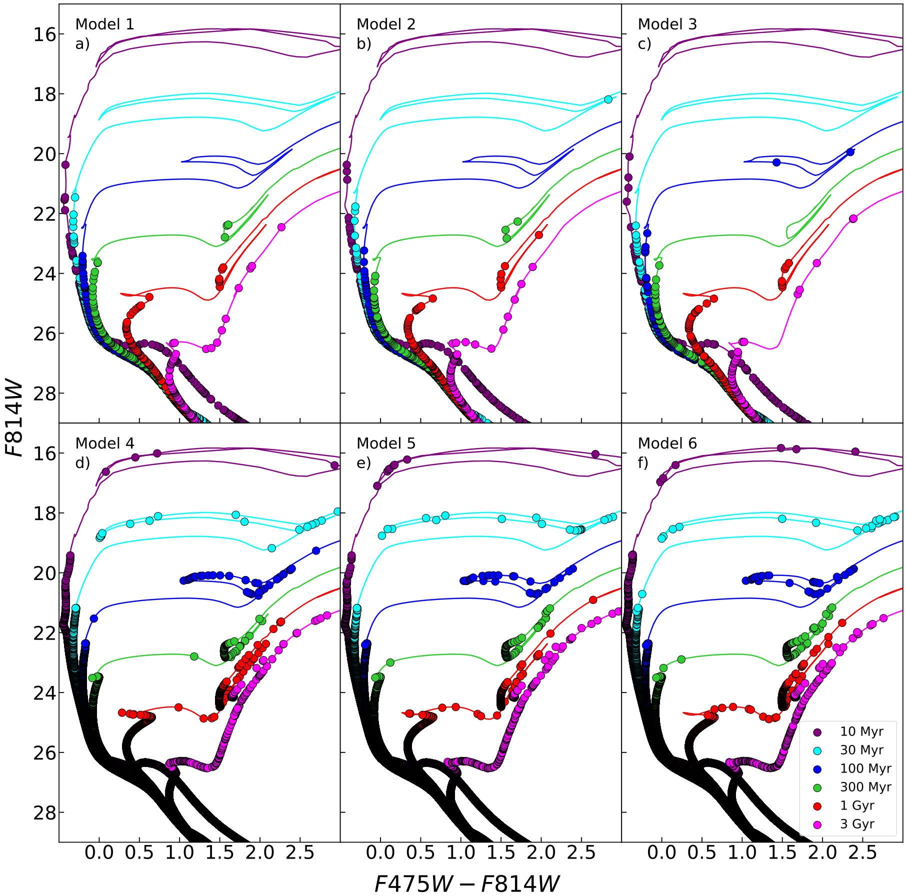

Figure 3.3. Colour–magnitude diagrams of simulated clusters with $\log_{10}(\mathrm{M}/\mathrm{M}_\odot) = 3.0$ (panels a–c) and $\log_{10}(\mathrm{M}/\mathrm{M}_\odot) = 4.5$ (panels d–f), at six ages (see legend). Coloured curves indicate PARSEC-COLIBRI isochrones; filled circles represent individual cluster stars.

three isochrone sets. In Fig. 3.5, we show results for the $t = 100\,\mathrm{Myr}$ case in TCDs and CMDs (results for 30 Myr and 300 Myr cases are presented in the Appendix; Figs. A1 and A2, respectively). In general, the distributions of stochastic models are broadly similar, regardless of the isochrones used for interpolation. The BaSTI version at 100 Myr shows a slightly smaller scatter, likely due to the BaSTI isochrone having the smallest and faintest blue loop (see Fig. 3.4d). At 30 Myr (see Fig. A1), the PARSEC-COLIBRI version demonstrates larger scatter, most probably reflecting a more detailed treatment of the blue loop, while at 300 Myr (see Fig. A2) they produce a slightly bluer cluster distribution in $F336W - F475W$ compared to MIST and BaSTI.

Overall, while differences between isochrone models can lead to variations in stochastic cluster simulations and results of their analysis, our choice of PARSEC-COLIBRI is well-motivated by several factors. These models provide extensive cov-

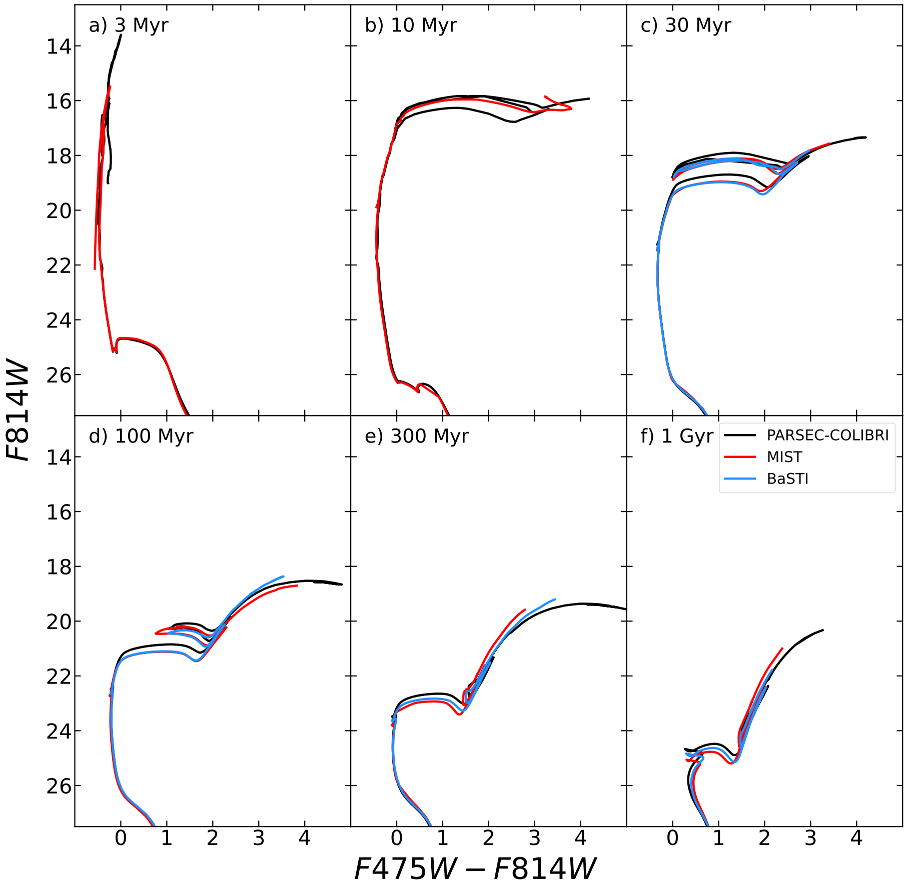

Figure 3.4. Comparison of isochrones from three stellar evolution models – PARSEC-COLIBRI, MIST, and BaSTI (see legend) – at six ages (indicated in the top-left corner of each panel). Apparent magnitudes were adjusted using the M 31 distance modulus, $m - M = 24.47$. BaSTI isochrones are not available at ages of 3 and 10 Myr.

erage of stellar parameters and include a detailed treatment of rapid transient evolutionary phases, which is essential for modelling realistic integrated cluster photometry. Although alternative isochrone models may offer advantages for specific applications or include certain evolutionary features not present in PARSEC isochrones, they often provide more limited parameter coverage and a less consistent treatment of rapid evolutionary stages, particularly at young ages.

3.4 Modelling realistic cluster images

The final step of the algorithm is to generate realistic mock observations of the simulated clusters, once they are projected onto a 2D plane. To model the images of indi-

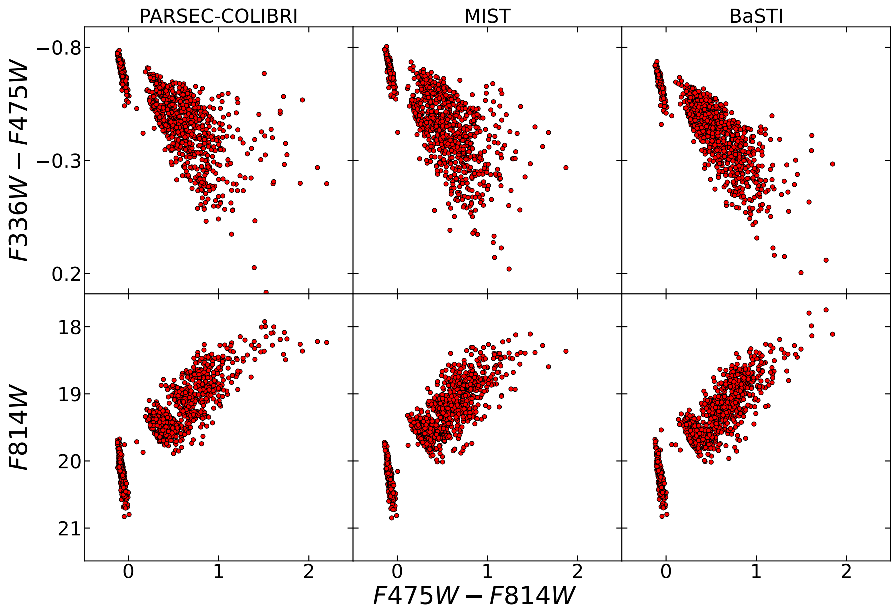

Figure 3.5. Comparison of integrated photometry for stochastic cluster models (t = 100 Myr, M = 1000 $M_{\odot}$) generated using different isochrone sets. Shown are 1000 IMF sampling realisations, each produced with PARSEC-COLIBRI, MIST, and BaSTI isochrones (indicated above each corresponding column). Top panels present two-colour diagrams, and bottom panels show colour-magnitude diagrams.

vidual stars, we use the `TinyTim`[2] package, which enables the modelling of PSFs for various HST instrument and passband combinations. Although the use of empirically constructed PSFs is recommended instead – since `TinyTim` is no longer updated and real PSFs evolve over time due to changes in HST instrument performance – we consider that `TinyTim` PSFs are sufficient and appropriate for the purposes of this study. This is because integrated cluster photometry is performed using apertures that are much larger than the full width at half maximum of these PSFs, such that small-scale differences in PSF structure have negligible effect on the total measured flux.

Each individual star is simulated by scaling the corresponding `TinyTim` PSF with star's total flux in a given passband, resulting in pixel flux values expressed in e^{-}/s. The total flux of a star in a given photometric passband ($F_{star,\ F?W}$) is calculated as:

$$F_{star,\ F?W} = 10^{-0.4\cdot(F?W - F?W_0)}, \tag{3.11}$$

where $F?W$ is the stellar magnitude in a given passband and $F?W_0$ is the corresponding photometric zeropoint. Zeropoints for the ACS camera were obtained using the ACS Zeropoints Calculator[3], while zeropoints for both channels of WFC3 were taken from the Space Telescope Science Institute (STScI)[4]. Artificial cluster images were

[2] https://www.stsci.edu/hst/instrumentation/focus-and-pointing/focus/tiny-tim-hst-psf-modeling

[3] https://www.stsci.edu/hst/instrumentation/acs/data-analysis/zeropoints

[4] https://www.stsci.edu/hst/instrumentation/wfc3/data-analysis/photometric-calibration

generated within $15'' \times 15''$ frames, corresponding to $\sim 57 \times 57$ pc at the distance of M 31. The resulting cluster images are stored in FITS file format.

3.5 Sample of cluster models

Here, we briefly present the sample of star cluster models used for the analysis in the following Chapters of this thesis. Using the algorithm described above, we generated a large grid of star cluster models and their corresponding images, covering the parameter space characteristic of real clusters observed in the disc of M 31 (Šablevičiūtė et al. 2006, 2007; Vansevičius et al. 2009; Johnson et al. 2015, 2016, 2022). It consists of 1400 grid nodes defined by combinations of four parameters: cluster initial mass, $\log_{10}(\mathrm{M}/\mathrm{M}_{\odot})$; age, $\log_{10}(t/\mathrm{yr})$; EFF power-law slope, γ; core radius, r_c, measured in arcsec. The values of these parameters are listed in Table 3.1. Each grid node contains 100 generated artificial clusters.

To evaluate, for the first time, uncertainties in cluster aperture photometry arising from the randomness of cluster projection along the line of sight (investigated in Chapter 4), we constructed a sub-grid of 500 nodes. For each of the 100 artificial clusters in these nodes, we generated 100 different 2D projections, to imitate observations from 100 viewing angles. The same set of 100 random projection angles, drawn from a uniform distribution over the unit sphere, was applied to all of these clusters. Taking into account the six passbands used in the PHAT survey, this resulted in more than 3×10^7 images. The parameters defining these 500 grid nodes are listed in Table 3.2.

Additionally, to investigate the effects of sky background on cluster completeness limits and detection reliability (Section 5.4), we generated a separate set of artificial clusters using the same modelling approach. Because the analysis required densely sampling the parameter space, rather than evaluating cluster properties only at discrete grid points, we constructed a continuous sample of 20 million artificial clusters. Their images were generated only in the $F475W$ passband to keep the computational costs manageable. Parameter ranges for these models are given in Table 3.3.

Table 3.1. Parameters of artificial star clusters. Their combinations define the nodes of the main model grid, each node containing 100 cluster models.

Parameter	Values
$\log_{10}(M/M_\odot)$	2.0, 2.5, 3.0, 3.5, 4.0, 4.5, 5.0
$\log_{10}(t/\mathrm{yr})$	6.5, 7.0, 7.5, 8.0, 8.5, 9.0, 9.5, 10.0
r_c	0.05″, 0.10″, 0.20″, 0.40″, 0.80″
γ	2.2, 2.4, 2.8, 3.5, 7.0

Table 3.2. Parameters of artificial star clusters. Their combinations define the subgrid nodes, each containing 100 cluster models and 100 viewing angles per cluster.

Parameter	Values
$\log_{10}(M/M_\odot)$	2.0, 2.5, 3.0, 3.5, 4.0
$\log_{10}(t/\mathrm{yr})$	7.0, 8.0, 9.0, 10.0
r_c	0.05″, 0.10″, 0.20″, 0.40″, 0.80″
γ	2.2, 2.4, 2.8, 3.5, 7.0

Table 3.3. Parameter ranges for the continuous sample of 20 million models in $F475W$ passband.

Parameter	Range of values
$\log_{10}(M/M_\odot)$	2.4–4.1
$\log_{10}(t/\mathrm{yr})$	6.5–10.1
r_c	0.05″–0.6″
γ	2.1–4.1

Chapter 4

Theoretical limits of star cluster aperture photometry

The content of this chapter is based on Daugevičius et al. (2024).

Aperture photometry is an excellent tool for studying large samples of star clusters in the local Universe, enabling the derivation of their parameters and the reconstruction of star formation histories in disc galaxies, as highlighted in Chapter 2. Previous studies (e.g., Fouesneau & Lançon 2010; Beerman et al. 2012; Anders et al. 2013; de Meulenaer et al. 2013, 2017) have provided important insights into certain limitations and uncertainties in the integrated photometry methods, particularly those arising from stochastic sampling of the IMF. However, the overall maximum accuracy of this approach and its fundamental limits remain to be characterised in a consistent and homogeneous way. A clear understanding of these intrinsic precision limits, which are primarily driven by stochastic effects, is essential to avoid over-interpreting observational data when studying the formation and evolution of star clusters and their host galaxies.

In this Chapter, we aim to estimate achievable accuracy limits of aperture photometry for star cluster studies in the local Universe. To achieve this, we employ the cluster models described in Chapter 3. The fact that we had simulated images of the same clusters observed from various viewing angles allows us, for the first time, to systematically assess the uncertainties in cluster aperture photometry introduced by projection effects, i.e. the random orientation of clusters towards our line of sight.

We stress that all experiments presented in this Chapter are performed under idealised conditions, with no sky background included in the cluster images. This means that all derived uncertainties and distorting effects discussed are at their minimum. The inclusion of any precision-limiting factors, such as sky background or contamination from bright resolved field stars, would further increase reported uncertainties, especially in the case of low-mass clusters. In other words, the results presented in this Chapter represent the most optimistic accuracy limits of aperture photometry for studying star clusters in the local Universe. Nonetheless, establishing these limits of precision is crucial for interpreting derived cluster properties, various relations among different parameters, and assessing the reliability of inferred star formation histories in nearby galaxies.

Before proceeding, we emphasise that clusters younger than 10 Myr are typically dominated by the MS O-B type stars, as RSGs and YSGs are generally still absent at these ages. Therefore, IMF-related stochastic effects in such systems are much weaker. However, these clusters are omitted from the following analysis in this Chapter because of more complex analysis required due to their location within natal star-forming clouds, from which they emerge on timescales of ~5–10 Myr (Knutas et al. 2025; Pedrini et al. 2026), and which introduce differential extinction effects, and enhanced density of bright resolved field stars.

4.1 Measuring stochastic cluster models

To investigate how stochastic effects limit the accuracy and applicability of the aperture photometry method for star cluster studies, we measured artificial cluster images (described in Chapter 3) following procedures similar to those applied by Naujalis et al. (2021) and Kriščiūnas et al. (2023). All photometric measurements were performed using tools from the `Python` library `photutils`[1], which is designed for photometric analysis of astronomical sources.

First, we measured radial flux growth curves (FGCs) up to an aperture radius (R_{ap}) of 7.0″ (corresponding to ~27 pc at the distance of M 31), using a step size of 0.02″. All apertures were centred on the central pixel of the frame. This procedure was performed in all six modelled passbands, allowing us to derive photometric properties of artificial clusters – fluxes, magnitudes, and colour indices (CIs) – for apertures of arbitrary radius up to 7.0″. FGCs also enable the determination of radii enclosing a given fraction of the total cluster flux, denoted as R_X. These radii are referred to as cluster structural parameters (or simply R parameters) hereafter, as their values and ratios provide information on cluster size, radial structure, and concentration. In this notation, X represents the percentage of total flux enclosed within a circular aperture of radius R_X.

The analysis of FGCs allows us to investigate how stochasticity in stellar mass and spatial distributions, as well as random cluster orientation, affects cluster aperture photometry and derived structural parameters. In Fig. 4.1, we show FGCs and colour images of the same simulated cluster observed from three different viewing angles. This figure demonstrates that, in addition to IMF and spatial distribution stochasticity, the orientation of a cluster along the line of sight can also evidently influence the shape of FGCs and the resulting structural parameters.

4.2 Photometric cluster properties

In this section, we investigate how the stochastic effects in low-mass star clusters, together with the choice of aperture size, influence measurements of cluster photometric parameters. IMF stochasticity, combined with methodological uncertainties are the key factors limiting the maximum achievable accuracy, reliability, and applicability of the aperture photometry method for deriving cluster physical and structural parameters.

First, we examine the impact of stochastic stellar sampling on integrated cluster magnitudes. In Fig. 4.2, we show the median $F475W$ magnitude, along with the 16th and 84th percentiles, depending on cluster mass and age. We find that at young ages

[1]`https://doi.org/10.5281/zenodo.596036`

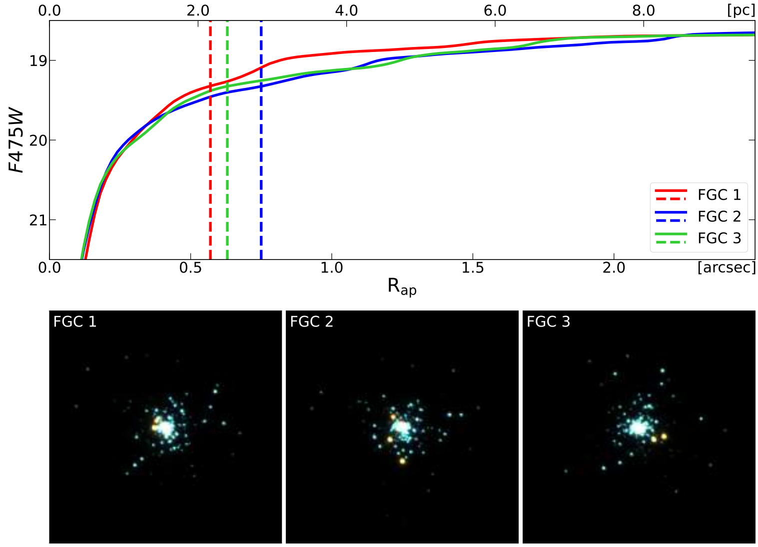

Figure 4.1. Flux growth curves (FGCs) in the $F475W$ passband for an artificial star cluster ($\log_{10}(t/\mathrm{yr}) = 8.0$, $\log_{10}(\mathrm{M}/\mathrm{M}_\odot) = 3.0$, $r_c = 0.2''$, and $\gamma = 2.8$) observed from three different viewing angles. The colour images are $15'' \times 15''$ frames constructed by combining $F336W$, $F475W$, and $F814W$ data as blue, green, and red channels, respectively, assuming the distance of M 31. Dashed vertical lines indicate the half-light radii measured for each projection.

($\log_{10}(t/\mathrm{yr}) \leq 7.0$), clusters with masses $\log_{10}(\mathrm{M}/\mathrm{M}_\odot) \lesssim 3.5$ exhibit a large scatter in magnitudes, with 16-84 percentile intervals exceeding 1 mag. This suggests that, at such ages, mass estimates based on aperture photometry may be subject to substantial uncertainties, since integrated optical magnitude often serves as a key constraint in determining cluster mass. It is noteworthy that at $\log_{10}(t/\mathrm{yr}) = 7.0$, the 16-84 percentile ranges for clusters with $\log_{10}(\mathrm{M}/\mathrm{M}_\odot) = 2.0$ and $\log_{10}(\mathrm{M}/\mathrm{M}_\odot) = 2.5$ partially overlap. Given that these masses differ by a factor of $\sim$3, this indicates that mass estimates based within this range can be particularly uncertain. However, we note that such uncertainties could potentially be reduced if additional constraints on cluster age are obtained, for example through CMD fitting.

These low-mass cluster at ages $t \leq 100$ Myr are of particular interest. In our cluster model sample, only $\sim$5% and $\sim$10% of clusters with masses $\log_{10}(\mathrm{M}/\mathrm{M}_\odot) = 2.0$ and 2.5, respectively, contain PMS stars at $\log_{10}(t/\mathrm{yr}) = 7.0$. At $\log_{10}(t/\mathrm{yr}) = 8.0$, these fractions increase to $\sim$11% and $\sim$37%. This indicates that, for the mass and age ranges considered, large magnitude variations (with 16–84 percentile ranges of $\sim$1.0–2.3 mag) are primarily driven by stochastic sampling of the upper MS.

At higher masses and older ages, the MS becomes well-sampled, and sparsely populated PMS evolutionary phases dominate the stochastic variations in integrated cluster photometry. In general, these variations decrease with age up to $\sim$1 Gyr for all considered cluster masses, but increase again by 10 Gyr. This behaviour can be explained by the fact that the MSTO becomes relatively faint at old ages (e.g., $F475W \approx 28.9$ at the distance of M 31, according to PARSEC-COLIBRI isochrone of 10 Gyr), and the cluster luminosity becomes dominated by stars in the stochastically populated RGB.

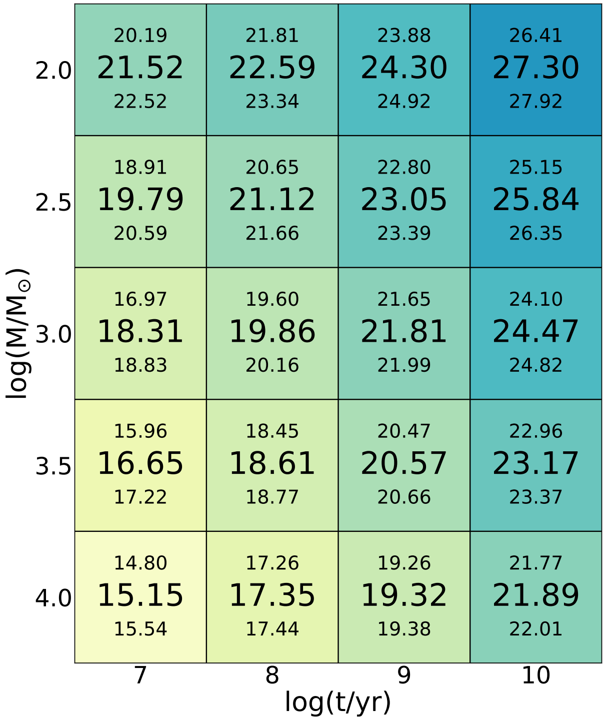

Figure 4.2. Apparent $F475W$ magnitudes of star clusters at the distance of M 31 depending on their mass and age. The central value in each cell represents the median $F475W$ magnitude for a given mass and age combination; meanwhile the upper and lower values show the 16th and 84th percentiles, respectively. Magnitudes were measured using a circular aperture of radius $R_{\rm ap} = 7.0''$.

The values presented in Fig. 4.2 can serve as a useful first-order approximation of completeness limits when analysing star cluster data from the M 31 PHAT (Johnson et al. 2012, 2015) and the M 33 PHATTER (Johnson et al. 2022) surveys. For example, when studying low-mass end of the cluster mass function, these results can help define a lower mass threshold above which the mass function can be reliably recovered without significant selection effects arising from limited catalogue completeness. These estimates can also be extended to studies of star cluster populations in more distant galaxies observed with HST (e.g., Scheepmaker et al. 2007; Bastian et al. 2012; Adamo et al. 2017; Cook et al. 2019; Brown & Gnedin 2021; Deger et al. 2022), provided that appropriate distance corrections, photometric transformations between passbands, and other systematic effects are properly accounted for. In addition, these results can provide a useful reference when planning and estimating achievable survey depth and scientific capabilities of future star cluster studies with current state-of-the-art and upcoming observatories. A prime example is the *Roman* Space Telescope and proposed large-scale programmes, such as the *Roman* Infrared Nearby Galaxies Survey (RINGS; Williams 2022; Thob et al. 2025).

A more qualitative assessment of the impact of stochastic stellar sampling on cluster photometry is presented in Figs 4.3 and 4.4. There we show TCDs and CMDs of

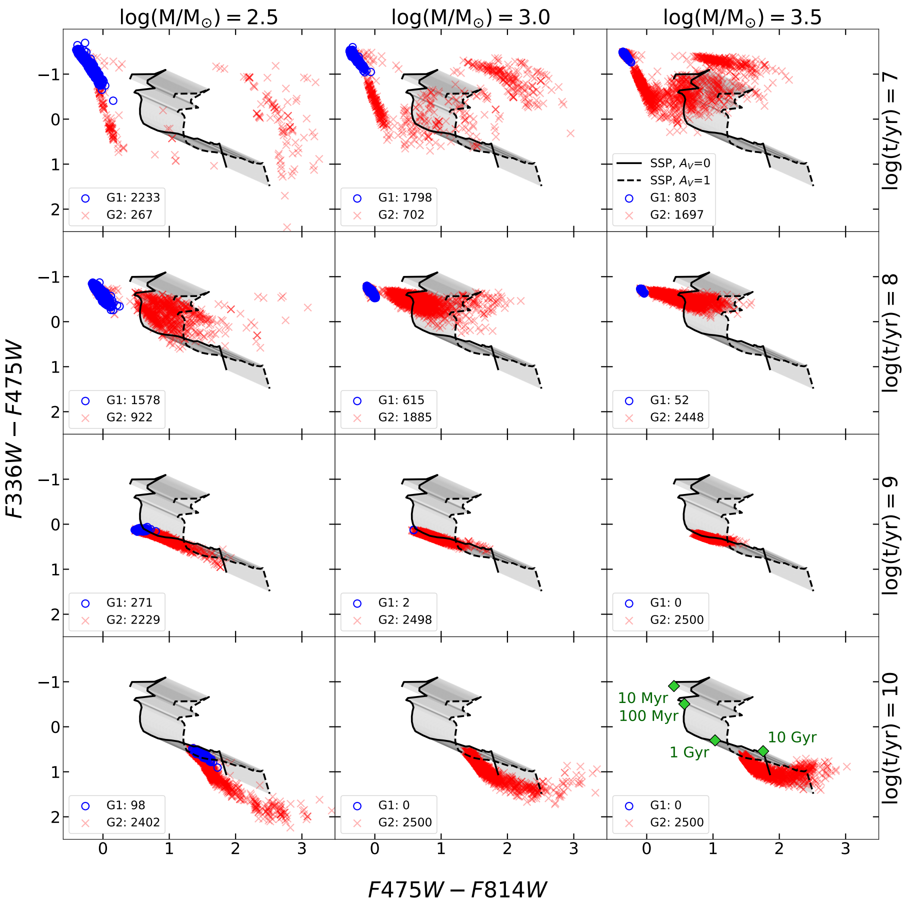

Figure 4.3. Two-colour diagrams of stochastic star cluster models. Each panel shows aperture photometry results for different combinations of cluster mass (indicated above the panels) and age (indicated to the right). The definitions of the G1 and G2 cluster groups are provided in the text. Black lines represent PARSEC-COLIBRI non-stochastic SSP models with solar metallicity, spanning ages from 10 Myr to 12.6 Gyr (Bressan et al. 2012; Marigo et al. 2017). Solid lines mark SSP models without interstellar extinction; dashed lines – with interstellar extinction of $A_V = 1$, calculated using the extinction law of Fitzpatrick (1999). Green diamond markers in bottom right panel shows four age-points of the non-stochastic SSP models. Photometric measurements were performed using circular apertures with a radius of $R_{\rm ap} = 3.0''$.

artificial clusters, with each panel corresponding to a different combination of initial cluster mass and age. Here, we divide clusters into two groups. The first group, denoted as G1, consists of clusters that do not contain any PMS stars, while the second group, G2, are those clusters that host at least one evolved PMS star. For comparison, non-stochastic SSP models with solar metallicity, based on PARSEC-COLIBRI stellar evolution models (Bressan et al. 2012; Marigo et al. 2017), are also shown. A general inspection of these diagrams reveals that low-mass clusters ($\log_{10}(M/M_\odot) \leq 4.0$)

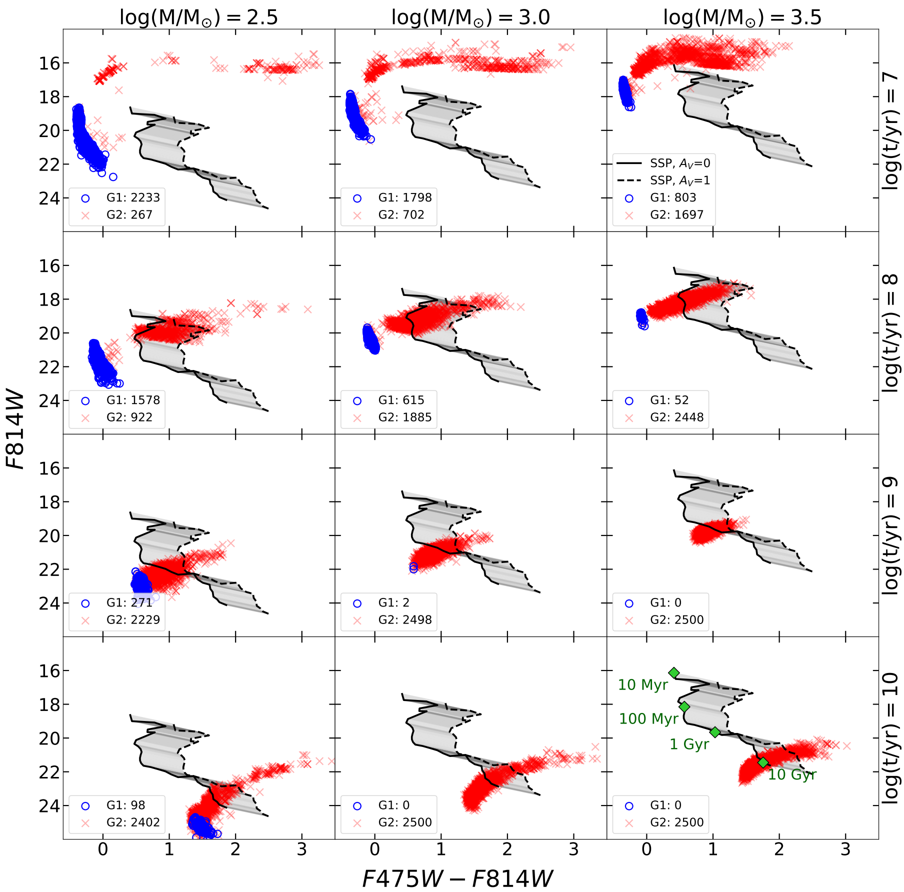

Figure 4.4. Same as in Fig. 4.3, but showing colour-magnitude diagrams.

exhibit large scatter in their photometric properties due to stochastic effects, with CIs and fluxes spanning multiple magnitudes. This behaviour is consistent with earlier studies of stochasticity in star cluster photometry (e.g., Deveikis et al. 2008; Fouesneau & Lançon 2010; Beerman et al. 2012; de Meulenaer et al. 2013). In general, the scatter increases for lower cluster masses and younger ages. These results indicate that stochasticity can introduce significant uncertainties and degeneracies (Worthey 1994; Bridžius et al. 2008; de Meulenaer et al. 2014) in the derived cluster parameters, such as age, mass, extinction, and metallicity. As seen in Figs 4.3 and 4.4, the brightest clusters with masses $\log_{10}(\mathrm{M}/\mathrm{M}_{\odot}) = 2.5$–$3.5$ can exhibit very similar colours and magnitudes in the visual to near-infrared wavelengths despite differences in their initial mass. This can make it difficult to disentangle cluster physical properties using integrated photometry alone.

Importantly, Figs 4.3 and 4.4 reveal that, for low-mass star clusters younger than $t \lesssim 1$ Gyr, the stochastic nature of the IMF gives rise to two photometrically distinct groups of clusters – G1 and G2. The distinction between these two groups is particularly pronounced at young ages ($t \lesssim 100$ Myr), but diminishes rapidly with increasing age. As the MSTO mass decreases over time, even low-mass clusters

($\log_{10}(M/M_\odot) \leq 3.0$) are sufficiently populated to include evolved stars.

Furthermore, we find that G1 clusters generally exhibit more consistent and robust photometric measurements, occupying much smaller and more confined region in TCDs and CMDs compared to G2 clusters. In contrast, G2 clusters tend to be redder, span a wider range of CIs, and are typically brighter. It is important to emphasize that, for clusters with $\log_{10}(M/M_\odot) < 4.0$, the large photometric differences between the two groups at young ages are driven by a small number – or, in many cases, a single – bright evolved PMS star, such as YSGs or RSGs, whose flux can dominate over the integrated cluster light of the whole remaining cluster. These findings are in agreement with Beerman et al. (2012) and suggest that more reliable photometry of young, low-mass clusters – and consequently more precise estimates of their physical parameters – can be achieved if the contributions of such bright evolved stars is explicitly accounted for, either by subtracting their flux or by avoiding them during aperture photometry measurements.

In agreement with previous studies (Deveikis et al. 2008; Bridžius et al. 2008; Fouesneau & Lançon 2010; Anders et al. 2013; de Meulenaer et al. 2013), Figs 4.3 and 4.4 also demonstrate that non-stochastic SSP models – commonly used to derive physical parameters of stellar populations – provide an inadequate approximation for low-mass star clusters affected by stochastic effects. At young ages ($t \leq 100$ Myr), non-stochastic SSP models occupy regions of TCDs and CMDs that are sparsely populated by stochastic cluster models, often lying between the two stochastic groups, G1 and G2, discussed above. As a result, they poorly represent the photometric properties of young clusters. At an age of $t = 1$ Gyr, the agreement between non-stochastic SSP models and stochastic cluster distributions improves; however, even then, stochastic clusters exhibit substantial scatter, spanning a wide range of non-stochastic SSP model ages. In addition, in TCDs, the direction of the stochastic spread closely follows the direction of interstellar reddening, making it difficult to discern the effects of stochasticity and interstellar extinction. Overall, these results further reinforce the established view that the use of non-stochastic SSP models to derive physical parameters of low-mass star clusters can be misleading, and that stochastic effects must be accounted for to obtain reliable estimates of cluster properties.

While stochasticity in low-mass star clusters is a significant and complex issue – introducing large variations in photometric properties among clusters with identical intrinsic physical parameters, and thereby hindering their accurate and robust determination – there are ways to mitigate and, at least partially, reduce these effects. Previous studies have shown that stochasticity problems can be confined to specific regions of TCDs (Whitmore et al. 2020, see also G1 and G2 groups in Figs. 4.3 and 4.4) or to particular cluster ages (e.g., as discussed above, the strongest effects occur when RSGs, YSGs, or other bright PMS stars are present). It is also important to note that stochastic effects can be significantly reduced by incorporating photometric data from additional passbands, such as ultraviolet, near-infrared (Bridžius et al. 2008; de Meulenaer et al. 2014), or Hα (Fouesneau et al. 2012; Whitmore et al. 2020, 2023).

More importantly for the purposes of this thesis, Beerman et al. (2012) demonstrated that imposing a limiting magnitude – i.e., considering only the flux from stars fainter than a given threshold, thereby excluding bright evolved cluster members from aperture photometry – can lead to more accurate determinations of cluster physical parameters, particularly for low-mass clusters. Although there have been attempts to account for or subtract individual bright resolved stars in photometric studies of clusters (Narbutis et al. 2014), performing accurate stellar PSF photometry in crowded environments, such as star clusters located in galactic discs, remains extremely challenging. This makes it difficult to reliably subtract individual bright PMS stars without compromising the integrity of the remaining cluster measurements. Nevertheless, the adaptive aperture photometry method described in Section 2.2 may also prove useful in this context.

As discussed previously, this approach was originally designed to exclude bright stars from old field stellar populations projected onto the cluster, which can introduce significant biases in CIs, typically leading to older inferred ages or higher extinctions, since such stars are often luminous in the infrared. However, evolved cluster members can also produce similar effects. As shown in Figs. 4.3 and 4.4, G2 clusters exhibit systematically redder CIs due to the presence of such stars. Therefore, excluding some of the evolved cluster members – particularly those located at larger distances from the cluster centre – from the photometric measurements could possibly result in more robust CIs and, consequently, more reliable estimates of cluster physical parameters.

While the method was successfully applied to the M 31 star clusters from the PHAT survey(Naujalis et al. 2021; Kriščiūnas et al. 2023), yielding cluster colours that better match stochastic models than those derived using the traditional aperture photometry approach, the adaptive aperture technique has not yet been extensively tested in controlled environments. In this study, we therefore apply the adaptive aperture method to background-free simulated cluster images in order to evaluate its performance under ideal conditions. In particular, we aim to test the key assumption underlying the method – that no significant colour gradients arise as a result of stochastic effects.

To evaluate potential biases arising from the use of smaller colour apertures (C), as opposed to the conventional T aperture approach, we define the difference $\Delta(\mathrm{CI})_{\mathrm{TC}}$ between these two measurements as:

$$\Delta(\mathrm{CI})_{\mathrm{TC}} = \mathrm{CI}_{\mathrm{T}} - \mathrm{CI}_{\mathrm{C}}, \tag{4.1}$$

where CI_{T} is the colour index measured using T aperture, and CI_{C} is the colour index measured using the C aperture. These differences for $F336W - F475W$ and $F475W - F814W$ CIs are shown as a function of the C aperture radius, R_{C}, and cluster parameters in Figs. 4.5 and 4.6.

Analysis of these CIs reveals no significant systematic gradients or biases, as the median $\Delta(\mathrm{CI})_{\mathrm{TC}}$ remains approximately zero for all C aperture sizes and cluster parameters. This justifies the main assumption of the adaptive aperture method. However despite this, a large scatter in $\Delta(\mathrm{CI})_{\mathrm{TC}}$ values persists, decreasing as the R_{C} increases, as indicated by the 16th–84th percentile ranges. More extended clusters – characterised by larger r_c and smaller γ values – exhibit greater dispersion in $\Delta(\mathrm{CI})_{\mathrm{TC}}$, which diminishes more slowly with increasing R_{C}. This trend reflects the higher stochastic variability in the central regions of less concentrated clusters, where small apertures capture only a fraction of the cluster's total light. The observed dependence on C aperture size implies that smaller apertures lead to greater uncertainties, and therefore it is generally advantageous to use a C aperture that is large as possible, as long as bright contaminants do not project within it. For example, Naujalis et al. (2021) and Kriščiūnas et al. (2023) typically adopted the criterion that R_{C} should be equal to or larger than the cluster's half-light radius, R_{50}.

In Figs. 4.5 and 4.6, we see that the scatter in $\Delta(\mathrm{CI})_{\mathrm{TC}}$ decreases markedly once

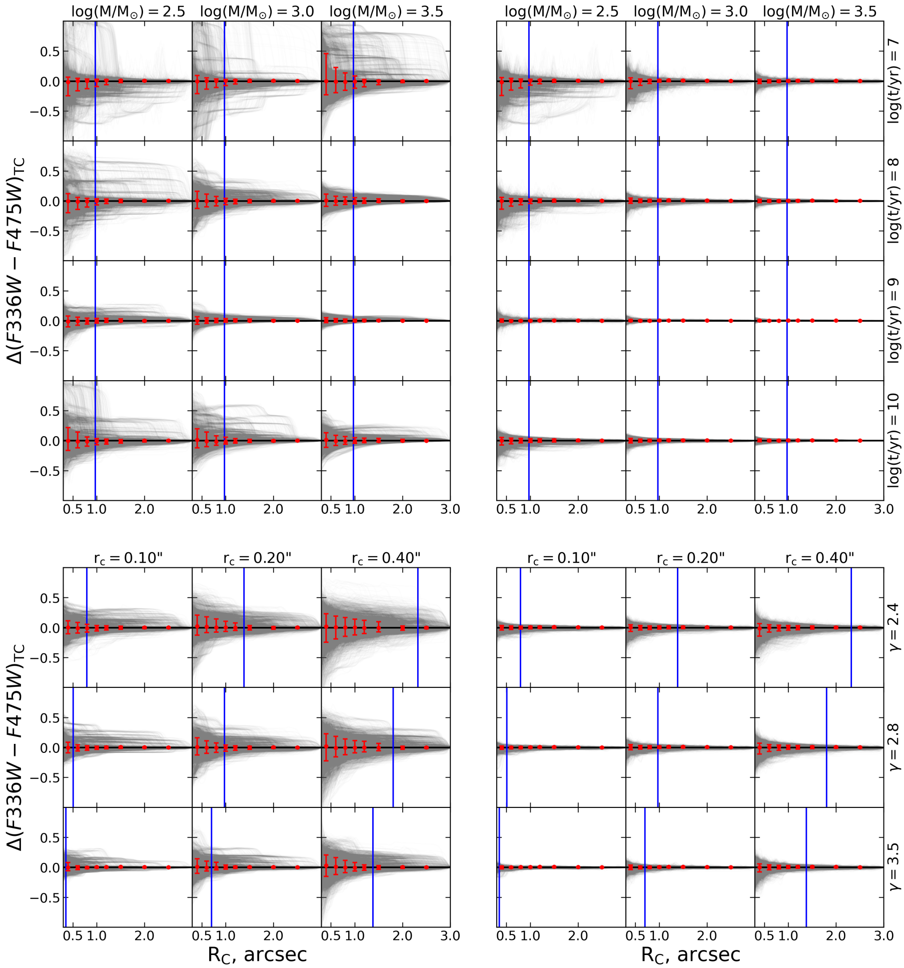

Figure 4.5. Differences in $F336W - F475W$ colours measured using T and C apertures as a function of C aperture radius, R_C. The differences for individual simulated clusters are shown as grey lines. The X-axis represents the C aperture radius, R_C, while a fixed T aperture radius of $R_T = 3.0''$ is used. Red markers indicate the median $\Delta(F336W - F475W)_{TC}$ for a given R_C, with error bars corresponding to the 16th–84th percentile range. Blue vertical lines mark radii equal to twice the half-light radius, $2\times R_{50}$, for the corresponding cluster parameters. The top-row panels show the dependence on cluster mass and age (for clusters with $r_c = 0.2''$ and $\gamma = 2.8$), while the bottom-row panels show the dependence on radial profile parameters (for clusters with $\log_{10}(M/M_\odot) = 3.0$ and $\log_{10}(t/\mathrm{yr}) = 8.0$). Panel blocks on the left show results when all cluster members are included in the photometric measurements, whereas the panel blocks on the right show results when PMS stars are subtracted prior to aperture photometry measurements.

the C aperture radius reaches approximately $2 \times R_{50}$. For instance, for clusters with $r_c = 0.1''$ and $\gamma = 2.4$, or $r_c = 0.2''$ and $\gamma = 2.8$, the half-light radii are ~0.4″ and

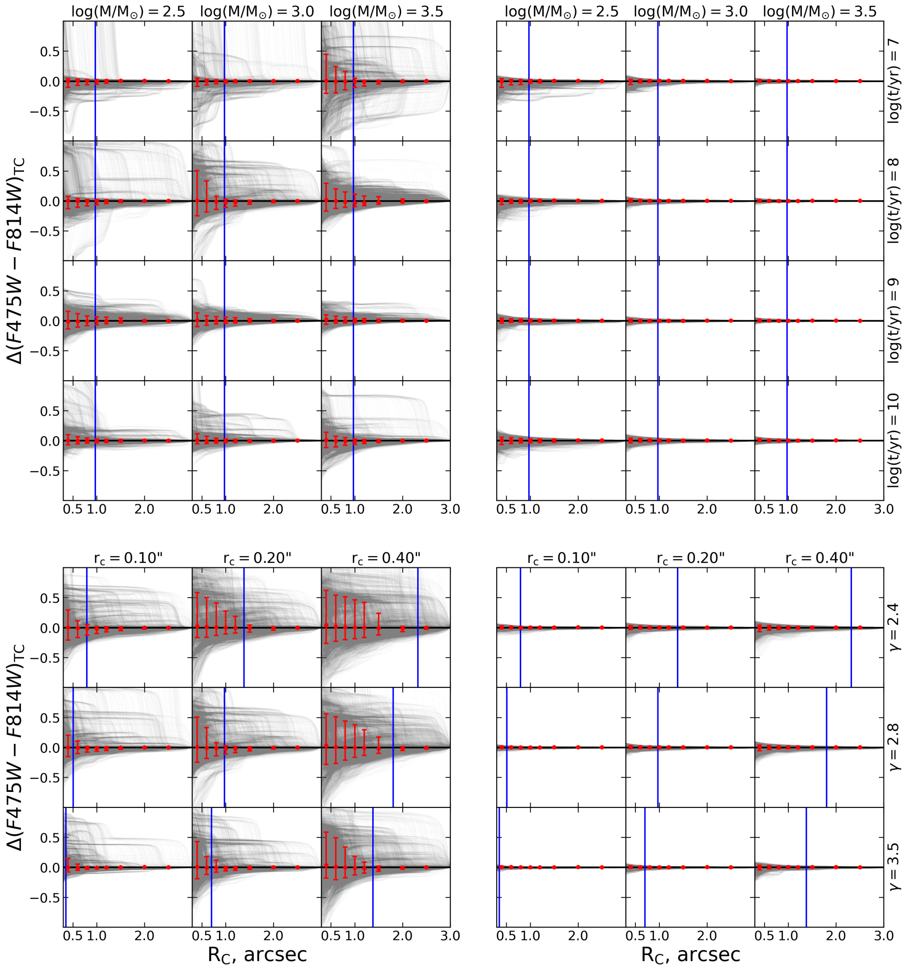

Figure 4.6. Same as Fig. 4.5, but showing results for $F475W - F814W$.

~0.5″, respectively, while a substantial reduction in $\Delta(\mathrm{CI})_{\mathrm{TC}}$ scatter – particularly in $F475W - F814W$ – occurs at $R_{\mathrm{C}} \approx 0.8$-$1.0''$. Similarly, for more extended clusters (e.g., $r_c = 0.2''$ and $\gamma = 2.4$, or $r_c = 0.4''$ and $\gamma = 3.5$), with $R_{50} \approx 0.7''$, the scatter decreases notably at C aperture radii of ~1.2-1.5″. Based on these trends, a practical guideline for selecting an aperture for colour measurements is to adopt $R_{\mathrm{C}} \gtrsim 2 \times R_{50}$ to minimise stochastic effects. Nevertheless, we stress that this recommendation may not be optimal in every case, and we encourage researchers using the adaptive aperture approach to experiment with aperture sizes tailored to their specific science goals.

We also observe that a number of clusters show particularly large $\Delta(\mathrm{CI})_{\mathrm{TC}}$ values, especially at young ages, for example $t = 10\,\mathrm{Myr}$ and $t = 100\,\mathrm{Myr}$, as illustrated in Figs. 4.5 and 4.6. In some cases, these differences reach ±1.0 mag or more. Importantly, most of these large colour discrepancies between T and C apertures manifest as abrupt jumps rather than gradual changes. The majority of these sudden changes are positive, indicating that measurements with T aperture yield systematically redder

CIs. At $t = 100\,\text{Myr}$, $F475W - F814W$ colour appears particularly sensitive to this effect, exhibiting a larger scatter in $\Delta(\text{CI})_{\text{TC}}$ compared to $F336W - F475W$. These results suggest that the primary cause of the largest differences between T and C aperture measurements is, once again, the presence of bright red evolved PMS stars. To test this hypothesis, we subtracted all PMS stars from the simulated cluster images prior to performing aperture photometry, with the resulting measurements shown in the right-hand block of panels in Figs. 4.5 and 4.6.

It is evident that after subtracting the PMS stars, the scatter in $\Delta(\text{CI})_{\text{TC}}$ is greatly reduced, abrupt colour jumps largely disappear, and the differences between T and C aperture measurements are generally close to zero, typically within ±0.1 mag (as shown by percentile ranges). The main exception occurs for the youngest, lowest-mass clusters ($\log_{10}(t/\text{yr}) = 7.0$; $\log_{10}(\text{M}/\text{M}_\odot) \leq 3.0$). In these cases, even after removing evolved stars, the $\Delta(\text{CI})_{\text{TC}}$ scatter remains substantial, reaching around ±0.5 mag and occasionally exceeding this. The scatter is slightly skewed towards negative values, indicating that C aperture measurements now produce redder colours than T aperture measurements. This reflects the stochastic sampling of the upper MS effect: in young, low-mass clusters, if the brightest MS stars lie outside the C aperture, it may produce significant differences between T- and C-based colours. Therefore, caution is advised when applying the adaptive aperture photometry method to very young clusters, as excluding the brightest MS stars can bias colours towards the red and lead to inaccurately derived physical parameters, namely age and extinction.

In the context of this thesis, it is worthy to consider that studies by Fleck et al. (2006) and Gaburov & Gieles (2008) have shown that if a strong mass segregation within a cluster is present, it can produce measurable radial colour gradients of up to 0.1-0.2 mag in $V - I$ or $V - K$ for young ($t < 100\,\text{Myr}$) star clusters. In such cases, the adaptive aperture method may be inadequate as it can introduce small but non-negligible biases in cluster colour measurements. However, Gaburov & Gieles (2008) demonstrated that for clusters of age $t = 10\,\text{Myr}$, a minimum mass of $\log_{10}(\text{M}/\text{M}_\odot) \approx 5.7$ is required for colour gradients caused by mass segregation to be distinguishable from stochastic variations. This implies that, for low-mass clusters, the key assumptions of the adaptive aperture photometry are reasonable and remain well justified.

Overall, the adaptive aperture photometry method provides a way to obtain more robust and consistent colour measurements. In particular, an appropriately chosen aperture can help exclude bright background stars and, in some cases, individual evolved cluster members located in the outer regions, whose inclusion would otherwise increase the uncertainty of derived parameters, as demonstrated by Beerman et al. (2012). This approach is especially effective for studies of low-mass star clusters in the local Universe, extending to distances of ~5 Mpc when high-resolution imaging from modern space-based observatories is available. At the resolution of HST – and comparable current or forthcoming facilities – bright field stars and evolved cluster members can be effectively excluded through a suitable choice of C aperture. Consequently, this method is well suited for studying star clusters in nearby galaxy discs, such as M 31 (Johnson et al. 2015) and M 33 (Johnson et al. 2022), as well as in more distant systems observed in large-scale HST surveys, including LEGUS (Adamo et al. 2017; Cook et al. 2019) and PHANGS-HST (Lee et al. 2022; Deger et al. 2022). Nevertheless, we emphasise that the adaptive aperture method is not universally optimal. Its effectiveness depends on a careful, case-specific choice of apertures, which can be non-trivial in complex environments. We suggest exploring multiple aperture configurations to identify the most suitable approach for a given scientific objective, and caution that any guidelines presented in this study or Naujalis et al. (2021) and Kriščiūnas et al. (2023) should not be applied uncritically.

4.3 Uncertainties of cluster photometry

Next, we aim to evaluate the intrinsic limits on the accuracy of cluster aperture photometry by examining different sources of uncertainty separately. One of the underlying contributions comes from statistical photometric errors associated with uncertainties in choosing aperture centring and size. We evaluate these effects following a procedure similar to that used by Naujalis et al. (2021) and Kriščiūnas et al. (2023). For this purpose, photometry was performed at nine slightly different positions by selecting a 3×3 grid of central pixels (at the pixel scale of the HST ACS/WFC camera, where 1 pixel=0.05″, or ~0.2 pc at the distance of M 31) in each simulated cluster image and centring the aperture on each of them. At every position, measurements were carried out using an aperture of the same radius, as well as two additional apertures with radii offset by ±1 pixel. In this way, for each cluster and its different projections, we obtained a set of 27 measurements of magnitudes and CIs for a given aperture radius. The resulting scatter in these measurements reflects the combined effect of aperture placement and size variations. We quantify this scatter as half of the 16th–84th percentile range, which is denoted as σ_{APT}.

Our approach of generating 100 independent realisations, i.e., producing 100 individual stochastic clusters in every node of the grid (clusters with identical age, mass, r_c, γ) by stochastically sampling both the IMF and spatial distributions of stars, allowed us to quantify the scatter in photometric parameters arising from these stochastic effects (GEN). We estimate this scatter as half of the 16th–84th percentile range of the resulting measurements for a given node, using an aperture of fixed size. This quantity is denoted as σ_{GEN}.

Furthermore, since for a subset of clusters (see Table 3.2) we generated images corresponding to 100 different viewing angles, thereby mimicking variations in line-of-sight projection, this allowed us to assess the impact of projection effects (ROT) on photometric measurements. We quantified the resulting scatter in cluster photometric parameters as half of the 16th–84th percentile range of measurements obtained from these different viewing angles. We refer to this source of uncertainty as σ_{ROT}.

In Fig. 4.7, we present uncertainties arising from these three sources for the $F336W-F475W$ and $F475W - F814W$ colours, shown as a function of aperture radius for four representative combinations of cluster age and mass ($\log_{10}(t/\mathrm{yr}) = 7$ and 10; $\log_{10}(\mathrm{M}/\mathrm{M}_{\odot}) = 2$ and 4). We use models with radial profile parameters of $r_c = 0.2''$ and $\gamma = 2.8$, which are consistent with typical star clusters in the discs of nearby galaxies (e.g., Larsen 2004; Scheepmaker et al. 2007; Mora et al. 2009; Bastian et al. 2012; Ryon et al. 2017; Brown & Gnedin 2021), including those observed in M 31 (Šablevičiūtė et al. 2006, 2007; Vansevičius et al. 2009). All three sources of uncertainty show a rapid decline with increasing aperture size, with the steepest decrease occurring in the aperture size range $R_{\mathrm{ap}} = 0.5''$ to $1.0''$. Beyond this, the uncertainties gradually stabilise, reaching an approximately constant value at $R_{\mathrm{ap}} \gtrsim 1.5''$. At such aperture sizes, the contribution from projection effects σ_{ROT} becomes negligible, dropping below ~0.01 mag. However, in Naujalis et al. (2021) and Kriščiūnas et al. (2023) studies of PHAT clusters, the adopted C aperture radii are often smaller

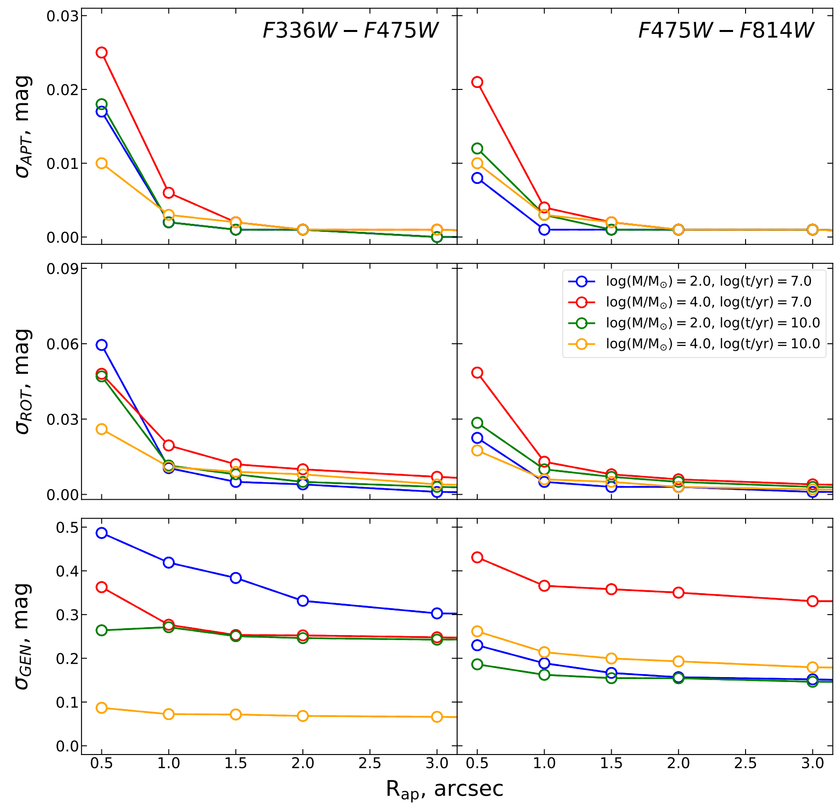

Figure 4.7. Star cluster aperture photometry errors and uncertainties of $F336W - F475W$ (left column) and $F475W - F814W$ (right column) CIs as a function of aperture radius, $R_{\rm ap}$. The top panels show the median uncertainties associated with aperture positioning and size effects ($\sigma_{\rm APT}$); the middle panels – the median scatter due to projection effects ($\sigma_{\rm ROT}$); bottom panels – the median scatter arising from stochastic stellar IMF and the spatial distribution sampling ($\sigma_{\rm GEN}$). Results are shown for clusters with radial profile parameters $r_c = 0.2''$ and $\gamma = 2.8$, for four different combinations of cluster age and mass (see legend).

than $1.5''$. As a result, projection effects can still contribute non-negligibly to the total photometric uncertainty and thus limit the achievable measurement accuracy. For more compact clusters, uncertainties from all three sources considered are generally smaller, particularly with apertures $R_{\rm ap} < 2''$. In contrast, more extended clusters require larger apertures for the uncertainties to stabilise and reach a roughly constant level (see Figs. A3 and A4 in the Appendix).

The key takeaway from these results is that uncertainties driven by GEN and ROT effects – with GEN typically dominating – are significantly larger than those introduced by aperture positioning and size biases (APT). This indicates that, under ideal conditions where background noise and field star contamination are perfectly accounted for, IMF stochasticity sets the fundamental limit on the accuracy of aperture photometry approach for star cluster studies. Nonetheless, it is important to recognise that the random uncertainty sources discussed here, are not the only limitation.

Systematic effects, most notably degeneracies between cluster physical parameters (Worthey 1994; Bridžius et al. 2008; Whitmore et al. 2023), can also play a crucial role. In certain regimes, such as old globular clusters or very young embedded clusters, these systematic effects may even dominate over stochastic photometric errors, ultimately being the primary limiting factor of the reliability of derived parameters.

We stress that projection effects represent a noticeable fraction of the total photometric error budget, and may require consideration in some particular cases. For example, in HST-based studies, for clusters of typical sizes at the distance of M 31, and for apertures with radii $R_{\mathrm{ap}} \leq 1.5''$, these effects can introduce average colour uncertainties of up to ~0.05 mag for typical M 31 clusters, and up to ~0.1 mag in individual cases, depending on cluster properties and the presence of PMS stars. Their impact is reduced for more massive and compact clusters, particularly when evolved stars are absent. We note that while increasing the aperture size helps to reduce the impact of projection effects, it also increases the likelihood of contamination from bright field stars, potentially degrading the overall photometric quality. Therefore, as discussed in previous section, the optimal aperture choice depends on the specific cluster characteristics, its environment, and the scientific goals, thus should be determined for each case individually.

4.4 Accuracy of cluster physical parameter determination

In this section, our goal is to assess the limits on the accuracy of cluster physical parameter determination based on aperture photometry, as imposed by stochastic effects in star clusters. We consider three parameters: age, mass, and interstellar extinction, defined as colour excess $E(B-V)$. For this purpose, we analysed a subset of artificial clusters and their photometric measurements. The parameters of the selected cluster models are listed in Table 4.1. In total, the analysis includes 1920 simulated clusters – 20 models for each of the 96 grid nodes.

Table 4.1. Parameters of cluster models used in physical parameter determination tests.

Parameter	Values
$\log_{10}(\mathrm{M}/\mathrm{M}_\odot)$	2.5, 3.0, 3.5, 4.0
$\log_{10}(\mathrm{t/yr})$	7.0, 8.0, 9.0, 10.0
r_c	0.10″, 0.40″
γ	2.2, 2.8, 7.0

For the parameter determination tests, we used photometric measurements of artificial clusters in all six modelled passbands, obtained with four apertures of following radii: $R_{\mathrm{ap}} = [0.5'', 1.0'', 2.0'', 7.0'']$. Each of the 1920 simulated clusters was measured using all four apertures. Cluster physical parameters – mass, age, extinction – were then derived by comparing these aperture photometry measurements with a large library of integrated photometry of stochastic cluster models. For this purpose, we adopted the method described in de Meulenaer et al. (2013, 2017) (see Section 2.1).

The cluster model grid used for parameter determination spans the following ranges:

age from $\log_{10}(t/\mathrm{yr}) = 6.0$ to 10.3 in steps of 0.02; mass from $\log_{10}(\mathrm{M}/\mathrm{M}_\odot) = 2.0$ to 7.0 in steps of 0.05; extinction from $E(B-V) = -0.03$ to 1.5 in steps of 0.01, assuming solar metallicity. This results in $\sim 4 \times 10^6$ grid nodes, with each node containing 10 000 stochastic clusters, yielding a total of $\sim 4 \times 10^{10}$ models. Parameter probabilities for each of the 1920 test clusters, measured through the four aforementioned apertures, were computed following Eqs. 2.1 and 2.2. The final cluster parameters were derived by selecting that parameter combination which corresponds to the maximum likelihood value.

To evaluate the accuracy of the derived parameters, we calculated the differences between the recovered and input values:

- $\Delta\log_{10}(t/\mathrm{yr}) = \log_{10}(t/\mathrm{yr}) - \log_{10}(t/\mathrm{yr})_{\mathrm{input}}$
- $\Delta\log_{10}(\mathrm{M}/\mathrm{M}_\odot) = \log_{10}(\mathrm{M}/\mathrm{M}_\odot) - \log_{10}(\mathrm{M}/\mathrm{M}_\odot)_{\mathrm{input}}$
- $\Delta E(B-V) = E(B-V) - E(B-V)_{\mathrm{input}}$.

Initially, we performed a preliminary analysis using two $E(B-V)_{\mathrm{input}}$ values, 0.0 and 0.5 mag. However, as the differences between the results for these two input values were found to be negligible, further we discuss only the results obtained for $E(B-V)_{\mathrm{input}} = 0.0$ mag.

In Fig. 4.8, we present the main results of the cluster parameter determination tests, where we show the median differences between recovered and input parameters versus cluster age. No significant variations were found in either the median values or the scatter of $\Delta\log_{10}(t/\mathrm{yr})$, $\Delta\log_{10}(\mathrm{M}/\mathrm{M}_\odot)$, and $\Delta E(B-V)$ when using apertures with radii $R_{\mathrm{ap}} = 1.0''$, $2.0''$, and $7.0''$. Likewise, these parameter differences show no clear dependence on the structural parameters r_c and γ. Therefore, we combined the results obtained from these three apertures into a single dataset, shown by blue open circles and lines in Fig. 4.8. Each data point in this case represents 480 artificial clusters measured through three aforementioned apertures, corresponding to a total of 1440 parameter differences. However, results obtained using the smallest aperture, $R_{\mathrm{ap}} = 0.5''$, exhibit noticeably contrasting distributions of parameter differences when compared to results for other three apertures. Therefore, we present $R_{\mathrm{ap}} = 0.5''$ results separately, marked by red open circles and dashed lines. Here, each data point corresponds to 480 artificial clusters. Error bars denote the 16th–84th percentile range of the respective parameter difference distributions.

A clear trend visible in Fig. 4.8 is the lower parameter accuracy when using the smallest aperture, $R_{\mathrm{ap}} = 0.5''$, compared to results based on measurements with larger apertures. For $R_{\mathrm{ap}} = 0.5''$ case, the medians of the parameter differences show significant offsets from zero, indicating the presence of systematic biases. It is also evident that results based on larger apertures are unbiased, with median values close to zero, and scatter being relatively small. This suggests that the distributions of parameter differences are much narrower for larger apertures, indicating higher precision and overall more reliable cluster parameter estimates.

We find that at $t = 10$ Myr, the medians of $\Delta\log_{10}(t/\mathrm{yr})$ and $\Delta\log_{10}(\mathrm{M}/\mathrm{M}_\odot)$ are both shifted by approximately +0.2 dex, indicating that older ages and higher masses are systematically inferred. This behaviour is expected, as an overestimation of age requires a corresponding increase in mass to match the observed integrated flux. This suggests that the use of such small apertures, $R_{\mathrm{ap}} \leq 0.5''$, for clusters at the distance of M 31 can introduce additional parameter degeneracies. More generally, it is evident

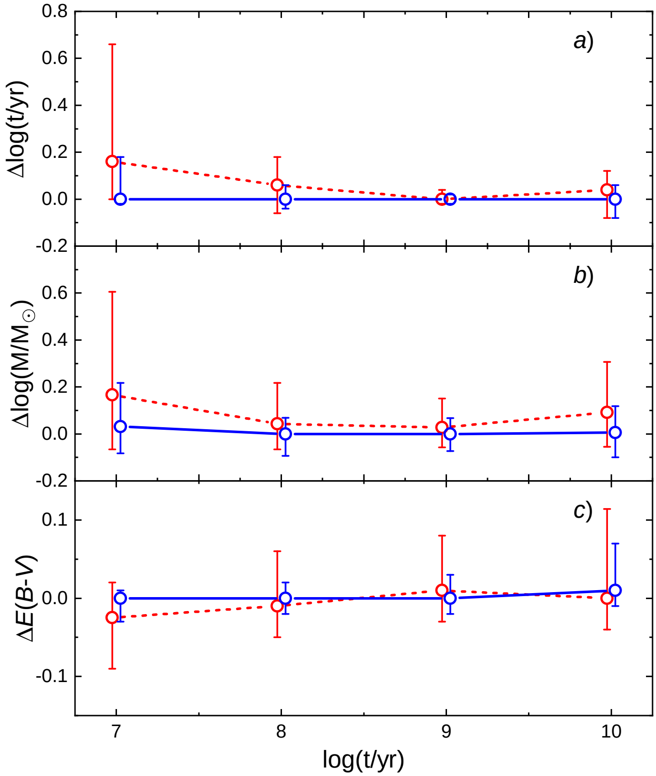

Figure 4.8. Results of star cluster physical parameter determination tests, shown as differences between the recovered and input parameter values. Panel a) presents age differences; panel b) shows mass differences; and panel c) displays colour excess, $E(B-V)$, differences. Red open circles mark median parameter differences derived from measurements obtained with an aperture of $R_{\rm ap} = 0.5''$. Blue open circles represent median differences based on measurements with apertures $R_{\rm ap} = 1.0''$, $2.0''$, and $7.0''$, combined into a single dataset. Error bars indicate the 16th–84th percentile ranges. For clarity, markers and connecting lines are slightly shifted along the X-axis relative to the original input value.

that the usage of such small apertures is not advised. This is consistent with the constraints applied for adaptive aperture method by Naujalis et al. (2021) and Kriščiūnas et al. (2023), which we already discussed in Section 4.2. While these previous studies demonstrated that adopting such rule leads to more robust photometric measurements, here we show that it also leads to more accurate determination of cluster physical parameters.

Importantly, we notice that parameter determination for $t = 10$ Myr clusters is problematic regardless of the aperture size, even when using $R_{\rm ap} = 7.0''$, which ensures that the total cluster flux is fully enclosed in for the most of our models. At this age, the 16th–84th percentile range of $\Delta\log_{10}(t/{\rm yr})$ is ~0.7 dex when using $R_{\rm ap} = 0.5''$ aperture, and reaches ~0.2 dex even when larger apertures are used. A similar behaviour is observed for $\Delta\log_{10}(\mathrm{M}/\mathrm{M}_\odot)$, where the spread spans ~0.7 dex for the smallest aperture, and reaches ~0.3 dex even for $R_{\mathrm{ap}} \geq 1.0''$. This is due to the strong impact of stochastic sampling of short-lived, luminous massive stars at young ages, whose presence or absence can dominate the integrated light and thus significantly affect the inferred physical parameters. In contrast, $\Delta E(B-V)$ exhibits a different trend, with the lowest accuracy found for the oldest, $t = 10$ Gyr, clusters.

Overall, these results reinforce the idea discussed in Section 4.2 (see also Figs. 4.3 and 4.4) that physical parameters of young star clusters derived from aperture photometry alone can be of limited accuracy. Considering that our analysis in this Chapter is based on idealised conditions without sky background (its effects are explored in Chapter 5), in realistic observational environments, the achievable accuracy is expected to be even lower. In agreement with Johnson et al. (2022), our findings indicate that for resolved and semi-resolved young clusters ($t \lesssim 40$ Myr), more reliable parameter estimates can generally be obtained using CMD-analysis-based methods (Dolphin 2002; Johnson et al. 2016; Čeponis et al. 2024; Zheng et al. 2025), rather than techniques relying solely on integrated photometry (Fioc & Rocca-Volmerange 1997; Deveikis et al. 2008; Fouesneau & Lançon 2010; de Meulenaer et al. 2013; Fouesneau et al. 2014; Krumholz et al. 2015; de Meulenaer et al. 2017). We suggest that ideally, the most robust constraints on physical parameters of young clusters ($t \lesssim 1$ Gyr) can be obtained by combining information from both CMD analysis and integrated photometry, when it is available. Finally, it should be emphasised that the accuracy of derived parameters also depends on the choice of stellar evolution and population synthesis models, since – as discussed in Section 3.3 – systematic differences between models can be substantial in some cases.

4.5 Uncertainties of cluster structural parameters

Our ability to study the dynamical evolution of extragalactic star clusters relies on the accuracy of their structural parameters. Thus, we examine how the stochastic effects in low-mass clusters influence the uncertainties of structural parameters derived from FGCs. For this purpose, we define the scatter in structural parameters arising from stochastic sampling of the IMF and stellar spatial distribution (σ_{GEN}), as well as from projection effects (σ_{ROT}), following the same approach as we did for photometric parameters in Section 4.3. In both cases, the scatter is quantified as half of the 16th–84th percentile range. Since the R parameters and their ratios depend strongly on the input EFF model parameters, we express these uncertainties in relative terms. Specifically, we define δ_{GEN} and δ_{ROT} as the ratios of σ_{GEN} and σ_{ROT} to the corresponding structural parameter median values, expressed in percent. We emphasise that the following analysis is based on structural parameters determined from FGCs in $F475W$ passband, as this filter in the PHAT survey offers the best signal-to-noise and relatively low contamination by resolved field stars.

In Fig. 4.9, we present δ_{GEN} and δ_{ROT} as functions of cluster age for the structural parameters R_{50}, R_{30}/R_{50}, R_{50}/R_{80}, considering three cluster masses ($\log_{10}(\mathrm{M}/\mathrm{M}_\odot) =$ 2, 3, and 4). There we use models with EFF profile parameters $r_c = 0.2''$ and $\gamma = 2.8$, which are representative of young clusters in galactic discs. The results show that GEN effects introduce substantial variations in the estimated cluster size, R_{50}, despite identical input parameters. This effect is particularly strong for very young clusters: at $t = 10$ Myr, δ_{GEN} exceeds ~40% across the entire mass range considered here.

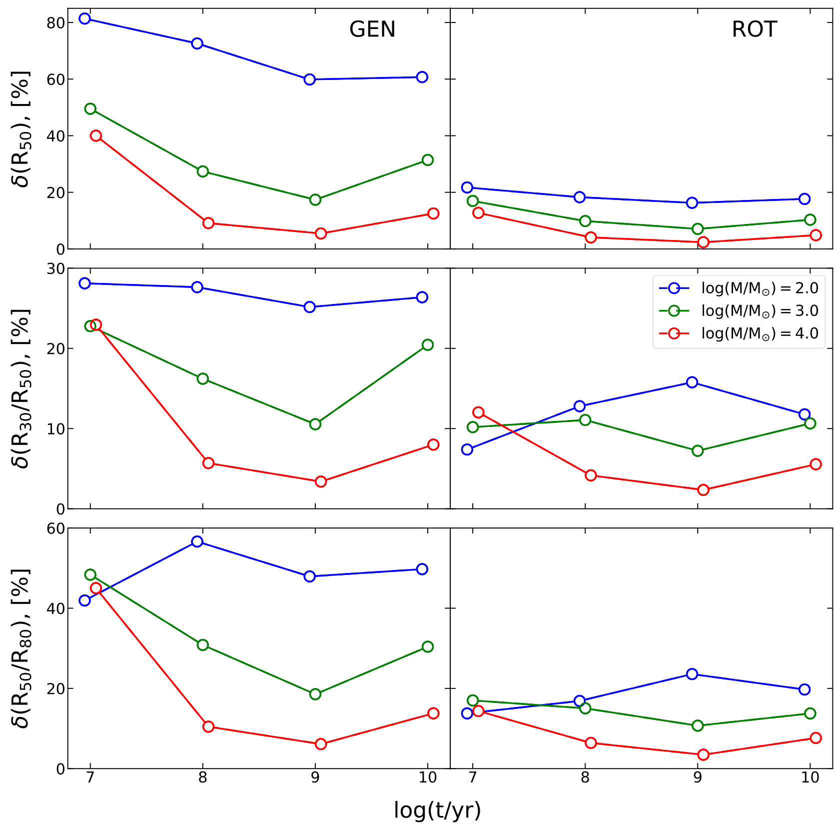

Figure 4.9. Relative uncertainties (in percent) of star cluster structural parameters as a function of cluster age. The left column shows median uncertainties due to stochastic sampling of the IMF and stellar spatial distribution, δ_{GEN}, while the right column presents uncertainties arising from cluster projection effects, δ_{ROT}. The top row shows the R_{50}, the middle row – the ratio R_{30}/R_{50}, and the bottom row – R_{50}/R_{80}. Results are shown for clusters with $r_c = 0.2''$ and $\gamma = 2.8$, for three different cluster masses (see legend). For visual clarity, blue and red markers and connecting lines are slightly offset along the X-axis relative to the input age values.

GEN effects produce R_{50} uncertainties of $\gtrsim$20% for clusters with $\log_{10}(\mathrm{M}/\mathrm{M}_\odot) \leq 3$ over the studied age interval. Only more massive clusters ($\log_{10}(\mathrm{M}/\mathrm{M}_\odot) = 4$) at intermediate ages (100 Myr and 1 Gyr) exhibit significantly smaller uncertainties, with δ_{GEN} dropping below 10%.

In contrast, ROT effects introduce smaller uncertainties in the FGC-based estimates of R_{50} than those caused by GEN effects across the full range of cluster masses and ages considered here. For clusters with $\log_{10}(\mathrm{M}/\mathrm{M}_\odot) \geq 3$, δ_{ROT} decreases below 10% at ages $\log_{10}(t/\mathrm{yr}) \geq 8$. At the youngest ages ($\log_{10}(t/\mathrm{yr}) = 7$), however, δ_{ROT} remains higher, ranging from ~10% to 20% depending on cluster mass. The lowest-mass clusters, $\log_{10}(\mathrm{M}/\mathrm{M}_\odot) = 2$, consistently exhibit the largest uncertainties due to projection effects, with δ_{ROT} staying at ~20% across the entire age range.

A comparison of the two structural parameter ratios considered here, R_{30}/R_{50} and

R_{50}/R_{80}, reveals that uncertainties induced by both GEN and ROT effects are consistently larger for R_{50}/R_{80} ratio across all examined ages. For $\log_{10}(\mathrm{M}/\mathrm{M}_\odot) \leq 3$ clusters, GEN effects result in uncertainties of ~10-30% for R_{30}/R_{50} and ~20-60% for R_{50}/R_{80}. In the same mass range, ROT effects introduce smaller variations, typically ~5-15% and ~10-25% for R_{30}/R_{50} and R_{50}/R_{80}, respectively. At $t = 10$ Myr, uncertainties for all considered cluster masses are $\delta_{\mathrm{GEN}} \gtrsim 20\%$ for R_{30}/R_{50} and $\delta_{\mathrm{GEN}} \gtrsim 40\%$ for R_{50}/R_{80}. In contrast, ROT effects at this age remain moderate, producing uncertainties of ~10% and ~15% for R_{30}/R_{50} and R_{50}/R_{80}, respectively. Overall, these results suggest that R_{30}/R_{50} is a more robust tracer of cluster structural profile and compactness than R_{50}/R_{80} when using FGC-based measurements. This likely reflects that the outer cluster regions are more susceptible to stochastic fluctuations, which more strongly affect parameters involving larger radii.

Figure 4.9 demonstrates that FGC-based structural parameters are generally more robust for higher mass clusters, with the exception of the youngest systems. In most cases, uncertainties driven by both GEN and ROT effects decrease with age up to ~1 Gyr, before increasing again at 10 Gyr. An interesting deviation from this behaviour is observed for the lowest mass clusters ($\log_{10}(\mathrm{M}/\mathrm{M}_\odot) = 2$), where δ_{ROT} exhibits an opposite age dependence for R_{30}/R_{50} and R_{50}/R_{80}. This trend can be explained in terms of stellar content: at very young ages (~10 Myr), such low-mass clusters are unlikely to host stars that are massive enough to have left the MS. But as the cluster ages and the mass at the MSTO decreases, evolved PMS stars begin to appear and can dominate the cluster flux. The stochastic presence of these dominant evolved stars increases the uncertainty of structural parameters, as the shapes of the low-mass cluster FGCs are highly sensitive to the spatial distribution of such stars within the cluster.

In Fig. 4.10, we present the relative uncertainties, δ_{GEN} and δ_{ROT}, for R_{50}, R_{30}/R_{50}, R_{50}/R_{80}, as functions of cluster core radius, r_c. The results are shown for three values of the EFF profile slope (γ = 2.2, 2.8, 7.0), using models with $\log_{10}(\mathrm{M}/\mathrm{M}_\odot) = 3$ and $\log_{10}(t/\mathrm{yr}) = 8$, representative of typical star clusters in M 31. In general, uncertainties coming from both sources are lower for more compact (i.e., smaller r_c and larger γ) clusters, indicating that more robust structural parameters can be determined for more concentrated objects. However, clusters with shallow profiles ($\gamma = 2.2$) exhibit a different behaviour: in this case, the relative uncertainties, particularly δ_{GEN}, decrease with increasing r_c value. A similar trend is also observed for $\gamma = 2.8$ models in the case of R_{50}/R_{80}. Such behaviour can be explained by the fact, that although the absolute uncertainties σ_{GEN} and σ_{ROT} increase with r_c, the corresponding structural parameter values grow more rapidly. As a result, when expressed in relative terms, the uncertainties δ_{GEN} and δ_{ROT} decrease at larger core radii.

To further explore the impact of stochastic stellar sampling on the measurements of star cluster structure, we examine the distribution of models in the R_{30}/R_{50} versus R_{50}/R_{80} parameter space (Figs. 4.11 and 4.12). The results are shown for both – when all sampled stars are included (red dots), and where PMS stars are removed prior to performing photometry (blue dots). Figure 4.11 illustrates how these distributions vary as a function of cluster mass and age. A prominent feature is the large scatter observed across many of the studied cluster mass-age combinations, with simulated clusters spanning most of the parameter space rather than gathering around well-defined regions. This effect is particularly strong for very low-mass clusters with $\log_{10}(\mathrm{M}/\mathrm{M}_\odot) \leq 2.5$ across the entire age range considered here. A similar level of

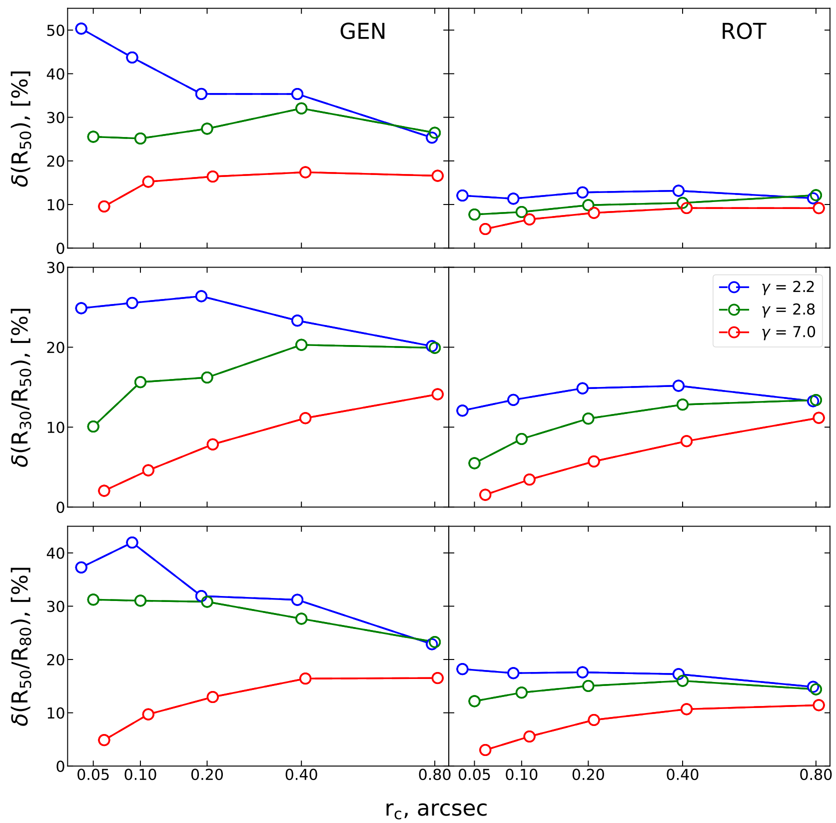

Figure 4.10. Relative uncertainties (in percent) of star cluster structural parameters as a function of cluster core radius, r_c. The left column shows median uncertainties due to stochastic sampling of the IMF and stellar spatial distribution, δ_{GEN}, while the right column presents uncertainties arising from cluster projection effects, δ_{ROT}. The top row corresponds to the R_{50}, the middle row to the ratio R_{30}/R_{50}, and the bottom row to R_{50}/R_{80}. Results are shown for clusters with $\log_{10}(\mathrm{M}/\mathrm{M}_{\odot}) = 3$ and $\log_{10}(t/\mathrm{yr}) = 8$, for three different γ values (see legend). For visual clarity, blue and red markers and connecting lines are slightly offset along the X-axis relative to the input r_c values. The X-axis is displayed using square-root scaling.

dispersion is also observed for very young ($t = 10\,\mathrm{Myr}$) clusters over a wide range of masses when evolved PMS stars are included, highlighting their dominant influence on the determined structural parameters based on FGC measurements.

A notable feature we observe for the lowest mass clusters ($\log_{10}(\mathrm{M}/\mathrm{M}_{\odot}) = 2$) across all ages, as well as for intermediate mass clusters ($\log_{10}(\mathrm{M}/\mathrm{M}_{\odot}) \leq 3$) at the age of $\log_{10}(t/\mathrm{yr}) = 7$, a substantial fraction of clusters occupy region of the R_{30}/R_{50} versus R_{50}/R_{80} parameter space where both ratios approach unity. This behaviour indicates that the radial flux profile is dominated by a single bright star, resulting in nearly identical values of R_{30}, R_{50}, and R_{80}. A similar effect is observed at $\log_{10}(t/\mathrm{yr}) = 7$ even for more massive clusters ($\log_{10}(\mathrm{M}/\mathrm{M}_{\odot}) = 3.5$) when PMS stars are not removed (see red dots in the corresponding panel of Fig. 4.11). In such case, this effect is most

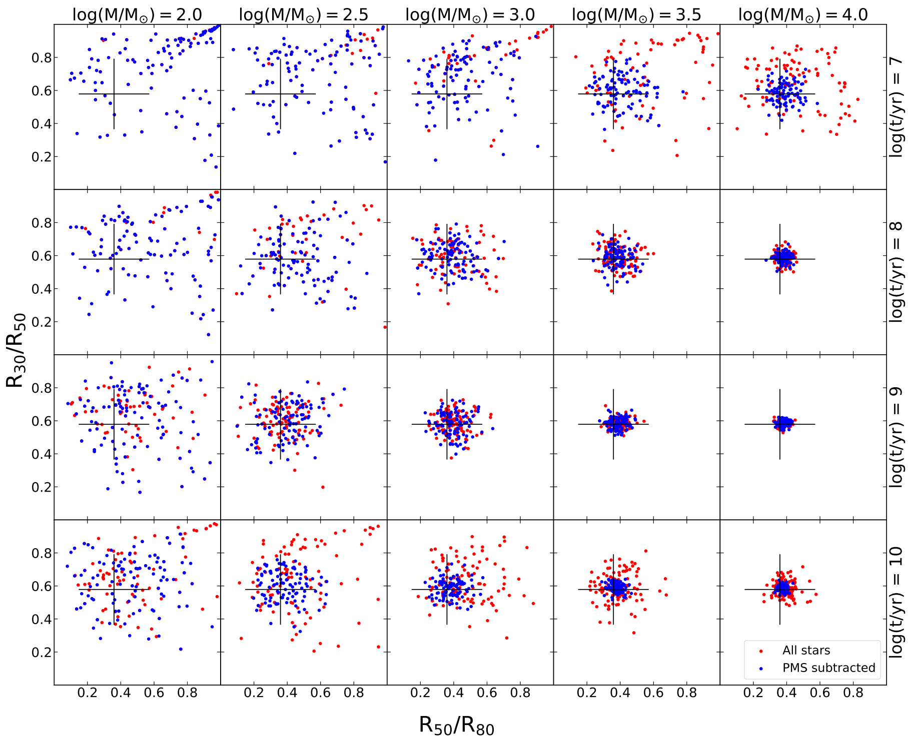

Figure 4.11. Effects of stochastic stellar sampling on cluster structural parameters for different cluster mass and age combinations. The X-axis shows R_{50}/R_{80}, while the Y-axis corresponds to R_{30}/R_{50}. Results are presented for clusters with $r_c = 0.2''$ and $\gamma = 2.8$. Red dots mark clusters containing all sampled stars, whereas blue dots represent clusters for which PMS stars were removed prior to photometric measurements. The crosshairs indicate the theoretical locations of star clusters derived from the input radial profile parameters.

likely driven by very luminous evolved stars, such as supergiants.

In contrast to the behaviour described above, more massive and older star clusters tend to occupy much more confined regions of the R_{30}/R_{50} versus R_{50}/R_{80} parameter space. In particular, clusters with masses $\log_{10}(\mathrm{M}/\mathrm{M}_\odot) \geq 3.5$ and ages $\log_{10}(t/\mathrm{yr}) \geq 8$ form well-defined and concentrated distributions, with this being most pronounced for $\log_{10}(\mathrm{M}/\mathrm{M}_\odot) = 4$ clusters. This indicates that stuctural parameters for such systems can be determined with good accuracy and reliability based on aperture photometry. At younger ages ($\log_{10}(t/\mathrm{yr}) = 7$), massive clusters with $\log_{10}(\mathrm{M}/\mathrm{M}_\odot) \geq 3.5$ show a noticeable improvement when PMS stars are subtracted (compare blue and red dots in Fig. 4.11). However, the most massive clusters ($\log_{10}(\mathrm{M}/\mathrm{M}_\odot) \geq 4$) at ~10 Myr, typically contain multiple luminous evolved stars. In realistic conditions, it is therefore difficult to remove all such stars without compromising the integrity of the cluster's integrated photometry, as some of the PMS stars are likely to reside in unresolved central regions of the cluster. Moreover, partial subtraction of such stars may introduce additional inconsistencies and increase the overall errors of the derived structural parameters.

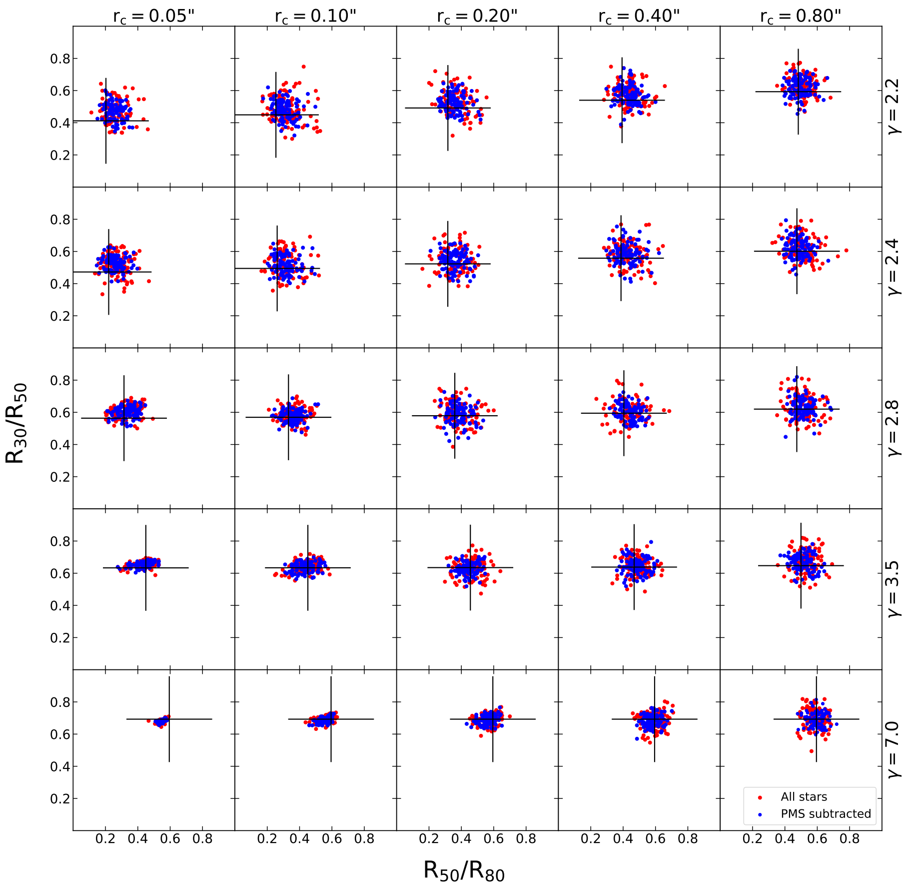

Figure 4.12. Effects of stochastic stellar sampling on cluster structural parameters for different radial profile parameters, r_c and γ. The X-axis shows R_{50}/R_{80}, while the Y-axis corresponds to R_{30}/R_{50}. Results are presented for clusters with $\log_{10}(\mathrm{M}/\mathrm{M}_\odot) = 3.5$ and $\log_{10}(t/\mathrm{yr}) = 8$. Red dots mark clusters containing all sampled stars, whereas blue dots represent clusters for which PMS stars were removed prior to photometric measurements. The crosshairs indicate the theoretical locations of star clusters derived from the input radial profile parameters.

Figure 4.12 shows the distribution of clusters in the same R parameter ratio space, but depending on radial profile parameters, r_c and γ, for models with $\log_{10}(\mathrm{M}/\mathrm{M}_\odot) = 3.5$ and $\log_{10}(t/\mathrm{yr}) = 8$. We find that the most compact studied clusters ($r_c = 0.05''$-$0.10''$, $\gamma = 3.5$-7.0) exhibit only a small dispersion. While more extended clusters generally show a somewhat larger scatter, the overall level remains relatively similar for models with $\gamma \leq 2.8$ and $r_c \geq 0.2''$. Notably, clusters tend to concentrate around distinct locations in the R_{30}/R_{50} versus R_{50}/R_{80} space depending on their r_c and γ values. This indicates that, for sufficiently massive clusters ($\log_{10}(\mathrm{M}/\mathrm{M}_\odot) > 3$), their positions in this parameter space can provide useful and meaningful constraints on their structural properties. On the contrary, for lower-mass clusters, the dispersion introduced by stochastic effects is too large, leading to significant overlap between models with different r_c and γ, and thus limiting the ability to reliably assess their structural characteristics.

In summary, the results presented in this section indicate that structural parameters of low-mass ($\log_{10}(\mathrm{M}/\mathrm{M}_\odot) \lesssim 3$) and young ($\log_{10}(t/\mathrm{yr}) \lesssim 8$) star clusters, when derived solely from FGC analysis, are subject to substantial uncertainties and should be interpreted with caution. Notably, we have shown that cluster projection (ROT) effects introduce uncertainties of ∼10-20% in cluster size estimates (R_{50}). However, stochastic stellar sampling (GEN effects) produce significantly larger scatter of structural parameters. Although Narbutis et al. (2014) demonstrated that accounting for bright resolved stars can improve the accuracy of structural parameters in the context of 2D image fitting, our results show that, for FGC-based methods, removing luminous evolved stars, while indeed improving the accuracy, does not fully mitigate these issues across all parameter regimes. This limitation is especially pronounced for low-mass ($\log_{10}(\mathrm{M}/\mathrm{M}_\odot) < 3$) and young ($\log_{10}(t/\mathrm{yr}) < 8$) clusters.

Taken together, these findings suggest that while standard aperture photometry approach can provide important insight about sizes and structure of clusters, it is insufficient for reliably characterising key structural aspects of star cluster populations, such as the mass–radius relation, dynamical evolution, and eventual disruption (Portegies Zwart et al. 2010; Krumholz et al. 2019; Adamo et al. 2020). More robust analyses require complementary techniques, such as careful treatment of individual luminous resolved stars (Beerman et al. 2012; Narbutis et al. 2014; Naujalis et al. 2021) or the application of 2D cluster image fitting methods (Larsen 1999; Narbutis et al. 2014; Brown & Gnedin 2021).

4.6 Summary

In this Chapter, we determined the intrinsic limits on the maximum achievable accuracy of aperture photometry in star cluster studies within the local Universe, as imposed by stochastic effects. This was accomplished by analysing FGCs of star cluster models presented in Chapter 3, under idealised conditions with no sky background, i.e., assuming perfect background subtraction. We note that the inclusion of additional sources of uncertainty, such as a noisy sky background or resolved bright field stars, would further increase the reported errors. Moreover, in some cases, systematic problems – such as parameter degeneracies (Worthey 1994; Bridžius et al. 2008; Whitmore et al. 2023) or differences between stellar evolution models – can have a stronger effect on the accuracy of derived cluster properties than stochasticity.

We have shown that clusters containing evolved, luminous PMS stars (G2) differ significantly in their photometric properties from those without such stars (G1). In particular, G2 clusters exhibit noticeably larger scatter and uncertainties in their photometric parameters. These results are in agreement with Beerman et al. (2012) and demonstrate that the absence of PMS stars leads to more consistent, predictable, and well-defined photometric properties, ultimately enabling a more robust derivation of cluster physical parameters.

We found no significant systematic differences or gradients in CIs when star clusters are measured using smaller (C) apertures compared to larger, conventional (T) apertures. This supports the use of the adaptive aperture photometry method, which minimises contamination of CI measurements by bright field stars and evolved cluster members. We therefore propose that this approach, with a careful, case-by-case selection of C apertures, can be applied to obtain more accurate photometric measurements of low-mass star clusters in the local Universe (at least out to distance ~5 Mpc with modern space-based observations).

Results of the physical parameter determination tests revealed that, to obtain accurate and reliable aperture-photometry-based cluster parameter estimates, CIs should be measured using apertures with radii larger than the clusters' half-light radii, as was commonly adopted by Naujalis et al. (2021) and Kriščiūnas et al. (2023). However, we found that the determination of parameters for very young star clusters (t = 10 Myr) remains problematic, regardless of the aperture size used. Consequently, CMD fitting methods (Dolphin 2002; Johnson et al. 2016; Čeponis et al. 2024; Zheng et al. 2025) are expected to provide more reliable estimates of physical parameters than integrated photometry for resolved and semi-resolved young ($t \lesssim 40$ Myr) star clusters. Ideally, combining results from both approaches can lead to the most robust constraints on cluster physical parameter estimates.

We have shown that FGC-based structural parameters for $\log_{10}(\mathrm{M}/\mathrm{M}_{\odot}) \lesssim 3$ and $\log_{10}(t/\mathrm{yr}) \lesssim 8$ clusters are poorly constrained and exhibit large uncertainties due to stochastic effects inherent to low-mass star clusters. For such objects, additional constraints or a careful treatment of bright resolved stars are required to reliably characterise their sizes and structural evolution.

Notably, we demonstrated that the randomness of low-mass star cluster viewing angles introduces measurable uncertainties of up to ~0.05 mag in CIs on average for typical M 31 clusters, and up to ~0.1 mag in individual cases, and typically ~10-20% uncertainties in structural parameters, depending on the interplay between cluster physical and radial profile parameters and aperture size. In some cases this effect should be included in the total error budget of aperture photometry measurements; however, it is generally much weaker than uncertainties arising from stochastic stellar sampling effects.

Chapter 5

Sky background effects

The content of this chapter is based on Daugevičius et al. (2025).

The previous Chapter established the optimistic intrinsic limits of aperture photometry accuracy and applicability under idealised, background-free conditions. In real observations, however, measurements are inevitably affected by the presence of a structured and often complex sky background, especially in the nearby galaxies where stellar populations are at least partially resolved. Multiple HST studies of star clusters in M 31 (Krienke & Hodge 2007, 2008; Hodge et al. 2009, 2010; Johnson et al. 2012) showed that the strongly variable background level within the disc, its estimation and subtraction, is one of the primary sources of photometric errors. Ground-based studies by Kodaira et al. (2004) and Narbutis et al. (2008) also reported that photometric uncertainties are largely driven by sky background variations and are difficult to reduce without interactive intervention. In addition, as mentioned earlier, bright field stars projected within the photometric aperture can significantly affect the measurements, complicating the derivation of cluster parameters and often introducing age–extinction degeneracies (de Meulenaer et al. 2017). Therefore, understanding the impact of background effects is crucial for the reliable interpretation of results derived from cluster aperture photometry.

In this Chapter, we extend the analysis to more realistic observational conditions and investigate how sky background influences the accuracy and applicability of aperture photometry for nearby extragalactic star clusters. To achieve this, we construct realistic mock observations by embedding simulated clusters into real M 31 imaging data spanning a range of stellar densities and background environments. We then measure these mock clusters and quantify photometric uncertainties, and how they depend on cluster properties, aperture size, and local background environment. We further determine optimal aperture sizes for colour measurements, and assess biases introduced by sky background effects. Finally, we examine catalogue completeness limits and selections effects, and how they may influence the capabilities of present and future star cluster surveys.

5.1 Background fields

To evaluate the impact of background effects on star cluster aperture photometry and catalogue completeness limits in the context of the PHAT survey, we placed simu-

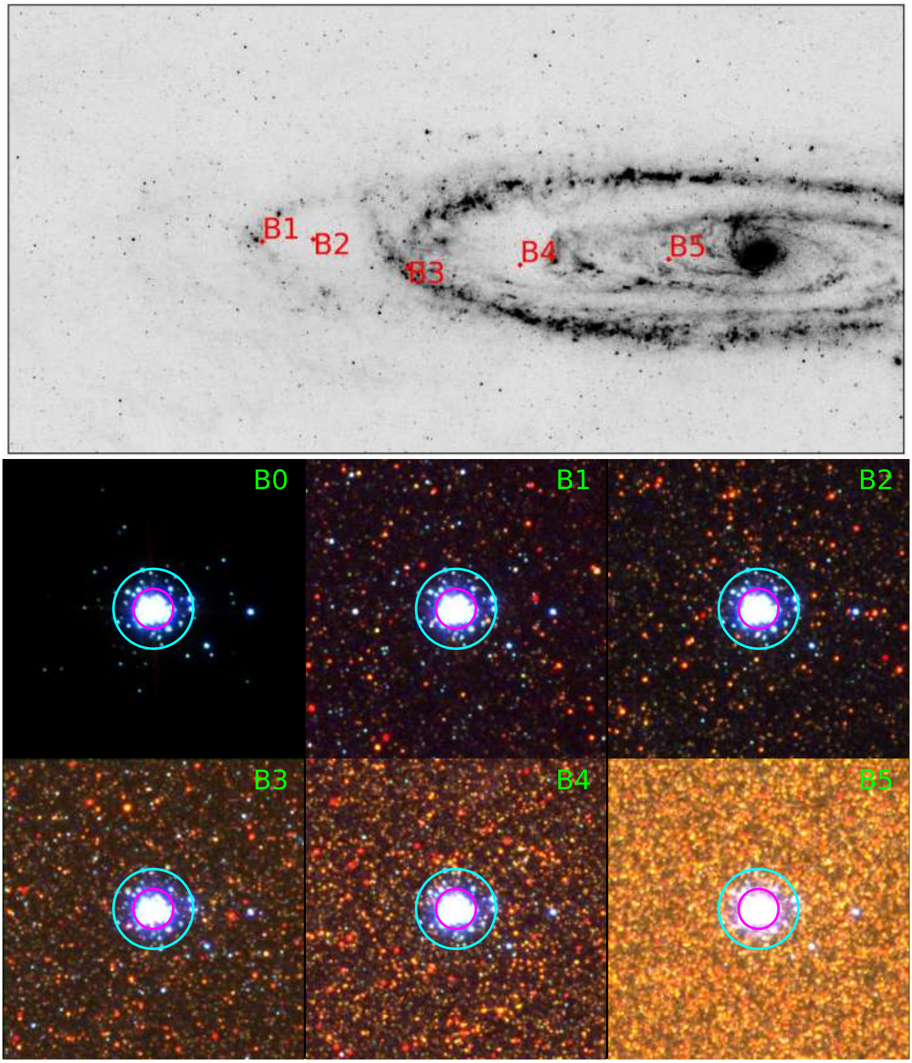

Figure 5.1. Background fields in the disc of M 31. The top panel shows a grey-scale 24 μm Multi-Band Imaging Photometer for *Spitzer* (*Spitzer*/MIPS) map of M 31, with the locations of the selected background fields (B1–B5) denoted by red markers. The bottom panels display images of a simulated star cluster with $\log_{10}(M/M_\odot) = 3.5$, $\log_{10}(t/\mathrm{yr}) = 7$, $r_c = 0.2''$, and $\gamma = 2.8$, placed in each of the background fields. B0 represents background-free case. Magenta and cyan circles mark circular apertures with radii $R_{\mathrm{ap}} = 1''$ and $2''$, respectively. The $15'' \times 15''$ colour images were produced by combining *F*336*W* (blue), *F*475*W* (green), and *F*814*W* (red) passband data.

lated clusters (described in Chapter 3; see Table 3.1) into five real background fields of varying stellar density in the M 31 disc (shown in Fig. 5.1), extracted from PHAT imaging data.

In the case of *F*275*W* and *F*336*W* passbands, the frames are significantly affected by a large number of cosmic-ray artefacts and other defects. Cosmic rays are high-energy particles that transfer their energy into detector pixels upon impact, producing signals that can mimic bright point sources similar to stars, with the strongest effect seen in UV passbands. If such contaminants fall within the aperture, they can introduce severe biases and errors into the integrated photometry measurements, potentially ruining them. Therefore, their removal is essential.

However, for these two UV passbands, only two repeated exposures are available in the PHAT survey, making standard automated cleaning techniques challenging and unreliable. Alternative novel methods (Chen et al. 2024) require data to be at a lower processing level, which were unavailable for this study. Consequently, we cleaned the selected background fields manually by removing the most prominent cosmic-ray artefacts using the `imedit` task from `PyRAF`[1], a `Python` environment for executing tasks from the original `IRAF` (Tody 1986) image reduction and analysis software package. The `imedit` tool enables a careful treatment of cosmic-ray defects by replacing affected pixel values with interpolated values derived from neighboring pixels.

The background fields are $17'' \times 17''$ square cut-outs, corresponding to a field of view ~65×65 pc at the distance of M 31, and thus larger than the $15'' \times 15''$ frames of the simulated clusters. This allowed us to place each artificial cluster at slightly different random positions within a given background field while preserving the same general background features. Such an approach helps mitigate potential systematic biases that could arise from placing all simulated clusters at the same location, which might contain peculiar features such as a bright background star, a dusty patch, or an unaccounted imaging defect.

We emphasise that the selected background fields were carefully chosen not only to span a range of stellar densities – which generally decreases with increasing radial distance from the galactic centre – but also to represent different types of physical environments. This is evident in Fig. 5.1, which shows *Spitzer*/MIPS 24 μm map of the M 31 disc together with colour images of an artificial cluster placed in each background field. Fields B1 and B3 are located within the prominent star-forming rings at $\sim$15 kpc and $\sim$10 kpc from the galactic centre, respectively, where conditions characteristic of star-forming regions – such as differential reddening caused by dense dusty structures and the presence of numerous bright, blue young field stars – are expected. In contrast, fields B2 and B4 lie in the inter-ring regions, where intermediate-age and old stellar populations dominate and irregular dust are much less prominent. Finally, field B5 represents the inner regions of the M 31 disc, characterised by an extremely high stellar density, a common feature in the central parts of galactic discs.

In Fig. 5.2, we present CMDs for each of the studied background fields. For the background-free (B0) case, we show the CMD of a massive ($\log_{10}(\mathrm{M}/\mathrm{M}_\odot) = 4.5$) simulated cluster at an age of $t = 100$ Myr, with stellar photometry errors assigned according to their brightness, based on PHAT photometry results from Williams et al. (2023). This serves as a reference for comparison with the CMDs of the B1–B5 background fields. Due to their location in star-forming regions, the CMDs of fields B1 and B3 exhibit prominent young MS populations; in particular, B1 field contains several bright upper MS stars comparable to those in the massive cluster model shown in the B0 CMD. Meanwhile, the remaining background fields are dominated by older stellar populations, such as RGB, AGB, and fainter MS stars. The dependence of the limiting magnitude on stellar density is also clearly visible. In the B5 field, a prominent MS is not observed, as the MSTO of the dominant old population lies below the limiting

[1] `https://iraf-community.github.io/pyraf.html`

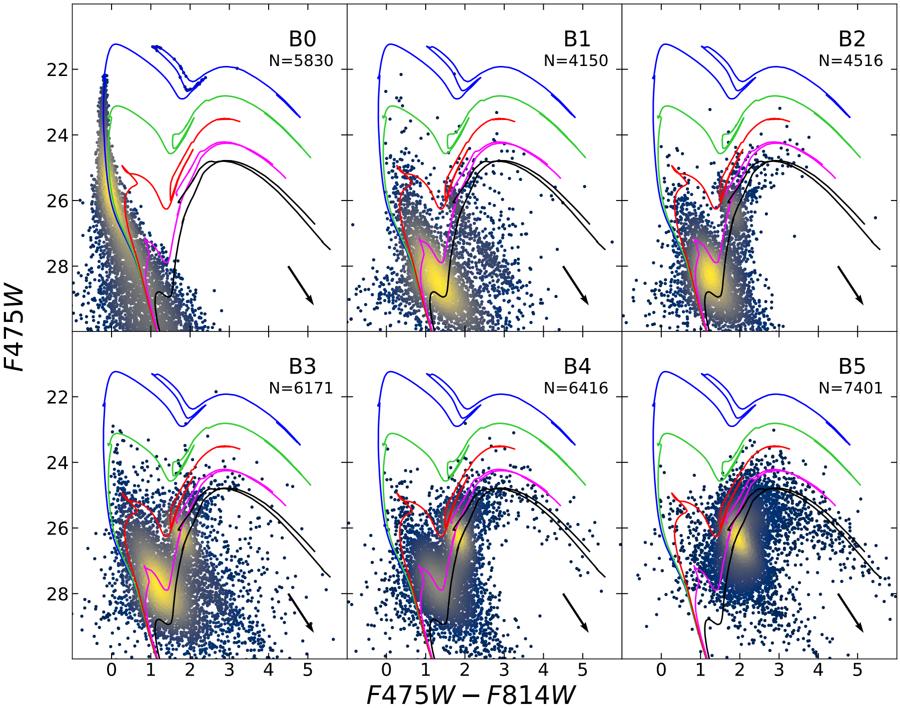

Figure 5.2. Colour-magnitude diagrams (CMDs) of the background fields. Each panel corresponds to a different field (B0–B5). For the background-free case (B0), the CMD of a simulated cluster with $\log_{10}(M/M_{\odot}) = 4.5$ and $\log_{10}(t/\mathrm{yr}) = 8.0$, and stellar photometry errors generated based on Williams et al. (2023), is shown. Stellar photometry for fields B1–B5 is taken from the PHAT stellar photometry catalogue of Williams et al. (2023). The CMDs for fields B1–B5 include all stellar sources within the corresponding $17'' \times 17''$ frames. The number of stars visible in each CMD is indicated below the field label. Coloured curves represent PARSEC-COLIBRI solar metallicity isochrones for ages $\log_{10}(t/\mathrm{yr}) = 8.0$ (blue), 8.5 (green), 9.0 (red), 9.5 (magenta), and 10.0 (black). The black arrow marks the extinction vector, calculated using the Fitzpatrick (1999) extinction law with $A_V = 1$.

magnitude due to the extreme crowding in this field. Moreover, all background fields exhibit some level of extinction, as indicated by the observed MSs in B1–B5 fields being shifted towards redder colours relative to the MSs of the isochrones.

An important feature to highlight is the presence of strong differential extinction in fields B1 and B3, which becomes particularly evident when comparing their red clump populations to those in B2 and B4. Fields B1 and B3 exhibit significantly broadened red clumps, spanning a wide range – up to several magnitudes – in both brightness and colour, with the direction of dispersion aligned closely with the extinction vector. Given that both B1 and B3 fields are located within star-forming rings, this suggests the presence of significant variations in extinction caused by complex dusty structures typical of such environments. As a large fraction of young clusters are found in such regions – including those in the disc of M 31 – it is reasonable to expect that at least some are affected by comparable levels of differential reddening, especially considering that such pronounced effects are evident within a relatively small field of view. Importantly, such variability in extinction across the cluster can bias integrated cluster photometry and significantly complicate the recovery of cluster physical parameters (Narbutis et al. 2007a; Bridžius et al. 2008).

We stress that the B3 field is located within one of the most prominent features of the M 31 disc – the 10 kpc star-forming ring – which hosts the majority of star clusters identified in the PHAT survey. On this basis, it is used extensively throughout this Chapter as a representative field when analysing various parameter dependencies.

5.2 Background estimation and aperture photometry

With the introduction of sky background, cluster aperture photometry becomes more complex than in the background-free case described in Section 4.1. Before integrated cluster magnitudes and colours can be derived, the sky background level must be subtracted from the flux measured within a given aperture. We note that all photometric procedures described below were performed using the `photutils` package, as in Section 4.1.

Although the use of a complex, interactive sky background level estimation technique, adopted by Naujalis et al. (2021) and Kriščiūnas et al. (2023), would be preferable, as it has been shown to yield robust and consistent photometric measurements, applying it to tens of thousands of simulated clusters is beyond the scope of this thesis. Instead, we employ the automated sky background determination method described by Johnson et al. (2012), which was used to produce the original photometric star cluster catalogues of the PHAT and PHATTER surveys (Johnson et al. 2012, 2015, 2022). This approach is well suited to our analysis, as our simulated cluster observations mimic those of the PHAT survey. Below, we briefly outline the main steps of the photometric procedure.

After an artificial star cluster is embedded into a given background field, we define a annular region centred on the cluster, with inner and outer radii of $1.2 \times R_{\rm ap}$ and $3.4 \times R_{\rm ap}$, respectively. For the purpose of estimating the sky background, an aperture with radius $R_{\rm ap} = 2.0''$ is adopted in all cases. This large ring is then subdivided into 10 smaller annular segments of equal area, each equivalent to the area of a circular aperture with $R_{\rm ap} = 2.0''$. Then, the integrated flux is evaluated within each of the 10 annular segments. To minimise contamination from bright background sources, cluster members, or other localised peculiar features, the resulting flux values are processed using an iterative 2σ-clipping procedure, which repeatedly removes flux values that lie more than two standard deviations from the mean, recalculating the mean and standard deviation after each iteration until no further outliers are identified. The final sky background level is then determined as the mean of the remaining flux values, while their standard deviation is adopted as the uncertainty of the background level estimate, σ_s.

As photometry is performed using multiple apertures of various sizes, the derived background level is scaled accordingly to match the corresponding aperture size. Importantly, the background estimation is carried out separately for every cluster after it has been inserted into the given background field. This approach provides a more realistic representation of observational conditions, as the sparse outer regions of the cluster can contribute to the background level estimate.

After determining the sky background level, aperture photometry of each artificial cluster is performed within a given background field using a range of apertures, with radii from $R_{\mathrm{ap}} = 0.5''$ to $5.0''$. This procedure is applied to all simulated star clusters, in all five background fields, with measurements in three PHAT passbands: $F336W$, $F475W$, and $F814W$. For comparison, and to identify and evaluate the impact of the sky background effects, measurements were also obtained for the same simulated clusters in the background-free B0 case using the same set of apertures.

Throughout the remainder of this Chapter, aperture sizes are often expressed in units of the cluster half-light radius, R_{50}. We stress that for each simulated cluster, a single R_{50} value is adopted, which is determined in the background-free B0 case from the FGC measured in the $F475W$ passband, as described in Section 4.1. When R_{50} is used to define the aperture size, we impose a lower limit of $R_{\mathrm{ap}} = 0.5''$, meaning that, if calculated aperture radius falls below this threshold, it is set to $0.5''$. For example, for a cluster with $R_{50} = 0.2''$ and an aperture defined as $R_{\mathrm{ap}} = 2 \times R_{50}$, the resulting aperture size would be $R_{\mathrm{ap}} = 0.4''$; however if the lower limit criterion is applied, it is increased to $R_{\mathrm{ap}} = 0.5''$. This constraint is motivated by the results presented in Sections 4.2 and 4.3 (see Figs. 4.5–4.7), which show that photometric measurements and their uncertainties become strongly affected by stochastic effects when small apertures ($R_{\mathrm{ap}} \lesssim 0.5''$) are used. Moreover, such small apertures lead to unreliable determinations of cluster physical parameters (see Section 4.4 and Fig. 4.8).

5.3 Photometric errors, optimal apertures, and systematic deviations

In this section, we investigate photometric errors and accuracy limits of aperture photometry in realistic galactic disc environments. For this experiment, we consider three different sources of error, one of which is statistical Poisson noise. However, since we use higher-level PHAT imaging products, where all available individual exposures have already been aligned, combined, and fluxes normalised to one-second exposures, it is non-trivial and complicated to determine these statistical errors correctly. To roughly approximate the impact of Poisson noise, we multiplied the one-second exposure fluxes by the corresponding PHAT imaging exposure times reported by Williams et al. (2014). The Poisson errors for the magnitude measurements are then evaluated using the following equation:

$$\sigma_p = 2.5 \log\left(1 + \frac{\sqrt{S_{cl}}}{S_{cl}}\right), \tag{5.1}$$

where S_{cl} is the cluster signal, defined as the one-second flux (F_{cl}) multiplied by the corresponding exposure time, measured within the selected aperture in the background-free (B0) frame.

The second source of uncertainty that we account for is related to potential biases in the positioning of the aperture. We evaluate it in a similar manner to σ_{APT}, as described in Section 4.3. For each simulated image, aperture photometry is performed by centring the aperture on each of the nine central pixels of the frame. In contrast to the procedure used to determine σ_{APT}, no additional ± 1 pixel offsets are applied here. Preliminary analysis for this experiment has shown that, under realistic conditions, uncertainties associated with aperture positioning dominate over those introduced by small variations in aperture size, which are therefore negligible in comparison. As a result, nine measurements of cluster magnitudes and CIs with an aperture of given size are obtained for each simulated observation. The corresponding magnitude uncertainty due to aperture positioning, σ_a, is estimated as half of the 16th–84th percentile range of these nine measurements. We emphasise that the σ_a uncertainty is measured when cluster is already placed in the background field, and for CIs it is determined directly from the nine CI measurements, rather than by propagating uncertainties of magnitudes from the individual passbands.

The third source of errors considered here is associated with the procedure of determining the sky background level. It was quantified using the following equation:

$$\sigma_b = 2.5 \log \left(1 + \frac{\sigma_s \cdot A_{\mathrm{ap}}}{F_{cl}} \right), \tag{5.2}$$

where σ_s is the uncertainty of the background level estimate introduced in Section 5.2, A_{ap} is the area of the selected aperture in pixels, and F_{cl} is the integrated one-second exposure flux of the cluster measured within that aperture in the B0 field.

Here, we do not include the photometric uncertainty terms σ_{GEN} and σ_{ROT} discussed in Section 4.3. The σ_{GEN} term is excluded because it describes the intrinsic scatter of photometric properties for clusters with the same physical parameters arising from stochastic IMF sampling, and therefore characterises an ensemble of clusters rather than the error of measurement of an individual cluster. The present analysis focuses on error sources associated with observations of each individual cluster. The σ_{ROT} contribution is also omitted. As described in Section 3.5 (see also Tables 3.1 and 3.2), multiple viewing angles were simulated only for a limited subset of cluster parameter combinations. Including σ_{ROT} would therefore prevent a homogeneous analysis over the full, more finely sampled parameter grid considered in this Chapter. Furthermore, preliminary tests showed that, once realistic sky background is introduced, the uncertainty sources influenced by background variations, σ_b and σ_a, generally exceed σ_{ROT}, which becomes negligible in most cases. Even in the most extreme situations, where σ_{ROT} reaches ~0.1 mag, the uncertainties associated with background estimation and aperture positioning remain significantly larger for such clusters.

Therefore, the total photometric error of a magnitude measured in a given passband was calculated as

$$\sigma_t = \sqrt{\sigma_p^2 + \sigma_b^2 + \sigma_a^2}. \tag{5.3}$$

For colour indices, the total photometric errors were obtained by combining in quadrature the σ_p and σ_b terms of the individual passbands, that comprise the given CI, together with the σ_a value determined directly for the corresponding CI. For example, for a $X - Y$ colour:

$$\sigma_{t,\, X-Y} = \sqrt{\sigma_{p,\, X}^2 + \sigma_{p,\, Y}^2 + \sigma_{b,\, X}^2 + \sigma_{b,\, Y}^2 + \sigma_{a,\, X-Y}^2}. \tag{5.4}$$

Of the three considered uncertainty sources, the background estimation term, σ_b, is dominant in most cases. This is consistent with previous HST studies of M 31 star clusters (Krienke & Hodge 2007, 2008; Hodge et al. 2009, 2010; Johnson et al. 2012, 2015). Nevertheless, there are specific situations in which the error due to aperture positioning, σ_a, exceeds σ_b. This typically occurs when a bright cluster member or a field star lies close to or straddles the boundary of the aperture. In contrast, the contribution from Poisson noise, σ_p, is generally much smaller than either of these two terms. In the remainder of this Chapter, only the combined errors are considered. For simplicity, the total uncertainties of both magnitudes and CIs are denoted as σ_t.

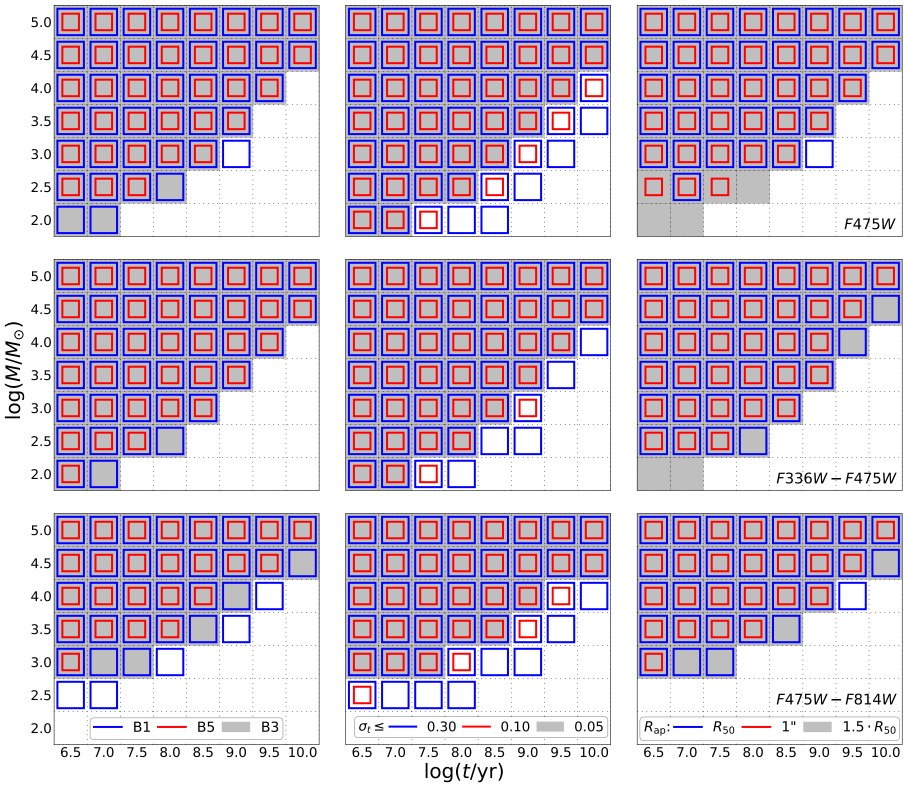

Figure 5.3. Regions of the cluster mass–age parameter space in which aperture photometry satisfies specified accuracy requirements. Grey regions and coloured squares denote combinations of cluster mass and age for which at least 50% of the simulated clusters (out of ~1300) have total photometric errors, σ_t, below the adopted threshold. The top, middle, and bottom rows of panels correspond to the *F*475*W* magnitude, *F*336*W* − *F*475*W*, and *F*475*W* − *F*814*W*, respectively. The left column compares results for different background fields, obtained with an aperture $R_{ap} = 1.5 \times R_{50}$, and error threshold $\sigma_t \leq 0.05$ mag applied. The middle column shows the dependence on the adopted σ_t threshold in the B3 field, using $R_{ap} = 1.5 \times R_{50}$. The right column presents the effect of aperture size in the B3 field, with a $\sigma_t \leq 0.05$ mag threshold adopted. All results shown are based on simulated clusters with half-light radii of $R_{50} = 0.25'' - 1.00''$.

Figure 5.3 presents the regions of cluster age–mass parameter space in which at least 50% of cluster models satisfy the adopted photometric accuracy criteria for *F*475*W*, *F*336*W* − *F*475*W*, and *F*475*W* − *F*814*W*. These regions are shown as functions of background field (B1, B3, and B5), photometric error threshold (σ_t = 0.05, 0.10, 0.30 mag), and aperture size ($R_{\rm ap}$). Our choice of these particular error threshold values is motivated by the discussion of de Meulenaer et al. (2015). That study suggests that integrated photometry accurate to $\sigma_t \leq 0.05$ mag is generally sufficient to determine cluster age, mass and extinction robustly, and additionally to constrain the metallicity of clusters older than 1 Gyr. Photometric errors of $\sigma_t \leq 0.10$ mag typically allows determining cluster age, mass, and extinction fairly accurately, provided that the metallicity is known or can be assumed. Finally, for errors of $\sigma_t \leq 0.30$ mag, only approximate estimates of cluster age and mass are generally achievable, assuming both extinction and metallicity are known.

The left column of Fig. 5.3 illustrates the dependence on the background environment by comparing results obtained in the B1, B3, and B5 fields using apertures with $R_{\rm ap} = 1.5 \times R_{50}$ and adopting an error threshold of $\sigma_t \leq 0.05$ mag. The results for $F475W$ and $F336W - F475W$ indicate that, in the UV and optical wavelength range, the limits of cluster age–mass parameter space in which sufficiently accurate photometry can be obtained, required for robust physical parameter determination, is only weakly affected by the stellar density and other environmental characteristics of the background field. A much stronger dependence is evident for $F475W - F814W$. This behaviour is driven by numerous bright red stars belonging to the old stellar populations of the M 31 disc, whose number density increases significantly towards the galactic centre.

These results imply that the primary limitation arises from our ability to perform precise photometry in the IR part of the spectrum – in this particular case, in the $F814W$ passband – where numerous bright red resolved background and foreground stars introduce significant contamination. In semi-resolved and resolved environments, more accurate measurements could possibly be achieved through the use of more sophisticated sky background estimation techniques, such as interactive approach (Naujalis et al. 2021; Kriščiūnas et al. 2023), methods that explicitly account for individual bright resolved stars (Narbutis et al. 2014), or more advanced automated algorithms (Pandey & Saha 2025).

The middle column of Fig. 5.3 presents the regions of cluster age–mass parameter space in which at least 50% of cluster models satisfy different photometric accuracy thresholds (σ_t = 0.05, 0.10, 0.30 mag). These results are shown for the B3 field, and using apertures with radii $R_{\rm ap} = 1.5 \times R_{50}$. As mentioned in Section 5.1, the majority of M 31 disc clusters are found in environments similar to B3; therefore, these limits may be regarded as representative of typical observational conditions. Taking into consideration results for both $F336W - F475W$ and $F475W - F814W$ CIs, we estimate the combined limiting cluster masses by linearly interpolating between the limits determined for each of these colours separately. At an age of $t = 1$ Gyr, only rather massive clusters (M $\gtrsim$ 5000 $M_\odot$) satisfy the most strict accuracy requirement of $\sigma_t = 0.05$ mag. In the case of $\sigma_t = 0.10$ mag, it can be achieved for 1600 $\lesssim$ M $\lesssim$ 5000 $M_\odot$ clusters, while $\sigma_t = 0.30$ mag can be reached for 500 $\lesssim$ M $\lesssim$ 1600 $M_\odot$ clusters. In comparison, at an age of $t = 100$ Myr, considerably lower mass clusters satisfy the same requirements. In this case, $\sigma_t = 0.05$ mag can be achieved for clusters with M $\gtrsim$ 1000 $M_\odot$. Meanwhile, $\sigma_t = 0.10$ mag criterion is met for clusters with masses 500 $\lesssim$ M $\lesssim$ 1000 $M_\odot$, whereas $\sigma_t = 0.30$ mag threshold can be reached by 200 $\lesssim$ M $\lesssim$ 500 $M_\odot$ clusters.

The rightmost column of Fig. 5.3 examines the effect of aperture size on the region of age–mass parameter space for which the precision requirement of $\sigma_t \leq 0.05$ mag is satisfied. The comparison is shown for the B3 field and includes three choices of aperture radius, $R_{\rm ap}$: a fixed radius of $1''$, R_{50}, and $1.5 \times R_{50}$. Apertures scaled to the individual cluster half-light radius generally provide more accurate photometry than a single fixed aperture applied to all clusters. The largest parameter-space region where $\sigma_t \leq 0.05$ mag can be achieved is reached for $R_{50} = 1.5 \times R_{50}$, in agreement with the conclusions reached throughout Chapter 4. Interestingly, an aperture of $R_{\rm ap} = R_{50}$ in some specific cases slightly outperforms $R_{\rm ap} = 1.5 \times R_{50}$. However, it was also shown in Chapter 4 that measurements obtained with such small apertures are more susceptible to stochastic effects, especially for compact clusters with $R_{50} \lesssim 0.5''$, in turn leading to highly uncertain estimates of cluster physical parameters. Thus, we reiterate our recommendation made in the previous Chapter that apertures smaller than the half-light radius should be employed with caution. They may still be useful in situations where contamination from the nearby bright field stars needs to be minimised (Narbutis et al. 2007b), but otherwise larger apertures than that are preferable.

To further elaborate on the aperture size recommendations for colour measurements suggested in Chapter 4, for each simulated cluster observation, we determined the optimal aperture radius, $R_{\rm opt}$, defined as the radius that results in the lowest σ_t. Figure. 5.4 shows how $R_{\rm opt}$, expressed in units of R_{50}, varies with the integrated cluster brightness in the $F475W$ passband for three different combinations of geometric parameters, r_c and γ. The green, blue, and red markers correspond to compact, typical M 31 disc, and extended clusters, respectively. A significant luminosity dependence is evident, with the optimal aperture size decreasing towards fainter clusters: over the 10 mag interval covered in $F475W$, $R_{\rm opt}$ changes by a factor of ~1.5 – between the faintest and brightest clusters. For cluster models representative of the typical M 31 disc clusters (blue symbols and curve), the optimal aperture for measuring CIs generally falls in the range (1–2)$\times R_{50}$. Considering the full range of cluster sizes explored in Fig. 5.4, the optimal aperture radii expressed in absolute units are relatively similar for both compact and extended clusters. In most cases, they range from ~$0.5''$ to $1.5''$. Thus, despite the diversity in cluster sizes, the aperture sizes that minimise photometric errors occupy a rather narrow interval. These results are in good agreement, and further support the aperture size recommendations established earlier in this thesis.

It is noteworthy that in $F475W - F814W$, $R_{\rm opt}$ is generally slightly smaller than in $F475W$ and $F336W - F475W$. We interpret this behaviour as being driven by the population of red resolved field stars. These stars are predominantly bright in the IR but relatively faint in UV–optical wavelengths, which makes their influence most pronounced for the $F475W - F814W$ colour among the photometric parameters considered in Fig. 5.4. This effect arises from the increasing likelihood of such stars falling within the aperture as its size grows; as a result, larger apertures lead to a gradual decrease in photometric accuracy. However, in the UV–optical bands, their contribution to the total uncertainty is minimal, allowing for slightly larger optimal apertures.

We also note that no significant differences are observed when results for other background fields are compared to the B3 field results presented in Fig. 5.4 and discussed above (see equivalent plots for other fields in Appendix, Fig. A5).

Having established how the optimal aperture size depends on cluster brightness and structure, we now examine whether measurements obtained with these apertures are biased by the presence of a real sky background. Figure 5.5 presents quantities

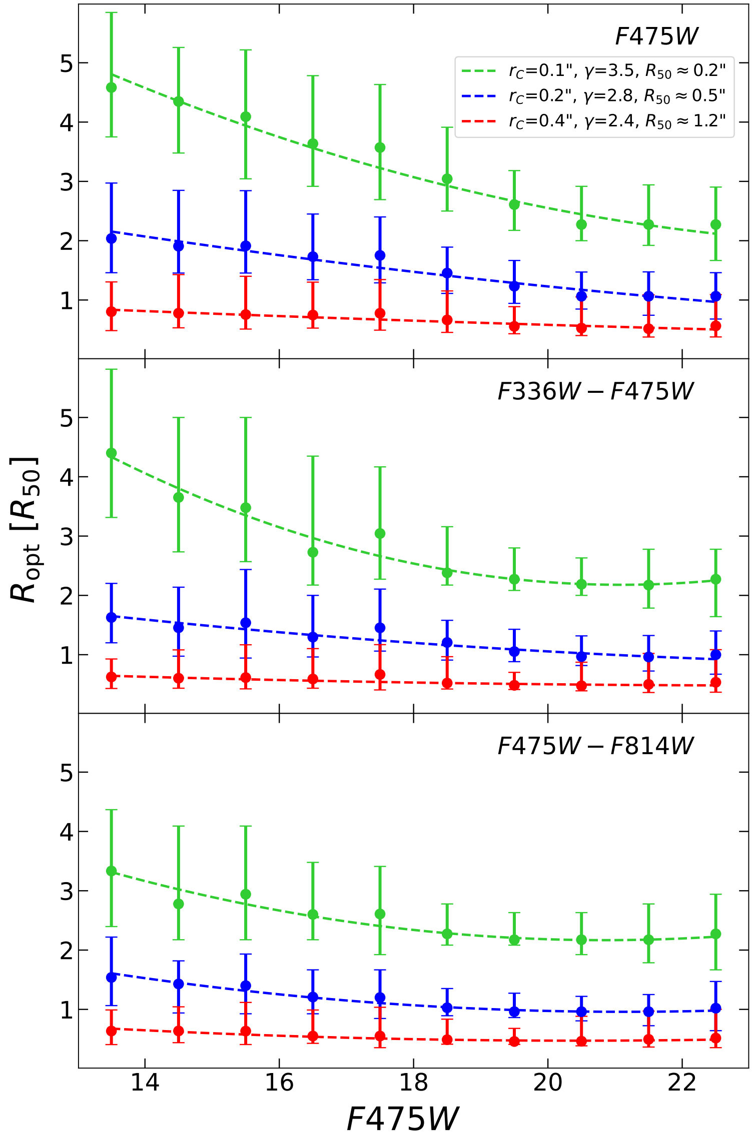

Figure 5.4. Optimal aperture radii, $R_{\rm opt}$, as a function of the integrated cluster $F475W$ magnitude measured in the B0 case. Top panel, middle, and bottom panels correspond to the $R_{\rm opt}$ for measuring the $F475W$, $F336W - F475W$, $F475W - F814W$, respectively. Results are shown for the B3 field and for three combinations of the geometric parameters, r_c and γ (see legend; the approximate median half-light radii, R_{50}, corresponding to each parameter combination are also indicated for reference). Markers show the median values of $R_{\rm opt}$, while the error bars indicate the 16th–84th percentile ranges. Dashed curves represent second-order polynomial least-squares fits to the medians.

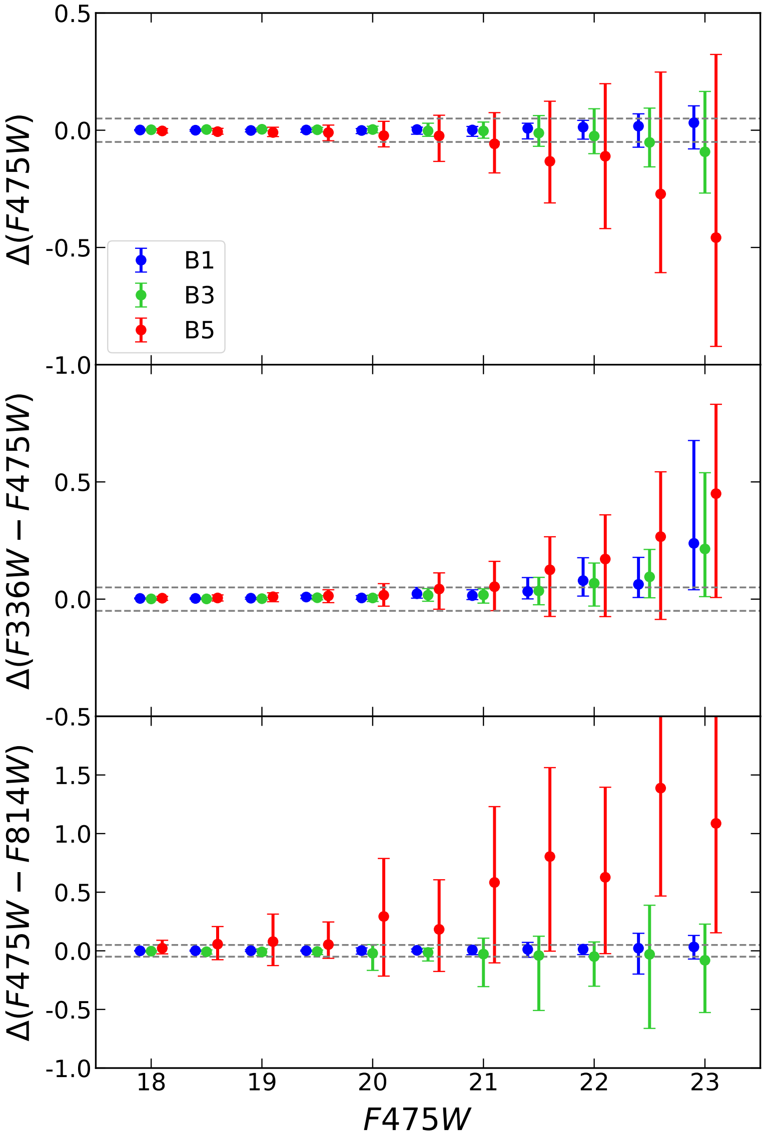

Figure 5.5. Systematic differences between photometric measurements obtained in the B1, B3, and B5 background fields and those measured in the background-free B0 case. The top, middle, and bottom panels show $\Delta(F475W)$, $\Delta(F336W - F475W)$, and $\Delta(F475W - F814W)$, respectively, plotted as a function of the cluster $F475W$ magnitude measured in B0. Here, Δ is defined as the measurement in a given background field minus the corresponding value in B0. Markers indicate median differences, while error bars show the 16th–84th percentile ranges. For visual clarity, the blue and red symbols are slightly offset along the X-axis. Grey dashed lines mark ± 0.05 mag deviation limits. Results are shown for artificial clusters with half-light radii in the range $R_{50} = 0.4'' - 0.6''$.

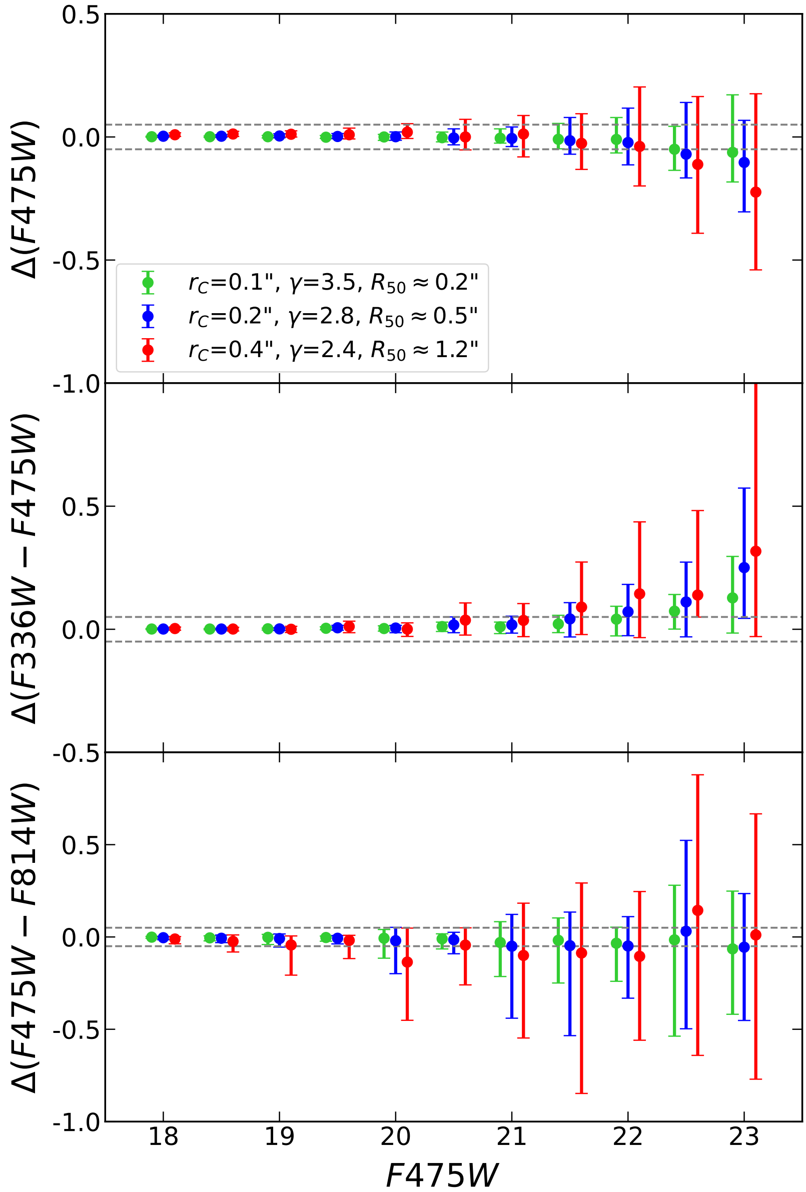

Figure 5.6. The same as in Fig.,5.5, but shown for the B3 field and for three different combinations of geometric parameters, r_c and γ (see legend). The corresponding approximate median half-light radii, R_{50}, are also indicated for reference. The green, blue, and red symbols represent compact, typical M 31 disc, and extended clusters, respectively. Markers indicate median differences, while error bars show the 16th–84th percentile ranges. For visual clarity, the blue and red symbols are slightly offset along the horizontal axis. Grey dashed lines mark ±0.05 mag deviation limits.

$\Delta(F475W)$, $\Delta(F336W - F475W)$, and $\Delta(F475W - F814W)$, defined as the difference between measurements obtained in one of the PHAT background fields (B1, B3, and B5 in this case) and those measured for the same clusters in the background-free B0 case. This enables us to directly evaluate whether noisy and variable backgrounds introduce systematic deviations into the aperture photometry measurements. We stress that, for this experiment, we used apertures with radii $R_{\rm opt}$.

For all three photometric parameters considered, we find that once a cluster becomes fainter than a certain limiting brightness – which depends on the background field – systematic biases begin to emerge and increase towards lower luminosities. Beyond this limit, faint clusters observed against a realistic background tend to appear brighter than in the ideal B0 case. Their colours are also typically shifted towards redder values. We attribute these effects to brighter-than-average resolved field stars, that fall within the aperture, whose contribution to the total measured flux becomes substantial. A notable exception is $F475W - F814W$ in the B3 field, where a weak trend towards bluer colours is present. Such behaviour can be associated to the comparatively rich population of young blue stars in that field. We suggest that similar biases may arise in other regions with ongoing star formation, such as the disc of M 33 or in starburst galaxies.

Among the three photometric parameters considered, the largest and earliest systematic deviations occur for $F475W - F814W$. In this case, the bias becomes notable at brighter cluster magnitudes than for $F475W$ magnitude or $F336W - F475W$. The reason is that the sky background in the M 31 disc is significantly brighter in the $F814W$ passband, reducing the contrast between the cluster and the surrounding field more severely than in the UV-optical filters. Overall, all of these effects described above can directly affect the derived physical parameters for star clusters. A cluster whose integrated magnitude is biased towards brighter values will most likely have its mass overestimated, while CIs shifted towards the redder values can lead to either systematically older ages, higher metallicities, or larger extinctions being inferred.

Figure 5.6 extends the same analysis to clusters of different sizes in the B3 field. At a given cluster brightness, larger and more extended clusters (red symbols) show both stronger systematic deviations and broader distributions of photometric parameter differences than compact ones. Furthermore, these deviations become apparent at brighter integrated magnitudes for larger clusters. This follows from a general trend that larger clusters are measured with larger apertures, which inevitably capture more background flux and therefore reduce the contrast between the signals from the cluster and the surrounding field. Larger apertures also increase the likelihood that a bright background/foreground star is included in the measurement.

5.4 Catalogue completeness and selection effects

We next consider two other important aspects of sky background effects in studies of star clusters within the galactic discs. Namely, it is the influence of background on completeness limits and on the reliability of cluster detection. Together, these effects set the boundaries of the accessible paramater space in which cluster analysis is possible. It must be properly characterised and understood to avoid over-intepretation of survey results. As mentioned in Section 3.5, for the analysis presented here, we used a continuous sample of 20 million cluster models, with their images generated only in the $F475W$ passband (see Table 3.3 for the ranges of cluster parameters).

To quantify cluster detectability and assess completeness limits in the context of the PHAT survey, we introduce the cluster-to-background signal ratio (CBR):

$$\mathrm{CBR} = \frac{F_{cl}}{F_{bg}}, \tag{5.5}$$

where F_{cl} is the cluster flux in the $F475W$ passband measured in the background-free B0 field, and F_{bg} is the background $F475W$ flux measured in one of the selected M 31 background fields (B1–B5). Both fluxes are measured within an aperture of radius $R_{\mathrm{ap}} = R_{50}$. The choice of such aperture is motivated by the fact that it captures only the brightest central part of the cluster, which provides the highest contrast against the surrounding field and is therefore most relevant for cluster detection in the presence of significant sky background signal. For clusters with $R_{50} < 0.5''$, we use $R_{\mathrm{ap}} = 0.5''$ apertures instead, to avoid strong stochastic effects that are present when using small apertures, as discussed in Sections 4.2, 4.3, and 5.2. Figure 5.7 demonstrates simulated cluster images of various age and mass combinations within the B0 and B3 fields. For each cluster in the B3 field, the corresponding CBR value is indicated.

For the following analysis, we adopt three CBR threshold values as approximate cluster detection criteria: CBR $\geq$ 2.5, CBR $\geq$ 1.0, and CBR $\geq$ 0.4. As can be seen in Fig. 5.7, clusters with CBR $\geq$ 1.0 can generally be distinguished from the surrounding background without significant difficulties. We therefore assume this threshold as representative of the cluster detection limit achievable through careful visual inspection by a human, such as in citizen science searches (e.g., Johnson et al. 2015). In contrast, clusters satisfying CBR $\geq$ 2.5 are approximately 1 mag brighter than the CBR $\geq$ 1.0 limit and are typically luminous enough to be identified even in a rapid visual search by an expert or by relatively simple automated detection methods. Conversely, CBR $\geq$ 0.4 corresponds to clusters ~1 mag fainter than the CBR $\geq$ 1.0 limit. We adopt it as an approximate estimate of the limiting depth potentially reachable by modern machine-learning (ML) approaches. This assumption is motivated by the results of Thilker et al. (2022), who demonstrated that ML-based cluster searches in nearby galaxies can result in catalogues deeper by about 1 mag compared to those constructed through visual human identification.

Figure 5.8 demonstrates regions of cluster age–mass parameter space for which in the PHAT survey at least 50% completeness can be achieved, depending on the adopted CBR detection threshold, background environment, and cluster geometric parameters. The top panel of Fig. 5.8 focuses on the B3 field and clusters with half-light radii in the range of typical M 31 disc clusters $R_{50} = 0.25'' - 1.00''$, comparing the three detection thresholds introduced above.

For the most conservative limit, CBR $\geq$ 2.5, which corresponds to clusters that can be easily detected in relatively shallow searches, the 50% completeness is achieved at masses of ~1300 $M_\odot$, ~2500 $M_\odot$, and ~8000 $M_\odot$ for ages of t = 100 Myr, 300 Myr, and 1 Gyr, respectively. When the threshold is lowered to CBR $\geq$ 1.0, representative of clusters detectable through careful visual human inspection, the 50% completeness limiting masses decrease to ~500 $M_\odot$, ~1000 $M_\odot$, and ~3000 $M_\odot$ for the same ages.

If an advanced detection method capable of reaching CBR $\geq$ 0.4 is used, the resulting catalogue can become significantly deeper. In such case, the 50% completeness limit is achieved at rather low masses of ~250 $M_\odot$ at 100 Myr, ~400 $M_\odot$ at 300 Myr, and ~1300 $M_\odot$ at 1 Gyr. Compared to the CBR $\geq$ 1.0 case, this corresponds to more than a factor of two improvement in the minimum detectable cluster mass. Interestingly, a similar gain in depth was reported by Thilker et al. (2022) for

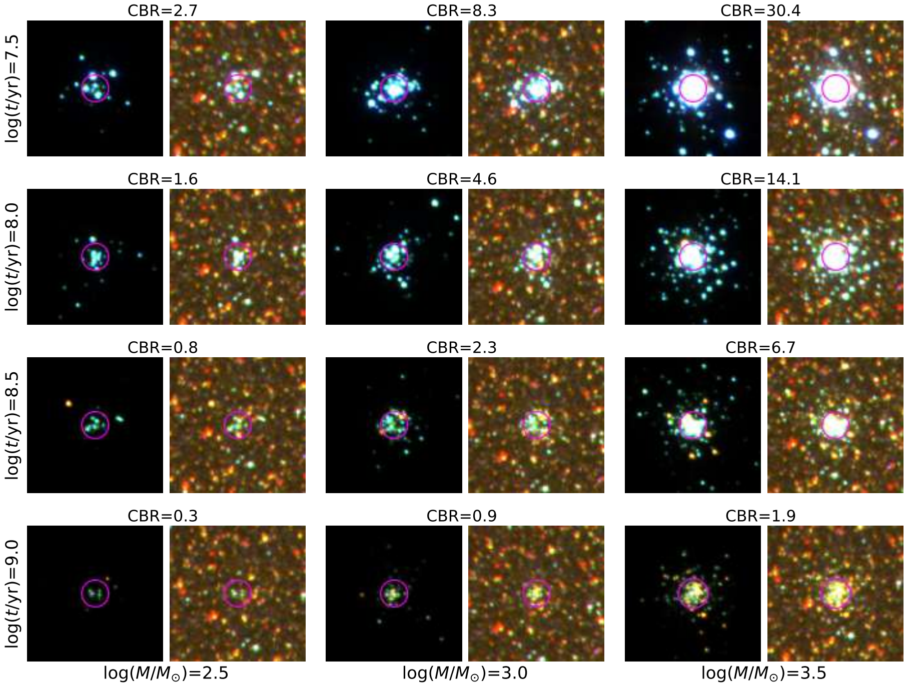

Figure 5.7. Images of artificial star clusters of different ages and masses shown in the B0 field (left panel in each pair) and in the B3 field (right panel). Cluster masses are indicated below each column, while ages are noted to the left of each row. All clusters were generated using $r_c = 0.2''$ and $\gamma = 2.8$ parameters. The cluster-to-background signal ratio, CBR (see definition in Section 5.4), calculated for the B3 field is given above each image pair. Magenta circles indicate apertures used to determine the CBR values. The $5'' \times 5''$ colour images were produced by combining $F336W$ (blue), $F475W$ (green), and $F814W$ (red) data.

the PHANGS-HST survey when comparing an advanced ML-based cluster detection algorithm with visual identification performed by experts.

The middle panel of Fig. 5.8 illustrates how the 50% completeness limits vary with the surrounding environment, the strongest influence being the radial distance from the galactic centre. The results shown were obtained for cluster of typical size, $R_{50} = 0.25'' - 1.00''$, assuming CBR ≥ 0.4 detection threshold. In general, we find a strong environmental dependence. From the sparse outer-disc regions to the extremely crowded inner fields, the survey depth at a given age changes by approximately an order of magnitude. For example, at 1 Gyr clusters with masses as low as $\sim$250 $M_{\odot}$ can still be recovered with 50% completeness in the B1 field. In the B3 field – representing a typical cluster environment in M 31 – this limit increases to $\sim$1300 $M_{\odot}$, while in the dense B5 field it is $\sim$3000 $M_{\odot}$. Such strong variation with the background field suggests that the depth of a cluster catalogue is determined not only by the detection method, but also by the local sky background against which the clusters are observed. Therefore, selection effects must be carefully taken into account when studying radial or environmental trends.

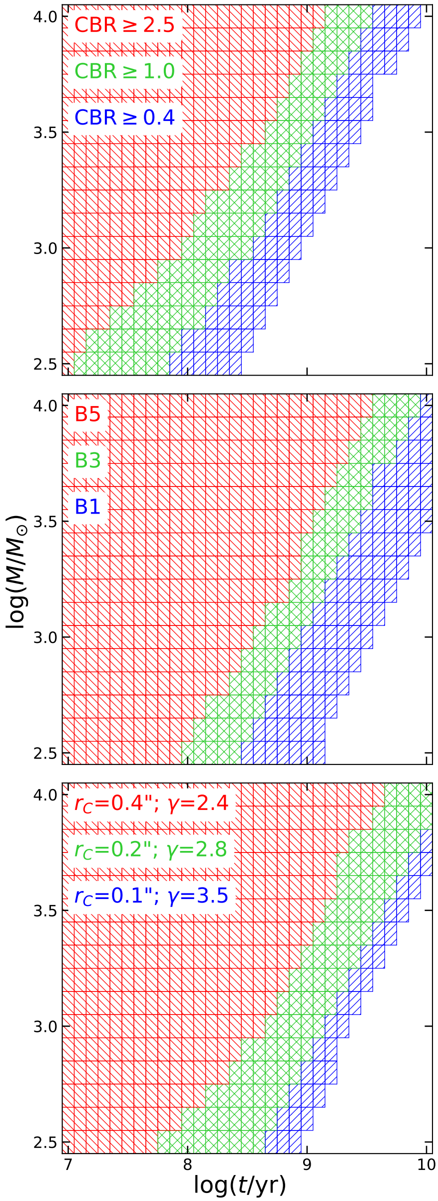

Figure 5.8. Regions of cluster age–mass parameter space in which at least 50% completeness is achieved. Top panel: dependence on the adopted CBR detection threshold, with results shown for the B3 field. Middle panel: dependence on the background environment, comparing the B1, B3, and B5 fields, assuming a detection threshold of CBR $\geq$ 0.4. Bottom panel: dependence on cluster size, with results shown for three different r_c—γ combinations in the B3 field, also assuming CBR $\geq$ 0.4 detection limit. The results presented in the top and middle panels are based on simulated clusters with half-light radii in the range $R_{50} = 0.25'' - 1.00''$.

The bottom panel of Fig. 5.8 shows how the completeness limits depend on the geometric parameters of clusters. The comparison is made for three r_c–γ combinations in the B3 field, assuming a detection threshold of CBR $\geq$ 0.4. A notably better performance in the case of more compact clusters is evident: the region of age–mass parameter space where at leas 50% completeness is achieved is significantly larger for compact (blue area) and typical-size clusters (green area) than for extended ones (red area). For instance, at t = 1 Gyr, the 50% completeness limit is ~400 $M_\odot$ for compact clusters, ~800 $M_\odot$ for the ones of characteristic size, and rises even to ~2500 $M_\odot$ for extended clusters.

These results highlight that, for studies involving star cluster sizes – including cluster size distribution, the mass–radius relation, dynamical evolution, and disruption processes such as tidal stripping and cluster dissolution (Portegies Zwart et al. 2010; Krumholz et al. 2019; Adamo et al. 2020; Brown & Gnedin 2021) – it is highly important to carefully account for selection effects related to cluster size. In nearby galaxies, where clusters are resolved or semi-resolved in modern space-based observations, catalogues are expected to be more incomplete for extended objects. Therefore, observed cluster samples in the discs of galaxies such as M 31 and M 33 can be biased towards more compact clusters. However, in more distant galaxies, the opposite effect may occur: due to limited spatial resolution, very compact clusters can remain unresolved, appear as point sources, and consequently be mistaken for individual stars (Larsen 2004; Ryon et al. 2017; Brown & Gnedin 2021; Maschmann et al. 2024).

It is noteworthy, Johnson et al. (2015) reported that the PHAT cluster catalogue is 50% complete down to masses of ~500 $M_\odot$ for clusters younger than 100 Myr. Our cluster models of 100 Myr age, assuming a detection threshold of CBR $\geq$ 1.0, yield essentially the same limiting mass. This agreement supports our assumption that the CBR $\geq$ 1.0 limit roughly corresponds to the sensitivity of visual human-eye searches. We note that Johnson et al. (2015) considered all clusters younger than 100 Myr, whereas our estimate applies to an exact age of 100 Myr; thus, the adopted CBR $\geq$ 1.0 detection threshold may be somewhat less restrictive than the practical limit achieved by the citizen-science search of Johnson et al. (2015). This suggests that the PHAT star cluster catalogue could likely still be extended to lower cluster masses ($M \lesssim 500\,M_\odot$), especially through the use advanced modern ML-based detection techniques (e.g., Bialopetravičius et al. 2019; Thilker et al. 2022).

Furthermore, we used the measured CBR values to estimate how selection effects influence the observed cluster mass function (CMF) in the context of the PHAT survey. We explore this in Fig. 5.9. As the intrinsic initial CMF, we adopted a Schechter function with power-law slope of $\beta = -2$ (Schechter 1976; Gieles 2009) and a truncation mass of $M_C = 10^4\,M_\odot$, consistent with the CMF results derived for the M 31 disc cluster population by Johnson et al. (2017). We emphasise that interstellar extinction is not included in the calculations of completeness and selection effects discussed below. In some cases this omission can have a substantial impact, particularly for very young clusters. As noted by Maschmann et al. (2024), UV–optical–near-IR observations of clusters younger than $t \lesssim$ 5-10 Myr can suffer from significantly stronger incompleteness, since they are often still embedded in their natal gas and dust clouds (Knutas et al. 2025; Pedrini et al. 2026). On this basis, to avoid presenting unrealistic and potentially misleading results, we restrict the following analysis to clusters older than 10 Myr.

The top panel of Fig. 5.9 compares the recovered CMFs for several cluster ages

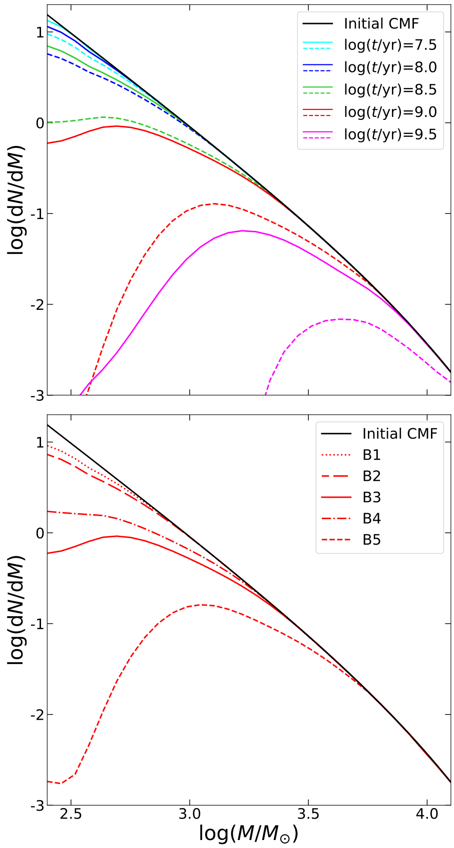

Figure 5.9. Selection effects on cluster mass functions (CMFs) caused by the cluster detection incompleteness. The initial CMF is shown by the black line and follows a Schechter function with a power-law index $\beta = -2$ and truncation mass $M_C = 10^4\ M_\odot$. Top panel: resulting CMFs for artificial clusters of different ages (see legend) in the B3 field, assuming detection thresholds of CBR $\geq$ 1.0 (dashed lines) and CBR $\geq$ 0.4 (solid lines). Bottom panel: CMFs for clusters of $\log_{10}(t/\mathrm{yr}) = 9.0$ age in the B1–B5 fields, representing the dependence on environment and radial distance from the centre of M 31, assuming a detection threshold of CBR $\geq$ 0.4. The results in both panels are based on simulated clusters with half-light radii in the range $R_{50} = 0.25'' - 1.00''$.

under two assumed detection thresholds: CBR $\geq$ 1.0 (dashed curves) and CBR $\geq$ 0.4 (solid curves). Since these results are based on the B3 field, they are representative of the typical conditions experienced by a majority of star clusters in the M 31 disc. For clusters younger than 100 Myr, a detection threshold of CBR $\geq$ 0.4 enables the CMF to be recovered down to masses of ~300 $M_\odot$. By comparison, if the effective cluster detection limit is closer to CBR $\geq$ 1.0, incompleteness begins to affect the observed CMF already below ~1000 $M_\odot$. At an age of 100 Myr these mass limits are ~600 $M_\odot$ and ~1800 $M_\odot$ for CBR $\geq$ 0.4 and CBR $\geq$ 1.0, respectively. Therefore, ML-based cluster detection methods have the potential to lower the minimum mass limit for reliable CMF studies by roughly a factor of three relative to visual human-eye searches. This suggests that, for young clusters in the disc of M 31 – and similarly also in M 33 – advanced cluster detection algorithms could make it possible to study the CMF in the very low-mass regime, which has so far remained largely unexplored in extragalactic cluster studies.

In the bottom panel of Fig. 5.9 we demonstrate that the recoverable CMF also depends strongly on the local environment, primarily through changes in stellar density with galactocentric distance. Here, we show the results for 1 Gyr age clusters assuming a detection threshold of CBR $\geq$ 0.4. In the sparse outer-disc environments represented by the B1 and B2 fields, the CMF can still be recovered down to masses of $\sim$500 $M_{\odot}$. In the more crowded B3 and B4 background fields, associated with the star-forming and intermediate-density regions, the corresponding mass limit increases to $\sim$1500 $M_{\odot}$. In the very dense inner-disc B5 field environment, the CMF is complete only above $\sim$3000 $M_{\odot}$. We note that the flat tail near $\sim$300 $M_{\odot}$ visible for the B5 field is not physical, but instead reflects small-number statistics caused from the very limited number of low-mass clusters satisfying detection limit in this particular case. Overall, these results show that the minimum cluster mass above which the CMF can be studied reliably varies by several times across the M 31 disc. This illustrates that in any study of the CMF, especially if radial trends are investigated, it is necessary to cautiously consider the strong environmental dependence of selection effects.

5.5 Summary

In this Chapter, we extended the analysis presented in Chapter 4 by investigating how sky background affects the accuracy and applicability of aperture photometry approach for star cluster studies in nearby galaxies. While the previous Chapter focused primarily on stochastic effects intrinsic to the clusters themselves, here we examined uncertainties and biases introduced by realistic galactic disc environments. To do this, we again employed the stochastic cluster models presented in Chapter 3 and placed them into five real background fields from the PHAT survey data (Dalcanton et al. 2012), selected to represent a broad range of stellar densities and environments found across the disc of M 31. These mock observations allowed us to reproduce, as closely as possible, the conditions under which PHAT star clusters are observed (Johnson et al. 2015). We then measured the resulting images using aperture photometry, estimated photometric uncertainties and deviations introduced by sky background effects, determined optimal aperture sizes, investigated cluster selections effects and completeness limits in the context of the PHAT survey.

Using these simulations, we identified the regions of cluster age–mass parameter space in which PHAT-quality photometry is sufficiently accurate to derive reliable physical parameters. In particular, we determined where photometric uncertainties are small enough to simultaneously constrain cluster age, mass, extinction, and metallicity (de Meulenaer et al. 2014, 2015). We found that these limits depend on the local background environment and on the aperture size used for the measurements. For clusters located in a typical M 31 disc field, our results show that at an age of 1 Gyr, reliable determination of age, mass, and extinction (assuming known metallicity) is possible for objects with $M \gtrsim 1600\ M_{\odot}$. However, the photometry is generally accurate enough only for rough age and mass estimates for clusters $500 \lesssim M \lesssim 1600\ M_{\odot}$. At $t = 100$ Myr these limits shift to lower masses, reaching $M \gtrsim 500\ M_{\odot}$ and $200 \lesssim M \lesssim 500\ M_{\odot}$, respectively.

An important result we found is that the optimal aperture size depends not only on cluster structure, as discussed in in Chapter 4, but also on cluster brightness once the sky background is introduced. We derived optimal aperture radii, R_{opt}, which yield the lowest photometric uncertainties, and showed that brighter clusters generally require larger apertures. Across the explored ~10 mag interval in luminosity, R_{opt} changes by roughly a factor of two, despite identical geometric parameters. For colour measurements of typical-size clusters, the optimal aperture radii are ~(1–2)×R_{50}, which is consistent with our recommendations suggested in Chapter 4. Results found in this Chapter further strengthen the conclusion that apertures smaller than the half-light radius for colour measurements should be avoided, because they are very sensitive to stochastic and sky background effects.

We also demonstrated that the sky background can introduce systematic biases to the measured photometric properties. For faint clusters, beyond a certain brightness threshold, integrated magnitudes and colours begin to deviate from their true values. In most cases, the affected clusters appear both brighter and redder than they intrinsically are, and these deviations increase for fainter and more extended systems. Such effects can lead to incorrect estimates of cluster physical parameters if they are not properly accounted for.

We also focused on the impact of the background environment on cluster detectability and catalogue completeness in the context of PHAT survey. We determined the regions of cluster age–mass parameter space in which at least 50% completeness can be achieved. In a typical M 31 cluster environment, the corresponding completeness limits are ~250 $M_{\odot}$ for 100 Myr age clusters, ~400 $M_{\odot}$ at 300 Myr, and ~1300 $M_{\odot}$ at 1 Gyr. However, these limits vary substantially across the M 31 disc. In the outer, low-density regions, considerably lower-mass clusters can be detected, whereas in the crowded inner disc the same completeness can only be reached for much more massive objects. We also found that in the PHAT survey, a significant selection bias towards more compact clusters may exist. Without accounting for this effect, investigations of cluster structure – including studies of cluster size distribution, various scaling relations, structural evolution, or cluster disruption – may yield misleading conclusions.

Finally, we explored how these completeness effects influence the observed CMF in the M 31 disc. We found that the minimum cluster mass above which the CMF can be studied reliably depends strongly on the local environment. At an age of 1 Gyr, the CMF can be recovered down to ~500 $M_{\odot}$ in the sparse outer disc, ~1500 $M_{\odot}$ in the intermediate-density and star-forming regions, and only ~3000 $M_{\odot}$ in the extremely crowded inner disc. These results stress that any attempt to investigate radial or environmental variations of the CMF in M 31 must include a careful treatment of completeness and selection effects.

Taken together, the results of this Chapter complement those of Chapter,4 and provide a more complete picture of the practical limitations of aperture photometry for star cluster studies in the nearby galaxies. They are particularly useful for planning future observations, interpreting existing survey catalogues, and developing automated ML-based methods for cluster detection and aperture photometry. The findings presented here indicate that future cluster identification and photometry algorithms will need to account explicitly for complex issues arising due to stochasticity and variations in the local background. Such tools will become increasingly important as upcoming wide-field surveys exponentially expand the amount of available star cluster data, making manual, highly interactive methods impractical.

Chapter 6

Star clusters in the disc of M 31

The content of this chapter is based on Kriščiūnas et al. (2026) and Daugevičius et al. (2026).

The previous two Chapters focused on determining the limits of the aperture photometry approach for studying star clusters in nearby galaxies, with particular emphasis on the M 31 PHAT survey. Having quantified these limitations – primarily arising from stochastic and sky background effects – we are now able to assess and demonstrate what important astrophysical insights into star cluster populations and their host galaxies can be reliably obtained from real observations when operating close to these limits.

In this Chapter, we turn to the star cluster population in the disc of M 31 and investigate what constraints can be placed on their formation and evolution despite these challenges. In particular, we focus on low and intermediate mass clusters (~300–30 000 $M_{\odot}$), a regime where stochastic effects are non-negligible and where previous extragalactic studies have been relatively limited. Owing to its proximity and availability of high-resolution imaging from PHAT survey, M 31 provides an ideal laboratory for such analysis within a disc of a spiral galaxy similar to the MW. The survey covers more than 20 kpc of radial distance in the north-eastern disc, enabling the investigation of clusters across a wide range of environments and physical properties.

Using cluster parameters derived from a combination of adaptive aperture photometry and resolved stellar photometry, and by employing statistical analysis, we aim to characterise the structural evolution of M 31 disc star clusters, and to examine correlations between their sizes and other key physical properties. Our ultimate goal is to improve the understanding of cluster formation and evolution, the underlying governing physical processes, and to provide observational constraints for theoretical models, particularly by extending the analysis into lower cluster mass regime than typically explored in previous extragalactic star cluster studies.

6.1 Star cluster data

We use a catalogue of physical and structural parameters for star clusters in the north-eastern part of the M 31 disc (Kriščiūnas et al. 2026), which is based on the PHAT survey observations (Dalcanton et al. 2012) and the original M 31 PHAT star cluster catalogue (Johnson et al. 2015). The cluster physical parameters provided in Kriščiūnas et al. (2026) catalogue were derived using PHAT cluster adaptive aperture photometry data presented by Naujalis et al. (2021) and Kriščiūnas et al. (2023), together with photometry of resolved stars from Williams et al. (2023), which was used to construct cluster CMDs.

Physical parameters (age, mass, and extinction) were determined assuming fixed solar metallicity. Preliminary estimates were obtained by comparing integrated aperture photometry measurements with stochastic stellar population models, following the methodology described in de Meulenaer et al. (2015, 2017). These parameters were subsequently refined through CMD analysis and isochrone fitting of resolved stars (Čeponis et al. 2024). For each cluster, the final values were derived through an interactive assessment of more than 150 diagnostic elements, including 1D and 2D probability maps, CMDs, as well as colour and single-passband images of the clusters and their surrounding regions. Thus, the final physical parameters combine constraints from both aperture photometry and CMD analysis, consistent with our conclusion in Section 4.4 that such an approach likely yields the most robust results.

Structural parameters were derived from flux growth curves, in a manner similar to that described in Section 4.1. In the following analysis, we consider the half-light radius, R_{50}, as well as R_{30} and R_{80}, which enclose 30% and 80% of the total cluster flux, respectively. Further details on the cluster parameter determination procedures are provided in Kriščiūnas et al. (2026).

The catalogue (Kriščiūnas et al. 2026) includes parameters for a sample of 1922 star clusters younger than 800 Myr. Their spatial distribution across the M 31 disc is shown in Fig. 6.1. The majority of clusters are located in regions of active star formation, as traced by strong dust emission seen in the 70 μm *Spitzer*/MIPS image, most prominently within the well-known 10 kpc ring. Following additional inspection of cluster images, growth curves, and CMDs, four objects (AP0906, AP4226, AP4633, AP4936) were excluded from further analysis, because we came to conclusion that their structural parameters cannot be determined reliably. This results in the final sample of 1918 clusters used for this study.

6.1.1 Consistency of structural parameter measurements

Since the major focus of this Chapter is structural evolution of star clusters in the M 31 disc, we first assess the consistency of the derived structural parameters. In Fig.6.2, we examine the robustness of structural parameters by comparing measurements obtained in three different passbands: $F336W$, $F475W$, and $F814W$. The comparison between the $F336W$ and $F475W$ filters shows that structural parameters derived in the near-UV and optical bands are in good agreement. No systematic offsets or biases are evident: the measurements closely follow the identity relation, with relatively small scatter.

In contrast, a mild systematic difference appears when comparing $F475W$ and $F814W$ measurements. For all three structural parameters considered here, values derived in $F814W$ tend to be systematically larger than those obtained in $F475W$. We suggest that such behaviour is most likely driven by sky background effects. In relatively sparse fields, resolved IR-bright field stars may not be fully accounted for when subtracting a constant background level. If such stars are projected near the outer regions of a cluster, yet remain within its photometric aperture, they can artificially increase the measured flux at large radii, leading to an overestimation of cluster size in the IR.

To test this interpretation, we employ realistic mock cluster observations used

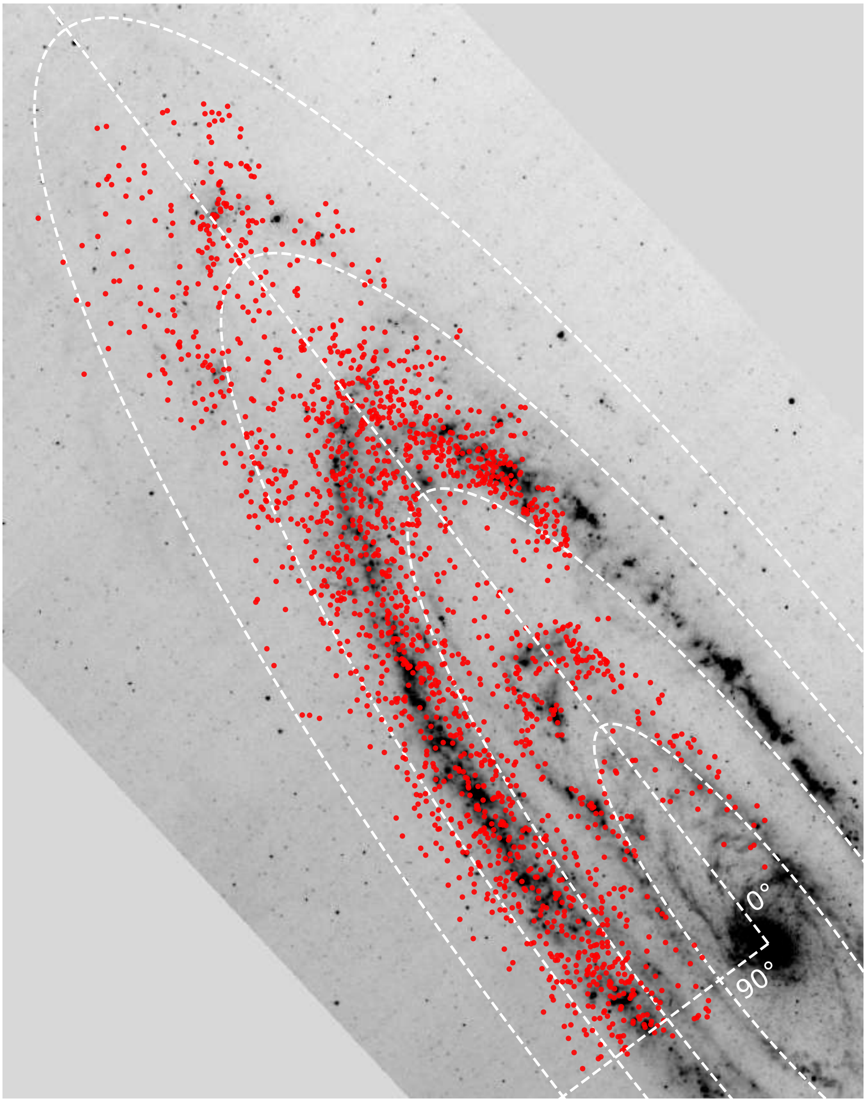

Figure 6.1. Spatial distribution of 1922 star clusters from the Kriščiūnas et al. (2026) catalogue. Cluster locations are shown as red dots on the 70 μm *Spitzer*/MIPS map of M 31. White ellipses indicate galactocentric distances of 5, 10, 15, and 20 kpc. North is up and east is to the left.

throughout Chapter 5. We consider models with $\log_{10}(\mathrm{M}/\mathrm{M}_{\odot}) = 3$ and ages of 100 and 300 Myr. Figure 6.3a shows a comparison of R_{50} measured in the $F475W$ and $F814W$ passbands in the absence of sky background (B0 field; see Fig 5.1). In this case, the R_{50} measurements are consistent between the optical and near-infrared bands: most clusters lie close to the identity line, with low scatter and no evident systematic bias. The remaining outliers, which show larger R_{50} differences between the bands,

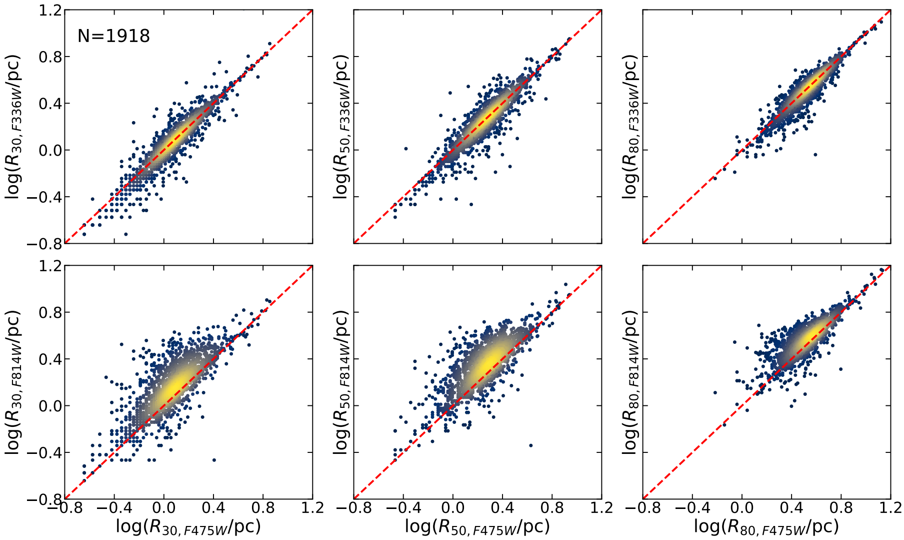

Figure 6.2. Comparison of star cluster structural parameters measured in three HST passbands. The top row shows comparisons between $F336W$ and $F475W$, while the bottom row compares $F475W$ and $F814W$. The left, middle, and right columns correspond to R_{30}, R_{50}, and R_{80}, respectively.

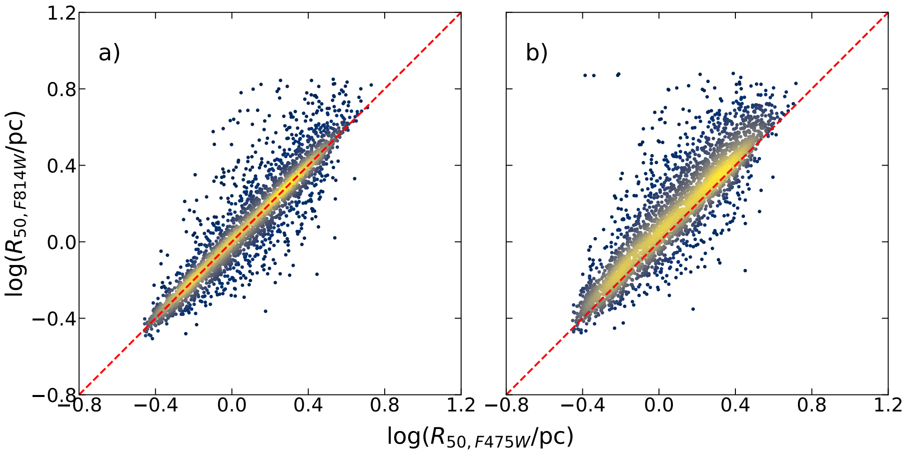

Figure 6.3. Impact of sky background on structural parameter measurements. Panel a) shows a comparison of R_{50} measured in $F475W$ and $F814W$ for cluster models without background (B0 field; see Fig.,5.1). Panel b) shows the same comparison for models embedded in a background field (B1; see Fig.,5.1). The sample includes clusters with $\log_{10}(M/M_{\odot}) = 3$ and ages of 100 and 300 Myr.

are primarily driven by stochastic effects discussed in Chapter 4. In particular, the presence of IR-bright PMS stars near the outer regions of a cluster can cause it to appear larger in $F814W$, whereas such stars located near the cluster centre may lead to an underestimation of its size relative to $F475W$.

Panel b) of Fig. 6.3 presents the same comparison for clusters inserted into a real, relatively sparse background field located at ~15 kpc from the M 31 centre (the B1 field; see Fig. 5.1). In this case, a behaviour similar to that observed in Fig. 6.2 emerges. A systematic shift is evident, with R_{50} values measured in $F814W$ being slightly larger than those in $F475W$, and the overall scatter increasing. Importantly, we do not observe significant differences when comparing R_{50} measured in $F475W$ with and without background. These results support our interpretation that the systematic offset seen in the IR arises due to sky background effects.

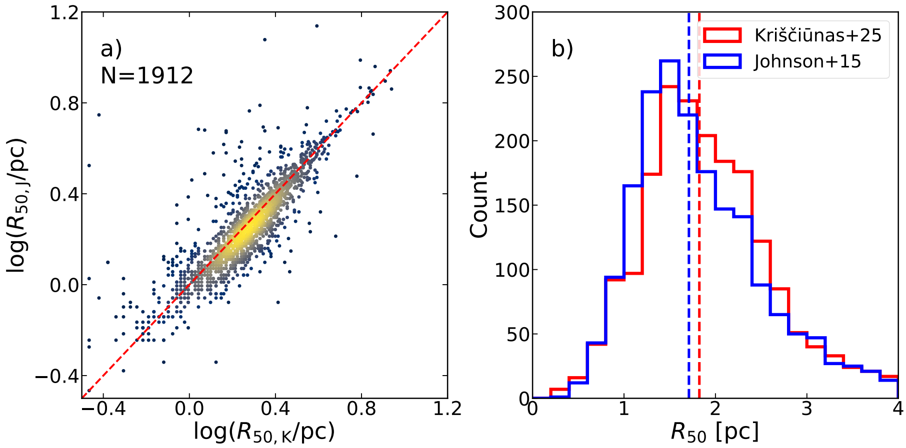

Figure 6.4. Comparison of cluster half-light radii, R_{50}, for objects common to the Kriščiūnas et al. (2026) and Johnson et al. (2015) catalogues. Panel a) shows R_{50} values from Kriščiūnas et al. (2026) on X-axis versus those from Johnson et al. (2015) on Y-axis, both in logarithmic scale. Panel b) presents distributions of R_{50} values in the two catalogues (see legend). Vertical dashed lines mark 3σ clipped medians of respective distributions.

To further evaluate the reliability of the structural parameters, in Fig. 6.4, we compare R_{50} measurements from Kriščiūnas et al. (2026) with those reported by Johnson et al. (2015) for clusters common to both catalogues (1912 objects in total). As shown in Fig. 6.4a, the two sets of measurements show a strong correlation, with most values in good agreement. The largest outliers can be attributed primarily to differences in the adopted photometric apertures and their centring. For example, in some cases Johnson et al. (2015) used apertures with radii larger by more than 1″ (corresponding to ~3.8 pc at the distance of M 31) compared to those used by Naujalis et al. (2021) or Kriščiūnas et al. (2023). This effect is most prominent for young clusters located within larger groups or associations of young stars. A small systematic offset is also present, with R_{50} values from Johnson et al. (2015) being slightly smaller on average than those reported by Kriščiūnas et al. (2026).

In Fig. 6.4b we show distributions of R_{50} in both catalogues. Overall, they appear similar and in good agreement, with no significant differences visible. After applying 3σ-clipping to reduce the influence of outliers, the difference between median half-light radii, $\tilde{R}_{50}$, is only ~0.1 pc: $\tilde{R}_{50} = 1.71^{+0.87}_{-0.53}$ pc for Johnson et al. (2015), and $\tilde{R}_{50} = 1.82^{+0.76}_{-0.57}$ pc for Kriščiūnas et al. (2026), where the uncertainties correspond to the 16th and 84th percentiles. Despite these small differences, the cluster size estimates are consistent between the two catalogues. In the remainder of this study, we adopt cluster structural parameters derived in the *F475W* passband. As already noted in Section 4.5, this filter provides the highest signal-to-noise ratio among the PHAT passbands, and is comparatively less affected by contamination from bright red field stars.

6.1.2 Overview of cluster parameters

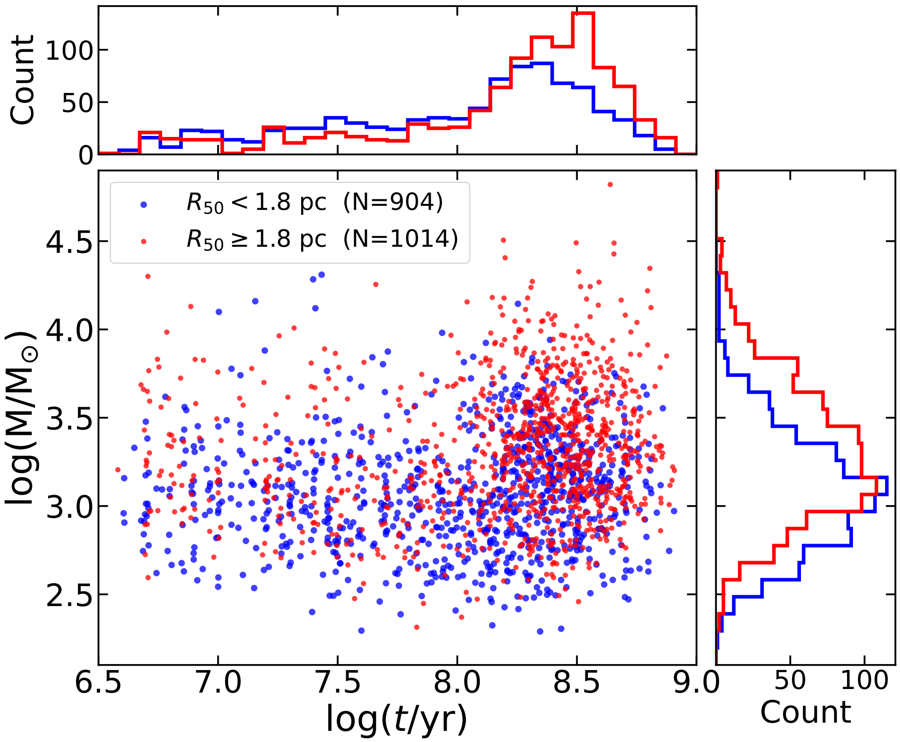

Figure 6.5. Mass–age diagram of M 31 star clusters. Objects are divided into two groups based on their half-light radii: compact (R_{50} < 1.8 pc; blue) and extended ($R_{50} \geq$ 1.8 pc; red) clusters. A small random Gaussian jitter is applied to the data points for visual clarity (σ = 0.01 in $\log_{10}(t/\mathrm{yr})$ and σ = 0.025 in $\log_{10}(\mathrm{M/M_\odot})$). The top panel shows the age distributions of both groups, while the right-hand panel presents their mass distributions.

In Fig. 6.5, we present an overview of the main star cluster parameters considered in further analysis. The figure shows cluster mass–age diagram, where objects are divided into two groups based on their R_{50}: more extended clusters ($R_{50} \geq$ 1.8 pc; red points), and more compact ones (R_{50} < 1.8 pc; blue points). Overall, the sample spans a broad mass range, from $\lesssim$300 M$_\odot$ to ~30 000 M$_\odot$, with the majority of clusters having masses $\gtrsim$1000 M$_\odot$. Decline in the number of low-mass clusters – most clearly seen in the mass distribution shown in the right-hand panel of Fig. 6.5 – is likely driven by selection effects (see Section 5.4) rather than reflecting a physical trend. In contrast, the observed decrease in the number of high-mass clusters (M $\gtrsim$ 2000 M$_\odot$) is more likely of physical origin, as this mass regime is expected to be largely unaffected by catalogue incompleteness, as shown in Section 5.4 (see Figs. 5.8 and 5.9).

The age distribution, shown in the top panel of Fig. 6.5, exhibits a prominent peak at ∼150-250 Myr, identified and discussed by Kriščiūnas et al. (2026). This feature likely indicates an episode of enhanced cluster formation, possibly triggered by an interaction with the satellite galaxy M 32 (Gordon et al. 2006; Block et al. 2006; Dierickx et al. 2014). The most consistent scenario is the one proposed by (Block et al. 2006), in which M 32 passed through the centre of M 31 ∼210 Myr ago. In addition, Vansevičius et al. (2009) reported a peak in cluster formation ∼70 Myr ago in the south-western part of the disc, which may be linked to a secondary passage of M 32 under the Block et al. (2006) scenario. The ∼200 Myr star formation burst is also supported by recent De Somma et al. (2025) study of Cepheid ages. A significant decline in cluster number beyond ∼300 Myr is likely a result of a combination of selection effects and cluster disruption.

It is also worth noting that, although majority of young systems ($t \lesssim 100$ Myr) have masses below 5000 $M_{\odot}$, there is a subset of rather massive objects, some exceeding ∼10 000 $M_{\odot}$. A considerable fraction of these are relatively extended ($R_{50} \geq 1.8$ pc), suggesting that they are unbound stellar associations rather than gravitationally bound star clusters.

When considering the two cluster size groups separately, the age distribution of extended clusters peaks at slightly older age compared to compact objects. Their mass distributions show that larger clusters tend to be more massive. While the difference in locations of peaks is modest, a more pronounced distinction is seen in the distribution tails: extended clusters exhibit a significantly stronger high-mass tail, whereas compact clusters dominate the low-mass end. This behaviour suggests a presence of the mass–radius relation, which is explored in more detail in the following sections of this Chapter.

6.1.3 Cluster sizes in Local Group spiral galaxies

Here, we examine the distribution of cluster half-light radii in the M 31 disc in more detail and compare it with those in other Local Group spiral galaxies (Fig. 6.6). For both M 33 and MW, we limit the samples to clusters younger than ∼800 Myr and $\log_{10}(M/M_{\odot}) \leq 5$ to ensure consistent comparison with M 31. The M 33 data are taken from the PHATTER star cluster catalogue (Johnson et al. 2022), where R_{50} values were derived using the same methodology as for M 31 clusters in Johnson et al. (2015). As shown in Section 6.1.1 (see Fig. 6.4), the R_{50} measurements adopted in this work from Kriščiūnas et al. (2026) are well correlated with those of Johnson et al. (2015) and exhibit consistent median values, thus a robust comparison with M 33 is also expected.

For the MW, cluster size estimates are taken from the Hunt & Reffert (2024) *Gaia* star cluster catalogue, where radii are derived using a different approach based on cluster member-stars counting. As an analogue of R_{50}, we use the on-sky projected radius enclosing 50% of cluster members within the best-fitting Jacobi radius (detailed definitions are provided in Hunt & Reffert (2024)). The Jacobi radius defines the boundary within which stars remain gravitationally bound to the cluster in the presence of the host galaxy's tidal field. This definition is therefore best suited for our analysis, as we aim to compare gravitationally bound systems. An alternative size measure reported

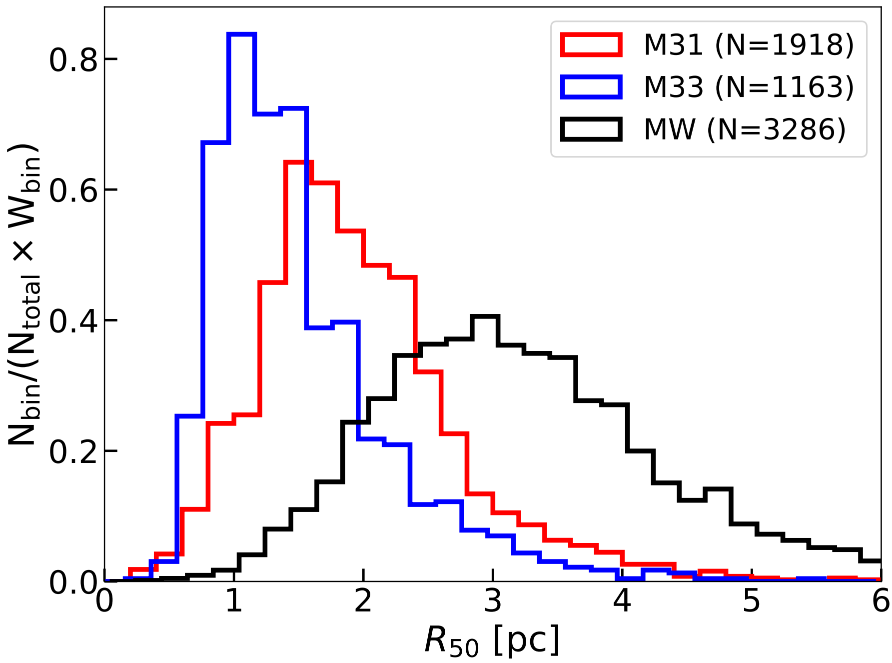

Figure 6.6. Comparison of star cluster size distribution in M 31 with those in other spiral galaxies of the Local Group. M 33 cluster data are taken from (Johnson et al. 2022). MW cluster data are from Hunt & Reffert (2024). Only clusters younger than 800 Myr and $\log_{10}(M/M_\odot) \leq 5$ are included for all galaxies. For visual clarity, the histograms for M 33 and MW are slightly offset relative to that of M 31.

in Hunt & Reffert (2024) – the radius enclosing 50% of all members, including those beyond the Jacobi radius – is affected by tidal tails, a feature that is generally not detectable at extragalactic distances, and which could possibly introduce inconsistencies in our analysis (E. L. Hunt, private communication). Therefore, the comparison with the MW cluster sample is less direct and should be interpreted with caution. We emphasise that we include only those MW objects that Hunt & Reffert (2024) classify as "open clusters".

Figure. 6.6 shows that MW star clusters are, on average, more extended than those in M 31 and M 33, while M 33 clusters are slightly more compact than those in M 31. The 3σ-clipped statistics for median half-light radius, $\tilde{R}_{50}$ (with ± 16th and 84th percentiles), are as follows: $\tilde{R}_{50} = 1.82^{+0.76}_{-0.57}$ pc for M 31; $\tilde{R}_{50} = 1.35^{+0.66}_{-0.45}$ pc for M 33; $\tilde{R}_{50} = 3.10^{+1.19}_{-0.95}$ pc for MW.

The MW cluster size distribution is broadly consistent with results for other nearby galaxies ($\lesssim$10 Mpc) outside the Local Group, where the typical peak of young cluster size distributions is $R_{50} \approx 3$ pc (Larsen 2004; Lee et al. 2005; Scheepmaker et al. 2007; Ryon et al. 2015, 2017; Brown & Gnedin 2021). On the other hand, star clusters in M 31 and M 33 appear to be noticeably more compact compared to those in other nearby galaxies. These discrepancies may partly arise from differences in size measurement techniques or selection effects. In particular, the discrepancy with the MW could be driven by the aforementioned inability to detect tidal tails in extragalactic clusters, which may lead to systematically underestimated cluster radii in M 31 and M 33. At the same time, an intrinsic environmental dependence of characteristic cluster size cannot be ruled out, especially given that previous studies (Kodaira et al. 2004; Vansevičius et al. 2009; San Roman et al. 2012) have also suggested a compact nature of star clusters in both M 31 and M 33.

For M 31, ground-based Subaru Suprime-Cam observations of the south-western part of the galaxy's disc (Kodaira et al. 2004; Šablevičiūtė et al. 2006, 2007; Vansevičius et al. 2009) indicate that clusters in this region are typically compact. In particular, Vansevičius et al. (2009) report a characteristic size of $R_{50} \sim 1.5$ pc, in good agreement with the results presented here, despite differences in instrumentation and methodology. Since our analysis focuses on the north-eastern part of the disc, this suggests that clusters are compact throughout the entire M 31 disc. A similar picure emerges for M 33. A study of 161 star clusters in M 33 based on the HST ACS/WFC observations (San Roman et al. 2009, 2012) has shown that clusters in M 33 seem to be generally smaller than those in the MW, M 31, and the Magellanic Clouds. Overall, results presented in Fig. 6.6 are consistent with these previously reported findings.

6.2 Star cluster structural evolution

We now focus on star cluster structural properties variation with age. Our aim is to characterise the structural evolution of gravitationally bound star clusters. However, as noted in Section 6.1.2, the Kriščiūnas et al. (2026) sample likely includes some stellar associations and other unbound, dissolving systems. To minimise contamination by such objects, we adopt the approach of Gieles & Portegies Zwart (2011), which is widely used in extragalactic cluster studies. To distinguish bound clusters from associations, Gieles & Portegies Zwart (2011) introduced the dynamical age, Π, defined as the ratio of cluster age, t, to the crossing time of member stars in the cluster, $t_{\rm cr}$:

$$\Pi = t/t_{\rm cr}, \qquad (6.1)$$

where crossing time is defined as follows:

$$t_{\rm cr} \equiv 10\left(\frac{R_{50}^3}{G\mathrm{M}}\right)^{1/2}, \qquad (6.2)$$

with G denoting the gravitational constant and M being the cluster's mass. According to Gieles & Portegies Zwart (2011), a distinction between bound and unbound objects can be made at $\Pi = 1$, where $\Pi > 1$ are bound clusters, while those with $\Pi < 1$ are likely unbound associations. They note, however, that while the $\Pi = 1$ boundary provides a robust distinction between clusters and associations for objects with $t \gtrsim 10$ Myr, it is less reliable at younger ages; nonetheless it still remains a practical separator even for $t < 10$ Myr objects.

Figure 6.7 shows R_{50} as a function of cluster age. The left panels present results for M 31 disc clusters: panel a) includes all 1918 objects considered in this study, while b) panel shows only those satisfying the $\Pi > 1$ selection criterion. When no constraint on Π is applied, no clear trend of cluster size expansion or contraction is visible. However, during the first ~50 Myr, the spread in R_{50} is significantly larger, with both more compact and more extended systems present compared to older populations. This may

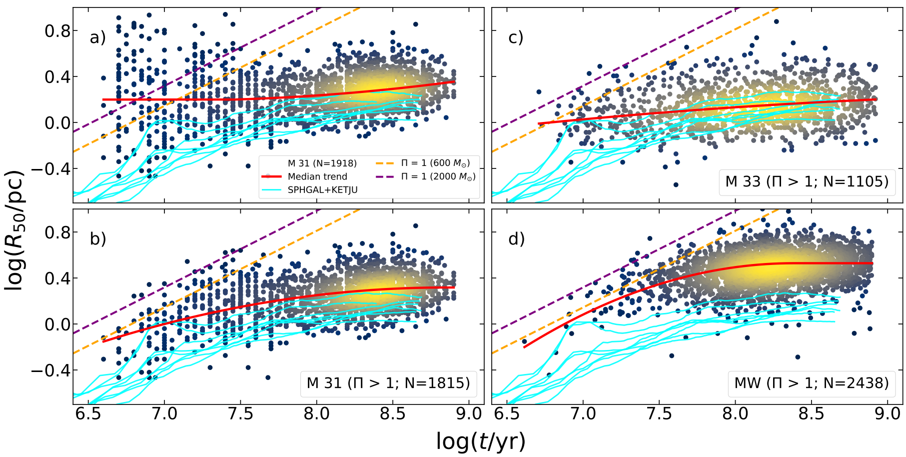

Figure 6.7. Cluster size as a function of age. Panel a) shows all 1918 M 31 objects considered in this study, while panel b) includes only those M 31 clusters satisfying the dynamical age criterion $\Pi > 1$. Panel c) presents results for M 33 star clusters from (Johnson et al. 2022) catalogue. Panel d) shows MW clusters from *Gaia* catalogue of Hunt & Reffert (2024); for the MW, only objects classified as "open clusters" in the catalogue are included. For M 33 and MW, we consider clusters with $t \leq 800$ Myr and $\log_{10}(M/M_\odot) \leq 5$ that satisfy the $\Pi > 1$ criterion. Red curves indicate the median trend of R_{50} evolution with age. Cyan curves show evolutionary tracks of individual star cluster models from the `SPHGAL+KETJU` simulation (Lahén et al. 2025), smoothed using a sliding window of width 0.2 dex in $\log_{10}(t/\mathrm{yr})$ axis. Dashed lines mark the $\Pi = 1$ boundaries for different cluster masses.

indicate ongoing structural evolution, where extended objects represent gradually dissolving unbound systems while compact clusters are expanding.

After applying the $\Pi > 1$ criterion to exclude objects that are most likely unbound, a clearer trend emerges: the median R_{50} increases with age. This growth occurs primarily within the first ~100 Myr, with the most significant apparent expansion happening during the first ~30 Myr. In this age interval, when adopting the $\Pi > 1$ limit, the median R_{50} increases by more than a factor of two – from ~0.6 pc to ~1.6 pc, corresponding to $\log_{10}(R_{50}/\mathrm{pc})$ from ~(-0.2) to ~0.2. We note that similar trend, albeit somewhat weaker, is visible when adopting a less strict threshold (e.g., $\Pi > 0.5$; Appendix, Fig. A6b). We emphasise that, unless stated otherwise, we restrict the sample to objects satisfying the $\Pi > 1$ in the following analysis.

The right-hand panels of Fig. 6.7 place these results for the M 31 disc in a broader context by showing the cluster size–age relation in other Local Group spiral galaxies. For M 33 and the MW, we use the aforementioned catalogues of Johnson et al. (2022) and Hunt & Reffert (2024), respectively. Similar to M 31, neither galaxy exhibits strong cluster size evolution beyond ~100 Myr. with the median R_{50} remaining approximately constant or showing only a mild increase. Given the early expansion observed in M 31, we examine this aspect in M 33 and the MW in more detail below.

For M 33, we do not see significant early evolution of R_{50} based on the Johnson et al. (2022) data (Fig. 6.7c). This could indicate that the rapid early cluster expansion observed in M 31 star clusters does not occur in M 33. However, we suggest that this difference may also arise from methodological effects. As noted in Section 6.1.3, R_{50} values in Johnson et al. (2022) are derived using the same approach as for M 31 clusters in Johnson et al. (2015). As discussed in Section 6.1.1 (see also Fig. 6.4), the largest outliers when comparing Johnson et al. (2015) and Kriščiūnas et al. (2026) estimates occur for young star clusters, for which Johnson et al. (2015) adopt significantly larger photometric apertures than Naujalis et al. (2021) or Kriščiūnas et al. (2023) for the same objects. As a result, for these young clusters, Johnson et al. (2015) typically derive larger R_{50} values than Kriščiūnas et al. (2026). A similar systematic effect in the case of M 33 sample could mask an underlying trend of early R_{50} expansion in this galaxy.

Previous studies of M 33 clusters can provide additional context. San Roman et al. (2012) investigated cluster structural parameters as a function of age for M 33 star clusters, although their sample mainly consists of objects with ages from 100 Myr to 1 Gyr. Importantly, they reported no correlation between R_{50} and cluster age, which is consistent with the trend shown in Fig. 6.7c and our results for M 31 star clusters over the same age range (Fig. 6.7b). However, San Roman et al. (2012) found that older clusters exhibit a broader range of core radii, r_c, suggesting possible structural evolution at later stages.

For the MW, Fig. 6.7d shows a strong increase in median cluster radius with age up to ~50 Myr. However, this trend closely follows the slope of the $\Pi = 1$ boundary, and the number of clusters younger than 10 Myr is relatively small. This suggests that, most likely, the apparent growth is largely driven by the adopted $\Pi > 1$ selection criterion. Therefore, we cannot confidently conclude that the observed behaviour, although similar to that seen in M 31, reflects a genuine structural evolution of MW clusters, especially given that the radii measurement method for Galactic clusters differs fundamentally from that used for extragalactic samples, as discussed in Section. 6.1.3.

A recent study by Della Croce et al. (2024) provides additional but important insight. They performed a systematic kinematic analysis of young ($t < 300$ Myr) MW star clusters based on the *Gaia* DR3 data. Importantly, they found that the majority of clusters younger than ~30 Myr are currently undergoing significant expansion, while older clusters are generally found to be compatible with the equilibrium state. This is highly consistent with our findings in the M 31. Furthermore, by comparing their results in the MW with N-body simulations of young star clusters (Livernois et al. 2021), Della Croce et al. (2024) showed that the observed expansion is consistent with systems experiencing violent relaxation and evolving towards virial equilibrium. They also suggest that residual gas removal and mass loss due to stellar evolution are likely to be key drivers of the observed expansion as well.

In the context of Local Group galaxies, it is also worth noting a study by Gatto et al. (2021), who analysed structural evolution of clusters in Magellanic Clouds by combining their sample of 134 Small Magellanic Cloud clusters with those in Large and Small Magellanic Clouds studied earlier by Mackey & Gilmore (2003a,b). Gatto et al. (2021) found that young clusters are compact and seem to undergo rapid expansion within the first 10–20 Myr, followed by a phase of little structural evolution over the next 200–300 Myr. This picture is generally in good agreement with our results for the M 31 disc clusters and the findings of Della Croce et al. (2024) in the MW. Additionally, Gatto et al. (2021) also reported an increasing spread in r_c at ages beyond ~200 Myr, similar to the trend identified by San Roman et al. (2012) for M 33 clusters.

In Fig. 6.7, we also compare our observational results with evolutionary tracks of individual clusters from the SPHGAL + KETJU simulations, which follow star cluster formation within a star-by-star galaxy model and include hydrodynamics, star formation, stellar evolution, and collisional gravitational interactions between stars and stellar remnants (Lahén et al. 2025). In particular, we use results from a simulation of a dwarf galaxy with 1% solar metallicity and virial mass of $4 \times 10^{10}\,M_\odot$. Unfortunately, comparable star-by-star simulations of low-mass cluster formation and evolution in M 31- or MW-like galaxies are not yet available. Despite the vast differences between the simulation setup and the environment of M 31, we find that the model evolutionary tracks agree well with our results when the $\Pi > 1$ selection criterion is applied. The offset in cluster sizes between the M 31 sample and SPHGAL + KETJU models is most likely a cluster mass effect – all simulated clusters have masses $\lesssim 800\,M_\odot$, whereas the majority of Kriščiūnas et al. (2026) objects are $\gtrsim 1000\,M_\odot$. We note that at increased metallicity (10% solar) the trend of model size evolution remains very similar (N. Lahén, private communication). Although the physical conditions in Lahén et al. (2025) simulations differ greatly from those in M 31 – making direct comparison and drawing concrete conclusions difficult – the general agreement between observations and state-of-the-art modelling results is encouraging, and hints towards a possible theoretical explanation of the apparent expansion of young clusters in the M 31 disc.

Lahén et al. (2025) find that clusters in SPHGAL + KETJU simulations become exposed within the first few Myr, once the first photoionizing stars ignite and their pre-SN stellar winds remove the remaining natal gas. This picture is supported by recent JWST studies of young embedded star clusters in nearby galaxies (Knutas et al. 2025; Pedrini et al. 2026), which show that clusters become fully exposed in ~6 Myr. As a result of this early gas expulsion, low-mass clusters experience heavy mass loss, significantly reducing their gravitational potential. Subsequent mass loss driven by stellar evolution and dynamical processes then leads to rapid cluster expansion shortly after the ignition of massive stars and onset of their feedback.

The agreement between our observational results and the SPHGAL + KETJU models suggests that a similar mechanism – driven primarily by internal cluster processes such as mass loss due to stellar feedback, stellar evolution, and internal gravitational interactions – may be responsible for the early structural evolution of star clusters in the M 31 disc. Notably, Jørgensen & Church (2025), who simulated the impact of GMCs on the evolution of young star clusters in M 51, found that such effects do not produce measurable or detectable impact on cluster structural properties over a timescale of 200 Myr. This further supports our interpretation that the increase of R_{50} with age observed in Fig. 6.7b mainly reflects ongoing internal cluster processes, rather than the effects of stochastic external perturbations, such as GMC encounters.

An alternative explanation for the observed trend of increasing R_{50} with age could be the presence of selection effects, in particular, those introduced by the adoption of a Π selection criterion. As shown in Fig. 6.7b, the slope of the $\Pi > 1$ boundary during the first ~30 Myr removes a substantial fraction of the youngest and most extended systems. Some of these could be large yet still gravitationally bound, introducing the possibility that the apparent growth is artificially induced by such selection. This effect becomes more pronounced when a stricter threshold (e.g., $\Pi > 2$; see Appendix, Fig. A6d) is applied. However, we note that very compact objects ($R_{50} \approx 0.5 - 1.0$ pc, corresponding to ~2.5–5.0 ACS/WFC pixels) are present among clusters younger than ~100 Myr but are largely absent at older ages. Based on the results discussed in Chapter 4 and Chapter 5, we argue that star clusters of this size in the 100–300 Myr age range should not be strongly affected by selection effects: they remain relatively bright and blue compared to the average sky background dominated by older stellar populations in the M 31 disc, and they are sufficiently extended to be distinguished from point sources.

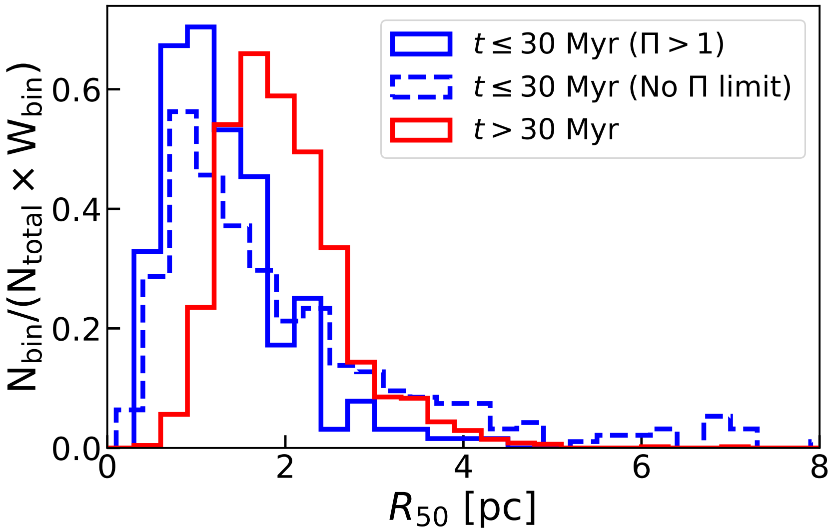

Figure 6.8. Comparison of cluster half-light radii, R_{50}, distributions for M 31 clusters younger than (blue line) and older than (red line) 30 Myr. Solid histograms show samples selected with the $\Pi > 1$ criterion, while the blue dashed histogram includes all young clusters without this selection.

To further illustrate that cluster sizes change significantly during the first tens of Myr in the M 31 disc, in Fig. 6.8, we compare R_{50} distributions of clusters younger than 30 Myr (blue line) with those older than 30 Myr (red line). A clear difference is evident between the two populations: the distribution for younger clusters peaks at $R_{50} \approx 1.0$ pc, whereas for older clusters it shifts to ~1.7 pc. We note that even without applying the Π selection, the distribution of young clusters remains broadly similar, as shown by the blue dashed histogram in Fig. 6.8; all clusters older than 30 Myr already satisfy the $\Pi > 1$ criterion. To quantify this difference, we performed Anderson–Darling test (Anderson & Darling 1954), comparing the $t > 30$ Myr sample with both Π-limited and non-limited samples of $t \leq 30$ Myr clusters. In both cases, we obtain a p-value < 0.001, corresponding to a <0.1% probability that the observed differences between samples arise by chance. We can therefore reject the null hypothesis – that the two samples are drawn from the same underlying distribution – with high confidence. This provides strong evidence that clusters younger than 30 Myr are truly more compact than their older counterparts, enabling us to more confidently interpret this as a signature of genuine physical expansion, rather than an artefact of selection effects. We emphasise that the timescale of this early expansion phase (~30 Myr) coincides with the lifetimes of SN progenitors, suggesting that stellar evolution processes, such as pre-SN winds of massive stars and SN feedback, may play a key role in driving the observed early cluster size growth.

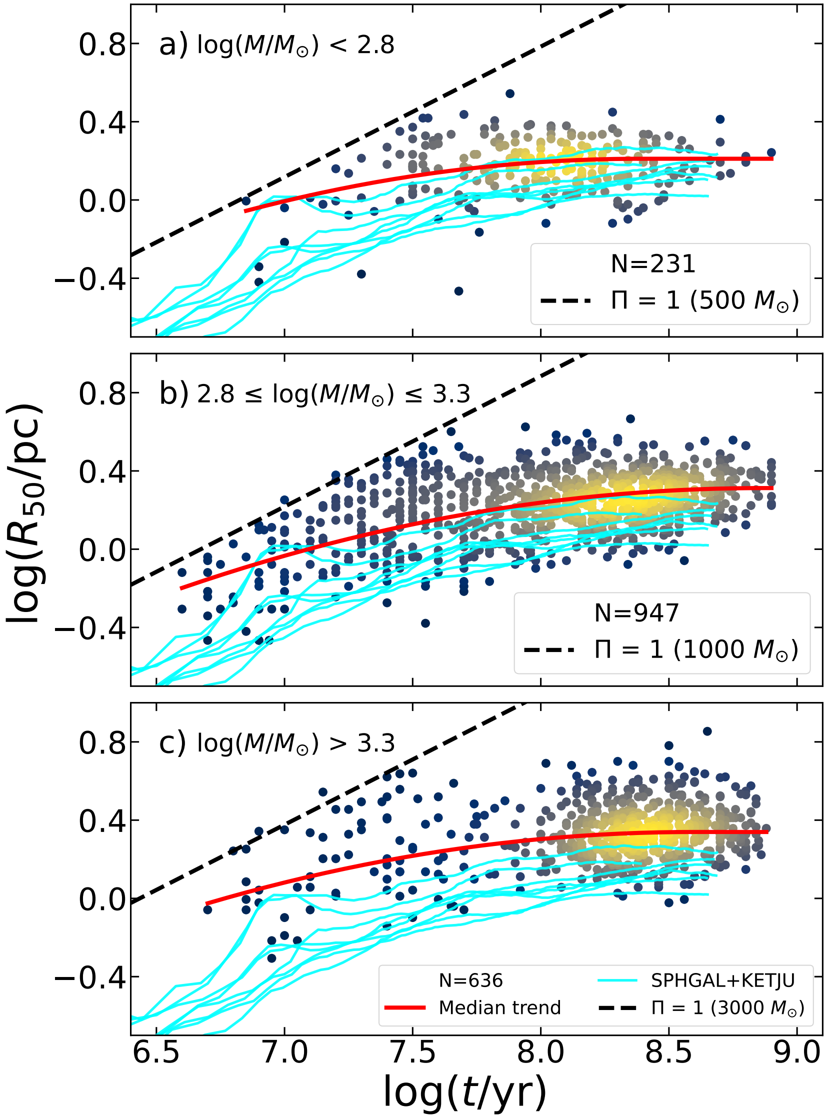

Figure 6.9. Half-light radius, R_{50}, versus age for M 31 disc clusters in three mass bins. Each panel shows a different cluster mass range, ordered from low (top) to high mass (bottom), with mass ranges indicated in panels. The $\Pi > 1$ criterion is applied in all panels. See the legend and Fig 6.7 caption for a description of the curves shown.

We also examine how the cluster size–age relation depends on cluster mass. Figure 6.9 shows R_{50} as a function of age for three mass intervals, ordered from the lowest masses in the top panel to the highest in the bottom panel. A clear increase in the characteristic R_{50} with age is present in all three mass bins shown. The median trend of R_{50} evolution is consistent with SPHGAL + KETJU models across the full mass range; we note that, the best agreement is seen for clusters with $2.8 \leq \log_{10}(M/M_{\odot}) \leq 3.3$.

At all ages, more massive clusters tend to have slightly larger median R_{50}. Indeed, a similar trend has been reported by Pfalzner et al. (2016) for embedded clusters in the solar neighbourhood, where more massive systems tend to possess larger initial radii. A dependence of cluster size on mass is also suggested by theoretical models (e.g., Gieles & Renaud 2016; Choksi & Kruijssen 2021; Grudić et al. 2021, 2023a). The cluster mass–radius relation is discussed further in Section 6.3.

Alternatively, larger radii of more massive clusters, already seen at young ages, may reflect their faster early expansion. This may appear counterintuitive, as one could expect more massive clusters to be more tightly bound, retain their residual gas longer, and thus preserve their initial structure longer. However, recent JWST studies (Knutas et al. 2025; Pedrini et al. 2026) suggest otherwise. They show that, in nearby galaxies more massive clusters emerge from their embedded phase to fully exposed phase on shorter timescales, implying that they lose a substantial fraction of their mass earlier and begin dynamical evolution sooner. Moreover, as seen in Fig. 6.9, star clusters of different masses have similar radii, indicating that more massive objects are denser. Higher densities correspond to shorter dynamical timescales, $t_{\rm dyn} \propto \rho^{-1/2}$, and therefore faster structural evolution. Additionally, the relation between cluster mass and the mass of the most massive member star (Zhou et al. 2026) implies that more massive clusters host higher-mass stars with shorter lifetimes. This leads to an earlier onset of SN feedback and a larger overall contribution from pre-SN stellar winds and SNe associated with massive stars. If early structural evolution is primarily driven by such stellar evolution processes, higher mass clusters may evolve more rapidly.

Next, we investigate the evolution of R_{30} and R_{80} alongside R_{50}. Figure 6.10 illustrates the age dependence of all three structural parameters together. Distribution centres for each age bin are marked by red dots, while coloured regions indicate the 1σ uncertainties of the distribution centres, derived from kernel density estimates (KDEs). Both the centres and their uncertainties are computed from 3σ-clipped samples to minimise the influence of outliers.

Because the parameters are intrinsically correlated, we perform two-dimensional σ-clipping using the Mahalanobis (1936) distance. For a given pair of parameters (e.g., $\log(R_{50})$ and $\log(R_{30})$), we estimate the mean vector $\bar{\mathbf{d}}$ and covariance matrix $\mathbf{C}$, and compute the squared Mahalanobis distance:

$$D^2 = (\mathbf{d} - \bar{\mathbf{d}})^{\rm T}\mathbf{C}^{-1}(\mathbf{d} - \bar{\mathbf{d}}), \tag{6.3}$$

where $\mathbf{d}$ is the data vector. Objects with $D > 3$ (corresponding to a correlated 3σ threshold) are excluded. This method effectively performs clipping within an ellipse aligned with the intrinsic covariance of the data, ensuring that correlations between parameters are properly taken into account. We adopt this approach for σ-clipping throughout the remainder of the study.

In Fig. 6.10, we observe that all three structural parameters are increasing with age. During the first ~40 Myr, this growth is steady; R_{30} and R_{50} appear to evolve at a similar rate, while R_{80} increases more slowly. Importantly, the most pronounced growth in all three parameters occurs within first few tens of Myr, supporting our earlier statement – based purely on R_{50} versus age analysis alone – that M 31 disc clusters undergo rapid and significant expansion during the first ~30 Myr. At later times, in the ~(40–200) Myr range, the evolution becomes more irregular, where one parameter may remain nearly constant while the others continue to increase. Beyond this phase, gradual expansion continues.

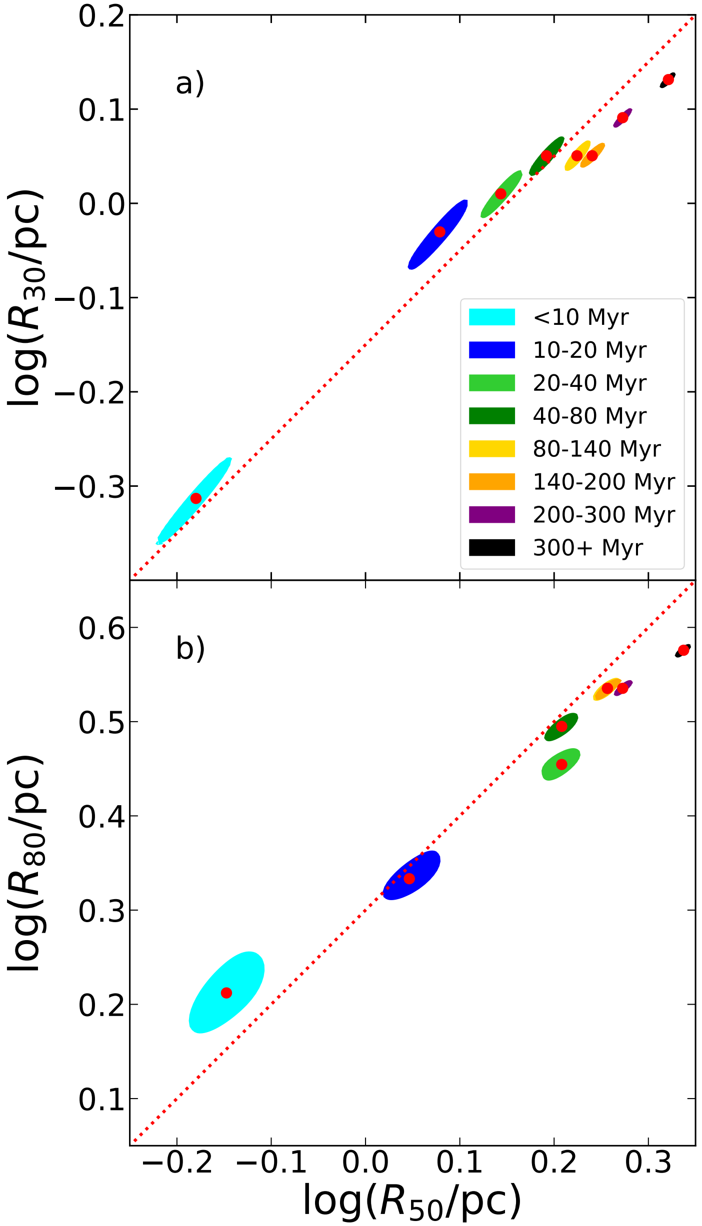

Figure 6.10. Evolution of star cluster structural parameters in the M 31 disc. Coloured regions show the 1σ uncertainty of the distribution centres (marked by red dots) for each age bin. Centres and their uncertainties are derived from 3σ-clipped cluster samples satisfying $\Pi > 1$ and including all cluster masses. We note that in b) panel, centroids and their uncertainty regions of 80–140 Myr and 140–200 Myr age bins overlap. The red dotted line marks the diagonal along which parameters on both axes change proportionally.

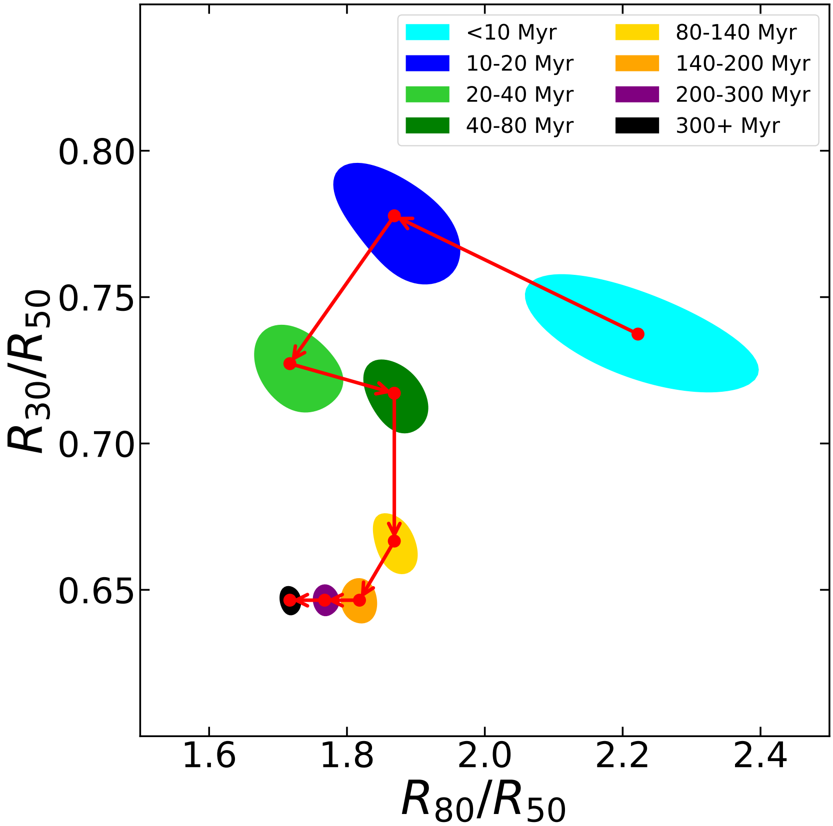

Figure 6.11. Evolution of R_{30}/R_{50} and R_{80}/R_{50} ratios of star clusters in the M 31 disc. Coloured regions show the 1σ uncertainty of the distribution centres (marked by red dots). Subsequent distribution centres are connected by red arrows. Centres and their uncertainties are derived from 3σ-clipped cluster samples satisfying $\Pi > 1$ and including all cluster masses.

Figure 6.11 shows the evolution in the R_{30}/R_{50} versus R_{80}/R_{50} plane, tracing the relative evolution of inner and outer cluster regions. During the first ~20 Myr, R_{30}/R_{50} remains nearly constant, while R_{80}/R_{50} decreases, confirming that R_{80} grows more slowly than R_{30} and R_{50}. Between ~20 Myr and 140 Myr, R_{80}/R_{50} stays roughly constant, whereas R_{30}/R_{50} decreases significantly, consistent with the nearly constant R_{30} seen in Fig. 6.10a. This timescale coincides with the lifetimes of massive stars, further supporting the idea that the observed structural evolution may be primarily linked to stellar-evolution-driven processes associated with these massive stars, such as SN feedback and stellar winds.

In recent years, increasing observational evidence for primordial mass segregation in young (proto-)clusters has emerged (e.g., Plunkett et al. 2018; Nony et al. 2021; Zhang et al. 2022; Xu et al. 2024), with more massive stars preferentially concentrated towards cluster centres. If such segregation is significant and cluster expansion is driven by stellar-evolution-induced mass loss, a more pronounced core expansion would be expected, which in this context could be observed as R_{30} increasing more rapidly than R_{50} and R_{80}. Although both R_{30} and R_{50} indeed grow faster than R_{80} during the first ~40 Myr (Fig. 6.10), we do not observe a clear difference between the evolution of R_{30} and R_{50}. Consequently, it remains difficult to confidently assess whether the observed behaviour provides clear evidence for the presence of initial mass segregation. Beyond ~140 Myr, the ratio R_{30}/R_{50} becomes stable and constant, while R_{80}/R_{50} continues to decrease gradually. This suggests that the outer regions expand more slowly than the inner parts.

Such structural evolution may indicate that clusters begin to approach a tidally limited regime: as their outer layers expand towards a tidal boundary imposed by the galactic tidal field, further growth of R_{80} is eventually suppressed, while the inner cluster regions continue to expand. Heggie & Hut (2003) argue that for tidally limited clusters undergoing mass loss, the effective radius should contract while the core expands. However, the continued increase of R_{50} observed here therefore implies that M 31 disc clusters are unlikely to be fully tidally limited, and instead evolve as isolated systems. At the same time, structural parameters derived from aperture photometry are subject to stochastic effects, as shown in Section 4.5 (see Figs. 4.11 and 4.12), and can provide inconclusive results. Although most clusters in the studied sample are more massive than 1000 $M_\odot$ and thus less sensitive to stochasticity, and the use of adaptive aperture photometry helps to reduce some of these effects associated with bright stars, these results should still be interpreted with caution. Nonetheless, the trends shown in Figs. 6.10 and 6.11 suggest that star clusters in the M 31 disc undergo rather complex structural evolution.

However, the observed variation of cluster structural properties with age may have an alternative explanation. If a significant cluster age gradient with galactocentric distance, R_{GC}, exists within the studied region of the M 31 disc, the apparent structural evolution could instead reflect environmental effects – such as variations in the galactic tidal field or location-dependent cluster structure – rather than expansion driven by internal evolutionary processes. Therefore, we examine whether any possible trends between cluster size and R_{GC} are present to assess if internal or environmental mechanisms drive the apparent structural evolution.

This is explored in Fig. 6.12. For this analysis, we restrict the sample to clusters located near the major axis, defined by azimuthal angles between –45° to +45° relative to it, as shown in the top panel of Fig. 6.12. This selection is motivated by the high inclination angle of M 31 (~77.5°), which introduces increasing uncertainty in R_{GC} for clusters located farther from the major axis due to de-projection effects. This is illustrated in the same panel: at projected distances of ~(10–15) kpc along the X-axis, beyond the black dashed line marking the +45° direction, three distinct ring structures begin to blend together as a result of these de-projection uncertainties.

The bottom panel of Fig. 6.12 shows R_{50} as a function of R_{GC} for three cluster age intervals. Overall, we detect no clear cluster size gradient with galactocentric distance in any age bin; however, a large scatter in R_{50} is observed at fixed R_{GC}. We note that the structural parameter ratios R_{30}/R_{50} and R_{50}/R_{80} exhibit similar behaviour, showing no evident radial dependence. A notable feature emerges for clusters younger than 100 Myr: three radial rings are clearly separated, whereas at older ages they are more blured. This may indicate that clusters migrate from their birth sites on timescales longer than ~100 Myr, suggesting that star clusters can serve as excellent tracers of past star-forming regions over extended periods.

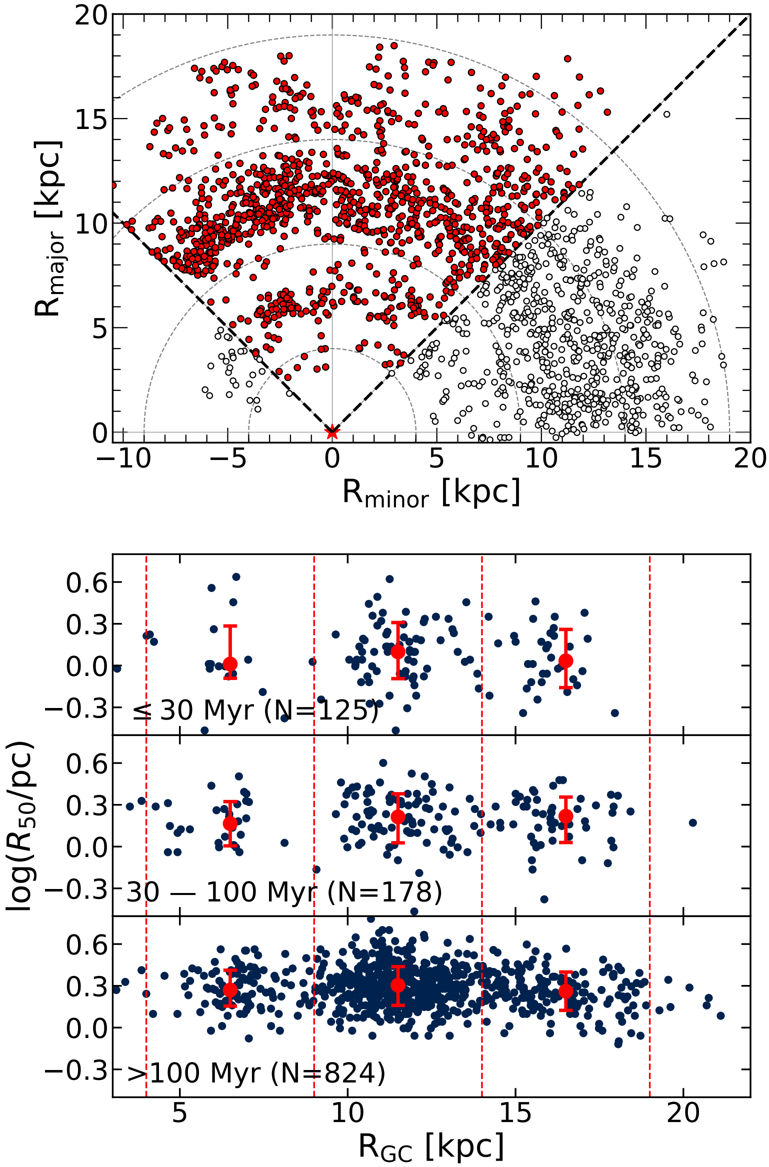

Figure 6.12. Dependence of cluster half-light radius (R_{50}) on galactocentric distance (R_{GC}). Only clusters near the major axis of the M31 disc are considered, defined by an azimuthal angle relative to the major axis of –45° to +45°. Top: the de-projected map of M31 disc clusters. The azimuthal angle cut is indicated by black dashed lines; clusters within the cut are shown as filled red symbols, while clusters outside are shown as open circles. Bottom: R_{50} as a function of R_{GC} for three age intervals (indicated in each panel). Red markers show the median R_{50} in each R_{GC} bin (their boundaries denoted by vertical red dashed lines), with error bars marking the 16th-84th percentile range. Only clusters satisfying $\Pi > 1$ are included in both panels.

Overall, we find no evidence for a correlation between cluster structure and their galactocentric distances. This implies that variations in the tidal field across the studied region of the M 31 disc do not significantly affect cluster structural properties. This supports our earlier interpretation that the observed structural evolution is primarily driven by internal cluster processes rather than environmental effects, and it reflects genuine evolution as clusters age.

To summarise the results presented in this Section, we find that gravitationally bound clusters in the M 31 disc undergo rapid expansion during the first ~30 Myr, with their sizes increasing by more than a factor of two. This behaviour is well reproduced by the SPHGAL + KETJU cluster models (Lahén et al. 2025), in which early residual gas expulsion leads to substantial mass loss and triggers rapid expansion driven by stellar evolution and internal dynamical processes. Our findings are also highly consistent with recent results for young clusters in the MW (Della Croce et al. 2024), where kinematic analysis based on *Gaia* data reveals that Galactic star clusters younger than 30 Myr are undergoing rapid expansion.

We further find that M 31 disc clusters show no size correlation with their distance from the galactic centre, suggesting that external tidal effects are likely to be insignificant or play only a minor role during the early stages of evolution. We therefore interpret the observed cluster structural evolution as the expansion of initially compact, not tidally limited clusters, driven mainly by stellar-evolution-induced mass loss and two-body relaxation, which happens after the early residual natal gas removal. Over time, these clusters are expected to gradually approach a tidally limited regime and eventually evolve towards virial equilibrium state.

6.3 Mass – radius relation

Another key property of star cluster populations that provides important constraints on theories of cluster formation and evolution, as discussed earlier, is the mass–radius relation, which we investigate in this section. Figure 6.13 shows the distribution of star clusters in the mass–R_{50} space for six cluster age bins. For reference, we include two commonly discussed scaling relations. The first is the constant density relation, $R_{50} \propto \mathrm{M}^{1/3}$ (green dash-dotted line), predicted by analytic and numerical models (e.g., Choksi & Kruijssen 2021; Grudić et al. 2021). The second is the equilibrium relation, $R_{50} \propto \mathrm{M}^{1/9}$ (red dashed line), derived from a model that incorporates the combined effects of tidal shocks and two-body relaxation (Gieles & Renaud 2016; Renaud 2018). The blue dashed contours represent KDEs: inner contour denotes area enclosing 39.3% of the KDE integral around the KDE peak (corresponding to the 1σ region), while the outer contour encloses 86.5% (2σ region). Segment-coloured curves show evolutionary tracks of SPHGAL + KETJU cluster models: red segment corresponds to the part of the track <10 Myr, green to 10–30 Myr, cyan to 30–100 Myr, and magenta to >100 Myr.

Panels a–c) of Fig. 6.13 clearly demonstrate the early cluster expansion discussed in Sec. 6.2, as the cluster distribution shifts upwards along the $\log_{10}(R_{50}/\mathrm{pc})$ with increasing age over the first few tens of Myr, similar to the behaviour seen in the evolutionary tracks of SPHGAL + KETJU models. A visual inspection of the KDE contours in the youngest bins (<10 Myr and 10–30 Myr) may suggest a steep mass–radius relation – potentially even steeper than $R_{50} \propto \mathrm{M}^{1/3}$. However, these age bins are affected by the adopted $\Pi > 1$ selection criterion and are therefore likely subject to selection

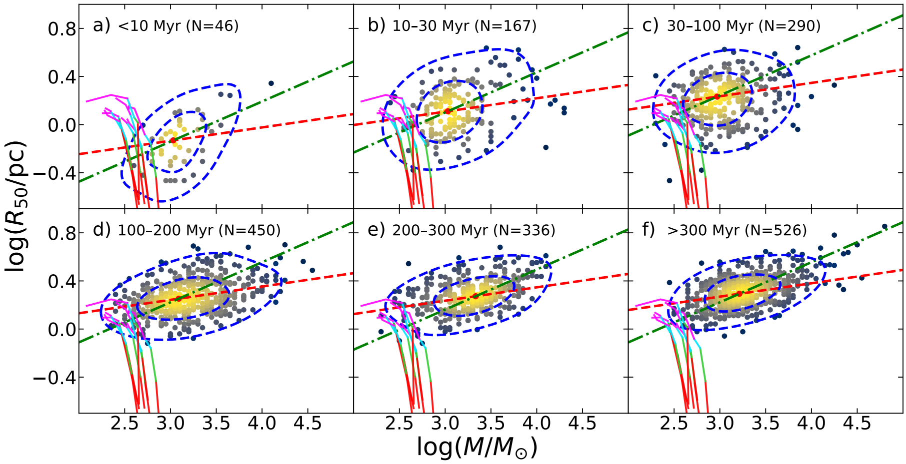

Figure 6.13. Evolution of the cluster mass–radius relation. Each panel shows R_{50} as a function of cluster mass for a different age interval (indicated in each panel). The number shown next to the age interval indicates the sample size. The constant density relation, $R_{50} \propto \mathrm{M}^{1/3}$ (green dash-dotted line), and the equilibrium relation, $R_{50} \propto \mathrm{M}^{1/9}$ (red dashed line), are shown for reference. Blue dashed contours represent KDEs: the inner contour encloses 39.3% of the KDE integral around the KDE peak (1σ region), and the outer contour encloses 86.5% (2σ region). Segment-coloured curves show evolutionary tracks of SPHGAL + KETJU models (Lahén et al. 2025), with colours indicating age ranges: <10 Myr (red), 10–30 Myr (green), 30–100 Myr (cyan), and >100 Myr (magenta). In all panels, only clusters satisfying the $\Pi > 1$ criterion are included.

effects. Although the analytic model of Choksi & Kruijssen (2021) predicts an initially steep relation, $R_{50} \propto \mathrm{M}^{1/2}$, which later evolves towards $R_{50} \propto \mathrm{M}^{1/3}$, and the first two age bins (panels a and b) may appear broadly consistent with this scenario, we cannot robustly confirm such a trend, especially considering that these young clusters are probably undergoing rapid structural evolution and are likely observed at different evolutionary stages. Consequently, we do not find compelling evidence to claim the presence of a pronounced mass–radius relation for clusters younger than 100 Myr (see Fig. 6.13a–c).

However, as observed in Fig. 6.13d–f, a shallow yet clear and significant mass–radius relation emerges for clusters older than ~100 Myr, once the apparent phase of rapid cluster structural evolution settles. The slope visually appears broadly similar across all subsequent age bins beyond 100 Myr, and lies between $R_{50} \propto \mathrm{M}^{1/3}$ and $R_{50} \propto \mathrm{M}^{1/9}$ scaling relations. Notably, the SPHGAL + KETJU evolutionary tracks fall within regions of mass–radius plane compatible with the observed distribution of M 31 disc clusters.

We present a more quantitative analysis of the mass–radius relation for M 31 disc clusters in Fig. 6.14a–b, where clusters are divided into two age groups: 10–100 Myr (panel a) and >100 Myr (panel b). In both cases, the distribution of clusters in the parameter space of $\log_{10}(R_{50}/\mathrm{pc})$ versus $\log_{10}(\mathrm{M}/\mathrm{M}_\odot)$ space is reasonably well approximated by a two-dimensional normal distribution (see blue dashed contours). We therefore characterise it using covariance (or confidence) ellipses derived from the co-

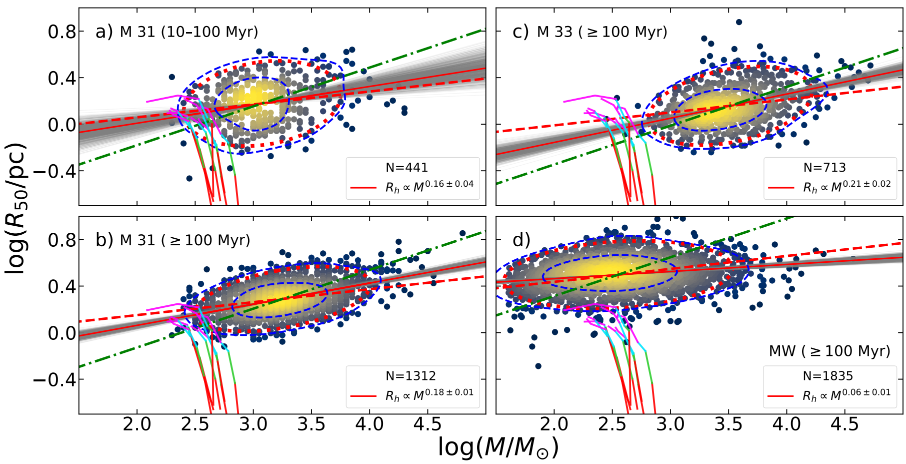

Figure 6.14. Star cluster mass–radius relations. Panel a) shows M 31 clusters with ages 10–100 Myr; panel b) presents M 31 clusters older than 100 Myr. Panel c) shows M 33 clusters older than 100 Myr from the PHATTER star cluster catalogue (Johnson et al. 2022). Panel d) shows the MW clusters older than 100 Myr from the Hunt & Reffert (2024) *Gaia* cluster catalogue (only objects classified as "open clusters" are included). Sample sizes are indicated in the legends. The red dotted lines show the 2σ covariance (confidence) ellipses, while the red solid lines indicate the slopes of their major axes; the numerical values of the slopes are given in the legends as the power-law indices of cluster mass–radius relations. Grey lines show individual slopes obtained from 1000 bootstrap resampling iterations. The constant density relation, $R_{50} \propto \mathrm{M}^{1/3}$ (green dash-dotted line), and the equilibrium relation, $R_{50} \propto \mathrm{M}^{1/9}$ (red dashed line), are shown for reference. Blue dashed contours represent KDEs: inner contour encloses 39.3% (1σ region) of the KDE integral around the KDE peak, and the outer contour encloses 86.5% (2σ region). Segment-coloured curves show evolutionary tracks of `SPHGAL` + `KETJU` models (Lahén et al. 2025), with colours indicating age ranges: <10 Myr (red), 10–30 Myr (green), 30–100 Myr (cyan), and >100 Myr (magenta). In all panels, we consider clusters with ages up to $t \leq 800$ Myr and $\log_{10}(\mathrm{M}/\mathrm{M}_\odot) \leq 5$ that satisfy the $\Pi > 1$ criterion.

variance matrix. The resulting 2σ covariance ellipses are shown as red dotted curves. We define the power-law index of the mass–radius relation as the slope of the major axis of the covariance ellipse. To estimate this slope and its uncertainty, we perform 1000 bootstrap resampling iterations, deriving a slope in each case (grey lines). The final power-law index is taken as the median of these individual slopes (red solid line), with the uncertainty defined as half the 16th-84th percentile range, which we find to be symmetrical.

For the younger clusters (10–100 Myr; Fig. 6.14a), we derive a shallow relation, $R_{50} \propto \mathrm{M}^{0.16\pm0.04}$. However, the uncertainty of the power-law index is relatively large. In addition, this cluster sample may be affected by selection effects associated with the adoption of $\Pi > 1$ threshold. These systems are also likely still undergoing rapid structural evolution and may represent a mixture of populations characterised by different mass–radius relation slopes. Consequently, we cannot confidently claim the presence of a well-defined and clear mass–radius relation in this age range.

For clusters older than 100 Myr, we obtain a more robust relation, $R_{50} \propto \mathrm{M}^{0.18\pm0.01}$ (Fig. 6.14b). In this age range, the $\Pi > 1$ criterion does not remove any objects, and thus no related selection effects are expected. Notably, after evolving for $\sim$100 Myr, SPHGAL + KETJU models occupy a region of parameter space that is compatible with the observed M 31 cluster distribution and the derived mass–radius relation. When the $t \geq 100$ Myr sample is divided into narrower age bins (as shown in Fig. 6.13d–f), the slope shows a slight increase with age: 0.15±0.02 for 100–200 Myr, 0.18±0.02 for 200–300 Myr, and 0.20±0.02 for >300 Myr. However, these values largely overlap within their uncertainties. Moreover, as shown in Figs 5.8 and 5.9, lower-mass clusters with $\mathrm{M} \lesssim 1000\,\mathrm{M}_{\odot}$ are expected to be increasingly affected by selection effects beyond 300 Myr. Therefore, the slight variation in slope could also be influenced by such effects. While this behaviour could hint at a possible weak steepening with age of the mass–radius relation beyond 100 Myr, we are unable to draw a definite conclusion that such a trend exists. Nonetheless, the main result remains that clusters older than 100 Myr in the M 31 disc exhibit a shallow mass–radius relation.

The derived slope for $t \geq 100$ Myr clusters is similar to that found in M 51 by Hwang & Lee (2010) (0.16±0.02), but shallower than relations reported for other individual galaxies outside the Local Group or for star cluster samples combined from multiple nearby galaxies ($R_{50} \propto \mathrm{M}^{0.25-0.33}$; Ryon et al. 2015; Krumholz et al. 2019; Cuevas-Otahola et al. 2021; Brown & Gnedin 2021). It is steeper than the Gieles & Renaud (2016) equilibrium relation ($R_{50} \propto \mathrm{M}^{1/9}$), yet significantly shallower than the $R_{50} \propto \mathrm{M}^{1/2}$ (Choksi & Kruijssen 2021), or $R_{50} \propto \mathrm{M}^{1/3}$ (Grudić et al. 2021) scalings, and slightly shallower than $R_{50} \propto \mathrm{M}^{0.25}$ relation (Grudić et al. 2023a).

We further compare the M 31 disc results with those for other Local Group galaxies. In the right panels of Fig. 6.14, we present mass–radius relations for clusters with $t \geq 100$ Myr in M 33 (Fig. 6.14c) and MW (Fig. 6.14d), derived using the same methodology and based on the cluster catalogues of Johnson et al. (2022) and Hunt & Reffert (2024), respectively. For M 33, we obtain a somewhat steeper but broadly similar relation, $R_{50} \propto \mathrm{M}^{0.21\pm0.02}$, compared to M 31. We note that, the Johnson et al. (2022) M 33 catalogue lacks clusters with $\mathrm{M} \leq 1000\ \mathrm{M}_{\odot}$ compared to the Kriščiūnas et al. (2026) M 31 sample, which may partly account for this difference.

In contrast, the MW shows a significantly shallower relation, $R_{50} \propto \mathrm{M}^{0.06\pm0.01}$, implying that cluster size is virtually independent of mass. This trend is consistent with results reported for some galaxies beyond the Local Group, where very shallow or absent mass–radius relations are found (Zepf et al. 1999; Larsen 2004; Bastian et al. 2005; Scheepmaker et al. 2007; Bastian et al. 2012; Ryon et al. 2017). Within the Local Group, Gatto et al. (2021) examined the core radius, r_c, and its correlation with cluster mass in the Small Magellanic Cloud. They derived the mass–core radius relation $r_c \propto \mathrm{M}^{0.34}$, consistent with the $\mathrm{M}^{1/3}$ scaling (Krumholz et al. 2019; Choksi & Kruijssen 2021; Grudić et al. 2021).

Finally, we examine the environmental/radial dependence of the mass–radius relation within the M 31 disc. In Fig. 6.15, we present clusters older than 100 Myr divided into three radial zones: $\mathrm{R_{GC}} \leq 9$ kpc, $9 < \mathrm{R_{GC}} < 14$ kpc, and $\mathrm{R_{GC}} \geq 14$ kpc. This division separates the three prominent radial rings where most of the studied clusters are located (see Fig. 6.12). For the inner and outer rings (Fig. 6.15a and c) we derive identical relations, $R_{50} \propto \mathrm{M}^{0.18}$. In the most populated middle ring (Fig. 6.15b) we obtain a nearly identical slope $R_{50} \propto \mathrm{M}^{0.19}$. Considering this and uncertainties of

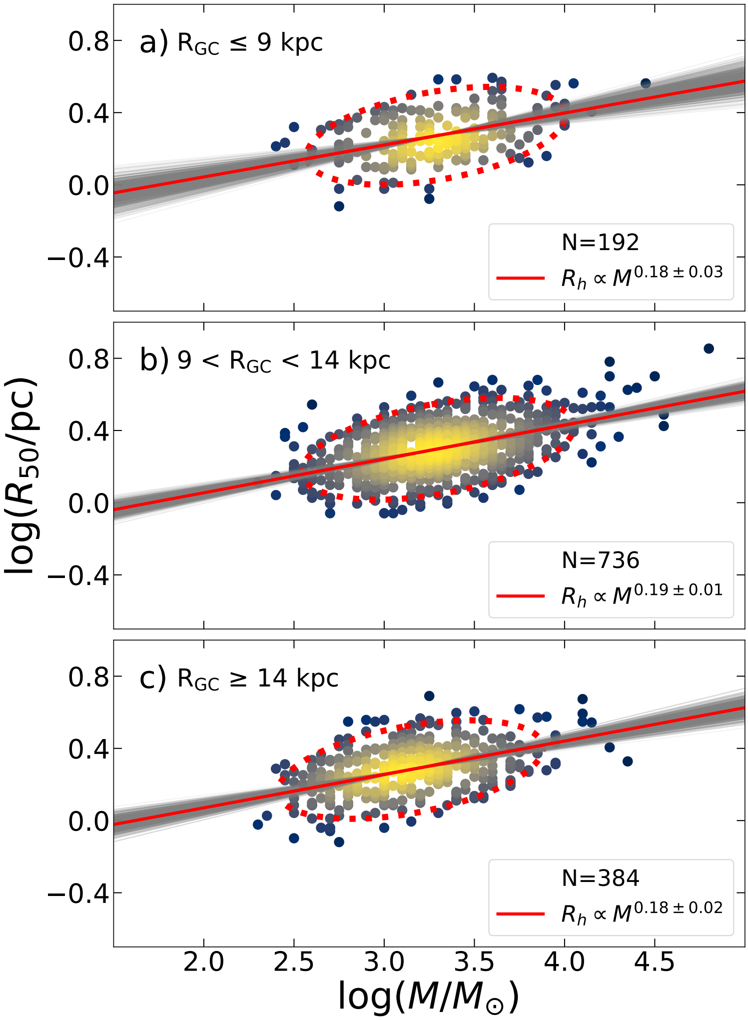

Figure 6.15. Mass–radius relation for M 31 disc clusters older than 100 Myr in three radial zones (indicated in each panel). Sample sizes are indicated in the legends. Red dotted lines show the 2σ covariance (confidence) ellipses, while red solid lines indicate the slopes of their major axes; the numerical values of the slopes are given in the legends as the power-law indices of cluster mass–radius relations. Grey lines show individual slopes obtained from 1000 bootstrap resampling iterations.

derived slopes, we can confidently claim that the mass–radius relation is fully consistent across all three radial zones. We therefore find no evidence for radial variation of the mass–radius relation within the M 31 disc. This further supports the idea that the tidal field gradient (or other environmental differences) across the sampled region is not strong enough to significantly influence cluster sizes on the studied timescales. Such behaviour is expected if clusters are not tidally limited, and their evolution is dominated by internal processes rather than external tidal effects. Alternatively, initial environmental differences could have been erased by efficient radial mixing within the disc. However, as discussed in Section 6.2 (see also Fig. 6.12), clusters likely remain close to their birth locations for at least ∼100 Myr or longer, making this scenario less probable.

Although we cannot draw firm conclusions based on the comparison among M 31, M 33, and MW (Fig. 6.14) – due to differences in instrumentation, cluster parameter determination methods, and sample sizes – the results nevertheless suggest that the cluster mass–radius relation varies substantially within the Local Group. When considered alongside the wide range of relations reported for more distant galaxies (e.g., Zepf et al. 1999; Larsen 2004; Bastian et al. 2005; Hwang & Lee 2010; Bastian et al. 2012; Ryon et al. 2015, 2017; Cuevas-Otahola et al. 2021; Brown & Gnedin 2021), this points towards a strong dependence of the mass–radius relation on galactic environment. Such diversity in scaling relations may arise from differences in physical conditions, including interstellar gas pressure and turbulence, cluster natal gas density and metallicity, tidal field strength and frequency of tidal shocks, as well as other processes governing star formation and cluster evolution. While no environmental dependence is observed within the M 31 disc itself (Fig. 6.15), the broader comparison with other nearby galaxies suggests that environmental effects may become more important when considering global galactic scales. We therefore emphasise the need for further theoretical work to explain these contrasting results and to better understand the origin of the mass–radius relation across diverse galactic disc environments.

6.4 Summary

In the previous Chapters, we established the practical limitations of the aperture photometry method for studying nearby extragalactic star clusters, primarily in the context of the M 31 PHAT survey. Building on this foundation, in this Chapter we analysed the M 31 cluster population at the edge of these limitations. We investigate the structural evolution of star clusters and the correlations between their sizes and other properties (age, mass, and galactocentric distance) in the M 31 disc. Our analysis is based on the Kriščiūnas et al. (2026) catalogue of cluster parameters, derived using adaptive aperture photometry measurements (Naujalis et al. 2021; Kriščiūnas et al. 2023) and photometry of individual resolved stars (Williams et al. 2023). The studied cluster sample comprises 1918 objects younger than 800 Myr.

We found that young clusters in the north-eastern part of the M 31 disc are predominantly compact, with a median half-light radius, $R_{50} \approx 1.8$ pc. This is consistent with earlier results for the south-western disc (Šablevičiūtė et al. 2006, 2007; Vansevičius et al. 2009), indicating that clusters are compact across the entire M 31 disc.

Furthermore, we showed that bound clusters undergo rapid expansion during the first ∼30 Myr, with R_{50} increasing by more than twice. We interpret the observed structural evolution as follows: after early removal of residual natal gas and associated mass loss, initially compact clusters expand rapidly due to internal cluster processes, such as subsequent stellar-evolution-driven mass loss and two-body relaxation, gradually evolving towards a tidally limited, virialised state. Importantly, these results are in good agreement with recent findings for young clusters in the MW by Della Croce et al. (2024), who report rapid and violent cluster expansion on a similar ∼30 Myr timescale based on *Gaia* kinematics.

We detected no significant dependence of cluster size on galactocentric distance. This suggests that the majority of young M 31 disc clusters are not yet tidally limited, and that the galactic field plays only a minor role in their early evolution. This further supports our interpretation that the observed early cluster structural evolution in the M 31 is driven by internal cluster processes. In addition, our results suggest inefficient cluster radial migration over ~100 Myr or possibly even longer timescales, implying that clusters can provide key insight into past star-forming regions over extended periods of time.

Finally, we found a rather uncertain mass–radius relation for clusters younger than 100 Myr. In contrast, clusters older than 100 Myr exhibit a more robust, albeit shallow, relation, $R_{50} \propto M^{0.18\pm0.01}$, with no significant radial dependence. While there are indications of a possible weak steepening beyond 100 Myr, once narrower age intervals are examined, we are unable to confirm genuine existence of such trend. However, this slope, together with the mass–radius relations we derived for M 33 and MW clusters, and those reported in more distant galaxies (e.g., Zepf et al. 1999; Larsen 2004; Bastian et al. 2005; Hwang & Lee 2010; Bastian et al. 2012; Ryon et al. 2015, 2017; Cuevas-Otahola et al. 2021; Brown & Gnedin 2021), highlight the need for further theoretical work to consistently explain a wide range of observed relations, and to better understand cluster formation and evolution across different galactic disc environments.

Conclusions

Since a large fraction of stars forms in clustered environments, star clusters are excellent tracers of the formation and evolution of galactic discs. Aperture photometry is one of the most efficient methods for studying large samples of extragalactic clusters across wide ranges of masses, ages, and environments. This approach, based on comparing observed integrated photometry with theoretical models, has been widely adopted for deriving extragalactic star cluster physical parameters. However, the practical limitations of the method – which are primarily imposed by stochastic and sky background effects – remained to be understood.

In this thesis, we have employed a large set of realistic stochastic star cluster models and their mock observations reproducing the conditions of the M 31 Panchromatic *Hubble* Andromeda Treasury (PHAT) survey (Dalcanton et al. 2012; Johnson et al. 2012, 2015) to investigate these limitations for studies of nearby galactic discs. We first explored idealised background-free conditions in order to determine the intrinsic maximum achievable accuracy limits imposed by stochastic effects in low-mass ($<10^4\,M_\odot$) star clusters.

We showed that clusters containing luminous post main-sequence (PMS) stars exhibit substantially larger scatter and uncertainties in their integrated photometric properties than clusters without such stars. We also demonstrated that adaptive aperture photometry procedures (Naujalis et al. 2021; Kriščiūnas et al. 2023) do not introduce systematic colour gradients and effectively reduce contamination from bright field stars and evolved cluster members, improving the overall consistency of photometric measurements. This supports its application to low-mass cluster studies in nearby galaxies ($\lesssim$5 Mpc) with a careful, case-by-case selection of apertures.

We found that physical parameters of very young star clusters remain difficult to constrain using integrated photometry alone, and CMD fitting methods (e.g., Johnson et al. 2016; Čeponis et al. 2024) are expected to provide more reliable estimates for resolved and semi-resolved systems younger than ~40 Myr. The most robust cluster parameters are therefore likely achieved by combining information obtained from both approaches.

The randomness of viewing angle for low-mass clusters introduces measurable uncertainties of up to ~0.05 mag in colour indices for typical M 31 clusters and up to ~0.1 mag in some individual cases, depending on cluster parameters and aperture setup. For structural parameters the uncertainties due to this effect can reach ~10-20%. However, these effects are generally weaker than those caused by stochastic stellar sampling.

By placing stochastic cluster models into real PHAT background fields, we investigated how sky background affects the accuracy and applicability of aperture photometry. We found that, in a typical M 31 disc environment, reliable age, mass, and extinction estimates, if known metallicity is assumed, can be obtained for clusters with M $\gtrsim$ 1600 $M_{\odot}$ at 1 Gyr and M $\gtrsim$ 500 $M_{\odot}$ at 100 Myr. Meanwhile, photometry is generally accurate enough only for rough age and mass estimates for clusters 500 $\lesssim$ M $\lesssim$ 1600 $M_{\odot}$ at 1 Gyr and 200 $\lesssim$ M $\lesssim$ 500 $M_{\odot}$ at 100 Myr.

We also demonstrated that apertures smaller than the half-light radius, R_{50}, are highly sensitive to stochastic and background effects and should therefore be avoided for colour measurements. For colour measurements of typical-size clusters, the optimal aperture radii are ~(1–2)×R_{50} according to our estimates.

Our analysis showed that catalogue completeness limits and selection effects depend strongly on the local environment within the M 31 disc. At an age of 1 Gyr, the cluster mass function can be reliably recovered down to ~500 $M_{\odot}$ in the sparse outer disc regions, ~1500 $M_{\odot}$ in the star-forming environments, and only ~3000 $M_{\odot}$ in the crowded inner disc. These results demonstrate that environmental completeness variations must be carefully accounted for in studies of star cluster populations.

Using the Kriščiūnas et al. (2026) catalogue of M 31 cluster parameters derived from adaptive aperture photometry (Naujalis et al. 2021; Kriščiūnas et al. 2023) and resolved stellar photometry (Williams et al. 2023), we investigated the structural evolution of star clusters in the M 31 disc at the boundary of the established practical limitations of aperture photometry approach. We showed that bound clusters undergo rapid expansion during the first ~30 Myr, with R_{50} increasing by more than a factor of two, from ~0.6 pc to ~1.6 pc. We detected no significant dependence of cluster size on galactocentric distance, suggesting that most young M 31 disc clusters are not yet tidally limited and that their early evolution is governed primarily by internal processes, such as stellar evolution and internal cluster dynamics. These results are also in good agreement with recent findings by Della Croce et al. (2024) for young clusters in the MW, where rapid and violent cluster expansion on a similar ~30 Myr timescale based on *Gaia* kinematics was found.

Finally, we investigated the M 31 disc cluster mass–radius relation. Our analysis suggests that clusters older than 100 Myr exhibit a shallow mass–radius relation, $R_{50} \propto M^{0.18\pm0.01}$, with no significant radial dependence across the disc. However, it is inconsistent with most of the analytical and numerical models of cluster formation and evolution (Renaud 2018; Choksi & Kruijssen 2021; Grudić et al. 2021, 2023a). Combined with the large variety of mass–radius relation slopes reported in other nearby galaxies (Larsen 2004; Bastian et al. 2005; Hwang & Lee 2010; Bastian et al. 2012; Ryon et al. 2015, 2017; Cuevas-Otahola et al. 2021; Brown & Gnedin 2021), this highlights the necessity of further theoretical work regarding cluster formation and evolution across different galactic disc environments.

Overall, the results of this thesis establish the practical accuracy and applicability limitations of aperture photometry for studies of nearby extragalactic star clusters. We expect these to be useful for planning future surveys, interpreting existing archival data, and developing novel methods for cluster detection and measurement. Meanwhile, our analysis of M 31 cluster sample demonstrates that, when stochastic and background effects are properly accounted for, aperture photometry remains a powerful method for investigating the evolution of star cluster populations and the galactic discs that host them.

Appendix

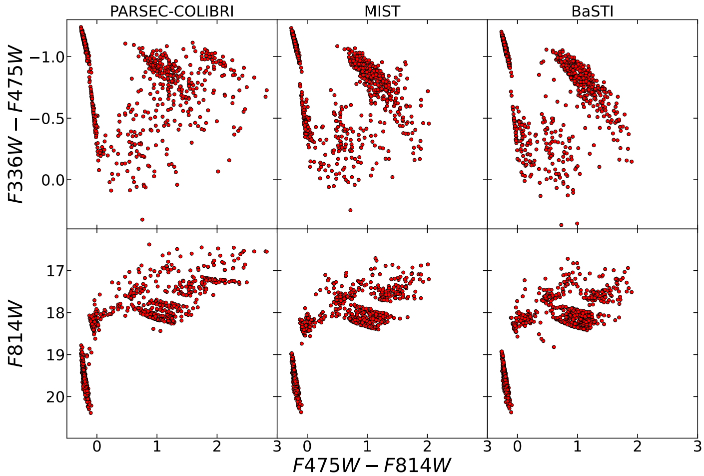

Figure A1. Same as Fig. 3.5, except results are shown for t = 30 Myr cluster models.

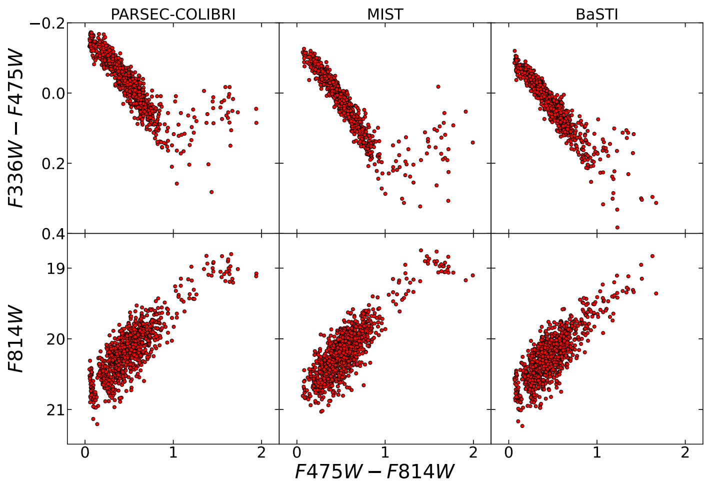

Figure A2. Same as Fig. 3.5, except results are shown for t = 300 Myr cluster models.

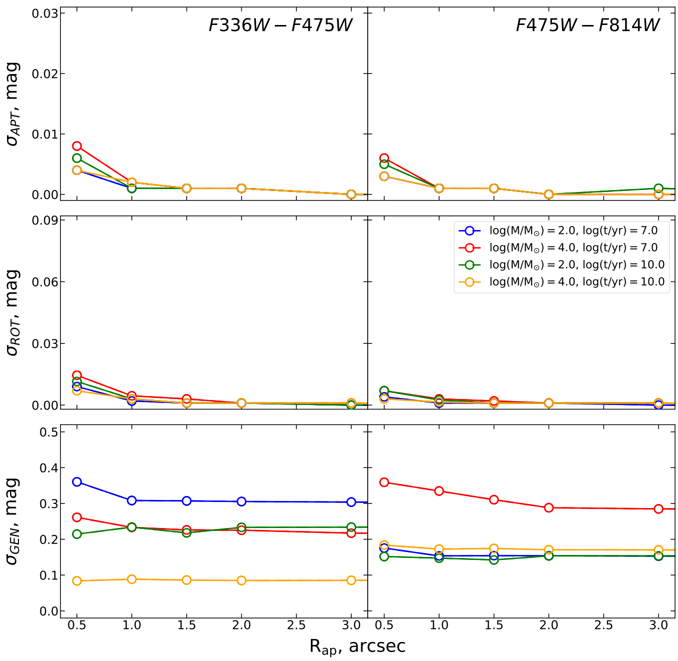

Figure A3. Same as Fig. 4.7, except results are shown for clusters with radial profile parameters $r_c = 0.1''$ and $\gamma = 3.5$.

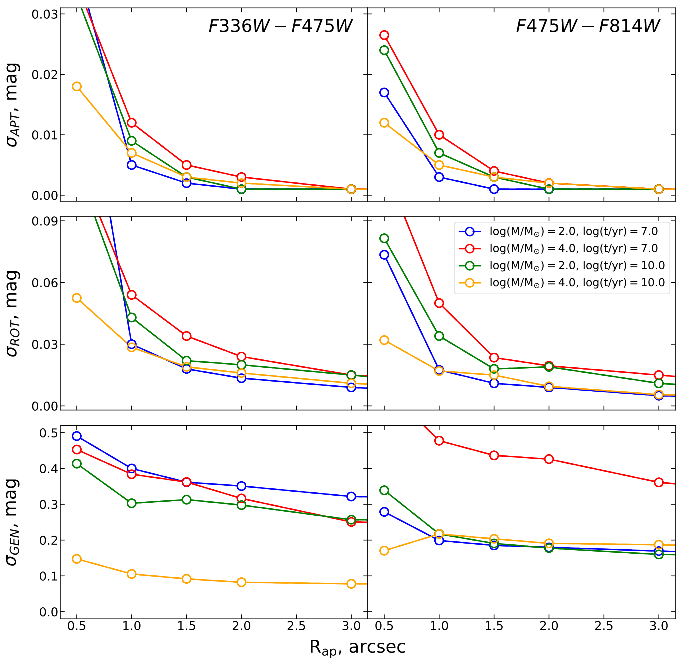

Figure A4. Same as Fig. 4.7, except results are shown for clusters with radial profile parameters $r_c = 0.4''$ and $\gamma = 2.4$.

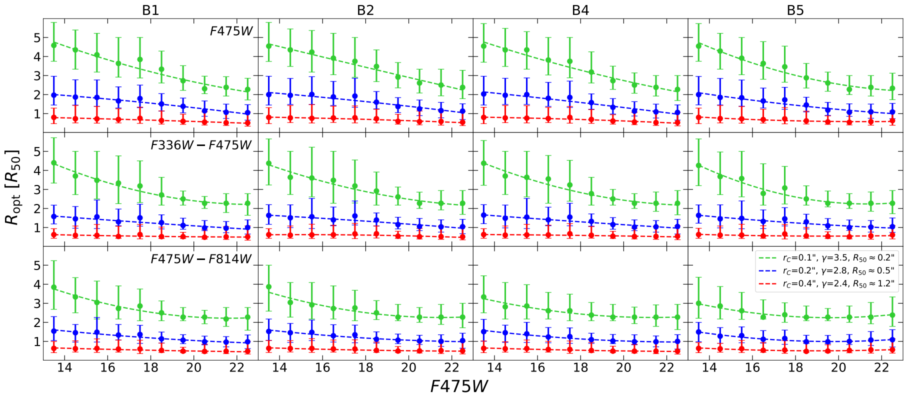

Figure A5. Same as Fig. 5.4, except showing results for other background fields, indicated above each column of panels.

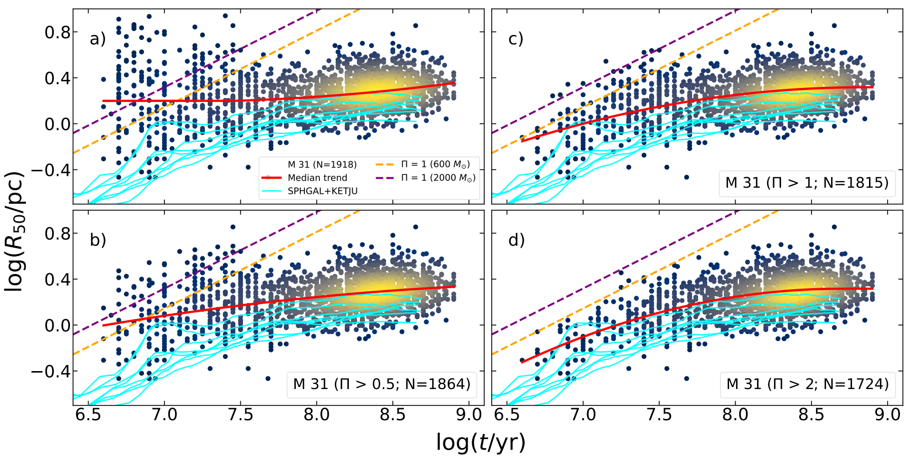

Figure A6. Same as Fig. 6.7, except all panels show results for M 31 but with different Π thresholds applied. Panel a) shows all objects (no Π cut); panel b) shows systems with $\Pi > 0.5$; panel c) $\Pi > 1$; and panel d) $\Pi > 2$.

Bibliography

Aarseth, S. J., Henon, M., & Wielen, R. 1974, A&A, 37, 183

Adamo, A. & Bastian, N. 2015, arXiv e-prints, arXiv:1511.08212

Adamo, A., Ryon, J. E., Messa, M., et al. 2017, ApJ, 841, 131

Adamo, A., Zeidler, P., Kruijssen, J. M. D., et al. 2020, Space Sci. Rev., 216, 69

Anders, P., Bissantz, N., Fritze-v. Alvensleben, U., & de Grijs, R. 2004, MNRAS, 347, 196

Anders, P., Kotulla, R., de Grijs, R., & Wicker, J. 2013, ApJ, 778, 138

Anderson, T. W. & Darling, D. A. 1954, Journal of the American Statistical Association, 49, 765

Astropy Collaboration, Price-Whelan, A. M., Sipőcz, B. M., et al. 2018, AJ, 156, 123

Astropy Collaboration, Robitaille, T. P., Tollerud, E. J., et al. 2013, A&A, 558, A33

Barmby, P., Holland, S., & Huchra, J. P. 2002, AJ, 123, 1937

Barmby, P. & Huchra, J. P. 2001, AJ, 122, 2458

Barmby, P., Huchra, J. P., Brodie, J. P., et al. 2000, AJ, 119, 727

Barmby, P., Perina, S., Bellazzini, M., et al. 2009, AJ, 138, 1667

Bastian, N., Adamo, A., Gieles, M., et al. 2012, MNRAS, 419, 2606

Bastian, N., Gieles, M., Lamers, H. J. G. L. M., Scheepmaker, R. A., & de Grijs, R. 2005, A&A, 431, 905

Bastian, N. & Lardo, C. 2018, ARA&A, 56, 83

Beerman, L. C., Johnson, L. C., Fouesneau, M., et al. 2012, ApJ, 760, 104

Bialopetravičius, J., Narbutis, D., & Vansevičius, V. 2019, A&A, 621, A103

Blaauw, A. 1964, ARA&A, 2, 213

Block, D. L., Bournaud, F., Combes, F., et al. 2006, Nature, 443, 832

Bressan, A., Marigo, P., Girardi, L., et al. 2012, MNRAS, 427, 127

Bressert, E., Bastian, N., Gutermuth, R., et al. 2010, MNRAS, 409, L54

Bridžius, A., Narbutis, D., Stonkutė, R., Deveikis, V., & Vansevičius, V. 2008, Baltic Astronomy, 17, 337

Brodie, J. P. & Strader, J. 2006, ARA&A, 44, 193

Brown, G. & Gnedin, O. Y. 2021, MNRAS, 508, 5935

Caldwell, N., Harding, P., Morrison, H., et al. 2009, AJ, 137, 94

Caldwell, N. & Romanowsky, A. J. 2016, ApJ, 824, 42

Caldwell, N., Schiavon, R., Morrison, H., Rose, J. A., & Harding, P. 2011, AJ, 141, 61

Cantat-Gaudin, T. 2022, Universe, 8, 111

Chandar, R., Whitmore, B. C., Dinino, D., et al. 2016, ApJ, 824, 71

Chemin, L., Carignan, C., & Foster, T. 2009, ApJ, 705, 1395

Chen, Z., Williams, B., Lang, D., et al. 2025, ApJ, 979, 35

Chen, Z., Zhang, K., Williams, B. F., & Durbin, M. 2024, ApJ, 962, 7

Choi, J., Dotter, A., Conroy, C., et al. 2016, ApJ, 823, 102

Choksi, N. & Kruijssen, J. M. D. 2021, MNRAS, 507, 5492

Colman, T. & Teyssier, R. 2020, MNRAS, 492, 4727

Cook, D. O., Lee, J. C., Adamo, A., et al. 2019, MNRAS, 484, 4897

Cuevas-Otahola, B., Mayya, Y. D., Puerari, I., & Rosa-González, D. 2020, MNRAS, 492, 993

Cuevas-Otahola, B., Mayya, Y. D., Puerari, I., & Rosa-González, D. 2021, MNRAS, 500, 4422

da Silva, R. L., Fumagalli, M., & Krumholz, M. 2012, ApJ, 745, 145

Dalcanton, J. J., Williams, B. F., Lang, D., et al. 2012, ApJS, 200, 18

Daugevičius, K., Kriščiūnas, E., Cicėnas, E., Stonkutė, R., & Vansevičius, V. 2024, A&A, 688, A131

Daugevičius, K., Kriščiūnas, E., Stonkutė, R., & Vansevičius, V. 2026, submitted for publication in A&A

Daugevičius, K., Stonkutė, R., Kriščiūnas, E., Cicėnas, E., & Vansevičius, V. 2025, A&A, 699, A290

de Meulenaer, P., Narbutis, D., Mineikis, T., & Vansevičius, V. 2013, A&A, 550, A20

de Meulenaer, P., Narbutis, D., Mineikis, T., & Vansevičius, V. 2014, A&A, 569, A4 de Meulenaer, P., Narbutis, D., Mineikis, T., & Vansevičius, V. 2015, A&A, 574, A66

de Meulenaer, P., Stonkutė, R., & Vansevičius, V. 2017, A&A, 602, A112

De Somma, G., Marconi, M., Ripepi, V., et al. 2025, ApJ, 984, L60

de Vaucouleurs, G., de Vaucouleurs, A., Corwin, Jr., H. G., et al. 1991, Third Reference Catalogue of Bright Galaxies, Vol. 1

Deger, S., Lee, J. C., Whitmore, B. C., et al. 2022, MNRAS, 510, 32

Della Croce, A., Dalessandro, E., Livernois, A., & Vesperini, E. 2024, A&A, 683, A10

Deveikis, V., Narbutis, D., Stonkutė, R., Bridžius, A., & Vansevičius, V. 2008, Baltic Astronomy, 17, 351

Dierickx, M., Blecha, L., & Loeb, A. 2014, ApJ, 788, L38

Dolphin, A. E. 2002, MNRAS, 332, 91

Dotter, A., Bauer, E. B., Park, M., et al. 2026, ApJS, 283, 64

Dreyer, J. L. E. 1888, MmRAS, 49, 1

D'Souza, R. & Bell, E. F. 2018, Nature Astronomy, 2, 737

Elson, R. A. W., Fall, S. M., & Freeman, K. C. 1987, ApJ, 323, 54

Ferguson, A. M. N. & Mackey, A. D. 2016, in Astrophysics and Space Science Library, Vol. 420, Tidal Streams in the Local Group and Beyond, ed. H. J. Newberg & J. L. Carlin, 191

Fioc, M. & Rocca-Volmerange, B. 1997, A&A, 326, 950

Fitzpatrick, E. L. 1999, PASP, 111, 63

Fleck, J. J., Boily, C. M., Lançon, A., & Deiters, S. 2006, MNRAS, 369, 1392

Forbes, D. A., Bastian, N., Gieles, M., et al. 2018, Proceedings of the Royal Society of London Series A, 474, 20170616

Fouesneau, M., Johnson, L. C., Weisz, D. R., et al. 2014, ApJ, 786, 117

Fouesneau, M. & Lançon, A. 2010, A&A, 521, A22

Fouesneau, M., Lançon, A., Chandar, R., & Whitmore, B. C. 2012, ApJ, 750, 60

Fumagalli, M., da Silva, R. L., & Krumholz, M. R. 2011, ApJ, 741, L26

Gaburov, E. & Gieles, M. 2008, MNRAS, 391, 190

Galleti, S., Federici, L., Bellazzini, M., Fusi Pecci, F., & Macrina, S. 2004, A&A, 416, 917

Gatto, M., Ripepi, V., Bellazzini, M., et al. 2021, MNRAS, 507, 3312

Gieles, M. 2009, MNRAS, 394, 2113

Gieles, M. & Portegies Zwart, S. F. 2011, MNRAS, 410, L6

Gieles, M. & Renaud, F. 2016, MNRAS, 463, L103

Gordon, K. D., Bailin, J., Engelbracht, C. W., et al. 2006, ApJ, 638, L87

Gouliermis, D. A. 2018, PASP, 130, 072001

Grudić, M. Y., Hafen, Z., Rodriguez, C. L., et al. 2023a, MNRAS, 519, 1366

Grudić, M. Y., Kruijssen, J. M. D., Faucher-Giguère, C.-A., et al. 2021, MNRAS, 506, 3239

Grudić, M. Y., Offner, S. S. R., Guszejnov, D., Faucher-Giguère, C.-A., & Hopkins, P. F. 2023b, The Open Journal of Astrophysics, 6, 48

Hammer, F., Yang, Y. B., Amram, P., et al. 2025, A&A, 694, A16

Hammer, F., Yang, Y. B., Wang, J. L., et al. 2018, MNRAS, 475, 2754

Heggie, D. & Hut, P. 2003, The Gravitational Million-Body Problem: A Multidisciplinary Approach to Star Cluster Dynamics

Hertzsprung, E. 1911, Publikationen des Astrophysikalischen Observatoriums zu Potsdam, 63

Hidalgo, S. L., Pietrinferni, A., Cassisi, S., et al. 2018, ApJ, 856, 125

Hodge, P., Krienke, O. K., Bianchi, L., Massey, P., & Olsen, K. 2010, PASP, 122, 745

Hodge, P. W. 1979, AJ, 84, 744

Hodge, P. W., Krienke, O. K., Bellazzini, M., et al. 2009, AJ, 138, 770

Hunt, E. L., Cantat-Gaudin, T., Anders, F., et al. 2026, A&A, 706, A341

Hunt, E. L. & Reffert, S. 2024, A&A, 686, A42

Hunter, J. D. 2007, Computing in Science & Engineering, 9, 90

Hwang, N. & Lee, M. G. 2010, ApJ, 709, 411

Johnson, L. C., Seth, A. C., Dalcanton, J. J., et al. 2016, ApJ, 827, 33

Johnson, L. C., Seth, A. C., Dalcanton, J. J., et al. 2017, ApJ, 839, 78

Johnson, L. C., Seth, A. C., Dalcanton, J. J., et al. 2012, ApJ, 752, 95

Johnson, L. C., Seth, A. C., Dalcanton, J. J., et al. 2015, ApJ, 802, 127

Johnson, L. C., Wainer, T. M., Torresvillanueva, E. E., et al. 2022, ApJ, 938, 81

Jørgensen, T. G. & Church, R. P. 2025, MNRAS, 543, 1410

Kang, Y., Rey, S.-C., Bianchi, L., et al. 2012, ApJS, 199, 37

Kharchenko, N. V., Piskunov, A. E., Schilbach, E., Röser, S., & Scholz, R.-D. 2013, A&A, 558, A53

Kim, S. C., Lee, M. G., Geisler, D., et al. 2007, AJ, 134, 706

King, I. 1962, AJ, 67, 471

Knutas, A., Adamo, A., Pedrini, A., et al. 2025, ApJ, 993, 13

Kodaira, K., Vansevičius, V., Bridzius, A., et al. 2004, PASJ, 56, 1025

Krause, M. G. H., Offner, S. S. R., Charbonnel, C., et al. 2020, Space Sci. Rev., 216, 64

Krienke, O. K. & Hodge, P. W. 2007, PASP, 119, 7

Krienke, O. K. & Hodge, P. W. 2008, PASP, 120, 1

Kriščiūnas, E., Daugevičius, K., Stonkutė, R., & Vansevičius, V. 2023, A&A, 677, A100

Kriščiūnas, E., Stonkutė, R., Daugevičius, K., & Vansevičius, V. 2026, submitted for publication in ApJS

Kroupa, P. 2001, MNRAS, 322, 231

Kruijssen, J. M. D., Pfeffer, J. L., Reina-Campos, M., Crain, R. A., & Bastian, N. 2019, MNRAS, 486, 3180

Krumholz, M. R., Fumagalli, M., da Silva, R. L., Rendahl, T., & Parra, J. 2015, MNRAS, 452, 1447

Krumholz, M. R., McKee, C. F., & Bland-Hawthorn, J. 2019, ARA&A, 57, 227

Lada, C. J. & Lada, E. A. 2003, ARA&A, 41, 57

Lahén, N., Rantala, A., Naab, T., et al. 2025, MNRAS, 538, 2129

Lamers, H. J. G. L. M. 2009, Ap&SS, 324, 183

Larsen, S. S. 1999, A&AS, 139, 393

Larsen, S. S. 2004, A&A, 416, 537

Lee, J. C., Whitmore, B. C., Thilker, D. A., et al. 2022, ApJS, 258, 10

Lee, M. G., Chandar, R., & Whitmore, B. C. 2005, AJ, 130, 2128

Leitherer, C., Schaerer, D., Goldader, J. D., et al. 1999, ApJS, 123, 3

Lewis, A. R., Dolphin, A. E., Dalcanton, J. J., et al. 2015, ApJ, 805, 183

Livernois, A., Vesperini, E., Tiongco, M., Varri, A. L., & Dalessandro, E. 2021, MNRAS, 506, 5781

Mackey, A. D. & Gilmore, G. F. 2003a, MNRAS, 338, 120

Mackey, A. D. & Gilmore, G. F. 2003b, MNRAS, 338, 85

Mahalanobis, P. C. 1936, Proceedings of the National Institute of Sciences of India, 2, 49

Maíz Apellániz, J. 2009, ApJ, 699, 1938

Marigo, P., Girardi, L., Bressan, A., et al. 2017, ApJ, 835, 77

Maschmann, D., Lee, J. C., Thilker, D. A., et al. 2024, ApJS, 273, 14

McConnachie, A. W., Irwin, M. J., Ferguson, A. M. N., et al. 2005, MNRAS, 356, 979

McLaughlin, D. E. & van der Marel, R. P. 2005, ApJS, 161, 304

Mora, M. D., Larsen, S. S., Kissler-Patig, M., Brodie, J. P., & Richtler, T. 2009, A&A, 501, 949

Narbutis, D., Bridžius, A., Stonkutė, R., & Vansevičius, V. 2007a, Baltic Astronomy, 16, 421

Narbutis, D., Semionov, D., Stonkutė, R., et al. 2014, A&A, 569, A30

Narbutis, D., Vansevičius, V., Kodaira, K., Bridžius, A., & Stonkutė, R. 2007b, Baltic Astronomy, 16, 409

Narbutis, D., Vansevičius, V., Kodaira, K., Bridžius, A., & Stonkutė, R. 2008, ApJS, 177, 174

Naujalis, R., Stonkutė, R., & Vansevičius, V. 2021, A&A, 654, A6

Nony, T., Robitaille, J.-F., Motte, F., et al. 2021, A&A, 645, A94

Pandey, P. & Saha, K. 2025, ApJS, 276, 52

Pedrini, A., Adamo, A., Calzetti, D., et al. 2026, Nature Astronomy

Peng, C. Y., Ho, L. C., Impey, C. D., & Rix, H.-W. 2002, AJ, 124, 266

Peng, C. Y., Ho, L. C., Impey, C. D., & Rix, H.-W. 2010, AJ, 139, 2097

Perina, S., Cohen, J. G., Barmby, P., et al. 2010, A&A, 511, A23

Perryman, M. A. C., Lindegren, L., Kovalevsky, J., et al. 1997, A&A, 323, L49

Pfalzner, S., Kirk, H., Sills, A., et al. 2016, A&A, 586, A68

Platais, I., Kozhurina-Platais, V., & van Leeuwen, F. 1998, AJ, 116, 2423

Plunkett, A. L., Fernández-López, M., Arce, H. G., et al. 2018, A&A, 615, A9

Portegies Zwart, S. F., McMillan, S. L. W., & Gieles, M. 2010, ARA&A, 48, 431

Puzia, T. H., Perrett, K. M., & Bridges, T. J. 2005, A&A, 434, 909

Rappenglück, M. A. 2001, Earth Moon and Planets, 85, 391

Renaud, F. 2018, New A Rev., 81, 1

Robitaille, T. & Bressert, E. 2012, APLpy: Astronomical Plotting Library in Python, Astrophysics Source Code Library, record ascl:1208.017

Russell, H. N. 1914, Popular Astronomy, 22, 275

Ryon, J. E., Bastian, N., Adamo, A., et al. 2015, MNRAS, 452, 525

Ryon, J. E., Gallagher, J. S., Smith, L. J., et al. 2017, ApJ, 841, 92

San Roman, I., Sarajedini, A., Garnett, D. R., & Holtzman, J. A. 2009, ApJ, 699, 839

San Roman, I., Sarajedini, A., Holtzman, J. A., & Garnett, D. R. 2012, MNRAS, 426, 2427

Schechter, P. 1976, ApJ, 203, 297

Scheepmaker, R. A., Haas, M. R., Gieles, M., et al. 2007, A&A, 469, 925

Skrutskie, M. F., Cutri, R. M., Stiening, R., et al. 2006, AJ, 131, 1163

Stetson, P. B. 1987, PASP, 99, 191

Tenjes, P., Tuvikene, T., Tamm, A., Kipper, R., & Tempel, E. 2017, A&A, 600, A34

Thilker, D. A., Whitmore, B. C., Lee, J. C., et al. 2022, MNRAS, 509, 4094

Thob, A., Sanderson, R., Williams, B., et al. 2025, in American Astronomical Society Meeting Abstracts, Vol. 246, 246th Meeting of the American Astronomical Society, 212.03

Tody, D. 1986, in Society of Photo-Optical Instrumentation Engineers (SPIE) Conference Series, Vol. 627, Instrumentation in astronomy VI, ed. D. L. Crawford, 733

Trumpler, R. J. 1930, Lick Observatory Bulletin, 420, 154

van der Marel, R. P., Fardal, M. A., Sohn, S. T., et al. 2019, ApJ, 872, 24

Vansevičius, V., Kodaira, K., Narbutis, D., et al. 2009, ApJ, 703, 1872

Vazdekis, A., Sánchez-Blázquez, P., Falcón-Barroso, J., et al. 2010, MNRAS, 404, 1639

Čeponis, M., Stonkutė, R., & Vansevičius, V. 2024, Lithuanian Journal of Physics, 64

Virtanen, P., Gommers, R., Oliphant, T. E., et al. 2020, Nature Methods, 17, 261

Šablevičiūtė, I., Vansevičius, V., Kodaira, K., et al. 2006, Baltic Astronomy, 15, 547

Šablevičiūtė, I., Vansevičius, V., Kodaira, K., et al. 2007, Baltic Astronomy, 16, 397

Wainer, T. M., Johnson, L. C., Seth, A. C., et al. 2022, ApJ, 928, 15

West, M. J., Côté, P., Marzke, R. O., & Jordán, A. 2004, Nature, 427, 31

Whitmore, B. C. 2009, Ap&SS, 324, 163

Whitmore, B. C., Chandar, R., Lee, J., et al. 2020, ApJ, 889, 154

Whitmore, B. C., Chandar, R., Lee, J. C., et al. 2023, MNRAS, 520, 63

Williams, B. F. 2022, Roman Infrared Nearby Galaxies Survey, NASA Proposal ID. 22-ROMAN22-0013

Williams, B. F., Dalcanton, J. J., Dolphin, A. E., et al. 2015, ApJ, 806, 48

Williams, B. F., Durbin, M., Lang, D., et al. 2023, ApJS, 268, 48

Williams, B. F., Durbin, M. J., Dalcanton, J. J., et al. 2021, ApJS, 253, 53

Williams, B. F. & Hodge, P. W. 2001a, ApJ, 559, 851

Williams, B. F. & Hodge, P. W. 2001b, ApJ, 548, 190

Williams, B. F., Lang, D., Dalcanton, J. J., et al. 2014, ApJS, 215, 9

Worthey, G. 1994, ApJS, 95, 107

Xu, F., Wang, K., Liu, T., et al. 2024, ApJS, 270, 9

Zepf, S. E., Ashman, K. M., English, J., Freeman, K. C., & Sharples, R. M. 1999, AJ, 118, 752

Zhang, Y., Tanaka, K. E. I., Tan, J. C., et al. 2022, ApJ, 936, 68

Zheng, Y., Yang, Y., Zhang, Y.-K., et al. 2025, ApJS, 279, 12

Zhou, J. W., Dib, S., & Kroupa, P. 2026, arXiv e-prints, arXiv:2603.11782

Santrauka

Įvadas ir motyvacija

Remiantis šiuolaikinėmis žiniomis, manoma, kad bent jau vietinėje Visatoje didelė dalis žvaigždžių gimsta galaktikų diskuose esančiuose žvaigždžių spiečiuose (Lada & Lada 2003). Tai tankūs žvaigždžių telkiniai, susiformuojantys tankiausiose kolapsuojančio molekulinių dujų debesies srityse. Dauguma šių žvaigždžių sistemų suyra per pirmąsias kelias dešimtis milijonų metų po susiformavimo (Lada & Lada 2003; Bressert et al. 2010; Portegies Zwart et al. 2010; Krumholz et al. 2019) ir taip papildo bei formuoja bendrą galaktikos žvaigždžių populiaciją. Tik nedidelė gravitaciškai susietų žvaigždžių spiečių dalis išgyvena ilgiau – dešimtis ar šimtus milijonų metų (Lamers 2009; Whitmore 2009). Todėl šių ilgai gyvuojančių sistemų tyrimai padeda geriau suprasti žvaigždėdaros procesus, taip pat galaktikų diskų formavimąsi ir evoliuciją, kadangi spiečiai suteikia informaciją apie ilgalaikę savo galaktikos žvaigždėdaros istoriją.

Nors natūralu tikėtis, kad išsamiausi žvaigždžių spiečių tyrimai turėtų būti įmanomi Paukščių Take (PT), mūsų Galaktikoje tokie tyrimai galimi tik palyginti nedidelėje kelių kiloparsekų (kpc) spindulio erdvėje (Kharchenko et al. 2013; Hunt & Reffert 2024). To priežastis yra Saulės sistemos padėtis Galaktikos diske, kur matomumą riboja stipri tarpžvaigždinė ekstinkcija – diske esančių dulkelių sukeliama šviesos sugertis ir sklaida. Todėl, siekiant geriau suprasti žvaigždžių spiečių formavimąsi ir evoliuciją platesniame aplinkos sąlygų ir spiečių parametrų diapazone, itin svarbūs yra užgalaktinių (esančių kitose galaktikose) žvaigždžių spiečių tyrimai.

Vienas efektyviausių tokių tyrimų metodų yra apertūrinė fotometrija, įgalinanti nustatyti fizinius ir struktūrinius žvaigždžių spiečių parametrus, remiantis jų integralinio šviesio matavimais. Šis metodas suteikia galimybę efektyviai analizuoti dideles spiečių imtis, todėl yra ypač naudingas atliekant artimų galaktikų diskų tyrimus. Vis dėlto integralinei fotometrijai būdingi reikšmingi neapibrėžtumai ir sistematiniai nuokrypiai, susiję su sudėtingais stochastiniais bei dangaus fono efektais. Nors šioms problemoms spręsti ir jų poveikiui mažinti buvo sukurti įvairūs nauji metodai (pvz. de Meulenaer et al. 2013, 2017; Naujalis et al. 2021), iki šiol trūko išsamaus ir homogeniško tyrimo, kuris visapusiškai atskleistų apertūrinės fotometrijos praktines ribas užgalaktinių žvaigždžių spiečių tyrimų kontekste.

Atsižvelgiant į minėtą mokslinę problematiką, šios disertacijos tikslas yra dvejopas. Pirma, siekiame nustatyti apertūrinės fotometrijos tikslumo ir pritaikomumo ribas artimų užgalaktinių spiečių tyrimuose. Tam naudojame stochastinius spiečių modelius ir realistiškus sintetinius jų stebėjimus, atitinkančius realių Andromedos galaktikos (M 31) spiečių vaizdus Panchromatic *Hubble* Andromeda Treasury apžvalgoje (PHAT; Dalcanton et al. 2012; Johnson et al. 2015). Dėmesys M 31 galaktikai ir PHAT apžvalgai grindžiamas M 31 artumu bei išskirtine PHAT duomenų kokybe ir erdvine skiriamąja geba, o tai suteikia unikalią galimybę detaliai tirti užgalaktinius spiečius spiralinėje galaktikoje, panašioje į PT. Šio darbo rezultatai bus naudingi interpretuojant esamus stebėjimus ir planuojant būsimas apžvalgas.

Antrasis šios disertacijos tikslas – ištirti M 31 disko žvaigždžių spiečių populiaciją atsižvelgiant į šias metodologines ribas. Analizuojant šią populiaciją siekiama geriau suprasti žvaigždžių spiečių formavimąsi ir evoliuciją M 31 ir kitose spiralinėse galaktikose, panašiose į PT. Šis tyrimas taip pat demonstruoja apertūrine fotometrija grįstų žvaigždžių spiečių tyrimų mokslinį potencialą ir išryškina pagrindines kryptis, kuriomis būtina tolesnė teorinių modelių, stebėjimų ir tyrimų metodologijos pažanga.

Darbo tikslas

Nustatyti apertūrinės fotometrijos taikymo ribas žvaigždžių spiečiams artimų galaktikų diskuose ir ištirti Andromedos galaktikos (M 31) spiečių struktūrinę evoliuciją.

Uždaviniai

- Sukurti platų stochastinių žvaigždžių spiečių modelių tinklą ir atlikti daugiaspalvius jo objektų matavimus.
- Nustatyti žvaigždžių spiečių apertūrinės fotometrijos taikymo ribas, kurias lemia stochastiniai efektai.
- Nustatyti dangaus fono įtaką spiečių apertūrinės fotometrijos tikslumui.
- Ištirti M 31 disko spiečių struktūros evoliuciją iki 800 Myr.

Rezultatai ir ginamieji teiginiai

1. Charakteringų mažos masės ($\lesssim 10^3 M_\odot$) žvaigždžių spiečių atveju, stebėjimo kampo stochastiškumas sukelia paklaidas iki $\sim$0.05 mag spalvos rodikliams ir iki 20% struktūriniams parametrams.
2. Tipiniuose M 31 PHAT laukuose patikimas spiečių amžiaus, masės ir ekstinkcijos nustatymas (žinant metalingumą) yra įmanomas 100 Myr amžiaus spiečams, kurių masė yra $M \gtrsim 500\,M_\odot$, ir 1 Gyr amžiaus spiečiams, kurių masė yra $M \gtrsim 1600\,M_\odot$.
3. Spiečių spalvos rodiklių matavimams naudojamų apertūrų spinduliai turi būti didesni už jų pusės šviesio spindulį (R_{50}); tipiniams M 31 disko spiečiams optimali apertūros spindulio vertė siekia iki $2\times R_{50}$.
4. M 31 spiečių masės funkcija ties 1 Gyr gali būti patikimai atkurta iki: $\sim$500 $M_\odot$ išoriniame diske; $\sim$1500 $M_\odot$ žvaigždėdaros srityse; $\sim$3000 $M_\odot$ centrinėje dalyje.
5. M 31 disko spiečiai iš pradžių yra kompaktiški, tačiau per pirmuosius $\sim$30 Myr, sparčiai plečiasi – jų R_{50} padidėja daugiau nei du kartus.
6. Senesni nei 100 Myr M 31 disko spiečiai pasižymi silpnu masės–spindulio sąryšiu, kuris nepriklauso nuo atstumo iki galaktos centro: $R_{50} \propto M^{0.18\pm0.01}$.

Autoriaus indėlis

Autorius sukūrė programas, reikalingas žvaigždžių spiečių modeliavimui ir apertūrinės fotometrijos stebėjimų matavimams. Autorius taip pat parengė testavimui fono laukus. Šioje disertacijoje pateiktus dirbtinių ir M 31 disko spiečių matavimus atliko autorius. Matavimų rezultatai buvo interpretuojami kartu su bendraautoriais. Autorius yra trijų publikacijų, sudarančių šios disertacijos pagrindą, pirmasis autorius. Be to, kaip bendraautorius prisidėjo prie dviejų publikacijų, skirtų M 31 žvaigždžių spiečių apertūrinės fotometrijos ir spiečių fizinių parametrų katalogų sukūrimui.

1 skyrius

Žvaigždžių spiečiai vietinėje Visatoje

Esminė problema pradedant tyrinėti žvaigždžių spiečius, yra tai, kaip šios sistemos turėtų būti apibrėžtos. Literatūroje pateikiama daugybė įvairių apibrėžimų ir bendro konkretaus sutarimo šiuo klausimu nėra. Spiečių apibrėžimo problematika išsamiai aptarta Krumholz et al. (2019) ir Krause et al. (2020) apžvalgose. Šios disertacijos kontekste mes naudojame minėtuose darbuose pasiūlytą apibrėžimą: žvaigždžių spiečius yra gravitaciškai surišta žvaigždžių grupė, kurią sudaro bent 12 žvaigždžių ir joje nedominuoja tamsioji materija. Toks apibrėžimas atskiria spiečius nuo daugianarių žvaigždžių sistemų ir galaktikų, taipogi reikalauja, kad toks objektas užimtų erdvės sritį, kurioje dominuoja spiečiaus savigravitacija, o ne išorinių potvyninių jėgų poveikis. Dvylikos žvaigždžių riba yra sąlyginė, kur pereinama nuo kelių kūnų prie daugelio (N-)kūnų žvaigždžių sistemų dinamikos.

Šiuolaikinės žinios apie žvaigždžių spiečius ir jų svarbą tiriant platų spektrą astrofizikinių procesų yra plačiai aptartos pastarojo dešimtmečio apžvalginiuose straipsniuose (pvz. Bastian & Lardo 2018; Renaud 2018; Krumholz et al. 2019; Adamo et al. 2020; Krause et al. 2020). Žvaigždžių spiečiai formuojasi tankiuose milžiniškų molekulinių debesų (GMC) regionuose, kai gravitacinio kolapso metu dujos virsta žvaigždėmis. Žvaigždėdara galiausiai sustoja dėl jaunų masyvių žvaigždžių išsklaidančių likusias dujas. Tankiausiuose regionuose, kur žvaigždėdaros efektyvumas gali būti pakankamai didelis, dalis susiformavusios sistemos gali išlikti gravitaciškai surišta. Naujausi tyrimai (Knutas et al. 2025; Pedrini et al. 2026) rodo, kad spiečiai išsivalo nuo likusių dujų per $\sim$5–10 Myr. Pirmuosius $\sim$100 Myr jų raidą daugiausia lemia stiprios potvyninės sąveikos gimtuosiuose žvaigždėdaros regionuose ir masės netekimas dėl žvaigždžių evoliucijos. Vėliau dominuoja dviejų kūnų relaksacijos procesai ir atsitiktiniai susidūrimai su GMC. Nors dauguma spiečių suyra per pirmuosius $\sim$10 Myr (Lada & Lada 2003; Lamers 2009; Whitmore 2009; Bressert et al. 2010), išgyvenę išsaugo informaciją apie galaktikos žvaigždėdaros istoriją ir dinaminę evoliuciją.

Detali užgalaktinių spiečių analizė tapo įmanoma tik per kelis pastaruosius dešimtmečius. Tai daugiausia susiję su *Hubble* kosminio teleskopo veikla. Ankstesnis supratimas apie spiečius didele dalimi rėmėsi PT tyrimais. Istoriškai PT žvaigždžių spiečiai skirstomi į du pagrindinius tipus: padrikuosius (OC) ir kamuolinius (GC) spiečius.

OC randami diske, jie paprastai yra jaunesni nei $\lesssim$10 Gyr, mažos masės ($\lesssim 10^4$ $M_\odot$). Mūsų nagrinėjami jauniausi disko spiečiai iš esmės atitinka OC populiaciją. Su jauniausiais OC ($\lesssim$100 Myr) glaudžiai susiję žvaigždžių asociacijos – panašios, bet gravitaciškai nesurištos, labiau išplitusios sistemos (Blaauw 1964; Gieles & Portegies Zwart 2011; Gouliermis 2018; Adamo et al. 2020; Krause et al. 2020). Tuo tarpu GC yra seni ($\gtrsim$10 Gyr), masyvūs ($M \gtrsim 10^4$ $M_\odot$) ir daugiausia randami Galaktikos hale bei baldže. Jie suteikia svarbios informacijos apie Galaktikos formavimąsi ir evoliuciją kosmologiniais laiko masteliais (West et al. 2004; Brodie & Strader 2006; Forbes et al. 2018; Kruijssen et al. 2019; Krause et al. 2020).

Ilgą laiką abu spiečių tipai laikyti paprastomis žvaigždžių populiacijomis (SSP), tai reiškia, kad susiformavo vieno žvaigždėdaros žybsnio metu ir visos žvaigždės yra tuo paties amžiaus bei cheminės sudėties. Tačiau dabar žinoma, kad dauguma GC turi kelias žvaigždžių populiacijas. Tuo tarpu, OC atveju yra duomenų, kad tokia prielaida teisinga (Bastian & Lardo 2018). Tai rodo, kad tradicinis OC–GC skirstymas nėra universalus, nors vis dar plačiai naudojamas net ir užgalaktinių spiečių tyrimuose.

Dėl Saulės sistemos padėties Galaktikos diske, PT disko spiečių tyrimai yra labai apriboti didelės tarpžvaigždinės ekstinkcijos ir su tuo susijusių selekcijos efektų (Hunt et al. 2026). Todėl norint suprasti globalius dėsningumus, įvairius sąryšius tarp spiečių savybių, aplinkos įtaką ir apskritai geriau suvokti spiečių formavimąsi bei evoliucija, būtini užgalaktinių spiečių tyrimai.

Vietinės grupės galaktikų diskuose esantys spiečiai buvo tirti ne kartą (pvz. Vansevičius et al. 2009; San Roman et al. 2012; Johnson et al. 2016, 2017; Gatto et al. 2021; Wainer et al. 2022), tačiau šios galaktikos danguje užima didelį plotą ir HST stebėjimams reikia labai daug laiko. Dėl to homogeniškų tyrimų, apimančių statistiškai dideles spiečių imtis nėra daug. Dauguma išsamesnių tyrimų buvo atliekami už Vietinės grupės ribų, tačiau jie apima tik gana masyvius spiečius ($\gtrsim 10^{3.5}$ $M_\odot$). Tad nepaisant keblumų, Vietinės grupės tyrimai yra labai reikalingi norint suprasti mažos masės spiečių, kurie sudaro daugumą tokių objektų, formavimąsi ir evoliuciją.

M 31 yra artimiausia reguliari spiralinė galaktika (Hammer et al. 2025). Dėl nedidelio atstumo (~785 kpc) HST išskiria atskiras jos žvaigždes ir spiečius, todėl M 31 yra viena geriausių laboratorijų žvaigždžių spiečių evoliucijai tirti. Ilgą laiką M31 spiečių tyrimai apsiribojo GC populiaciją (Barmby & Huchra 2001; Barmby et al. 2002; Galleti et al. 2004; Caldwell et al. 2009, 2011), o detalūs disko spiečių tyrimai tapo įmanomi tik su HST (Williams & Hodge 2001b,a; Hodge et al. 2009, 2010). Pirmasis homogeniškas M 31 disko spiečių tyrimas (Kodaira et al. 2004; Narbutis et al. 2008; Vansevičius et al. 2009), apimantis didelį plotą pietvakarinėje galaktikos dalyje, buvo atliktas antžeminiu Subaru teleskopu. Šis tyrimas parodė, kad M 31 disko spiečiai skiriasi nuo PT spiečių ir yra labai kompaktiški – tipinis pusės šviesio spindulys ~1.5 pc.

Didelė pažanga pasiekta atlikus PHAT (Panchromatic *Hubble* Andromeda Treasury) apžvalgą (Dalcanton et al. 2012). Ji apima apie trečdalį viso disko, iki maždaug 20 kpc nuo galaktikos centro. Stebėjimai atlikti šešiose fotometrinėse juostose, kurios aprėpia plačią spektrinę sritį: artimą UV ($F275W$ ir $F336W$), optinę ($F475W$ ir $F814W$) ir artimą IR ($F110W$ and $F160W$). PHAT spiečių kataloge (Johnson et al. 2015) identifikuota daugiau nei 2700 kandidatų, jų duomenys panaudoti M 31 spiečių populiacijos tyrimams (Johnson et al. 2016, 2017; de Meulenaer et al. 2017). Panašus projektas įgyvendintas ir pietvakarinėje M 31 dalyje (PHAST; Chen et al. 2025), todėl galima tikėtis proveržio tiriant M 31 žvaigždžių spiečius.

2 skyrius

Žvaigždžių spiečių apertūrinė fotometrija

2.1 Standartinė apertūrinė fotometrija

Apertūrinė fotometrija – vienas efektyviausių plačiai taikomų metodų, įgalinančių tirti dideles užgalaktinių žvaigždžių spiečių imtis. Šio metodo pagrindas yra spiečiaus spinduliuotės srauto matavimas apertūroje. Svarbus tokių matavimų aspektas – tikslus fono lygio atėmimas, kadangi į apertūrą patenka taip pat ir fono – ne spiečiaus objektų – skleidžiamas signalas. Baigtinio dydžio apertūra nesurenka viso spiečiaus spinduliuotės srauto, todėl norint nustatyti pilnutinį integralinį srautą, yra apskaičiuojama apertūrinė korekcija, naudojant augimo kreivę (kumuliatyvus radialinis srauto profilis), dirbtinius spiečius, ar empirinius sąryšius (Stetson 1987). Augimo kreivė dažnai naudojama ir nustatant spiečiaus struktūrinius parametrus, pvz. pusės šviesio spindulį (pvz. Johnson et al. 2012, 2015; Naujalis et al. 2021; Kriščiūnas et al. 2023).

Žvaigždžių spiečių fiziniai parametrai (amžius, masė, metalingumas ir tarpžvaigždinė ekstinkcija) nustatomi iš apertūrinės fotometrijos matavimų naudojant žvaigždžių populiacijų sintezės (SPS) metodą. Pagrindinis SPS algoritmų principas – pasirenkama tam tikra žvaigždėdaros istorija, pradinė žvaigždžių masės funkcija (IMF) ir pagal tai sugeneruojami žvaigždžių amžių bei masių skirstiniai populiacijoje. Tuomet naudojant žvaigždžių atmosferų ir evoliucijos modelius suskaičiuojamas sintetinės populiacijos integralinis spektras, kurį galima naudoti apskaičiuojant ryškius skirtingose fotometrinėse sistemose. Realaus spiečiaus fizinius parametrus galima įvertinti lyginant jo integralinius ryškius ir spalvos rodiklius su teorinėmis SPS modelių vertėmis (Anders et al. 2004; Bridžius et al. 2008).

Spiečių atveju dažniausiai taikoma SSP prielaida, t.y., visos spiečiaus žvaigždės gimė vieno žvaigždėdaros žybsnio metu ir yra to paties amžiaus bei cheminės sudėties. Klasikiniuose SPS modeliuose (Fioc & Rocca-Volmerange 1997; Leitherer et al. 1999) laikoma, kad žvaigždžių masių skirstinys idealiai atitinka teorinę IMF. Tačiau pastebėta, kad pastaroji prielaida nėra tinkama mažos masės ($<10^4\ M_\odot$) spiečiams, kuriuose reikšmingas stochastiškas retų, vėlesnių evoliucijos stadijų žvaigždžių pasiskirstymas (Deveikis et al. 2008; Maíz Apellániz 2009; Fouesneau & Lançon 2010; Beerman et al. 2012; Anders et al. 2013; de Meulenaer et al. 2013). Dėl šios priežasties, jauni mažos masės spiečiai gali turėti vieną ar kelias supermilžines žvaigždes, kurios nustelbia visas likusias spiečiaus nares ir reikšmingai pakeičia spiečiaus integralinius fotometrinius parametrus. Tai sukelia sistematines spiečių fizinių parametrų paklaidas, jei yra naudojami standartiniai SPS algoritmai.

Šiuolaikiniai metodai atsižvelgia į šiuos efektus, dažniausiai naudojant sintetinius spiečius, sugeneruotus taikant stochastinės IMF modeliavimą (Deveikis et al. 2008; Fouesneau & Lançon 2010; Fouesneau et al. 2014; de Meulenaer et al. 2013, 2017; Krumholz et al. 2015). Tokiu būdu sugeneruojamas platus modelių tinklas, dengiantis didelį galimų parametrų diapazoną. Tokiame tinkle kiekvienas parametrų rinkinys turi daug stochastinių realizacijų, su kuriomis galima lyginti stebimų spiečių integralinės fotometrijos rezultatus, ir nustatyti geriausiai stebėjimus atitinkančią parametrų kombinaciją.

Nepaisant to, kad tokie metodai įskaito IMF stochastiškumo įtaką, jie vis tiek susiduria su rimtomis problemomis, jeigu spiečių integralinių ryškių ir spalvos rodiklių nustatymui naudojamos standartinės apertūrinės fotometrijos procedūros. Beerman et al. (2012) parodė, kad mažos masės spiečių atveju, kai į matavimo apertūrą patenka viena ar kelios ryškios pagrindinę seką palikusios (PMS) spiečiaus žvaigždės, stebimos didelės spiečiaus ryškio ir spalvos variacijos. Tai savo ruožtu daro didelę neigiamą įtaką nustatytų fizinių parametrų tikslumui. Taip pat, de Meulenaer et al. (2017) pademonstravo, kad apertūros viduje besiprojektuojančios ryškios fono žvaigždės gali reikšmingai iškraipyti fotometrinius matavimus ir taip apsunkinti fizinių parametrų nustatymą bei sustiprinti amžiaus–esktinkcijos parametrų išsigimimą.

2.2 Adaptyvi apertūrinė fotometrija

Siekiant sumažinti PMS žvaigždžių efektus, Naujalis et al. (2021) pasiūlė naują adaptyvios apertūrinės fotometrijos metodą, kuris pagrįstas spiečių spinduliuotės srauto augimo kreivių fotometrinėse juostose matavimu. Spiečius matuojamas naudojant dvi kocentrines apertūras – didesnioji skirta viso srauto matavimui (T apertūra), o mažesnioji (C apertūra) parenkama taip, kad apimtų tik centrinę spiečiaus dalį ir kuo mažiau įtrauktų fono ar evoliucionavusių spiečiaus žvaigždžių. C apertūros naudojimas, įgalina atlikti matavimus, kurie yra mažiau paveikti stochastinės ryškių žvaigždžių taršos. Verta paminėti, kad Naujalis et al. (2021) ir Kriščiūnas et al. (2023) naudojo C apertūras, kurių spindulys, R_{C}, lygus arba didesnis nei spiečiaus pusės šviesio spindulys.

Taikant šį metodą, matavimai $F475W$ fotometrinėje juostoje, kuri PHAT apžvalgoje pasižymi didžiausiu signalo–triukšmo santykiu (S/N) ir yra mažiau paveikta senų M 31 lauko žvaigždžių taršos, yra atraminiai. Šioje juostoje suskaičiuojama apertūrinė korekcija (AC), kuri yra skirtumas tarp ryškių pamatuotų T ir C apertūrose:

$$F475W_{\mathrm{AC}} = F475W_{\mathrm{T}} - F475W_{\mathrm{CA}}. \tag{2.1}$$

Galutiniai, spalviškai derantys tarpusavyje, ryškiai (C) suskaičiuojami pagal formulę:

$$F\#W_{\mathrm{C}} = F\#W_{\mathrm{CA}} + F475W_{\mathrm{AC}}, \tag{2.2}$$

čia ”#” žymi HST trijų skaičių fotometrinės juostos kodą, $F\#W_{\mathrm{CA}}$ – ryškis atitinkamoje juostoje išmatuotas C apertūroje. Tokia ryškio transformacija gerai tinka spiečiams, kurių spalvos rodiklis už R_{C} ribų mažai kinta.

Nors adaptyvi apertūrinė fotometrija reikšmingai sumažino sistematines spiečių fotometrijos paklaidas, integralinės fotometrijos fundamentinės ribos dar nebuvo iki galo suprastos. Būtent tai ir yra vienas iš pagrindinių šios disertacijos tikslų.

2.3 Alternatyvūs spiečių fizinių parametrų nustatymo metodai

Apertūrinė fotometrija nėra vienintelis metodas, tinkamas nustatyti žvaigždžių spiečių parametrus, todėl, siekiant geriau suprasti apertūrinės fotometrijos vietą bendrame spiečių tyrimo kontekste, svarbu nors trumpai aptarti ir alternatyvius metodus bei jų taikymo ribas.

Tiksliausi metodai remiasi individualių spiečiaus žvaigždžių CMD analize. Tokių algoritmų veikimas yra pagrįstas stebimų CMD lyginimu su sintetinėmis CMD arba teorinėmis izochronomis (pvz. Dolphin 2002; Johnson et al. 2016; Wainer et al. 2022; Čeponis et al. 2024; Zheng et al. 2025). Šiais metodais galima gana tiksliai nustatyti spiečių parametrus, tačiau tam reikia gilių ir aukštos erdvinės skyros stebėjimų, todėl jie taikomi tik palyginti artimiems ir jauniems spiečiams. Pavyzdžiui, Wainer et al. (2022) parodė, kad remiantis HST stebėjimais kaimyninėse M 31 ir M 33 galaktikose toks metodas tinkamas tik spiečiams jaunesniems nei 300 Myr ir masyvesniems nei 1000 $M_{\odot}$.

Kitas svarbus metodas yra spektroskopija. Šiuo atveju stebėti integraliniai spiečių spektrai lyginami su teoriniais modeliais arba etaloniniais (žinomų spiečių) spektrais. Spektroskopiniais metodais galima tiksliau nustatyti spiečių metalingumą ir efektyviau atskirti parametrų išsigimimus nei plačiajuostės fotometrijos atveju (Worthey 1994; Caldwell et al. 2009; Vazdekis et al. 2010). Tačiau šiam metodui reikalingi didelio S/N spektrai, todėl jis gali būti taikomas tik ryškiems ir masyviems, į kamuolinius spiečius panašiems, užgalaktiniams spiečiams.

Nors CMD ir spektroskopiniais metodais nustatyti spiečių parametrai atskirais atvejais yra tikslesni, apertūrinės fotometrijos metodas daug plačiau pritaikomas. Kadangi šis metodas remiasi suintegruotos visų spiečiaus žvaigždžių šviesos matavimu ir nereikalauja labai didelio S/N, jis gali būti taikomas mažesnės masės, tolimesniems ir platesnio amžių intervalo spiečiams, taip reikšmingai padidinant galimų tirti objektų skaičių.

3 skyrius

Stochastiniai žvaigždžių spiečių modeliai

Siekdami įvertinti apertūrinės fotometrijos metodo tikslumo ir pritaikomumo ribas artimų galaktikų diskuose esančių žvaigždžių spiečių tyrimuose, naudojome stochastinius spiečių modelius, sugeneruotus mūsų sukurtu algoritmu (Daugevičius et al. 2024). Jis skirtas modeliuoti dirbtinius trimačius (3D) spiečius ir realistiškus jų vaizdus, projektuojant į dvimatę (2D) plokštumą iš įvairių stebėjimo krypčių. Algoritmo veikimas paremtas ankstesnių spiečių ir jų vaizdų modeliavimo kodų principais (Deveikis et al. 2008; Bialopetravičius et al. 2019). Spiečius modeliavome taip, kad jie atitiktų realius M 31 spiečius, stebimus PHAT apžvalgoje (Dalcanton et al. 2012; Johnson et al. 2015). Šiame skyriuje pateikiame trumpą algoritmo aprašymą.

3.1 Spiečiaus žvaigždžių generavimas

Individualių spiečiaus žvaigždžių pradinės masės generuojamos taikant Monte Carlo metodą, kur tikimybes apibrėžia IMF, kuri nusako kiek populiacijoje turi būti žvaigždžių dN tam tikrame masių intervale dm. Mes naudojame plačiai taikomą Kroupa (2001) IMF, kuri apibrėžiama kelių dalių laipsnine funkcija:

$$\xi(\mathrm{m}) = \mathrm{d}N/\mathrm{dm} = C_{\mathrm{IMF}} \cdot b_i \cdot \mathrm{m}^{-\alpha_i}, \tag{3.1}$$

čia α_i yra IMF laipsnio rodiklis masių intervale $[\mathrm{m}_{i-1}, \mathrm{m}_i]$, C_{IMF} yra funkcijos normavimo konstanta, o b_i yra funkcijos tolydumą bei nenutrūkstamumą užtikrinanti konstanta. Pradinės žvaigždžių masės generuojamos intervale nuo 0.1 iki 100 $\mathrm{M}_\odot$, kuriame Kroupa IMF yra dviejų dalių laipsninė funkcija:

$$\begin{cases} \alpha_1 = 1.3, & \mathrm{m} < 0.5\,\mathrm{M}_\odot; \\ \alpha_2 = 2.3, & \mathrm{m} \geq 0.5\,\mathrm{M}_\odot. \end{cases} \tag{3.2}$$

Žvaigždžių erdvinis pasiskirstymas taip pat modeliuojamas taikant Monte Carlo metodą. Žvaigždžių padėtys spiečiuje generuojamos pagal Elson-Fall-Freeman (EFF; Elson et al. 1987) radialinį profilį, kuris gerai atitinka daugelio jaunų spiečių stebėjimus įvairiose artimose galaktikose (pvz. Elson et al. 1987; Larsen 1999, 2004;

McLaughlin & van der Marel 2005; Bastian et al. 2012; Cuevas-Otahola et al. 2020; Brown & Gnedin 2021). Kadangi mes siekiame kuo realistiškiau atkurti būtent jaunus spiečius, kurie yra ypač jautrūs stochastiniams efektams, EFF profilio pasirinkimas yra pagrįstas. EFF modelio radialinis tankio profilis aprašomas funkcija:

$$\rho(r) = \rho_0 \left(1 + \frac{r^2}{r_0^2}\right)^{-(\gamma+1)/2}, \tag{3.3}$$

kur ρ_0 yra centrinis spiečiaus tankis, r – deprojektuotas trimatis atstumas nuo spiečiaus centro, r_0 – EFF skalės spindulys, o γ – laipsnio rodiklis, apibrėžiantis profilio elgseną išorinėse spiečiaus srityse. Žvaigždžių erdvinis pasiskirstymas pagal šį profilį generuojamas pagal Aarseth et al. (1974) pasiūlytą algoritmą, kuris originaliai naudojamas priskirti pradines žvaigždžių padėtis dinaminiuose N-kūnų spiečių modeliuose.

Siekiant sumodeliuoti visą spiečių, individualių žvaigždžių (t.y. jų pradinių masių ir padėčių spiečiuje) generavimo algoritmas yra kartojamas tol, kol bendra spiečiaus masė tam tikro dydžio sferoje pasiekia arba šiek tiek viršija nustatytą tikslinę masę. Šiame darbe naudojome 7.5″ spindulio sferą, kuri ties M 31 galaktikos atstumu atitinka ~28.5 pc. Kuomet yra pasiekiama arba viršijama nustatyta spiečiaus masės riba, žvaigždžių generavimas yra sustabdomas ir suskaičiuojama bendra masė įtraukiant paskutinę sugeneruotą žvaigždę ir ją atmetant. Variantas, kuris duoda mažiausią nuokrypį nuo tikslinės masės yra parenkamas kaip galutinis spiečiaus modelis.

Sugeneravus žvaigždžių mases ir jų erdvinį pasiskirstymą, kiekvienai žvaigždei priskiriami fotometriniai ryškiai pagal jos masę ir modeliuojamo spiečiaus amžių. Tai atliekama interpoliuojant pagal žvaigždės masę atitinkamo amžiaus PARSEC-COLIBRI žvaigždžių evoliucijos modelių izochroną (Bressan et al. 2012; Marigo et al. 2017). Šiame darbe naudojamos Saulės metalingumo izochronos ir daroma prielaida, kad tarpžvaigždinė ekstinkcija yra lygi nuliui.

Kadangi siekiame modeliuoti spiečius, atitinkančius PHAT apžvalgoje stebimus realius M 31 spiečius, izochronos interpoliuojamos šešiose HST fotometrinėse juostose. Izochronose pateikti absoliutūs ryškiai transformuojami į regimuosius, naudojant M 31 atstumo modulį $(m - M)_0 = 24.47$ (McConnachie et al. 2005).

3.2 Realistiškų spiečių vaizdų generavimas

Paskutinis algoritmo etapas yra dirbtinių spiečių realistiškų stebėjimų modeliavimas, projektuojant juos į 2D plokštumą. Individualių žvaigždžių vaizdams modeliuoti naudojamas `TinyTim`[1] paketas, įgalinantis generuoti įvairių HST instrumentų ir filtrų kombinacijų 2D taško sklaidos funkcijas (PSF). Kiekviena žvaigždė modeliuojama atitinkamą `TinyTim` PSF padauginant iš jos srauto vienoje iš fotometrinių juostų. Ši procedūra atliekama visose šešiose PHAT apžvalgoje naudojamose juostose. Dirbtinių spiečių vaizdai generuojami 15″ × 15″ dydžio ir atitinka maždaug 57 × 57 pc ties M 31 atstumu. Spiečių vaizdai išsaugomi FITS formato failuose.

[1] https://www.stsci.edu/hst/instrumentation/focus-and-pointing/focus/tiny-tim-hst-psf-modeling

3.3 Spiečių modelių imtis

Aprašytu metodu sugeneravome spiečių modelių ir jų vaizdų tinklą, apimantį realiems M 31 disko spiečiams būdingą parametrų erdvę (Šablevičiūtė et al. 2006, 2007; Vansevičius et al. 2009; Johnson et al. 2015). Pagrindinį tinklą sudaro 1400 mazgų, apibrėžtų pradine spiečiaus mase $\log_{10}(M/M_\odot)$, amžiumi $\log_{10}(t/\mathrm{yr})$, EFF profilio rodikliu γ ir branduolio spinduliu r_c. Kiekviename mazge sugeneruota po 100 spiečių.

Stebėjimo krypties stochastiškumo įtakai apertūrinei fotometrijai įvertinti (žr. 4 skyriuje), sumodeliavome papildomą 500 mazgų potinklį, kuriame kiekvienam spiečiui sugeneravome po 100 projekcijų iš atsitiktinių stebėjimo kampų. Atsižvelgiant į šešias PHAT fotometrinės juostas, iš viso sugeneravome daugiau nei 3×10^7 vaizdų.

5.4 poskyrio analizei sugeneravome atskirą tolydžią 20 milijonų sintetinių spiečių imtį, kurios vaizdai generuoti tik $F475W$ juostoje. Modeliai skaičiuoti tuo pačiu algoritmu, tačiau parametrų vertės atsitiktinai parinktos iš tolydžių intervalų.

3.1 lentelė. Sintetinių žvaigždžių spiečių pagrindinio modelių tinklo parametrai. Kiekviename mazge generuojama 100 nepriklausomų stochastinių modelių.

Parameter	Values
$\log_{10}(M/M_\odot)$	2.0, 2.5, 3.0, 3.5, 4.0, 4.5, 5.0
$\log_{10}(t/\mathrm{yr})$	6.5, 7.0, 7.5, 8.0, 8.5, 9.0, 9.5, 10.0
r_c	0.05″, 0.10″, 0.20″, 0.40″, 0.80″
γ	2.2, 2.4, 2.8, 3.5, 7.0

3.2 lentelė. Sintetinių spiečių potinklio parametrai. Kiekviename mazge generuojama 100 nepriklausomų modelių ir po 100 stebėjimo krypčių kiekvienam modeliui.

Parameter	Values
$\log_{10}(M/M_\odot)$	2.0, 2.5, 3.0, 3.5, 4.0
$\log_{10}(t/\mathrm{yr})$	7.0, 8.0, 9.0, 10.0
r_c	0.05″, 0.10″, 0.20″, 0.40″, 0.80″
γ	2.2, 2.4, 2.8, 3.5, 7.0

3.3 lentelė. Tolydžios 20 milijonų modelių $F475W$ juostoje imties parametrų ribos.

Parameter	Range of values
$\log_{10}(M/M_\odot)$	2.4 – 4.1
$\log_{10}(t/\mathrm{yr})$	6.5 – 10.1
r_c	0.05″ – 0.6″
γ	2.1 – 4.1

4 skyrius

Apertūrinės fotometrijos taikymo ribos

Apertūrinė fotometrija yra efektyvus metodas tiriant dideles žvaigždžių spiečių imtis vietinėje Visatoje ir rekonstruojant žvaigždėdaros istorijas diskinėse galaktikose (žr. 2 skyrių). Ankstesni tyrimai (pvz. Fouesneau & Lançon 2010; Beerman et al. 2012; Anders et al. 2013; de Meulenaer et al. 2013, 2017) parodė, kad mažos masės spiečių atveju reikšmingus neapibrėžtumus daugiausia lemia IMF stochastiškumas. Tačiau metodo tikslumo ir pritaikomumo ribos dar nėra išsamiai ištirtos, nors tai būtina patikimam stebėjimų duomenų interpretavimui.

Šiame skyriuje nustatome apertūrinės fotometrijos ribas, sukeliamas stochastinių efektų, neatsižvelgdami į dangaus fono efektus. Todėl gauti neapibrėžtumai ir nuokrypiai atitinka optimistinę, didžiausio galimo tikslumo ribą; įtraukus fono triukšmą ir ryškių lauko žvaigždžių taršą, tikslumas būtų mažesnis.

4.1 Stochastinių spiečių modelių matavimai

Siekiant ištirti, kaip stochastiniai efektai riboja spiečių apertūrinės fotometrijos tikslumą, atlikome dirbtinių spiečių vaizdų fotometrinius matavimus, taikant metodiką, panašią į Naujalis et al. (2021) ir Kriščiūnas et al. (2023).

Visose šešiose fotometrinėse juostose išmatavome radialines srauto augimo kreives (FGC) iki 7.0″ spindulio, 0.02″ žingsniu. Iš jų nustatėme integralinius ryškius ir spalvos rodiklius bei struktūrinius parametrus R_X, atitinkančius spindulį, kuriame sutelkta X procentų viso spiečiaus srauto. FGC analizė leidžia įvertinti žvaigždžių masių ir erdvinio pasiskirstymo stochastiškumo bei stebėjimo krypties įtaką fotometriniams ir struktūriniams matavimams.

4.2 Spiečių fotometrinės savybės

Šiame poskyryje nagrinėjame stochastinių efektų ir apertūros dydžio įtaką mažos masės spiečių fotometrijai. Šie veiksniai riboja apertūrinės fotometrijos tikslumą ir patikimumą nustatant spiečių fizinius ir struktūrinius parametrus.

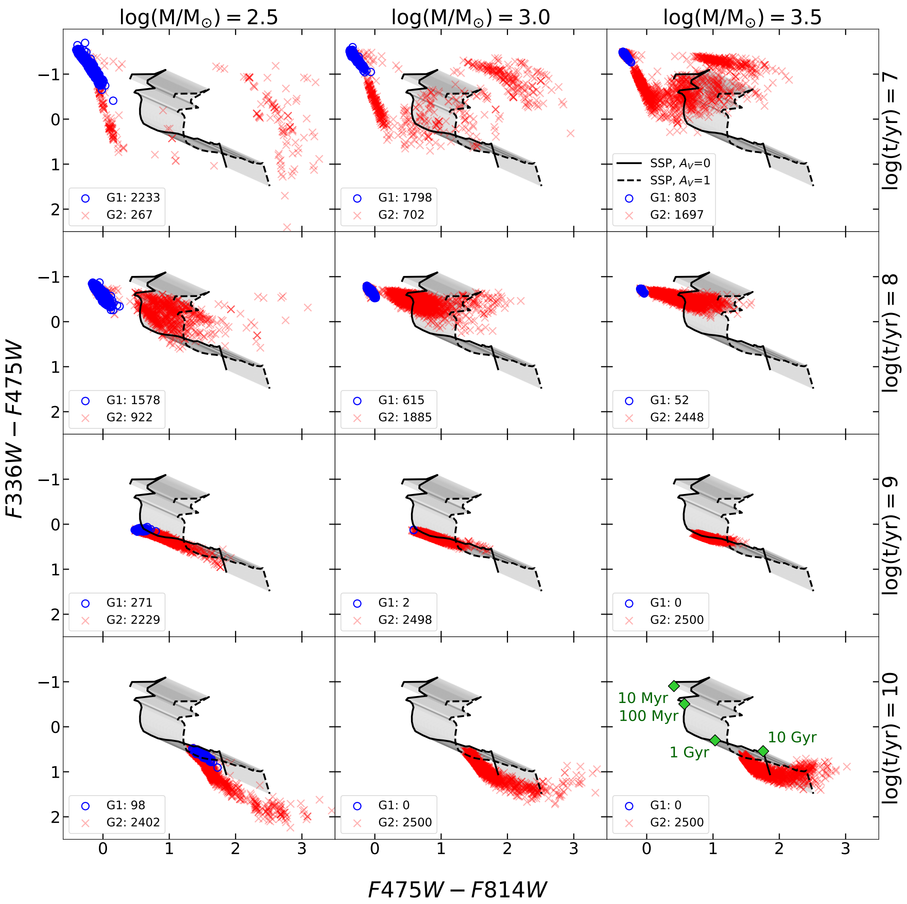

4.1 pav. Stochastinių žvaigždžių spiečių modelių dvispalvės diagramos. Kiekviena panelė rodo apertūrinės fotometrijos rezultatus skirtingoms spiečių masės (nurodyta virš panelių) ir amžiaus (nurodyta dešinėje) kombinacijoms. G1 ir G2 spiečių grupių apibrėžimai pateikti tekste. Juodos linijos žymi nestochastinius PARSEC-COLIBRI SSP Saulės metalingumo modelius, apimančius amžių intervalą nuo 10 Myr iki 12.6 Gyr (Bressan et al. 2012; Marigo et al. 2017, ištisinės linijos – be tarpžvaigždinės ekstinkcijos; brūkšninės linijos – su $A_V = 1$ ekstinkcija, apskaičiuota naudojant Fitzpatrick 1999 ekstinkcijos kreivę). Žali simboliai žymi keturis skirtingus nestochastinių SSP modelių amžiaus taškus. Fotometriniai matavimai atlikti naudojant $R_{\rm ap} = 3.0''$ apertūras.

TCD (4.1 pav.) ir CMD (4.2 pav.) rodo, kad mažos masės spiečiai ($\log_{10}(M/M_\odot) \leq 4.0$) pasižymi didele fotometrinių parametrų sklaida, stiprėjančia mažėjant masei ir amžiui. Ryškiausi spiečiai $\log_{10}(M/M_\odot) = 2.5$–$3.5$ intervale gali turėti labai panašius ryškius ir spalvos rodiklius, nepaisant masės skirtumo. Tai gali sukelti reikšmingus neapibrėžtumus nustatant spiečių fizinius.

Jaunų mažos masės spiečius galime išskirti į dvi fotometriškai besiskiriančias grupes: G1, neturinčius evoliucionavusių PMS žvaigždžių, ir G2, turinčius bent vieną ryškią PMS žvaigždę. G2 spiečiai įprastai yra ryškesni ir raudonesni, nes viena ar kelios YSG arba RSG žvaigždės gali dominuoti bendrą srautą. Atskyrimas ypač ryškūs $t \lesssim 100$ Myr spiečiams.G1 spiečių fotometrinės savybės yra geriau apibrėžtos, todėl ryškių evoliucionavusių žvaigždžių pašalinimas gali pagerinti fizinių parametrų nustatymo patikimumą (Beerman et al. 2012).

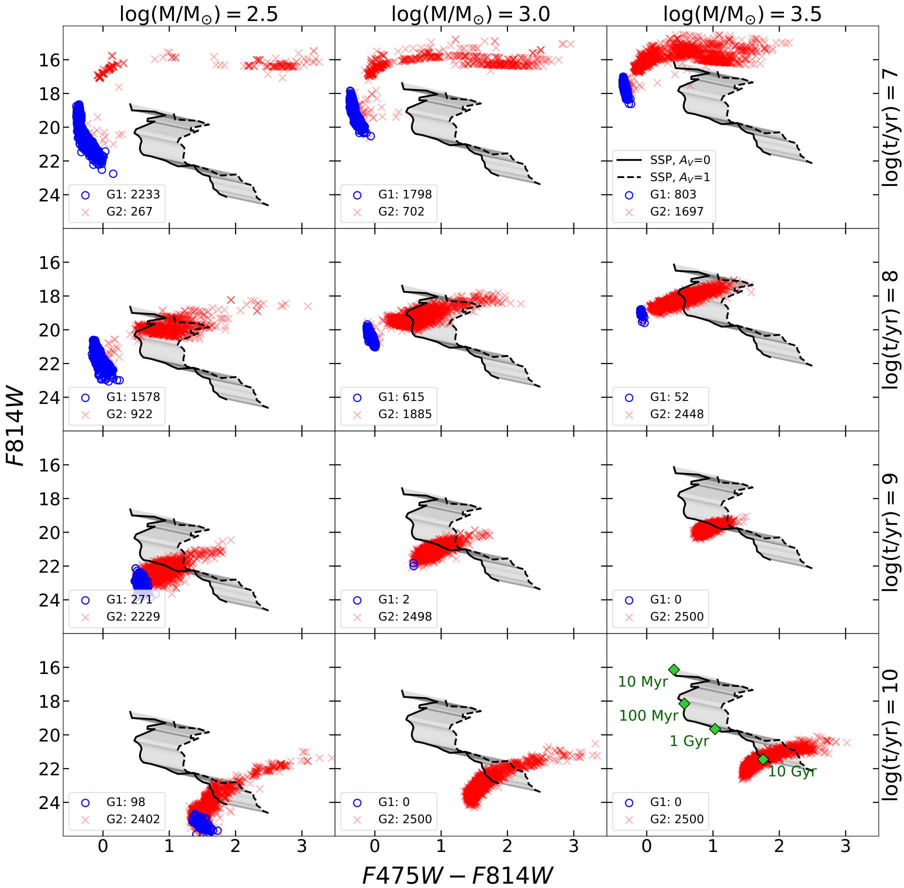

4.2 pav. Tas pats kaip 4.1 pav., tačiau čia pateiktos spalvos–ryškio diagramos.

Stochastinius dirbtinius spiečius palyginome su nestochastiniais PARSEC-COLIBRI (Bressan et al. 2012; Marigo et al. 2017) SSP modeliais. Nestochastinė aproksimacija yra netinkama mažos masės spiečiams, ypač $t \leq 100$ Myr atveju, todėl jų fiziniams parametrams nustatyti būtina atsižvelgti į stochastinius efektus (Deveikis et al. 2008; Fouesneau & Lançon 2010; de Meulenaer et al. 2013).

Stochastinių efektų įtaką galima sumažinti įtraukiant papildomas fotometrines juostas, pvz., UV ar artimąją IR (Bridžius et al. 2008; de Meulenaer et al. 2014), bei Hα (Fouesneau et al. 2012; Whitmore et al. 2020, 2023). Tam gali būti naudinga ir adaptyvi apertūrinė fotometrija, mažinanti ryškių fono ar spiečiaus pakraščiuose esančių PMS žvaigždžių įtaką.

Nors adaptyvi apertūrinė fotometrija sėkmingai pritaikyta PHAT spiečiams (Naujalis et al. 2021; Kriščiūnas et al. 2023), metodas kontroliuojamose sąlygose dar ne-

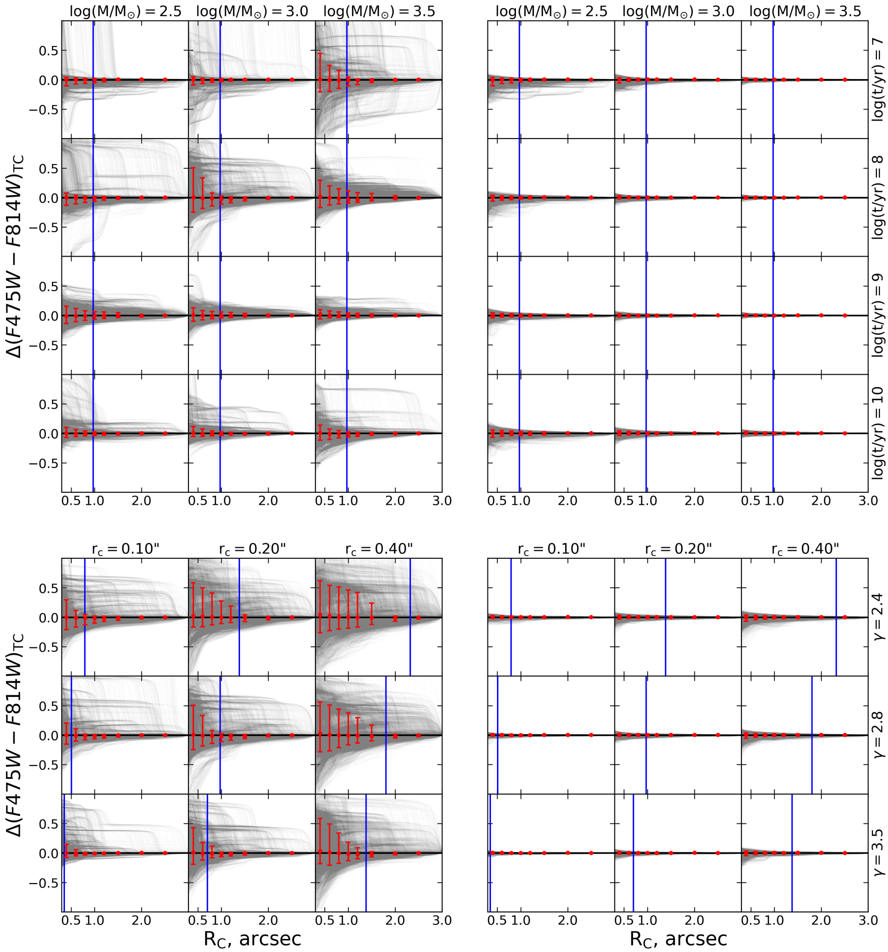

4.3 pav. $F475W - F814W$ spalvos rodiklio skirtumai tarp T ir C apertūrų matavimų, kaip R_{C} funkcija. Individualių spiečių skirtumus žymi pilkos linijos, Raudoni simboliai – medianines $\Delta(F475W - F814W)_{\mathrm{TC}}$ vertes, o „ūsai" – 16–84 procentilių intervalą. Fiksuotas T apertūros spindulys yra $R_{\mathrm{T}} = 3.0''$. Mėlynos vertikalios linijos žymi spindulius, lygius $2 \times R_{50}$. Panelių blokai viršuje rodo priklausomybę nuo spiečiaus masės ir amžiaus (spiečiams su $r_c = 0.2''$ ir $\gamma = 2.8$), apačioje – nuo radialinio profilio parametrų (spiečiams su $\log_{10}(\mathrm{M/M_{\odot}}) = 3.0$ ir $\log_{10}(t/\mathrm{yr}) = 8.0$). Kairėje esančiuose panelių blokuose pateikti rezultatai, kai į fotometrinius matavimus įtraukiamos visos spiečiams priklausančios žvaigždės, o dešinėje – pašalinus PMS žvaigždes.

buvo išsamiai išbandytas. Todėl šiame darbe metodą taikome dirbtiniams spiečių vaizdams be dangaus fono, siekiant įvertinti jo veikimą idealiomis sąlygomis ir patikrinti ar, stochastiniai efektai nesukuria reikšmingų spalvos rodiklių gradientų.

Siekiant įvertinti sistematinius nuokrypius naudojant mažas spalvines apertūras (C), apibrėžiame spalvos rodiklių skirtumą:

$$\Delta(\mathrm{CI})_{\mathrm{TC}} = \mathrm{CI}_{\mathrm{T}} - \mathrm{CI}_{\mathrm{C}}, \tag{4.1}$$

kur CI_T ir CI_C yra spalvos rodikliai, išmatuoti naudojant T ir C apertūras. 4.3 pav. parodyta $\Delta(F475W-F814W)_{TC}$ priklausomybė nuo C apertūros spindulio R_C ir spiečiaus parametrų.

Reikšmingų sistematinių spalvos rodiklio gradientų nėra – medianinė $\Delta(CI)_{TC}$ reikšmė išlieka artima nuliui. Tačiau matoma didelė sklaida, kuri mažėja didėjant R_C ir yra didesnė dideliems, mažiau koncentruotiems spiečiams. Sklaida reikšmingai sumažėja, kai $R_C \gtrsim 2 \times R_{50}$, todėl tai gali būti praktiška ir naudinga rekomendacija C apertūros dydžiui.

Jauni (t = 10–100 Myr) spiečiai pasižymi itin didelėmis, dažniausiai teigiamomis $\Delta(CI)_{TC}$ reikšmėmis, kartais siekiančiomis net ±1.0 mag ar daugiau. Staigūs spalvos šuoliai rodo, kad juos daugiausia lemia ryškios raudonos PMS žvaigždės. Tai patvirtina matavimai pašalinus PMS žvaigždes (žr. dešiniuosius 4.3 pav. panelių blokus): sklaida sumažėja, spalvos šuoliai išnyksta, o skirtumai dažniausiai neviršija ±0.1 mag.

Išimtis yra jauniausi mažos masės spiečiai ($\log_{10}(t/\mathrm{yr}) = 7.0$; $\log_{10}(\mathrm{M}/\mathrm{M}_\odot) \leq 3.0$), kurių sklaida gali siekti apie ±0.5 mag. Šiuo atveju T ir C matavimų skirtumas yra neigiamas, t.y. C apertūros matavimai yra raudonesni. Šuoliai iš neigiamos skirtumo pusės greičiausiai susiję su viršutinės MS žvaigždžių stochastiškumu, kai ryškiausios MS žvaigždės nepatenka į C apertūrą.

Taigi, tinkamai parinkta C apertūra gali sumažinti ryškių fono žvaigždžių bei tam tikrais atvejais evoliucionavusių spiečiaus žvaigždžių įtaką ir pagerinti spiečių spalvos rodiklių bei fizinių parametrų nustatymo patikimumą (Beerman et al. 2012). Šis metodas naudingas tiriant artimų galaktikų diskuose esančius spiečius, kuomet naudojami aukštos skyros kosminių teleskopų stebėjimai (Johnson et al. 2015, 2022; Adamo et al. 2017; Cook et al. 2019; Deger et al. 2022).

4.3 Spiečių fotometrijos neapibrėžtumai

Esminėms apertūrinės fotometrijos tikslumo riboms įvertinti nagrinėjome tris neapibrėžtumų šaltinius: apertūros centro ir dydžio parinkimą (APT), stochastinius IMF ir žvaigždžių erdvinio pasiskirstymo efektus (GEN) bei projekcijos efektus (ROT). APT atveju kiekvieną spiečių matavome devyniose centro padėtyse ir su trimis apertūros dydžiais (dviejų iš jų spinduliai nuo originalaus skiriasi ±1 vaizdo elementu), iš viso gaudami 27 matavimus. GEN ir ROT neapibrėžtumai nustatytu atitinkamai iš 100 nepriklausomų spiečiaus realizacijų ir 100 stebėjimo krypčių kiekvienam spiečiui. Visais atvejais neapibrėžtumą prilyginome pusei 16–84 procentilių intervalo ir žymime σ_{APT}, σ_{GEN} bei σ_{ROT}.

4.4 pav. rodo trijų neapibrėžtumo šaltinių įverčius $F336W - F475W$ ir $F475W - F814W$ spalvos rodikliams, priklausomai nuo apertūros spindulio. Čia pateikiame rezultatus keturioms masės ir amžiaus kombinacijoms ($\log_{10}(t/\mathrm{yr}) = 7.0$ ir 10.0; $\log_{10}(\mathrm{M}/\mathrm{M}_\odot) = 2.0$ ir 4.0) su profilio parametrais $r_c = 0.2''$ ir $\gamma = 2.8$, kurie atitinka tipinius spiečius stebimus artimų galaktikų diskuose (e.g., Larsen 2004; Šablevičiūtė et al. 2006, 2007; Vansevičius et al. 2009; Ryon et al. 2017; Brown & Gnedin 2021). Visi neapibrėžtumai mažėja didėjant apertūrai, ypač intervale nuo $R_{\mathrm{ap}} = 0.5''$ iki $1.0''$, o ties $R_{\mathrm{ap}} \gtrsim 1.5''$ stabilizuojasi ir pasiekia daugmaž pastovų lygį ir tampa labai maži ($\sigma_{\mathrm{ROT}} \lesssim 0.01$). Verta paminėti, kad kuo spiečiai kompaktiškesni, tuo paklaidos apskritai yra mažesnės.

GEN ir ROT efektų sukeliami neapibrėžtumai (ypač dominuoja GEN) yra stipriai didesni už APT paklaidas. Idealizuotų sąlygų (kuomet nėra su fonu susijusių efektų)

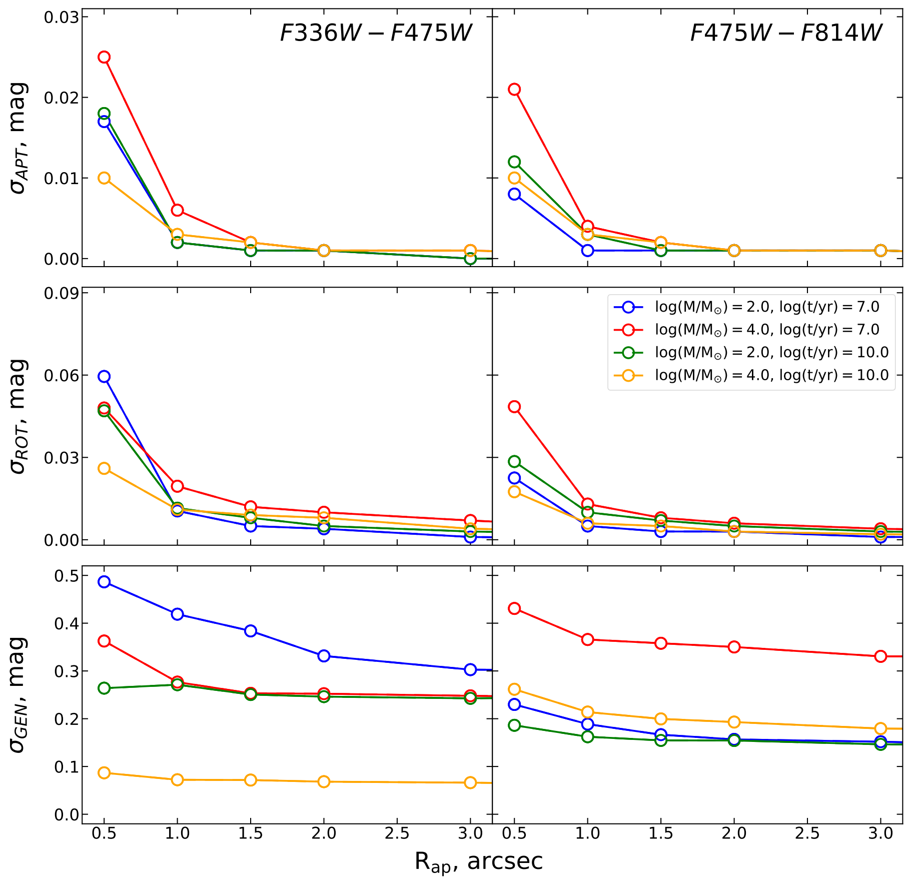

4.4 pav. Žvaigždžių spiečių apertūrinės fotometrijos spalvos rodiklių neapibrėžtumų priklausomybė nuo apertūros spindulio $R_{\rm ap}$: $F336W - F475W$ (kairysis stulpelis) bei $F475W - F814W$ (dešinysis stulpelis). Viršutinės panelės rodo sklaidą dėl apertūros padėties ir dydžio efektų ($\sigma_{\rm APT}$); vidurinės panelės – sklaidą dėl projekcijos efektų ($\sigma_{\rm ROT}$); apatinės panelės – sklaidą dėl žvaigždžių IMF ir erdvinio pasiskirstymo stochastiškumo ($\sigma_{\rm GEN}$). Rezultatai pateikti spiečiams, kurių radialinio profilio parametrai: $r_c = 0.2''$ ir $\gamma = 2.8$; keturioms skirtingoms spiečių amžiaus ir masės kombinacijoms (žr. legendą).

atveju fundamentalią apertūrinės fotometrijos tikslumo ribą lemia IMF stochastiškumas. Tačiau kai kuriais atvejais svarbūs ir sistematiniai efektai, pvz., fizinių parametrų išsigimimai (Worthey 1994; Bridžius et al. 2008; Whitmore et al. 2023).

Projekcijos efektai sudaro pastebimą bendrų fotometrinių paklaidų dalį ir atskirais atvejais gali reikėti į juos atsižvelgti. HST stebėjimų atveju, M 31 atstumu esantiems tipiniams spiečiams, naudojant $R_{\rm ap} \leq 1.5''$ apertūras, projekcijos efektai spalvos rodikliams paprastai sukelia iki ~0.05 mag, o pavieniais atvejais iki ~0.1 mag neapibrėžtumą. Šių efektų įtaka mažėja masyviems ir kompaktiškiems spiečiams bei naudojant didesnes apertūras, tačiau pastarosios didina fono žvaigždžių taršos riziką. Optimali apertūra priklauso nuo spiečiaus bei jo aplinkos ir turi būti parenkama individualiai.

4.4 Fizinių parametrų nustatymo tikslumas

Šiame poskyryje mūsų tikslas – įvertinti, kokias spiečių fizinių parametrų tikslumo ribas galime pasiekti apertūrinės fotometrijos metodais. Nagrinėjame tris parametrus: amžių, masę bei tarpžvaigždinę ekstinkciją, išreikštą per spalvos ekscesą $E(B-V)$. Analizavome nedidelę 1920 dirbtinių spiečių imtį – po 20 nepriklausomų realizacijų kiekviename iš 96 potinklio mazgų, kurių parametrai pateikti 4.1 lentelėje.

4.1 lentelė. Spiečių modeliai naudoti fizinių parametrų nustatymo testuose.

Parameter	Values
$\log_{10}(\mathrm{M}/\mathrm{M}_{\odot})$	2.5, 3.0, 3.5, 4.0
$\log_{10}(\mathrm{t}/\mathrm{yr})$	7.0, 8.0, 9.0, 10.0
r_c	0.10″, 0.40″
γ	2.2, 2.8, 7.0

Naudojome visų šešių juostų fotometriją, atliktą su $R_{\mathrm{ap}} = [0.5'', 1.0'', 2.0'', 7.0'']$ apertūromis. Fizinius parametrus nustatėme lygindami matavimus su dideliu stochastinių modelių integralinės fotometrijos katalogu, naudojant de Meulenaer et al. (2013, 2017) metodą (žr. 2.1 poskyrį). Naudojome modelių tinklą, apimantį $\log_{10}(t/\mathrm{yr}) = 6.0$–$10.3$, $\log_{10}(\mathrm{M}/\mathrm{M}_{\odot}) = 2.0$–$7.0$ ir $E(B-V) = -0.03$–1.5, taikant Saulės metalingumo prielaidą.

Tikslumą vertinome pagal skirtumus tarp nustatytų ir tikrųjų parametrų verčių:

- $\Delta\log(t/\mathrm{yr}) = \log(t/\mathrm{yr}) - \log(t/\mathrm{yr})_{\mathrm{input}}$
- $\Delta\log(\mathrm{M}/\mathrm{M}_{\odot}) = \log(\mathrm{M}/\mathrm{M}_{\odot}) - \log(\mathrm{M}/\mathrm{M}_{\odot})_{\mathrm{input}}$
- $\Delta E(B-V) = E(B-V) - E(B-V)_{\mathrm{input}}$.

Pirminiai testai su $E(B-V)_{\mathrm{input}} = 0.0$ ir 0.5 mag neparodė reikšmingų skirtumų, todėl toliau nagrinėjamas tik $E(B-V)_{\mathrm{input}} = 0.0$ mag atvejis.

4.5 pav. pateikiame pagrindinius spiečių parametrų nustatymo testų rezultatus, parodančius medianinius skirtumus tarp nustatytų ir tikrųjų parametrų priklausomai nuo spiečių amžiaus. Rezultatai, gauti naudojant $R_{\mathrm{ap}} = 1.0''$, $2.0''$ ir $7.0''$ apertūra esminių skirtumų neturėjo, taip pat nenustatėme aiškios priklausomybės nuo r_c ir γ. Todėl šie rezultatai buvo apjungti į vieną imtį (mėlyni simboliai). Tuo tarpu, naudojant $R_{\mathrm{ap}} = 0.5''$ gauti skirtumų skirstiniai ženkliai skyrėsi nuo rezultatų, gautų matuojant su didesnėmis apertūromis, todėl juos pateikiame atskirai (raudoni simboliai). Paklaidų „ūsai" žymi skirtumų skirstinių 16–84 procentilių intervalą.

Naudojant $R_{\mathrm{ap}} = 0.5''$ apertūrą, parametrų nustatymo tikslumas yra mažesnis nei su didesnėmis apertūromis. $R_{\mathrm{ap}} = 0.5''$ atveju parametrų skirtumų medianos yra reikšmingai pasislinkusios nuo nulio, o tai rodo sistematinių nuokrypių egzistavimą. Parametrų skirtumų skirstiniai naudojant didesnes apertūras yra siauresni, ir nustatomi parametrai yra tikslesni bei patikimesni.

$t = 10$ Myr atveju naudojant $R_{\mathrm{ap}} = 0.5''$, spiečių amžius ir masė sistemingai pervertinami maždaug +0.2 dex, o sklaida siekia ~0.7 dex. Todėl, labai mažų apertūrų (M 31 spiečių atveju $R_{\mathrm{ap}} \leq 0.5''$) naudoti nerekomenduojama. Tiesa, net ir su didesnėmis apertūromis jauniausių spiečių parametrų nustatymas išlieka sudėtingas: amžiaus ir masės skirtumų sklaida siekia ~0.2 dex. To priežastis yra trumpai gyvuojančių ryškių

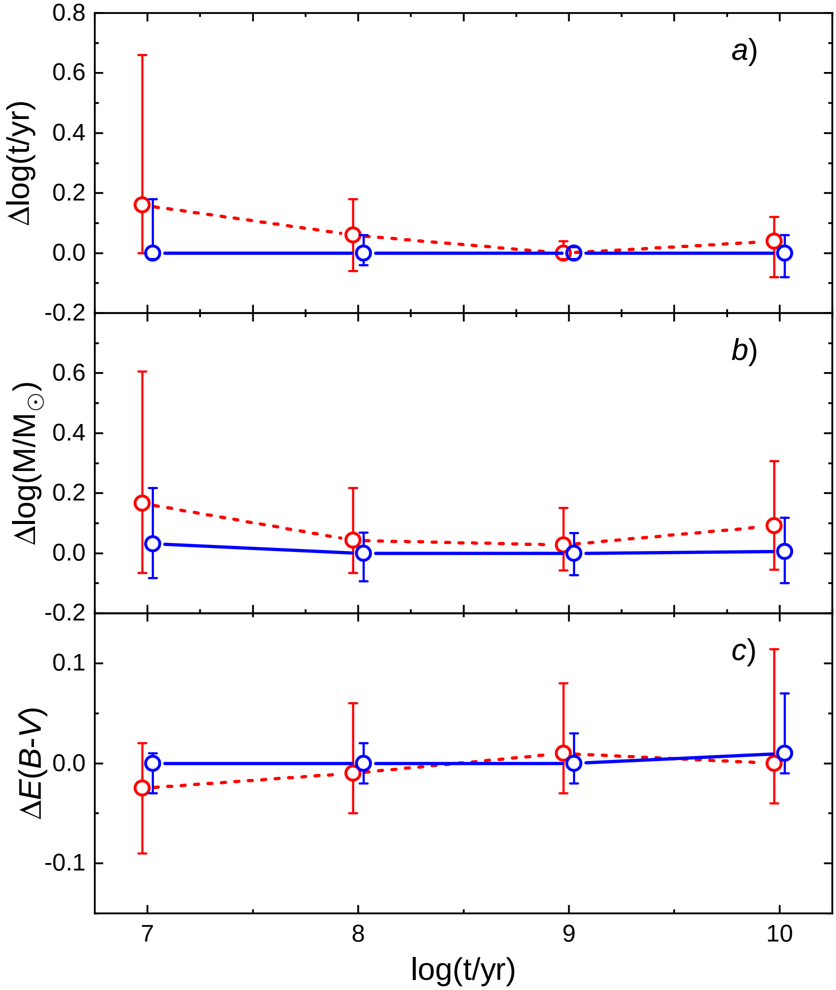

4.5 pav. Žvaigždžių spiečių fizinių parametrų nustatymo testų rezultatai, pateikti kaip skirtumai tarp atkurtų ir tikrųjų parametrų verčių. a) panelė rodo amžiaus skirtumus; b) – masės skirtumus; c) – spalvos eksceso $E(B-V)$ skirtumus. Raudoni apskritimai žymi medianinius parametrų skirtumus, gautus naudojant $R_{ap} = 0.5''$ apertūros matavimus. Mėlyni apskritimai rodo medianinius skirtumus, nustatytus naudojant $R_{ap} = 1.0''$, $2.0''$ ir $7.0''$ apertūrų matavimus, juos sujungus į vieną duomenų rinkinį. Paklaidų „ūsai" atitinka 16–84 procentilių intervalus. Aiškumo dėlei simboliai ir juos jungiančios linijos šiek tiek pastumti išilgai X ašies nuo tikrųjų amžiaus reikšmių.

masyvių žvaigždžių stochastinis poveikis, nes jų buvimas ar nebuvimas pasižymi dominuojančia įtaka integralinei spiečiaus fotometrijai, ir tai gali reikšmingai paveikti parametrus.

Taigi, jaunų spiečių fizinių parametrų nustatymas vien iš apertūrinės fotometrijos matavimų yra riboto tikslumo, o realiomis sąlygomis, esant dangaus fonui, tikslumas bus dar mažesnis. Kaip ir Johnson et al. (2022), mūsų rezultatai rodo, kad jauniems ($t \lesssim 1$ Gyr) išskiriamiems arba pusiau išskiriamiems į žvaigždes spiečiams patikimesnius fizinius parametrus galime gauti taikant CMD analizę (Dolphin 2002; Johnson et al. 2016; Čeponis et al. 2024; Zheng et al. 2025). Mūsų manymu, tiksliausi ir patikimiausi parametrų įverčiai $t \lesssim 1$ Gyr spiečiams nustatomi derinant CMD analizę ir integralinės fotometrijos rezultatus.

4.5 Spiečių struktūrinių parametrų neapibrėžtumai

Galimybės tirti užgalaktinių spiečių dinaminę evoliuciją priklauso nuo jų struktūrinių parametrų įvertinimo tikslumo, todėl toliau nagrinėjame, kokią įtaką iš FGC nustatomų struktūrinių parametrų tikslumui turi stochastiniai efektai. Tokiu pačiu principu kaip 4.3 poskyryje, t.y. imant skirstinių 16–84 procentilių intervalus, įvertinome struktūrinių parametrų neapibrėžtumus dėl IMF ir žvaigždžių erdvinio pasiskirstymo stochastiškumo (σ_{GEN}) bei dėl projekcijos efektų (σ_{ROT}). Kadangi struktūriniai parametrai labai priklauso nuo EFF modelio parametrų, nagrinėjame santykinius neapibrėžtumus (santykiai tarp absoliučių neapibrėžtumų ir atitinkamų parametrų medianų) δ_{GEN} ir δ_{ROT}, išreikštus procentais. Toliau pateikta analizė pagrįsta rezultatais $F475W$ juostoje.

4.6 pav. parodytos δ_{GEN} ir δ_{ROT} vertės priklausomai nuo spiečių amžiaus ir masės R_{50}, R_{30}/R_{50}, R_{50}/R_{80} parametrų atveju. Čia pateikti $r_c = 0.2''$ ir $\gamma = 2.8$ modelių rezultatai. Matome, kad GEN efektai sukelia didelę R_{50} sklaida, nors spiečiai sugeneruoti su tais pačiais modelių parametrais. Didžiausi neapibrėžtumai nustatyti labai jauniems spiečiams – $t = 10$ Myr atveju δ_{GEN} viršija $\sim$40%. Mažos masės objektams $\log_{10}(\mathrm{M}/\mathrm{M}_{\odot}) \leq 3.0$ GEN efektai sukelia $\sim$20% neapibrėžtumą, o tik vidutinio amžiaus (100 Myr ir 1 Gyr) masyvesni spiečiai ($\log_{10}(\mathrm{M}/\mathrm{M}_{\odot}) = 4.0$) pasižymi $\delta_{\mathrm{GEN}} \lesssim 10\%$ paklaidomis.

ROT efektai sukelia mažesnius R_{50} neapibrėžtumus nei GEN efektai visame nagrinėjamame masių bei amžių intervale. Didesnės masės spiečiams $\log_{10}(\mathrm{M}/\mathrm{M}_{\odot}) \geq 3.0$, δ_{ROT} nukrenta žemiau 10% ties $\log_{10}(t/\mathrm{yr}) \geq 8.0$ amžiais, tačiau ties $\log_{10}(t/\mathrm{yr}) = 7.0$ išlieka apie 10–20%. Mažiausios masės spiečiams, $\log_{10}(\mathrm{M}/\mathrm{M}_{\odot}) = 2.0$, δ_{ROT} yra $\sim$20% visame amžių intervale.

Palyginus santykius R_{30}/R_{50} ir R_{50}/R_{80}, matome, kad abiejų tipų efektai didesnius neapibrėžtumus sukelia R_{50}/R_{80} atveju. GEN efektai $\log_{10}(\mathrm{M}/\mathrm{M}_{\odot}) \leq 3.0$ spiečiams lemia $\sim$10-30% R_{30}/R_{50} paklaidas, o R_{50}/R_{80} atveju – $\sim$20-60%. Tame pačiame masių intervale ROT efektai sukelia mažesnius neapibrėžtumus: $\sim$5-15% ir $\sim$10-25% R_{30}/R_{50} bei R_{50}/R_{80} atvejais, atitinkamai. Tai rodo, kad R_{30}/R_{50} yra patikimesnis spiečių struktūros ir kompaktiškumo įvertis nei R_{50}/R_{80}, kadangi išorinės spiečių sritys yra jautresnės stochastiniams efektams.

4.6 pav. rodo, kad iš FGC nustatomi struktūriniai parametrai paprastai patikimesni didesnės masės spiečiams, išskyrus pačius jauniausius amžius. Daugeliu atvejų GEN ir ROT efektų sukeltos paklaidos mažėja iki maždaug $\sim$1 Gyr amžiaus, o ties 10 Gyr vėl padidėja. Išimtis stebima $\log_{10}(\mathrm{M}/\mathrm{M}_{\odot}) = 2.0$ objektams, kuriems matome priešingą δ_{ROT} priklausomybę nuo amžiaus. Labai jauni mažos masės spiečiai dažniausiai neturi PMS žvaigždžių, tačiau laikui bėgant juose atsiranda ryškių dominuojančių PMS žvaigždžių. Stochastiškas tokių žvaigždžių pasiskirstymas mažos masės spiečiuose gali stipriai paveikti FGC formą, o tai padidina struktūrinių parametrų neapibrėžtumą.

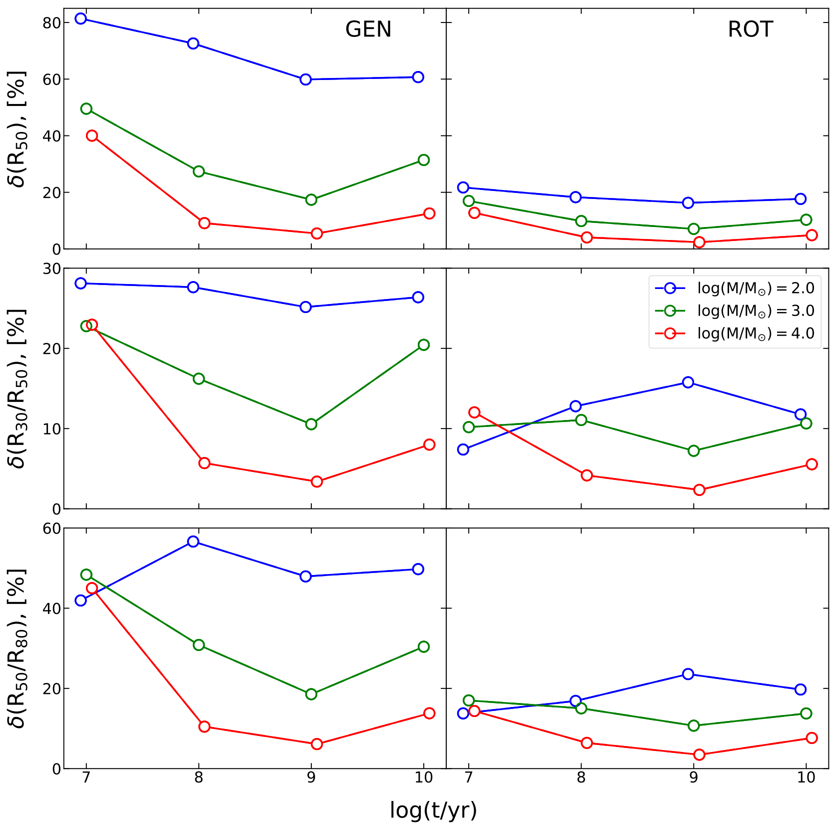

4.6 pav. Santykinių (išreikštų procentais) spiečių struktūrinių parametrų paklaidų priklausomybė nuo amžiaus. Kairysis stulpelis rodo medianinius neapibrėžtumus dėl IMF ir žvaigždžių erdvinio pasiskirstymo stochastiškumo (δ_{GEN}), o dešinysis – paklaidas, atsirandančias dėl spiečių projekcijos efektų (δ_{ROT}). Viršutinė panelių eilė vaizduoja rezultatus R_{50} atveju, vidurinė – R_{30}/R_{50}, o apatinė – R_{50}/R_{80}. Rezultatai pateikti dirbtiniams spiečiams su $r_c = 0.2''$ ir $\gamma = 2.8$ parametrais, trijų skirtingų spiečių masių atveju (žr. legendą). Dėl aiškumo mėlyni ir raudoni simboliai (bei jungiančios linijos) yra šiek tiek pastumti išilgai X ašies nuo tikrųjų amžiaus reikšmių.

Apibendrinant, mažos masės ($\log_{10}(\mathrm{M}/\mathrm{M}_\odot) \lesssim 3.0$) ir jaunų ($\log_{10}(t/\mathrm{yr}) \lesssim 8.0$) spiečių struktūriniai parametrai, nustatyti remiantis vien FGC analize, pasižymi dideliais neapibrėžtumais ir turėtų būti interpretuojami atsargiai. Projekcijos efektai R_{50} atveju gali sukelti iki 10-20% paklaidą, tačiau IMF stochastiškumas sukelia ženkliai didesnius neapibrėžtumus ir yra pagrindinis paklaidų šaltinis. Nors ryškių žvaigždžių pašalinimas lemia didesnį struktūrinių parametrų tikslumą, tai visų problemų pilnai neišsprendžia, ypač mažos masės jauniems spiečiams. Standartinė apertūrinė fotometrija gali būti naudinga, tačiau nėra pakankama spiečių struktūros charakterizavimui. Todėl aukšto tikslumo analizei reikalingi papildomi metodai, tokie kaip individualių ryškių žvaigždžių įskaitymas (Narbutis et al. 2014; Naujalis et al. 2021) arba detalus 2D paviršinio šviesio modeliavimas (Larsen 1999; Narbutis et al. 2014; Brown & Gnedin 2021).

5 skyrius

Dangaus fono efektai

Realių stebėjimų sąlygomis apertūrinės fotometrijos tikslumą labai įtakoja netolygus dangaus fonas ir ryškios lauko žvaigždės, galinčios iškraipyti spiečių fotometriją ir lemti netiksliai nustatytus fizinius parametrus (Kodaira et al. 2004; Narbutis et al. 2008; Krienke & Hodge 2007, 2008; Hodge et al. 2009, 2010; Johnson et al. 2012; de Meulenaer et al. 2017).

Šiame skyriuje sintetinius spiečius įterpėme į tikrus skirtingo žvaigždžių tankio M 31 disko vaizdus ir įvertinome dangaus fono poveikį fotometrinėms paklaidoms bei jų priklausomybę nuo spiečių parametrų ir apertūrų dydžių.

5.1 Fono laukai

Siekiant įvertinti fono poveikį spiečių apertūrinės fotometrijos ir katalogo pilnumo riboms PHAT apžvalgos kontekste, dirbtinius spiečius (žr. 3 skyrių, 3.1 lentelę) įterpėme į penkis tikrus M 31 diske esančius fono laukus, kurie pasižymi skirtingu žvaigždžių tankiu (5.1 pav.). Fono laukai yra $17'' \times 17''$ dydžio, o tai M 31 atstumu atitinka $\sim 65 \times 65$ pc. Jie yra didesni nei $15'' \times 15''$ dirbtinių spiečių kadrai, o tai leido kiekvieną spiečių įterpti šiek tiek skirtingose atsitiktinėse padėtyse tame pačiame fono lauke, išlaikant tas pačias charakteringas lauko savybes. Tai sumažino sistematinių efektų riziką, kurie galėtų atsirasti visus modelius talpinant toje pačioje vietoje.

Fono laukai buvo parinkti, kad apimtų skirtingus žvaigždžių tankius ir atspindėtų įvairias M 31 diske esančias aplinkas. 5.1 pav. galima pamatyti, kad B1 ir B3 laukai yra aktyvios žvaigždėdaros žieduose ($\sim$15 kpc ir $\sim$10 kpc nuo galaktikos centro), kur būdinga stipri diferencialinė ekstinkcija ir didelis ryškių jaunų žvaigždžių tankis. Tuo tarpu B2 ir B4 laukai yra tarpinėse srityse, kur dominuoja senesnės populiacijos žvaigždės ir yra mažiau dulkių. B5 laukas atspindi centrinę M 31 disko dalį, pasižyminčią itin dideliu žvaigždžių tankiu. Atkreipiame dėmesį, kad B3 laukas yra vienoje pagrindinių M 31 disko struktūrų – 10 kpc žvaigždėdaros žiede, kuriame randama didžioji dalis PHAT apžvalgoje identifikuotų spiečių. Dėl šios priežasties B3 laukas šiame skyriuje plačiai naudojamas analizuojant įvairias parametrų priklausomybes, kaip reprezentatyvus fono laukas, atitinkantis tipines M 31 disko spiečių aplinkos sąlygas.

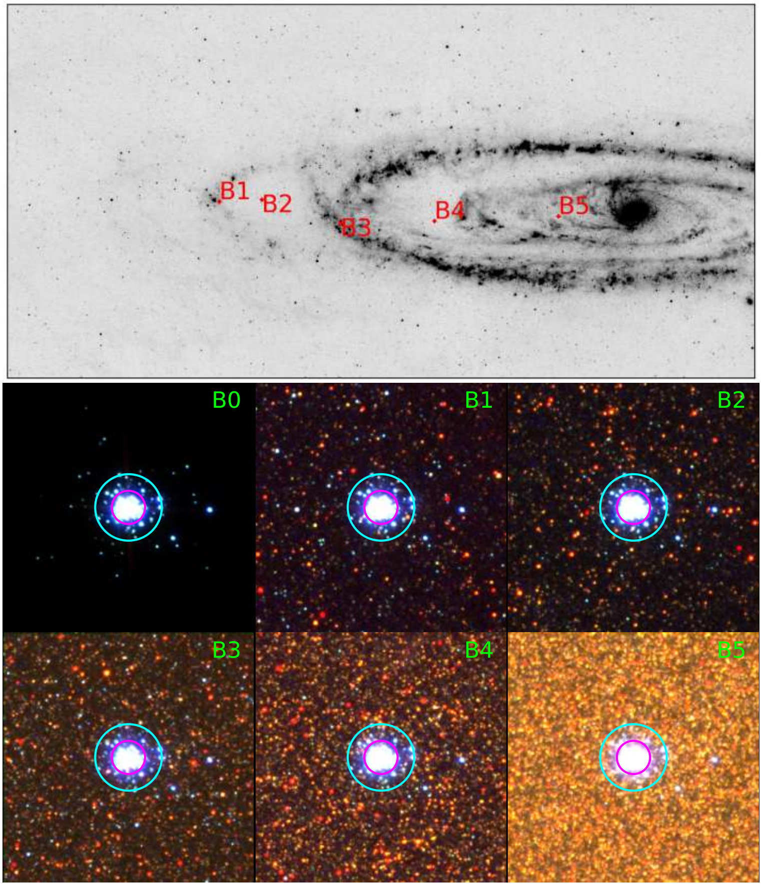

5.1 pav. Fono laukai M 31 diske. Viršutinėje panelėje pavaizduota 24 μm *Spitzer*/MIPS M 31 nuotrauka, kurioje pasirinktų fono laukų (B1–B5) vietos pažymėtos raudonais simboliais. Apatinės panelės rodo dirbtinio spiečiaus ($\log_{10}(M/M_\odot) = 3.5$, $\log_{10}(t/\mathrm{yr}) = 7.0$, $r_c = 0.2''$ ir $\gamma = 2.8$) vaizdus, jį patalpinus į kiekvieną iš fono laukų. B0 žymi atvejį be fono. Violetiniai ir žydri apskritimai žymi apertūras, kurių spinduliai yra atitinkamai $R_{\mathrm{ap}} = 1''$ ir $2''$. $15'' \times 15''$ spalvoti vaizdai gauti sukombinavus $F336W$ (mėlyna), $F475W$ (žalia) ir $F814W$ (raudona) fotometrinių juostų duomenis.

5.2 Fono lygio nustatymas ir apertūrinė fotometrija

Šiame tyrime pritaikėme Johnson et al. (2012) automatinį fono nustatymo metodą, naudotą PHAT ir PHATTER spiečių fotometrijai (Johnson et al. 2012, 2015, 2022). Aplink kiekvieną į fono lauką įterptą spiečių išskiriamas žiedas, kurio ribos yra $1.2 \times R_{\mathrm{ap}}$ ir $3.4 \times R_{\mathrm{ap}}$. Fono lygio įvertinimui visais atvejais naudojama $R_{\mathrm{ap}} = 2.0''$ apertūra. Šis žiedas padalijamas į 10 mažesnių, vienodo ploto žiedų, kurių kiekviename apskaičiuojamas integralinis srautas. Šiems 10 įverčių pritaikome 2σ atmetimo procedūrą. Likusių verčių vidurkį laikėme galutiniu fono lygiu, o jų standartinis nuokrypis prilyginamas fono lygio paklaidai, σ_s. Kadangi fotometrija kiekvienam modeliui atliekama su įvairaus dydžio apertūromis, fono lygio vertė yra perskaičiuojama taip, kad atitiktų pasirinktos apertūros dydį. Fono lygis įvertinamas kiekvienam spiečiui atskirai po jo įterpimo į fono lauką.

Nustačius fono lygį, atliekami apertūrinės fotometrijos matavimai su apertūromis nuo $R_{\text{ap}} = 0.5''$ iki $5.0''$ trijose PHAT juostose ($F336W$, $F475W$, $F814W$), visuose penkiuose fono laukuose ir befoniu (B0) atveju.

Toliau apertūrų dydžiai išreiškiami R_{50} vienetais, naudojant B0 atveju iš $F475W$ FGC nustatytą vertę. Taikome minimalią $R_{\text{ap}} = 0.5''$ ribą, nes mažesnės apertūros yra pernelyg jautrios stochastiniams efektams (žr. 4.2–4.4 poskyrius).

5.3 Fotometrinės paklaidos ir optimalios apertūros

Šiame poskyryje nagrinėjame apertūrinės fotometrijos paklaidas ir tikslumo ribas realistiškomis galaktikų diskų sąlygomis. Analizėje įtraukiami trys pagrindiniai paklaidų šaltiniai: statistinis puasoninis triukšmas, paklaida susijusi su apertūros pozicionavimu, bei paklaidų šaltinis susijęs su dangaus fono lygio neapibrėžtumu. Toliau nagrinėjame tik apibendrintas paklaidas, kurias žymime σ_t, ir į kurias įtraukiame visus tris anksčiau minėtus paklaidų šaltinius.

5.2 pav. pavaizduotos spiečių amžiaus–masės parametrų erdvės sritys, kuriose bent 50% modelių atitinka užduotus tikslumo kriterijus $F475W$, $F336W - F475W$ ir $F475W - F814W$ matavimams. Rezultatai parodyti skirtingiems fonams (B1, B3, B5), paklaidų riboms ($\sigma_t = 0.05, 0.10, 0.30$ mag) ir apertūrų dydžiams (R_{ap}). Paklaidų ribos pasirinktos remiantis de Meulenaer et al. (2015). Esant $\sigma_t \leq 0.05$ mag galima patikimai nustatyti spiečiaus amžių, masę, ekstinkciją ir senesnių nei 1 Gyr spiečių metalingumą. Kai $\sigma_t \leq 0.10$ mag amžius, masė ir ekstinkcija dar gali būti nustatomi gana tiksliai, laikant, kad metalingumas yra žinomas. Esant $\sigma_t \leq 0.30$ mag, dažniausiai įmanoma tik apytiksliai įvertinti amžių ir masę, laikant ekstinkciją ir metalingumą žinomais.

Kairysis 5.2 pav. stulpelis rodo fono aplinkos įtaką, lyginant B1, B3 ir B5 laukus. Fono įtaka stipriausia $F475W - F814W$ spalvai dėl ryškių raudonų lauko žvaigždžių taršos $F814W$ juostoje. UV ir optinių matavimų tikslumas nuo fono savybių priklauso silpniau. Didesnį matavimų tikslumą būtų galima pasiekti taikant pažangesnius fono nustatymo metodus (Narbutis et al. 2014; Naujalis et al. 2021; Kriščiūnas et al. 2023; Pandey & Saha 2025).

Viduriniame 5.2 pav. stulpelyje parodytos amžiaus–masės parametrų erdvės sritys, kuriose bent 50% modelių atitinka skirtingus fotometrinio tikslumo kriterijus ($\sigma_t = 0.05, 0.10, 0.30$ mag). Tiesiškai interpoliuojant tarp rezultatų, gautų $F336W-F475W$ ir $F475W - F814W$ spalvos rodikliams atskirai, gauname, kad B3 ties $t = 1$ Gyr $\sigma_t = 0.05$ mag kriterijų atitinka M $\gtrsim$ 5000 $M_\odot$ spiečiai. $\sigma_t = 0.10$ mag riba pasiekiama $1600 \lesssim M \lesssim 5000\ M_\odot$ spiečiams, o $\sigma_t = 0.30$ mag – $500 \lesssim M \lesssim 1600\ M_\odot$ objektams. $t = 100$ Myr spiečiams šios masės ribos yra žemesnės: $\sigma_t = 0.05$ mag pasiekiama jau ties $M \gtrsim 1000\ M_\odot$. Tuo tarpu $\sigma_t = 0.10$ mag pasiekiama $500 \lesssim M \lesssim 1000\ M_\odot$ masės spiečiams, o $\sigma_t = 0.30$ mag – $200 \lesssim M \lesssim 500\ M_\odot$.

Dešiniajame 5.2 pav. stulpelyje nagrinėjamas apertūros dydžio efektas parametrų erdvės sričiai, kurioje galima pasiekti $\sigma_t \leq 0.05$ mag tikslumą B3 atveju. Palyginami trys R_{ap} variantai: fiksuota $1''$, R_{50} ir $1.5 \times R_{50}$. Individualiai pagal R_{50} parinktos apertūros paprastai padeda atlikti tikslesnę apertūrinę fotometriją nei fiksuota $1''$ apertūra. Plačiausia parametrų erdvės sritis, kur galioja $\sigma_t \leq 0.05$ mag kriterijus,

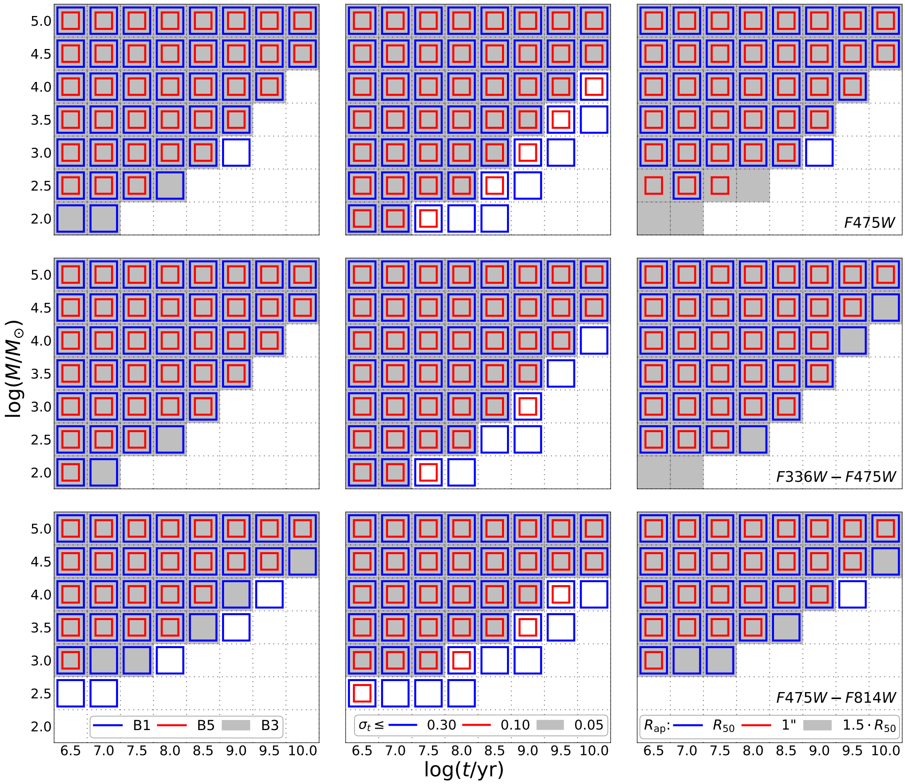

5.2 pav. Spiečių masės–amžiaus parametrų erdvės sritys, kuriose apertūrinė fotometrija atitinka nustatytus tikslumo reikalavimus. Pilkos sritys ir spalvoti kvadratai žymi masės ir amžiaus kombinacijas, kurių atveju bent 50% dirbtinių spiečių (iš ∼1300) pasižymi mažesne apibendrinta fotometrine paklaida σ_t nei pasirinkta tikslumo riba. Viršutinėje, vidurinėje ir apatinėje panelių eilėse pateikti rezultatai $F475W$ ryškiui, $F336W - F475W$ ir $F475W - F814W$, atitinkamai. Kairiajame stulpelyje palyginti skirtingų fono laukų rezultatai, gauti naudojant $R_{\rm ap} = 1.5 \times R_{50}$ apertūrą ir taikant $\sigma_t \leq 0.05$ mag tikslumo ribą. Vidurinysis stulpelis rodo priklausomybę nuo pasirinktos σ_t ribos B3 lauko atveju, naudojant $R_{\rm ap} = 1.5 \times R_{50}$ apertūrą. Dešiniajame stulpelyje parodytas apertūros dydžio efektas B3 lauko atveju, taikant $\sigma_t \leq 0.05$ mag ribą. Pateikti rezultatai gauti matuojant $R_{50} = 0.25'' - 1.00''$ dydžio dirbtinius spiečius.

gaunama naudojant $R_{50} = 1.5 \times R_{50}$. Mažesnės apertūros gali sumažinti fono taršą (Narbutis et al. 2007b), tačiau yra jautresnės stochastiniams efektams, todėl daugeliu atvejų rekomenduojama rinktis $R_{\rm ap} > R_{50}$.

Siekiant patikslinti 4 skyriuje pateiktas apertūrų dydžio rekomendacijas, kiekvienam spiečiui nustatėme optimalų apertūros spindulį $R_{\rm opt}$, atitinkantį mažiausią σ_t vertę. 5.3 pav. matome, kad blausesniems spiečiams optimalios apertūros yra mažesnės. Tipiniams M 31 spiečiams $R_{\rm opt}$ varijuoja (1–2)$\times R_{50}$ intervale. $F475W - F814W$ spalvai optimalios apertūros paprastai yra mažesnės dėl ryškių raudonų fono žvaigždžių taršos. Kituose fono laukuose nustatytos panašios tendencijos.

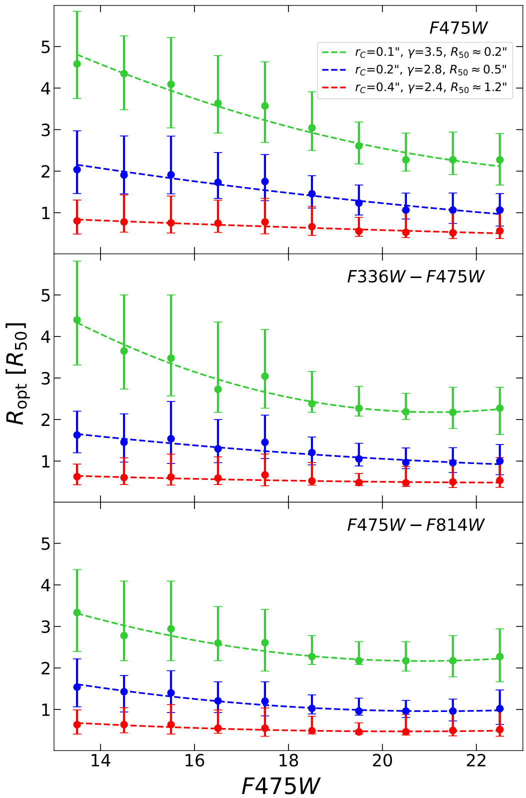

5.3 pav. Optimalūs apertūrų spinduliai, R_{opt}, priklausomai nuo integralinio spiečiaus $F475W$ ryškio, pamatuoto B0 atveju. Viršutinė, vidurinė ir apatinė panelės rodo R_{opt} vertes, skirtas $F475W$, $F336W - F475W$ ir $F475W - F814W$ matavimams, atitinkamai. Rezultatai pateikti B3 laukui ir trims geometrinių parametrų r_c bei γ kombinacijoms (žr. legendą; čia taip pat nurodytos medianinės R_{50} vertės atitinkamai parametrų kombinacijai). Simboliai rodo medianines R_{opt} reikšmes, o paklaidų „ūsai" – 16–84 procentilių intervalus. Punktyrinės kreivės žymi prie medianų mažiausių kvadratų metodu priderintas antro laipsnio polinomines funkcijas.

5.4 Katalogo pilnumas ir selekcijos efektai

Toliau nagrinėjame dangaus fono įtaką spiečių aptikimo ir katalogo pilnumo riboms. Šie aspektai apibrėžia spiečių analizės galimybių ribas ir parametrų erdvę, kurioje galime patikimai interpretuoti rezultatus. Tam naudojome tolydžią 20 milijonų modelių imtį, suskaičiuotą $F475W$ juostoje (žr. 3.3 lentelę). Šiuo tikslu spiečiaus kontrastą fono atžvilgiu apibrėžiame santykiu:

$$\mathrm{CBR} = \frac{F_{cl}}{F_{bg}}, \tag{5.1}$$

čia F_{cl} yra spiečiaus $F475W$ srautas B0 atveju, o F_{bg} – fono $F475W$ srautas pasirinktame M 31 fono lauke; abu srautai matuojami su $R_{\mathrm{ap}} = R_{50}$ apertūra. Kai spiečiaus $R_{50} < 0.5''$, naudojame minimalią $R_{\mathrm{ap}} = 0.5''$ apertūrą, siekiant išvengti stiprių stochastinių efektų. 5.4 pav. pateikiame dirbtinių spiečių pavyzdžius B0 ir B3 laukuose bei jų CBR reikšmes.

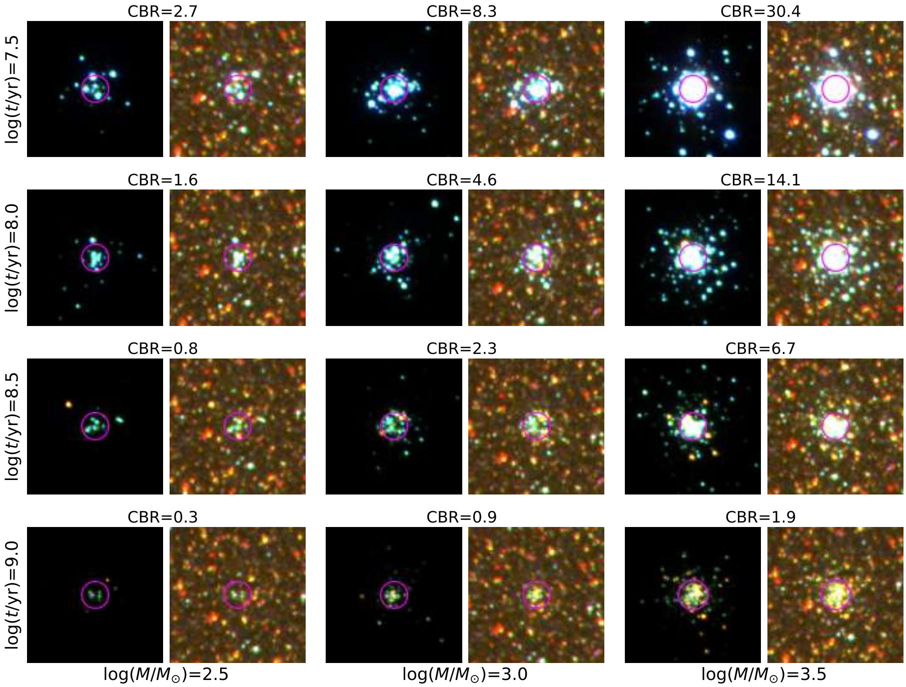

5.4 pav. Skirtingo amžiaus ir masės dirbtinių spiečių vaizdai B0 lauke (kairioji panelė kiekvienoje poroje) ir B3 lauke (dešinioji panelė). Spiečių masės nurodytos po kiekvienu stulpeliu, o amžiai – kiekvienos eilutės kairiojoje pusėje. Visi pavaizduoti spiečiai sugeneruoti naudojant $r_c = 0.2''$ ir $\gamma = 2.8$ parametrus. Virš kiekvienos vaizdų poros pateiktas spiečiaus ir fono signalų santykis CBR (žr. apibrėžimą 5.4 poskyryje), apskaičiuotas B3 laukui. Violetiniai apskritimai žymi apertūras, naudotas CBR vertėms nustatyti. $5'' \times 5''$ spalvoti vaizdai gauti sukombinavus $F336W$ (mėlyna), $F475W$ (žalia) ir $F814W$ (raudona) duomenis.

Spiečius su CBR $\geq$ 1.0 įprastai galime nesunkiai atskirti nuo fono vizualinės paieškos metu, todėl šį kriterijų laikome žmogaus atliekamos paieškos riba. CBR $\geq$ 0.4 atitinka apie 1 mag blausesnius objektus, kuriuos potencialiai gali aptikti šiuolaikiniai mašininio mokymosi (ML) algoritmai (Thilker et al. 2022).

Naudodami CBR reikšmes įvertinome selekcijos efektų įtaką stebimai spiečių masės funkcijai (CMF) PHAT kontekste (žr. 5.5 pav.). Pradinę CMF aprašėme Schechter laipsnine funkciją su rodikliu $\beta = -2$ (Schechter 1976; Gieles 2009) ir charakteringa funkcijos lūžio mase $M_C = 10^4\ M_\odot$. Tai atitinka M 31 disko spiečių populiaciją (Johnson et al. 2017).

Viršutinėje 5.5 pav. panelėje lyginame atkurtas CMF skirtingiems amžiams, taikant dvi aptikimo ribas: CBR $\geq$ 0.4 ir CBR $\geq$ 1.0. Čia pateikiame B3 lauko rezultatus. Jaunesniems nei 100 Myr spiečiams CBR $\geq$ 0.4 sąlyga užtikrina CMF iki ~300 $M_\odot$, o CBR $\geq$ 1.0 atveju pilnumo efektai pasidaro pastebimi jau ties ~1000 $M_\odot$. Ties 300 Myr šios ribos atitinkamai yra ~600 $M_\odot$ ir ~1800 $M_\odot$. Tai rodo, kad naudojant

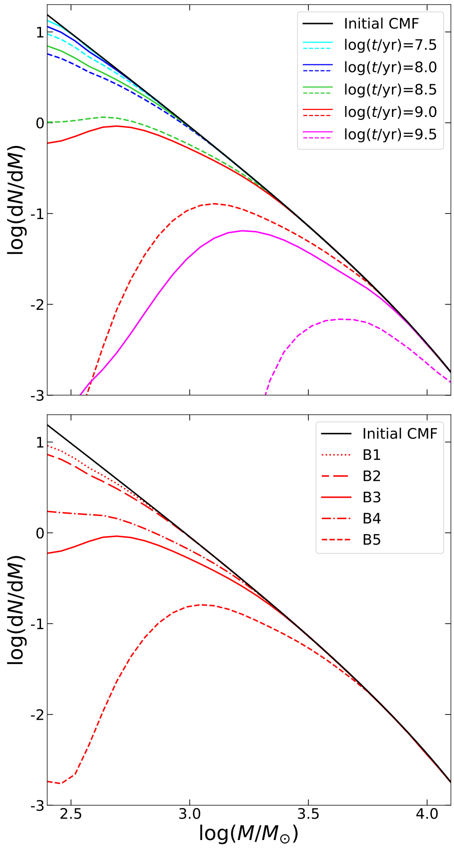

5.5 pav. Spiečių masės funkcijos (CMF) selekcijos efektai. Pradinė CMF (juoda linija) aprašoma Schechter funkcija su laipsnio rodikliu $\beta = -2$ ir charakteringa funkcijos lūžio mase $M_C = 10^4\,M_\odot$. Viršutinė panelė: skirtingo amžiaus dirbtinių spiečių CMF (žr. legendą) B3 lauko atveju, taikant CBR ≥ 1.0 (punktyrinės linijos) ir CBR ≥ 0.4 (ištisinės linijos) aptikimo kriterijus. Apatinė panelė: $\log_{10}(t/\mathrm{yr}) = 9.0$ amžiaus spiečių CMF B1–B5 laukuose; čia parodyta priklausomybė nuo aplinkos ir atstumo iki M 31 centro, taikant CBR ≥ 0.4 aptikimo kriterijų. Rezultatai gauti $R_{50} = 0.25'' - 1.00''$ dydžio dirbtiniams spiečiams.

ML aptikimo metodus galima pasiekti ~3 kartus mažesnę minimalią spiečių masę, lyginant su vizualine paieška, o tai M 31 (taip pat ir M 33) disko atveju įgalintų atlikti patikimus CMF tyrimus net ir labai mažos masės spiečių srityje.

Apatinėje 5.5 pav. panelėje matome, kad atkuriama CMF stipriai priklauso nuo aplinkos. Ties $t = 1$ Gyr ir esant CBR ≥ 0.4 aptikimo ribai, išorinę disko aplinką atitinkančiuose B1 ir B2 laukuose CMF atkuriama iki ~500 $M_\odot$. B3 ir B4 fono laukuose, kurie atitinka žvaigždėdaros ir vidutinio tankio sritis, ši masės riba pasislenka jau ties ~1500 $M_\odot$. B5 lauke, kuris atitinka labai tankią vidinę disko dalį, CMF galima atkurti jau tik virš ~3000 $M_\odot$. Taigi patikimai atkuriamos CMF masės riba M 31 diske kinta kelis kartus, todėl atliekant CMF tyrimus, ypač susijusios su jos radialinėmis priklausomybėmis, būtina atsižvelgti į aplinkos lemiamus selekcijos efektus.

6 skyrius

Žvaigždžių spiečiai M 31 diske

Šiame skyriuje nagrinėjame M 31 disko mažos ir vidutinės masės (~300–30 000 $M_{\odot}$) spiečių populiaciją, jų formavimąsi ir evoliuciją. Dėl M 31 artumo ir aukštos PHAT apžvalgos erdvinės skyros galima išsamiai tirti šiuos, ankstesniuose užgalaktinių spiečių darbuose menkai nagrinėtus, objektus.

6.1 Spiečių duomenys

Tyrime naudojame M 31 žvaigždžių spiečių fizinių ir struktūrinių parametrų katalogą (Kriščiūnas et al. 2026), sudarytą remiantis adaptyvios apertūrinės fotometrijos matavimais (Naujalis et al. 2021; Kriščiūnas et al. 2023) bei išskirtų žvaigždžių fotometrija (Williams et al. 2023). Spiečių amžius, masė ir ekstinkcija nustatyti apertūrinės fotometrijos rezultatus lyginant su stochastiniais modeliais (de Meulenaer et al. 2015, 2017) bei patikslinti naudojant CMD ir izochronų derinimą (Čeponis et al. 2024). Struktūriniai parametrai buvo apskaičiuoti iš srauto augimo kreivių. Šį katalogą sudaro 1922 spiečiai jaunesni nei 800 Myr. Po papildomos peržiūros šiam tyrimui pašaliname 4 objektus, todėl galutinė tiriama imtis – 1918 spiečių.

6.1 pav. parodytas spiečių masės–amžiaus skirstinys. Čia objektai suskirstyti pagal R_{50} į kompaktiškus ($R_{50} < 1.8$ pc, mėlyni simboliai) ir labiau išplitusius ($R_{50} \geq 1.8$ pc, raudoni simboliai). Spiečių masės apima platų intervalą nuo $\lesssim$300 $M_{\odot}$ iki 30 000 $M_{\odot}$, tačiau didžioji dalis objektų M $\gtrsim$ 1000 $M_{\odot}$. Nedidelis mažos masės spiečių skaičius susijęs su selekcijos efektais, o didelių masių spiečių (M $\gtrsim$ 2000 $M_{\odot}$) skaičiaus mažėjimas greičiausiai yra fizikinės kilmės (žr. 5.4 poskyrį).

Amžiaus skirstinyje matomas ryškus pikas ties ~150-250 Myr, kuris indikuoja tuo metu padidėjusią spiečių formavimosi spartą, galimai dėl sąveikos su galaktika M 32 prieš ~210 Myr (Block et al. 2006). Šio žvaigždėdaros žybsnio egzistavimą implikuoja ir Cefeidžių žvaigždžių tyrimai (De Somma et al. 2025). Po ~300 Myr stebimas reikšmingas spiečių skaičiaus mažėjimas, kurį greičiausiai nulemia selekcijos ir spiečių išardymo efektų kombinacija.

Jauni ($t \lesssim$ 100 Myr) objektai dažniausiai yra mažos masės, tačiau yra ir keletas masyvių ($\gtrsim$ 10 000 $M_{\odot}$), kurie pasižymi dideliu dydžiu – tikėtina, kad pastarieji yra gravitaciškai nesurištos žvaigždžių asociacijos. Lyginant dvi spiečių dydžio grupes, didesni spiečiai vidutiniškai yra šiek tiek senesni ir masyvesni, bei jų masių skirstinys pasižymi platesne didelės masės „uodega", o kompaktiški labiau dominuoja

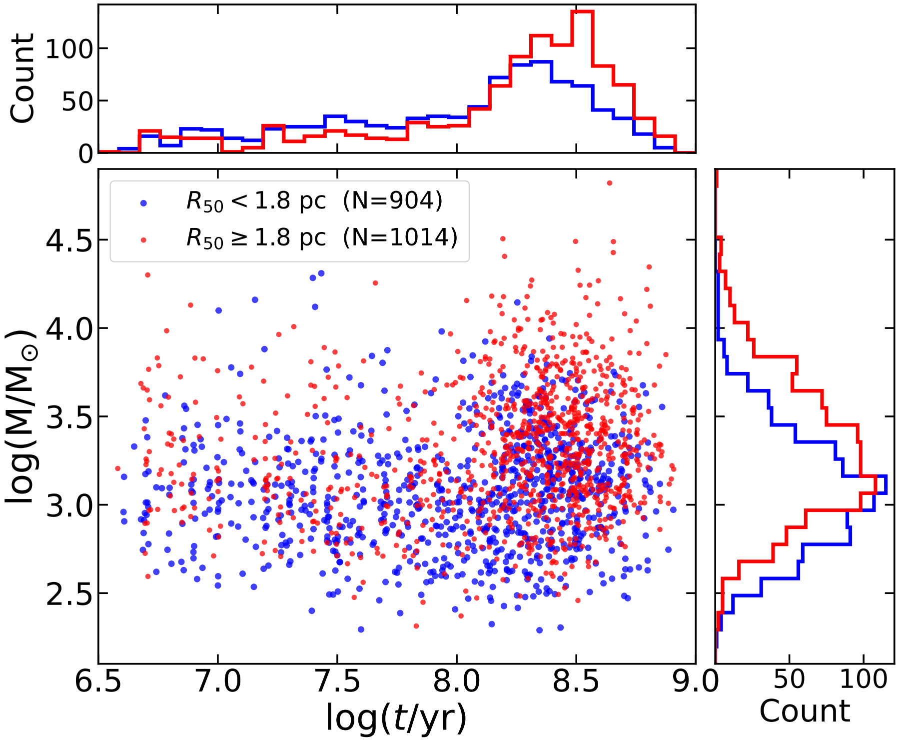

6.1 pav. M 31 žvaigždžių spiečių masės–amžiaus diagrama. Objektai suskirstyti į dvi grupes pagal pusės šviesio spindulį: kompaktiški ($R_{50} < 1.8$ pc; mėlyna spalva) ir išplitę ($R_{50} \geq 1.8$ pc; raudona spalva) spiečiai. Siekiant geresnio vizualaus aiškumo, duomenų taškams pridėtas nedidelis atsitiktinis poslinkis pagal Gauso skirstinį (σ = 0.01 pagal $\log_{10}(t/\text{yr})$ ir σ = 0.025 pagal $\log_{10}(\text{M}/\text{M}_\odot)$). Viršutinėje panelėje pateikti abiejų grupių amžių skirstiniai, o dešinėje – jų masių skirstiniai.

mažų masių srityje. Tai rodo galimą spiečių masės–spindulio sąryšį, kurį plačiau nagrinėjame 6.3 poskyryje.

6.2 pav. lyginame M 31 disko spiečių R_{50} skirstinį su skirstiniais M 33 ir PT galaktikose (jų spiečių imtys apribotos iki $\log_{10}(\text{M}/\text{M}_\odot) \leq 5.0$ ir ~800 Myr). M 33 duomenys paimti iš PHATTER spiečių katalogo (Johnson et al. 2022). PT spiečių dydžiai paimti iš Hunt & Reffert (2024) *Gaia* spiečių katalogo. Mes analizei naudojame tik tuos PT spiečius, kuriuos Hunt & Reffert (2024) klasifikuoja kaip "open clusters", t.y. padrikuosius spiečius. Tiesa, PT spiečiams dydžio įvertinimo metodika drastiškai skiriasi ir yra paremta individualių spiečiaus žvaigždžių-narių skaičiavimu. Todėl palyginimas su PT yra mažiau tiesioginis ir turėtų būti interpretuojamas atsargiai.

PT spiečiai vidutiniškai yra didesni nei M 31 ir M 33, o M 33 spiečiai yra šiek tiek kompaktiškesni nei M 31. Medianinės R_{50} vertės (po 3σ atmetimo) yra: M 31 – $\tilde{R}_{50} = 1.82^{+0.76}_{-0.57}$ pc; M 33 – $\tilde{R}_{50} = 1.35^{+0.66}_{-0.45}$ pc; PT – $\tilde{R}_{50} = 3.10^{+1.19}_{-0.95}$ pc. Čia paklaidos žymi 16–84 procentilius. PT spiečių dydžiai atitinka kitų artimų galaktikų spiečių skirstinius, kur jaunų spiečių charakteringas dydis yra $R_{50} \approx 3$ pc (Larsen 2004; Lee et al. 2005; Scheepmaker et al. 2007; Ryon et al. 2015, 2017; Brown & Gnedin 2021).

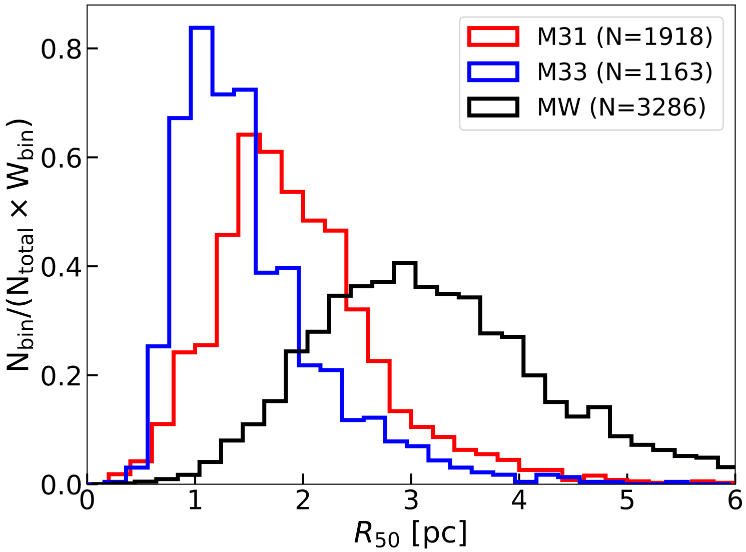

6.2 pav. M 31 žvaigždžių spiečių dydžių skirstinio palyginimas su kitų Vietinės grupės spiralinių galaktikų duomenimis. M 33 spiečių duomenys paimti iš Johnson et al. (2022) katalogo, o PT – iš Hunt & Reffert (2024) katalogo. Visoms galaktikoms įtraukti tik jaunesni nei 800 Myr spiečiai. Siekiant vizualaus aiškumo, M 33 ir PT histogramos šiek tiek pastumtos M 31 histogramos atžvilgiu.

M 31 ir M 33 spiečiai atrodo kompaktiškesni. Šiuos skirtumus gali lemti tiek aplinkos veiksniai, tiek selekcijos efektai, tačiau svarbus veiksnys gali būti ir nevienoda dydžių įvertinimo metodika. M 31 atveju, ankstesni antžeminiai Subaru stebėjimai (Kodaira et al. 2004; Šablevičiūtė et al. 2006, 2007; Vansevičius et al. 2009) taip pat indikuoja, kad šiai galaktikai būdingi kompaktiški spiečiai ($R_{50} \sim 1.5$ pc). Panašios išvados gautos ir M 33 galaktikai: ankstesni HST tyrimai rodo, kad jos spiečiai įprastai mažesni nei PT, M 31 ar Magelano Debesyse (San Roman et al. 2009, 2012).

6.2 Žvaigždžių spiečių struktūrinė evoliucija

Toliau nagrinėjame spiečių dydžio evoliuciją. Siekiame tirti gravitaciškai surištų, ilgai gyvuojančių spiečių evoliuciją, tačiau tikėtina, kad Kriščiūnas et al. (2026) imtyje yra ir nesurištų asociacijų. Kad sumažinti tokių objektų įtaką, pritaikėme Gieles & Portegies Zwart (2011) dinaminio amžiaus kriterijų Π, kuris apibrėžiamas kaip spiečiaus amžiaus t ir žvaigždžių perėjimo per spiečių laiko t_{cr} santykis:

$$\Pi = t/t_{cr}, \tag{6.1}$$

kur perėjimo per spiečių laikas

$$t_{cr} \equiv 10 \left(\frac{R_{50}^3}{GM} \right)^{1/2}, \tag{6.2}$$

čia G – gravitacijos konstanta, M – spiečiaus masė. objektai su $\Pi > 1$ laikomi gravitaciškai surištais spiečiais, o su $\Pi < 1$ – nesurištomis asociacijomis (Gieles & Portegies Zwart 2011).

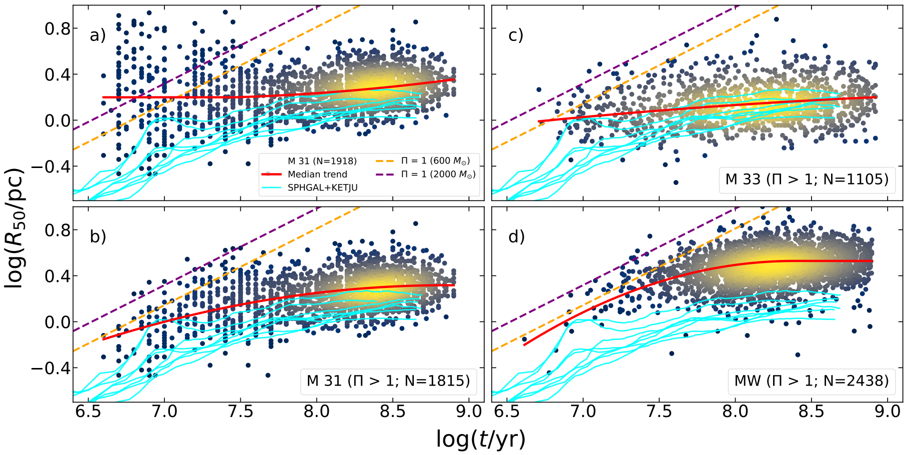

6.3 pav. Spiečių dydžio priklausomybė nuo amžiaus. a) panelėje parodyti visi 1918 M 31 objektai, o b) panelėje – tik tie, kurie atitinka dinaminio amžiaus kriterijų $\Pi > 1$. c) panelėje parodyti M 33 žvaigždžių spiečiai iš Johnson et al. (2022) katalogo. d) panelėje – PT spiečiai iš Hunt & Reffert (2024) *Gaia* katalogo; čia įtraukti tik tie PT objektai, kurie kataloge klasifikuojami kaip „padrikieji spiečiai". M 33 ir PT atvejais įtraukti tik $t \leq 800$ Myr ir $\log_{10}(\mathrm{M}/\mathrm{M}_{\odot}) \leq 5.0$ spiečiai, kurie atitinka $\Pi > 1$ kriterijų. Raudonos kreivės rodo medianinę R_{50} evoliuciją. Žydros kreivės rodo individualių spiečių iš SPHGAL + KETJU modelio (Lahén et al. 2025) evoliucinius trekus. Šie trekai apglotninti su slenkančiu pagal $\log_{10}(t/\mathrm{yr})$ ašį 0.2 dex pločio langu. Punktyrinės linijos žymi $\Pi = 1$ ribą skirtingoms spiečių masėms.

6.3 pav. (a ir b panelėse) parodyta M 31 disko spiečių R_{50} priklausomybė nuo amžiaus: a) visi 1918 objektų, b) tik atitinkantys $\Pi > 1$ kriterijų. Neapribojus imties pagal Π, aiškios spiečių plėtimosi ar traukimosi tendencijos nematyti, tačiau jaunesni nei ~50 Myr objektai pasižymi daug didesne dydžių sklaida. Tai gali rodyti vykstančią struktūrinę evoliuciją, kai dideli objektai yra gravitaciškai nesurištos, efektyviai ardomos sistemos, o maži objektai – kompaktiški, besiplečiantys spiečiai. Pritaikius $\Pi > 1$ kriterijų, M 31 spiečių medianinis R_{50} didėja su amžiumi. Sparčiausias augimas vyksta per pirmuosius ~30 Myr, kai R_{50} padidėja daugiau nei du kartus – nuo ~0.6 pc iki ~1.6 pc; vėliau augimas suletėja. M 33 ir PT spiečiams po ~ 100,Myr taip pat aiškios dydžio kaitos beveik nematyti.

6.3 pav. stebėjimų rezultatai palyginti su SPHGAL+KETJU hidrodinaminiais spiečių modeliais (Lahén et al. 2025). Mes naudojome 1% saulės metalingumo nykštukinės galaktikos (virialinė masė $4 \times 10^{10}\,\mathrm{M}_{\odot}$) modeliavimo rezultatus. Nepaisant labai skirtingų fizinių sąlygų, evoliuciniai trekai gerai atitinka M 31 stebėjimų rezultatus taikant $\Pi > 1$ kriterijų. Modeliuose ankstyvą spiečių plėtimąsi lemia dujų pašalinimas, žvaigždžių evoliucija ir vidiniai dinaminiai procesai, silpninantys spiečiaus gravitacinį potencialą. Tokį scenarijų palaiko ir JWST stebėjimai, rodantys, kad spiečiai iš gimtųjų debesų išnyra per ~6 Myr (Knutas et al. 2025; Pedrini et al. 2026).

Sutapimas tarp mūsų rezultatų ir SPHGAL + KETJU modelių leidžia manyti, kad ankstyvą M 31 spiečių plėtimąsi greičiausiai lemia vidiniai procesai,o ne išorinės perturbacijos, pavyzdžiui susidūrimai su GMC (Jørgensen & Church 2025). Nors stebimas M 31 spiečių dydžio augimas gali būti bent iš dalies susijęs su $\Pi > 1$ kriterijaus taikymu, kompaktiškų 100–300 Myr spiečių trūkumas rodo, kad bent dalis dydžio augimo yra fizinė.

Siekiant įsitikinti, kad M 31 disko spiečių dydžiai iš tiesų kinta per pirmas kelias dešimtis Myr, 6.4 pav. palyginome jaunesnių nei 30 Myr ir senesnių spiečių R_{50} skirstinius. Jaunesnių nei 30 Myr spiečių R_{50} skirstinio maksimumas yra ties $\sim$1.0 pc, o senesnių – ties $\sim$1.7 pc. Svarbu tai, kad šis skirtumas išlieka ir netaikant Π atrankos. Taigi, jaunesni nei 30 Myr spiečiai iš tiesų yra kompaktiškesni, o stebimas R_{50} didėjimas greičiausiai atspindi realų fizinį spiečių plėtimąsi. Šio ankstyvo plėtimosi trukmė ($\sim$30 Myr) sutampa su masyvių žvaigždžių gyvavimo trukme, todėl tikėtina, kad reikšmingą vaidmenį evoliucijoje gali turėti žvaigždžių vėjai bei supernovų grįžtamasis ryšys.

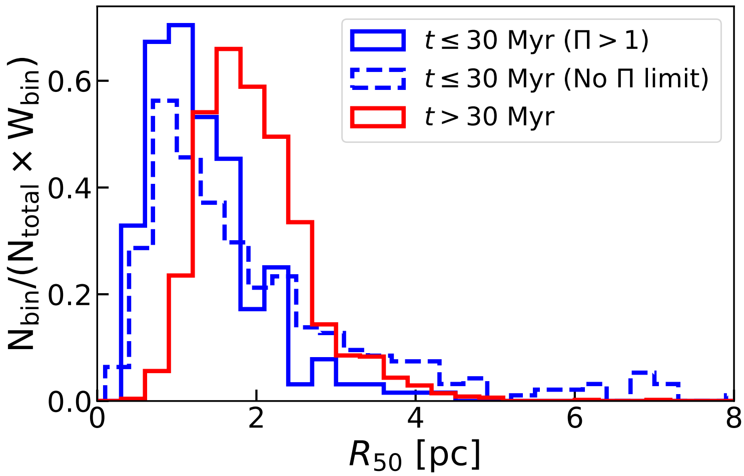

6.4 pav. R_{50} skirstinių palyginimas tarp jaunesnių nei 30 Myr (mėlyna) ir senesnių nei 30 Myr (raudona) M 31 spiečių. Ištisinėmis linijomis žymimos histogramos rodo imtis, atrinktas taikant $\Pi > 1$ kriterijų, o mėlyna punktyrinė histograma apima visus jaunus spiečius, netaikant selekcijos pagal Π.

6.3 Masės – spindulio sąryšis

Dar viena svarbi spiečių populiacijos savybė yra masės–spindulio sąryšis, kuris padeda geriau apibrėžti galimas spiečių formavimosi ir evoliucijos teorijas. 6.5 pav. rodo spiečių pasiskirstymą masės–R_{50} erdvėje šešiuose amžiaus intervaluose. Palyginimui pateikti du teoriniai sąryšiai: pastovaus tankio $R_{50} \propto \mathrm{M}^{1/3}$ (Choksi & Kruijssen 2021; Grudić et al. 2021) ir $R_{50} \propto \mathrm{M}^{1/9}$ (Gieles & Renaud 2016; Renaud 2018) pusiausvyros, kurią lemia potvyniniai smūgiai ir relaksacijos procesai. Taip pat parodyti ir `SPHGAL` + `KETJU` evoliuciniai trekai. 6.5 pav. a–c panelėse aiškiai matome ankstyvą spiečių plėtimąsi: per pirmuosius keliasdešimt Myr spiečių R_{50} didėja kaip ir `SPHGAL` + `KETJU` trekai. Jauniausių spiečių atveju (<10 Myr ir 10–30 Myr) gali susidaryti stataus sąryšio įspūdis, tačiau šias imtis veikia $\Pi > 1$ atranka ir susiję galimi selekcijos efektai. Dėl patikimų įrodymų trūkumo, negalima teigti, jog jaunesnių nei 100 Myr spiečių atveju egzistuoja aiškus masės–spindulio sąryšis. Senesniems nei ~100 Myr spiečiams išryškėja aiškus, nors ir gana silpnas, sąryšis (žr. 6.5 pav. d–f). Jo polinkio kampas yra tarp $R_{50} \propto M^{1/3}$ ir $R_{50} \propto M^{1/9}$. `SPHGAL` + `KETJU` trekai gerai atitinka stebimą M 31 disko spiečių pasiskirstymą.

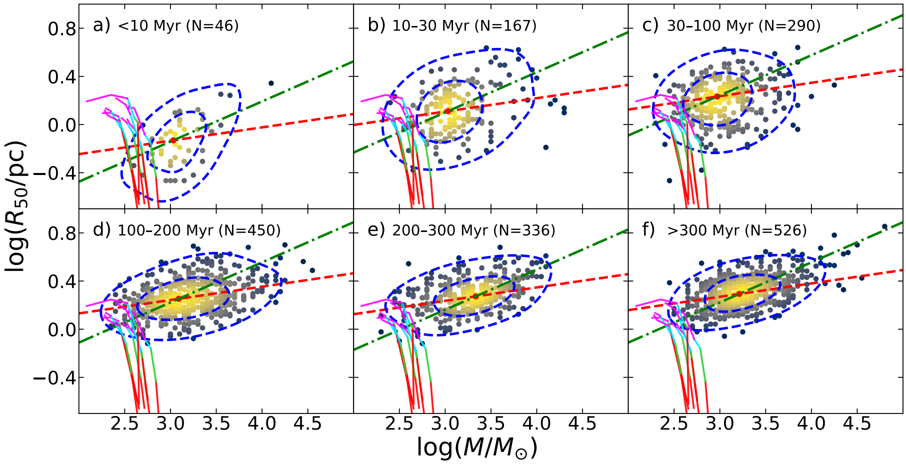

6.5 pav. Spiečių masės–spindulio sąryšio evoliucija. Kiekvienoje panelėje vaizduojama R_{50} priklausomybė nuo masės skirtingiems amžių intervalams (nurodyta panelių viršuje). Skaičius šalia amžiaus intervalo nurodo imties dydį. Palyginimui parodyti pastovaus tankio $R_{50} \propto M^{1/3}$ (žalia punktyrinė–taškinė linija) ir pusiausvyros $R_{50} \propto M^{1/9}$ (raudona punktyrinė linija) sąryšiai. Mėlyni punktyriniai kontūrai žymi skirstinio KDE: vidinis kontūras apima 39.3% KDE integralo aplink maksimumą (1σ sritis), o išorinis – 86.5% (2σ sritis). Segmentais nuspalvintos kreivės rodo `SPHGAL` + `KETJU` evoliucinius trekus (Lahén et al. 2025); spalvos atitinka amžiaus intervalus: <10 Myr (raudona), 10–30 Myr (žalia), 30–100 Myr (žydra) ir >100 Myr (violetinė). Visose panelėse įtraukti tik $\Pi > 1$ kriterijų atitinkantys spiečiai.

Detalesnė masės–spindulio sąryšio analizė pateikta 6.6 pav.. Pasiskirstymas parametrų erdvėje aproksimuojamas kovariacijos elipse, o sąryšio laipsnio rodiklį apibrėžiame per šios elipsės didžiosios ašies polinkio kampą. Jaunesniems spiečiams (10–100 Myr, 6.6 pav.a) gauname silpną sąryšį $R_{50} \propto M^{0.16\pm0.04}$, tačiau laipsnio rodiklio paklaida santykinai didelė ir šis įvertis nėra pakankamai apibrėžtas dėl Π atrankos ir ankstyvos struktūrinės evoliucijos poveikio. Senesniems nei 100 Myr spiečiams gauname patikimesnį sąryšį: $R_{50} \propto M^{0.18\pm0.01}$. Po ~100 Myr evoliucijos `SPHGAL` + `KETJU` modeliai gerai atitinka stebimą M 31 spiečių pasiskirstymą ir nustatytą masės–spindulio sąryšį. Gauta priklausomybė panaši į Hwang & Lee (2010) rezultatą M 51 spiečiams (0.16±0.02), bet silpnesnė nei kitose artimose galaktikose ($R_{50} \propto M^{0.25-0.33}$; Ryon et al. 2015; Krumholz et al. 2019; Cuevas-Otahola et al. 2021; Brown & Gnedin 2021). Mūsų nustatytas M 31 spiečių sąryšis statesnis nei teorinis Gieles & Renaud (2016) pusiausvyros sąryšis ($R_{50} \propto M^{1/9}$), tačiau reikšmingai silpnesnis nei kiti teoriniai sąryšiai: $R_{50} \propto M^{1/2}$ (Choksi & Kruijssen 2021), $R_{50} \propto M^{1/3}$ (Grudić et al. 2021) ar $R_{50} \propto M^{1/4}$ (Grudić et al. 2023a). Svarbu paminėti, jog nustatytas M 31

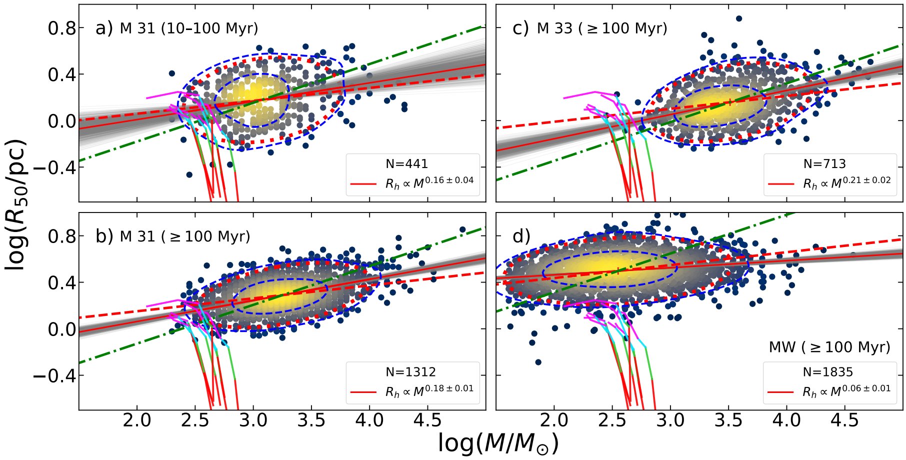

6.6 pav. Žvaigždžių spiečių masės–spindulio sąryšiai. a) panelėje parodyti 10–100 Myr amžiaus M 31 spiečiai, o b) panelėje – senesni nei 100 Myr M 31 spiečiai. c) panelėje – senesni nei 100 Myr M 33 spiečiai (Johnson et al. 2022). d) panelėje – senesni nei 100 Myr PT spiečiai (Hunt & Reffert 2024); čia įtraukti tik PT spiečiai, kurie klasifikuoti kaip „padrikieji spiečiai". Imčių dydžiai (N) nurodyti legendose. Raudonos taškinės linijos žymi 2σ kovariacijos elipses, o raudonos ištisinės linijos – jų didžiųjų ašių polinkio kampus; legendose pateiktos šių polinkio kampų vertės kaip masės–spindulio sąryšio laipsnio rodikliai. Pilkos linijos rodo 1000 individualių polinkio kampų, gautų taikant pakartotinės atrankos metodą. Palyginimui parodyti pastovaus tankio $R_{50} \propto \mathrm{M}^{1/3}$ (žalia punktyrinė–taškinė linija) ir pusiausvyros $R_{50} \propto \mathrm{M}^{1/9}$ (raudona punktyrinė linija) sąryšiai. Mėlyni punktyriniai kontūrai žymi skirstinio KDE: vidinis kontūras apima 39.3% KDE integralo aplink maksimumą (1σ sritis), o išorinis – 86.5% (2σ sritis). Segmentais nuspalvintos kreivės rodo `SPHGAL` + `KETJU` evoliucinius trekus (Lahén et al. 2025); spalvos atitinka amžiaus intervalus: <10 Myr (raudona), 10–30 Myr (žalia), 30–100 Myr (žydra) ir >100 Myr (violetinė). Visose panelėse įtraukti tik $\Pi > 1$ kriterijų atitinkantys spiečiai.

spiečių masės–spindulio sąryšis nepriklauso nuo galaktocentrinio atstumo.

M 33 spiečiams ($t \geq 100$ Myr; žr. 6.6 pav.c) gauname panašų, kiek statesnį sąryšį $R_{50} \propto \mathrm{M}^{0.21 \pm 0.02}$, o PT jis beveik išnyksta: $R_{50} \propto \mathrm{M}^{0.06 \pm 0.01}$. Nors dėl skirtingų metodų, instrumentų bei imčių dydžių negalime pateikti tvirtų išvadų, M 31, M 33 ir PT palyginimas rodo, kad spiečių masės–spindulio sąryšis tarp Vietinės grupės galaktikų gali reikšmingai skirtis. Kartu su plačia rezultatų įvairove kitose artimose galaktikose, galima manyti, kad šis sąryšis priklauso nuo galaktinės aplinkos. Skirtumus gali lemti tokie veiksniai kaip taržvaigždinės terpės slėgis, dujų tankis, metalingumas, potvyninės jėgos, turbulencija ar žvaigždėdaros sąlygos. Nors M 31 diske aplinkos įtakos nerandame, platesnis skirtingų galaktikų palyginimas rodo, kad globalūs galaktikos masto efektai gali būti svarbūs. Todėl ateityje reikalingi tolimesni teoriniai tyrimai, siekiant geriau suprasti masės–spindulio sąryšio kilmę įvairiose aplinkose ir siekiant paaiškinti plačią stebėjimų įvairovę.

Išvados

Kadangi didelė dalis žvaigždžių formuojasi spiečiuose, jie gerai tinka tirti galaktikų diskų formavimąsi bei evoliuciją. Apertūrinė fotometrija yra vienas efektyviausių metodų tiriant dideles užgalaktinių spiečių imtis, apimančias plačius masių, amžių ir aplinkos sąlygų intervalus. Šis metodas, pagrįstas stebėjimų ir teorinių modelių integralinės fotometrijos palyginimu, plačiai naudojamas užgalaktinių žvaigždžių spiečių fiziniams parametrams nustatyti. Vis dėlto, praktinės metodo ribos, kurias daugiausia lemia spiečių stochastiniai ir dangaus fono efektai, iki šiol nebuvo pilnai atskleistos.

Šiame darbe sukūrėme didelį realistiškų stochastinių žvaigždžių spiečių modelių banką ir atlikome jų sintetinius stebėjimus. Visas tyrimas buvo atliekamas imituojant realias M 31 Panchromatic *Hubble* Andromeda Treasury (PHAT) apžvalgos sąlygas (Dalcanton et al. 2012; Johnson et al. 2012, 2015). Mes ištyrėme apertūrinės fotometrijos metodo taikymo ribotumus spiečių galaktikų diskuose tyrimui. Išnagrinėjome idealizuotas sąlygas (neatsižvelgiant į dangaus fono problematiką) siekdami nustatyti didžiausią įmanomai pasiekiamą tikslumą, kurį lemia mažos masės ($<10^4\,M_\odot$) spiečių stochastinė prigimtis.

Parodėme, kad spiečiai, turintys pagrindinę seką palikusių (PMS) žvaigždžių, pasižymi gerokai didesne integralinių fotometrinių parametrų sklaida nei spiečiai be tokių žvaigždžių. Taip pat nustatėme, kad adaptyvios apertūrinės fotometrijos metodas (Naujalis et al. 2021; Kriščiūnas et al. 2023) nesukuria sistematinių spalvos rodiklių gradientų ir efektyviai sumažina ryškių lauko žvaigždžių bei evoliucionavusių spiečiaus narių sukeliamą fotometrinę taršą, o tai sudaro sąlygas tikslesniems fotometriniams matavimams. Nustatėme, kad šis matavimo metodas tinka mažos masės spiečių tyrimams artimose galaktikose ($\lesssim$5 Mpc), jei apertūros atidžiai parenkamos individualiai kiekvienam spiečiui.

Parodėme, kad labai jaunų žvaigždžių spiečių fizinius parametrus sunku patikimai nustatyti naudojant vien apertūrinę fotometriją, todėl išskiriamiems ar pusiau išskiriamiems į žvaigždes jaunesniems nei $\sim$40 Myr spiečiams papildomai reikia naudoti ir CMD analizės metodą (pvz. Johnson et al. 2016; Čeponis et al. 2024). Tiksliausi spiečių parametrai gaunami kartu derinant abu metodus.

Tipinių mažos masės spiečių stebėjimo krypties atsitiktinumas vidutiniškai sukelia iki $\sim$0.05 mag spalvos rodiklių neapibrėžtumus, o individualiais atvejais net $\sim$0.1 mag. Struktūrinių parametrų atveju sklaida dėl šio efekto gali siekti $\sim$20%. Tačiau šie efektai paprastai yra mažiau reikšmingi už žvaigždžių masių ir erdvinio pasiskirstymo stochastiškumo sukeliamą poveikį.

Patalpindami stochastinius spiečių modelius į tikrus PHAT fono laukus, ištyrėme dangaus fono įtaką apertūrinės fotometrijos tikslumui. Parodėme, kad tipinėje M 31 disko aplinkoje patikimus amžiaus, masės ir ekstinkcijos įverčius (esant žinomam metalingumui) galima nustatyti spiečiams, kurių M $\gtrsim$ 1600 $M_\odot$ ties 1 Gyr ir M $\gtrsim$ 500 $M_\odot$ ties 100 Myr. Tuo tarpu, spiečiams 500 $\lesssim$ M $\lesssim$ 1600 $M_\odot$ ties 1 Gyr ir 200 $\lesssim$ M $\lesssim$ 500 $M_\odot$ ties 100 Myr apertūrinės fotometrijos metodu galima nustatyti tik apytikslius amžiaus ir masės įverčius.

Taip pat parodėme, kad matavimai su apertūromis, mažesnėmis už pusės šviesio spindulį R_{50}, yra labai jautrūs stochastiniams ir fono efektams, jų reikėtų nenaudoti. Charakteringo dydžio spiečių spalvos rodiklių matavimui optimalūs apertūrų spinduliai yra ~(1–2)×R_{50}.

Mūsų analizė atskleidė, kad katalogų pilnumo ribos ir selekcijos efektai priklauso nuo vietinės aplinkos galaktikos diske. M 31 disko atveju, ties 1 Gyr amžiumi spiečių masės funkciją galima patikimai atkurti iki ~500 $M_\odot$ retose išorinio disko srityse, iki ~1500 $M_\odot$ žvaigždėdaros regionuose ir tik iki ~3000 $M_\odot$ tankioje centrinėje disko dalyje. Tai rodo, kad aplinkos nulemtas katalogo pilnumo variacijas būtina atidžiai įvertinti tiriant disko spiečių populiacijas.

Tirdami žvaigždžių spiečių struktūrinę evoliuciją M 31 diske, parodėme, kad gravitaciškai surišti spiečiai per pirmuosius ~30 Myr sparčiai plečiasi: jų R_{50} padidėja daugiau nei du kartus – nuo ~0.6 pc iki ~1.6 pc. Manome, kad jų ankstyvą evoliuciją daugiausia lemia vidiniai procesai – žvaigždžių evoliucija ir spiečiaus žvaigždžių tarpusavio dinaminė sąveika. Tai gerai sutampa su Paukščių Tako jaunų spiečių tyrimo rezultatais (Della Croce et al. 2024), kur pagal *Gaia* kinematiką taip pat nustatytas spartus plėtimasis per panašų ~30 Myr laikotarpį.

Taip pat ištyrėme M 31 disko spiečių masės–spindulio sąryšį. Parodėme, kad senesni nei 100 Myr spiečiai pasižymi silpnu, bet aiškiu sąryšiu – $R_{50} \propto M^{0.18\pm0.01}$. Nustatėme, kad šis sąryšis neturi reikšmingos radialinės priklausomybės galaktikos diske.

Apibendrinant, darbo rezultatai suteikė daug naujų žinių apie praktines apertūrinės fotometrijos tikslumo ir pritaikomumo ribas užgalaktinių žvaigždžių spiečių tyrimui. Mūsų rezultatai bus naudingi planuojant būsimas dangaus apžvalgas, interpretuojant archyvinius duomenis ir kuriant naujus spiečių aptikimo bei matavimo metodus. Mūsų M 31 disko spiečių analizė rodo, kad tinkamai įvertinus stochastinius ir fono efektus, apertūrinė fotometrija yra patikimas bei efektyvus metodas, įgalinantis sėkmingai tirti žvaigždžių spiečių populiacijas ir jų galaktikų diskų evoliuciją.

Curriculum Vitae

Name:	Karolis
Surname:	Daugevičius
Place of birth:	Klaipėda, Lithuania
E-mail:	karolis.daugevicius@ftmc.lt

Education:

2022 – 2026	Center for Physical Sciences and Technology (FTMC) *Ph.D. studies*.
2020 – 2022	Vilnius University, Faculty of Physics *Master's degree (Cum Laude)*.
2016 – 2020	Vilnius University, Faculty of Physics *Bachelor's degree*.
2012 – 2016	Klaipėda Ąžuolynas Gymnasium *High school education*.

Work experience:

2024-01 – now	Center for Physical Sciences and Technology, *Junior Researcher*.
2022-10 – 2024-01	Center for Physical Sciences and Technology, *Senior Engineer*.
2020-10 – 2022-10	Center for Physical Sciences and Technology, *Engineer*.
2020-07 – 2025-01	Lithuanian Museum of Ethnocosmology, *Tour guide*.
2019-07 – 2020-07	Center for Physical Sciences and Technology, *Technician*.

Gyvenimo aprašymas

Vardas:	Karolis
Pavardė:	Daugevičius
Gimimo vieta:	Klaipėda, Lietuva
El. paštas:	karolis.daugevicius@ftmc.lt

Išsilavinimas:

2022 – 2026	Fizinių ir technologijos mokslų centras (FTMC), Megasistemų fizikos laboratorija, *Doktorantura.*
2020 – 2022	Vilniaus universitetas, Fizikos fakultetas, *Fizikos magistro laipsnis (Cum Laude).*
2016 – 2020	Vilniaus universitetas, Fizikos fakultetas, *Fizikos bakalauro laipsnis.*
2012 – 2016	Klaipėdos Ąžuolyno gimnazija, *Vidurinis išsilavinimas.*

Profesinė veikla:

2024-01 – dabar	Fizinių ir technologijos mokslų centras (FTMC), *Jaunesnysis mokslo darbuotojas.*
2022-10 – 2024-01	Fizinių ir technologijos mokslų centras (FTMC), *Vyresnysis inžinierius.*
2020-10 – 2022-10	Fizinių ir technologijos mokslų centras (FTMC), *Inžinierius.*
2020-07 – 2025-01	Lietuvos etnokosmologijos muziejus, *Ekskursijų vadovas.*
2019-07 – 2020-07	Fizinių ir technologijos mokslų centras (FTMC), *Technikas.*

NOTES

NOTES

NOTES

NOTES

Vilnius University Press
Saulėtekio al. 9, LT-10222 Vilnius
e-mail: info@leidykla.vu.lt, www.leidykla.vu.lt
www.bookshop.vu.lt, www.journals.vu.lt
Print run copies 15